

# Tuning Emulsion Chemistry to Control Electrospun Fiber Morphology, Topography, and Drug Release

By

© 2021

Pamela M. Johnson

B.S. Chemical Engineering, Bucknell University, 2017

Submitted to the graduate degree program in Bioengineering and the Graduate Faculty of the University of Kansas in partial fulfillment of the requirements for the degree of Doctor of Philosophy.

---

Chair: Jenny Robinson, Ph.D.

---

Stevin Gehrke, Ph.D.

---

Prajna Dahr, Ph.D.

---

Mike Hageman, Ph.D.

---

Audrey Lamb, Ph.D.

Date Defended: April 26<sup>th</sup>, 2021

The dissertation committee for Pamela M. Johnson certifies that this is the approved version of the following dissertation:

Tuning Emulsion Chemistry to Control Electrospun Fiber Morphology,  
Topography, and Drug Release

---

Chair: Jenny Robinson, Ph.D.

---

Stevin Gehrke, Ph.D.

---

Prajna Dahr, Ph.D.

---

Mike Hageman, Ph.D.

---

Audrey Lamb, Ph.D.

Date Accepted: May 13<sup>th</sup>, 2021

## ABSTRACT

Electrospinning is a complex fabrication technique capable of producing non-woven mesh with fiber diameters in the nanometer to micrometer scale. Applications for mesh with fibers at this scale are promising in many fields, including tissue engineering and drug delivery. Emulsion electrospinning is a subset of electrospinning and is particularly promising for drug delivery applications because it facilitates encapsulation of aqueously soluble drugs such as peptides and proteins and maintains the bioactivity of the encapsulated macromolecules. Although emulsion electrospinning has successfully been used to encapsulate macromolecules, a mechanistic understanding of how each compositional parameter in emulsions impact the resulting mesh characteristics has not been fully explored. The studies in this embodied work evaluate the effect of each component of emulsion solution chemistry on mesh characteristics. Specifically, solution chemistry components in water-in-oil emulsions, including the composition of the organic phase, the mobility and chemistry of surfactants, and the internal phase volume fraction, were evaluated. The effect of emulsion solution chemistry at varying relative humidity levels was also explored to determine the interrelated impacts of solution chemistry and humidity on the electrospinning process. Mesh characteristics of fiber morphology, surface topography, fiber volume fraction, and diameter were all evaluated because they are all capable of affecting cell response and drug release profiles. Drug release and drug loading of both a hydrophobic and hydrophilic model drug were also evaluated in systems created with different processing parameters.

The results indicate that each component in an emulsion must be carefully selected for a given system, as they all affect mesh characteristics. The conductivity and evaporation of the organic phase solvent played a prominent role in determining the size and morphologies of electrospun fibers. The surfactant chemistry and ability to relocate to both the surface of the fibers

and the interfacial areas was also important in producing meshes with controlled and consistent characteristics. The impact of internal phase volume fraction changed depending on other factors in the system, highlighting the sensitivity of an emulsion electrospinning system to its tuning parameters. The drug release and loading were both altered by surfactant, offering a view of how emulsion electrospinning could be used to tailor therapeutic release profiles. Including an internal phase improved burst effects for the hydrophilic model drug. Overall, these studies demonstrate the importance of compositional control of emulsions to dictate emulsion electrospun mesh characteristics. Tuning electrospun meshes with solution chemistry is a promising method for additional control of electrospun fibers and new areas of application such as drug delivery and cell response.

## ACKNOWLEDGEMENTS

Conducting research at the graduate level is such a privilege, and I am forever grateful for this incredible journey. From exploring the theoretical principles underlying scientific data to evaluating studies critically, my understanding has grown in leaps and bounds through the doctoral experience. This growth was possible due to the extraordinary support and mentorship of my advisor, committee members, Bioengineering program, lab team, and family.

I am deeply grateful for my phenomenal advisor, Dr. Jenny Robinson, who encouraged me, challenged me, and consistently pushed me to unlock potential in ways I could never imagine. She nurtured me as a scientist and as a mentor, clearing a path for both my personal growth and for sharing my enthusiasm and knowledge with other students. Her never-ending energy and search for what is possible have taught me to seek out every opportunity to pursue areas I am passionate about. Through her compassionate communication, I do not doubt that I am just one of many whose lives will be touched by Dr. Robinson's drive to encourage and support young women interested in pursuing careers in science.

I would like to thank my committee of brilliant and supportive faculty who helped me grow throughout my time at KU. Dr. Stevin Gehrke taught me the fundamentals of polymers and, through his targeted questions, a better understanding when evaluating my research studies. Dr. Mike Hageman has been excellent in helping me think through the drug release effects, mentorship through the NIH T32 training program, and professional development by bringing world-class speakers for the Roadmap to Drug Discovery class. I enjoyed working for Dr. Prajna Dhar in her heat transfer class as a graduate teaching assistant. She is incredibly perceptive in her ability to ask

just the right questions to get students to think more deeply and self-discover their understanding of concepts. More than once, her kind approach and astute people skills resulted in getting to the heart of the matter and moments of enlightenment for her students – and myself. Dr. Audrey Lamb is a mentor and a fabulous role model. As a strong researcher, she knows what it takes to progress and has gone out of her way multiple times to provide guidance and professional advice. I've had the pleasure of learning from her in the classroom and outside it when considering a career path through the Biotechnology Certificate Program and graduate studies/senate leadership.

I would also like to thank the support of the University of Kansas and the Bioengineering Program. Denise Bridwell, our program coordinator, has believed in me, advocated on my behalf, and helped me get to where I am today. Her dedication to the program and endless encouragement energized me. She is both wonderful as a person and very good at what she does. Dr. Ken Fischer, our program director, has gone out of his way time and time again to support me through recommendation letters and award nominations. Knowing he was cheering for me, such as during the Three Minute Thesis finalist competition, gave me the confidence to strive for more and consistently do my very best.

I am thankful to all the lab members of the Robinson lab. In particular, Dr. Kelsey Knewton is thoughtful, kind, and one of the best bakers I have ever met. She went out of her way to *volunteer* to proofread my dissertation, which is an incredibly generous gift. Phil Elrod has helped me with future directions for developing a device to cryofracture electrospun fibers. He also has a habit of going out of his way to help others – including once during a snowstorm with a dead car battery – driving me to campus to complete research on time. To other graduate lab members Jesus Gonzalez Flores, Jenn Robinson, Jacob Hodge, Kevin Chavez, and John Bradford, whose camaraderie, support, and discussions made lab work more meaningful. To undergraduate lab members Joe

Fritz, Katie Donnelly, Anna Troffimoff, Vy Ly, and Austin Abbott, whom I have had the pleasure of both mentoring and learning from and who have helped progress the research to where it is today. A special thank you goes out to Justin Lehtinen, an undergraduate student whom I have watched grow into an exceptional scientist over the past four years while working together. He has spent many late nights in the lab helping gather data and asking questions that have made me critically think through my study designs and analysis of the results.

I would like to thank the Howard Hughes Medical Institute Gilliam Fellowship and National Institutes of Health Pharmaceutical Aspects of Drug Delivery Training Program for financially supporting my doctoral studies and creating a community of support and collaboration among peer graduate students. These opportunities open the door to scientists of all backgrounds to pursue their dreams, push the boundaries of new research, and help the community around me.

I sincerely appreciate my parents for their constant encouragement while I pursued my passion and education. They unfailingly picked up the phone at all hours and listened to my venting about failed experiments and exhaustion, and they responded with sage wisdom that kept me going. Finally, I would like to thank my fiancé Ethan Blumer, an amazingly gifted individual, for his unwavering support. Throughout my studies, he not only did more than his fair share of household chores to give me the time I needed to focus in the lab, but he spent countless late nights proofing abstracts, listening to me practice presentations, and knowledgeably providing just the right feedback that helped me achieve this goal.

## NOMENCLATURE

AlCl <sub>3</sub>	Aluminum chloride
AFM	Atomic force microscopy
ALP	Alkaline phosphatase
ANOVA	Analysis of variance
BMSC	Bone derived mesenchymal stem cells
BSP	Bone sialoprotein
CaCl <sub>2</sub>	Calcium Chloride
CHCl <sub>3</sub>	Chloroform
CLFM	Confocal laser scanning microscopy
DAPI	4',6-Diamidino-2-phenylindole
DCM	Dichloromethane
DMF	N, N-Dimethylformamide
DNA	Deoxyribose nucleic acid
FA	Formic acid
FDA	Food and Drug Administration
FGF-2	Fibroblast growth factor
GAG	Glycosaminoglycans
GFAP	Glial fibrillary acidic protein
HEPA	High efficiency particulate air
HFIP	1,1,1,3,3,3-Hexafluoro-2-isopropanol
HLB	Hydrophilic lipophilic balance
HMHEC	Hydroxyethyl cellulose
hMSC	Human mesenchymal stem cells
HTAB	Hexadecyl trimethyl ammonium bromide
Li	Lithium



LiCl	Lithium chloride
MeOH	Methanol
MPEG	Methoxy poly(ethylene glycol)
MSC	Mesenchymal stem cells
NIPS	Non-solvent induced phase separation
NSCs	Neural progenitor/stem cells
OCN	Osteocalcin
O/W	Oil in Water
PAN	Polyacrylonitrile
PDLLA	Poly(DL-lactide)
PEO	Polyethylene oxide
PES	Polyethersulfone
PGPR	Polyglycerol polyricinoleate 4125
PLA	Poly(lactic acid)
PLGA	Poly(lactic-co-glycolic acid)
PLLA	Poly(L-lactide)
PLLACL	Poly(L-lactide-co-e-caprolactone)
Pluronic-F108	Poly(ethylene glycol)-block-poly(propylene glycol)-block-poly(ethylene glycol)
POC	Pre-osteoblast cells
PS	Polystyrene
PVA	Polyvinylalcohol
PVB	Polyvinyl butyral
PVDF	Polyvinylidene fluoride
RNA	Ribonucleic acid
RO	Reverse osmosis
RPM	Revolutions per minute
SDS	Sodium dodecyl sulfate
SEM	Scanning electron microscopy

Span 40	Sorbitan monopalmitate
Span 80	Sorbitan monooleate
Span 85	Sorbitan trioleate
TBAB	Tetrabutylammonium bromide
TBAC	Tetrabutylammonium chloride
TCP	Tricalcium phosphate
TCPS	Tissue culture polystyrene
TEAC	Tetraethylammonium chloride
THF	Tetrahydrofuran
TIPS	Thermally induced phase separation
Triton X-100	Octyl phenol ethoxylate
VIPS	Vapor induced phase separation
W/O	Water in Oil

## TABLE OF CONTENTS

	Page
ABSTRACT.....	iii
ACKNOWLEDGEMENTS.....	v
NOMENCLATURE.....	viii
TABLE OF CONTENTS.....	xi
LIST OF FIGURES.....	xiii
LIST OF TABLES.....	xxvi
CHAPTER 1: INTRODUCTION AND BACKGROUND.....	1
1.1 Applications of Electrospinning.....	1
1.2 History of Electrospinning.....	15
1.3 Electrospinning Mechanism.....	16
1.4 Parameters Affecting the Collection of Electrospun Mesh.....	18
1.5 Electrospun Mesh Characteristics.....	28
1.6 Knowledge Gap.....	37
1.7 Approach.....	38
1.8 Bibliography.....	40
CHAPTER 2: DETERMINING THE ROLE THAT SOLVENT VOLATILITY, CONDUCTIVITY, SOLUBILITY, AND MISCIBILITY PLAY IN ELECTROSPUN FIBER DIAMETER AND MORPHOLOGY.....	48
2.1 Introduction.....	48
2.2 Materials and Methods.....	54
2.3 Results and Discussion.....	59
2.4 Conclusion.....	81
2.5 Bibliography.....	83
CHAPTER 3: DETERMINING THE ROLE OF NON-IONIC SURFACTANT LOCATION AND CHEMISTRY IN ELECTROSPINNING.....	86
3.1 Introduction.....	86
3.2 Materials and Methods.....	96
3.3 Results and Discussion.....	103
3.4 Conclusion.....	153

3.5 Bibliography.....	154
3.6 Appendix.....	156
CHAPTER 4: DETERMINING THE EFFECTS OF INCREASING INTERNAL PHASE VOLUME FRACTION ON FIBER MORPHOLOGY, SURFACE TOPOGRAPHY, AND DIAMETER.....	158
4.1 Introduction.....	158
4.2 Materials and Methods.....	162
4.3 Results and Discussion.....	165
4.4 Conclusion.....	214
4.5 Bibliography.....	218
CHAPTER 5: DETERMINING THE EFFECTS OF DRUG RELEASE FROM POROUS ELECTROSPUN FIBERS AND COMPARING RELEASE OF HYDROPHILIC AND HYDROPHOBIC MODEL DRUGS.....	221
5.1 Introduction.....	221
5.2 Materials & Methods.....	226
5.3 Results and Discussion.....	235
5.4 Conclusion.....	256
5.5 Bibliography.....	257
CHAPTER 6: CONCLUSIONS.....	259
6.1 Summary.....	259
6.2 Significance of Work.....	260
6.3 Future Directions and Challenges.....	265

## LIST OF FIGURES

- Figure 1.1: A. MSC in chondrogenic culture seeded on electrospun mesh with fiber diameters of  $440 \pm 20$  nm and  $4300 \pm 800$  nm at seeding densities of 100k, 500k, 2000k, and 4000k for 3 weeks and 6 weeks, a. cross-sections mesh with cells seeded at 400k, for 6 weeks, and stained with DAPI nuclear staining (blue), b. total cellular DNA content c. total GAG content, d. total collagen content. B. Schwann cells seeded on electrospun mesh with fiber diameters of  $293 \pm 65$ ,  $759 \pm 179$  nm, and  $1325 \pm 383$  nm, a. neurofilament-stained cells, b. migration distance, and c. neurite length and cell migration. C. NSCs seeded on control TCP and electrospun mesh with diameters of  $283 \pm 45$  nm,  $749 \pm 153$  nm,  $1452 \pm 312$  nm, and a. stained with Ki-67 antibody (pink) and nestin (green) b. fraction of positive stained markers nestin, Tuj-1, RIP, and GFAP c. relative proliferation with 0, 5, and 20 ng/mL FGF-2. Figures reproduced with permission and originally published by A. Bean et al. in *Biomedical Materials*<sup>29</sup> B. Wang et al. in *Acta Biomaterialia*,<sup>30</sup> C. and Christopherson et al. in *Biomaterials*.<sup>31</sup> ..... 5
- Figure 1.2: Electrospun fibers with smooth topography, 153 nm shish kebob topography, and 338 nm shish kebob topography A. SEM images of fiber topography B. SEM images of TCP mineralization C. BMSC with F-actin stain (red) and nucleus stain (blue) D. BMSC cultured in osteogenic induction medium and stained for OCN (red) and nuclei (blue) E. proliferation of BMSC after 1, 4, and 7 days F. differentiation of BMSC in osteogenic induction medium measured by OCN and ALP biomarkers. Figures originally published by Liu et al. in *European Polymer Journal* and reproduced with permission.<sup>32</sup> ..... 8
- Figure 1.3: A. Electrospun mesh with smooth fibers fabricated with PLA, with 70:30 PLA: chitosan and 70:30 PLA: chitosan with island topography. A-C. SEM images of topography, D-F. adherence of POCs stained with TRITC-phalloidin (red) and DAPI nucleus (blue), G. OCN expression in POCs cultured for 7 and 14 days, H. ALP activity of POCs cultured for 3, 7, 14, and 21 days. Figures reproduced with permission and originally published by Xu et al. in *ACS Applied Materials & Interfaces*.<sup>33</sup> ..... 10
- Figure 1.4: Electrospun mesh with increasing surface topography A-C. SEM images showing increasing surface topography, D-F. representative fluorescent images of POCs stained with F-actin (red) and cell nucleus (blue), G. ALP activity after 7 and 21 days. Genetic expression at 7 and 21 days of H. BSP I. RUNX2 J. COL-1A1. Figures reproduced with permission and originally published by Chen et al. in *Acta Biomaterialia*.<sup>35</sup> ..... 11
- Figure 1.5: Fluorescent images of fibroblasts cell growth after 1, 3, and 5 days of cell culture on the different substrates: (a) TCPS, (b) Glass coverslips, (c) PDLLA films, (d) PDLLA fibers, (e) chitosan fibers, and (f) chitosan /PDLLA dual-layer fibers. Figure reproduced with permission and originally published by Chen et al. in the *Journal of Membrane Science*.<sup>24</sup> ..... 12

Figure 1.6: Schematic of electrospinning set up and resulting electrospun mesh. Figure modified from a figure published by Johnson et al. in <i>Biomaterials Science</i> and reproduced with permission. <sup>47</sup> .....	16
Figure 1.7: Electrospinning variables categorized by solution parameters, process parameters, and surrounding conditions that influence fiber diameter, morphology, and internal architecture. Figure originally published by Vellayappan et al. in <i>RCS Advances</i> and reproduced with permission. <sup>57</sup> .....	19
Figure 1.8: Schematic demonstrating the effect of increasing voltage on the Taylor cone shape. Figure originally published by Sill et al. in <i>Biomaterials</i> and reproduced with permission. ....	20
Figure 1.9: Taylor cone shape change with increasing flow rate. Figure originally published in <i>Advanced Drug Delivery Reviews</i> by Rutledge et al. and reproduced with permission. <sup>63</sup> .....	21
Figure 1.10: A. Schematic describing the VIPS mechanism for templating fiber porosity. B. Schematics describing the TIPs mechanism in a ternary phase diagram superimposed with spinodal and binodal curves and phase diagram and resulting polymer film morphology from passing through the homogeneous region and the unstable region. Figures reproduced with permission and originally published by A. Yazgan et al. in <i>Scientific Reports</i> , B. a. Fashandi et al. in <i>Polymer</i> , and b. Kim et al. in <i>AICHE Journal</i> . <sup>58,75,78</sup> .....	25
Figure 1.11: SEM images of A. smooth, B. shish kebab, C. island-like, D. lamellar, E-H. porous, I-J. longitudinal wrinkle, and K-L. cactus-like electrospun fiber topographies. All images reproduced with permission and originally published by A,E. Chen et al. in <i>Biomaterialia</i> , B. Liu et al. in 2021, C. Xu et al. in <i>Applied Material and Interfaces</i> , D. Elishav in 2019, F,G,I. Yazgan et al. in 2017, H,J,K. Zaarour et al. in 2018, and L. Mobasheri et al. in 2019. <sup>32,33,35,75,76,91,92,95</sup> .....	29
Figure 1.12: SEM images illustrating the effect of increasing polymer concentration on fiber morphology. As the concentration of polymer increased, morphology transitioned from droplets to bead on string to cylindrical fibers. Image reproduced with permission and originally published by Chen et al. in <i>Journal of Membrane Science</i> . <sup>24</sup> .....	31
Figure 1.13: (a) Image of the electrospinning jet demonstrating secondary branching occurring during the electrospinning flight. (b) Reconstructed rendering of the electrospinning jets with branching shown in part a. Figure originally published by Yarin et al. in the <i>Journal of Applied Physics</i> and reproduced with permission. <sup>97</sup> .....	32
Figure 1.14: A. Schematic of electrospun fiber flattening into a ribbon morphology as it dries. B. SEM images of ribbon morphology seen in electrospun fibers. C. Fiber branching observed in ribbon shaped fibers. Figures originally published by Koombhongse et al. in the <i>Journal of Polymer Science</i> and reproduced with permission. <sup>69</sup> .....	33
Figure 1.15. A. Mechanism of nanoweb formation proposed by free droplet expansion in an electric field. B. SEM image of nylon-6 electrospun fibers with nanowebbing. C. High magnification of nanowebs shown in B. Figures originally published by Ding et al. in <i>Nanotechnology</i> and reproduced with permission. <sup>102</sup> .....	35

Figure 1.16. A. SEM images representing nanoweb formation with increasing concentrations of TBAC (a. 0.02 mol/L, b. 0.05 mol/L, c. 0.10 mol/L, d. 0.15 mol/L). B. Figure is illustrating fiber branching as a mechanism for nanowebbing. C. High-speed image of electrospun jets containing a. polymer solution with no salt and b. polymer solution with salt. Figures originally published by Li et al. in <i>Materials and Design</i> and reproduced with permission. <sup>105</sup> .....	36
Figure 1.17: A. Formation of nanowebbs between neighboring jets during electrospinning collection mechanism. B. Collection of nanowebbs produced with multiwall carbon nanotubes. Figures originally published by Massaglia et al. in <i>RCS Advances</i> and reproduced with permission. <sup>107</sup> .....	37
Figure 2.1: Polystyrene electrospun fibers fabricated with increasing ratios of solvents THF: DMF demonstrating the topographical and morphological effects of solvent volatility and conductivity. Figure originally published by Liu et al. and reproduced with permission. <sup>14</sup> .....	51
Figure 2.2: Formation of clogging at the needle tip over time caused by rapid evaporation of the solvent. Figure reproduced from the thesis of Knopf 2009 with permission. <sup>23</sup> .....	53
Figure 2.3: Representative SEM images of electrospun fibers fabricated with solvents CHCl <sub>3</sub> , DCM, 3:1 CHCl <sub>3</sub> : MeOH, 3:1 CHCl <sub>3</sub> : DMF.....	60
Figure 2.4: SEM images of electrospun fibers fabricated with DCM at low and high relative humidity, highlighting the morphological presence of branching and beading at high relative humidity. ....	62
Figure 2.5: SEM images of electrospun fibers fabricated with 3:1 CHCl <sub>3</sub> : DMF at low and high relative humidity. ....	63
Figure 2.6: SEM images of electrospun fiber fabricated with 3:1 CHCl <sub>3</sub> : MeOH at low and high relative humidity. ....	65
Figure 2.7: Fiber topography of electrospun fibers fabricated with CHCl <sub>3</sub> , DCM, 3:1 CHCl <sub>3</sub> : DMF, and 3:1 CHCl <sub>3</sub> : MeOH at low and high relative humidity.....	66
Figure 2.8: Fiber diameter of samples electrospun in CHCl <sub>3</sub> solvent at high and low relative humidity compared with Welch's test. * p ≤ 0.05; ** p ≤ 0.01; *** p ≤ 0.001; ****p ≤ 0.0001.....	69
Figure 2.9: Representative SEM images of samples electrospun in solvents CHCl <sub>3</sub> , DCM, 3:1 CHCl <sub>3</sub> : DMF, 3:1 CHCl <sub>3</sub> : MeOH at high and low relative humidity. Overall average fiber diameter for each set of parameters. Histograms were constructed to display the distribution of all fiber diameters measured for each sample group.....	70
Figure 2.10: Fiber diameter of samples electrospun in DCM solvent at high and low relative humidity compared with Welch's test. * p ≤ 0.05; ** p ≤ 0.01; *** p ≤ 0.001; ****p ≤ 0.0001.....	71
Figure 2.11: Fiber diameter of samples electrospun in 3:1 CHCl <sub>3</sub> : DMF solvent at high and low relative humidity compared with Welch's test. * p ≤ 0.05; ** p ≤ 0.01; *** p ≤ 0.001; ****p ≤ 0.0001 .....	72
Figure 2.12: Fiber diameter of samples electrospun in 3:1 CHCl <sub>3</sub> : MeOH solvent at high and low relative humidity compared with Welch's test. * p ≤ 0.05; ** p ≤ 0.01; *** p ≤ 0.001; p ≤ 0.0001 .....	73

Figure 2.13: Analysis of fiber diameter electrospun in solvents CHCl <sub>3</sub> , DCM, 3:1 CHCl <sub>3</sub> : DMF, 3:1 CHCl <sub>3</sub> : MeOH at high and low relative humidity. * p ≤ 0.05; ** p ≤ 0.01; *** p ≤ 0.001; p ≤ 0.0001 .....	74
Figure 2.14: Representative SEM images of samples electrospun in solvents CHCl <sub>3</sub> , DCM, 3:1 CHCl <sub>3</sub> : DMF, 3:1 CHCl <sub>3</sub> : MeOH at high and low relative humidity, and representative fiber collection on collection plate (white circles). Increasing conductivity and relative humidity demonstrate larger collection areas, indicating a greater amplitude of whipping or multiple fiber jets/branching.....	75
Figure 2.15: Representative SEM images of electrospun mesh fabricated with increasing collection needle tip to collection plate distances of 15, 20, 25, and 30 cm and at applied voltages of 12, 15, 18, 21, 24 kV. ....	77
Figure 2.16: Heat map of average fiber diameters in μm illustrating the effects of collection distance and applied voltage. ....	79
Figure 3.1: Graphs demonstrating the effect of surfactant concentration on fiber diameter and A. solution conductivity for anionic surfactant (SDS), cationic surfactant (HTAB), and non-ionic surfactant Triton X-100 B. surface tension for non-ionic surfactant Triton X-100. Data replotted from A. Zheng et al. and B. Wang et al. <sup>9,12</sup> .....	90
Figure 3.2: A. Schematic of a cross-sectional emulsion electrospun fiber with surfactant arranged both with the internal phase and at the surface of the fiber. B. Schematic of the emulsion electrospinning process with surfactant relocation to the surface of the fiber. C. AFM images of fibers with no surfactant and surfactant demonstrating smoothing of the surface. D. SEM Cross-sectional images of fibers with 2.5%, 7.5%, and 15% w/w surfactant electrospun at 60% relative humidity showing smooth surface with increasing surfactant. E. SEM images of electrospun fibers fabricated at high relative humidity with no surfactant and surfactant showing reduced porosity with surfactant. Figures reproduced with permission and originally published by A& C Li et al. in 2009 in <i>Colloids and Surfaces B: Biointerfaces</i> , B. Li et al. in 2010 in <i>Colloids and Surfaces B: Biointerfaces</i> , D. by Yazgan et al. in <i>Polymer</i> , E. Johnson et al. in <i>Biomaterials Science</i> . <sup>4,7,11,25</sup> .....	92
Figure 3.3: Graphs of water droplet contact angle on electrospun fibers versus A. time for samples with and without surfactant, B. time for increasing concentration of surfactant, C. concentration of non-ionic surfactant Triton-X fabricated with solvents formic acid (FA) and 2:1 FA: DCM, D. concentration of cationic surfactant TEBAC, anionic surfactant SDS, and non-ionic surfactants Span 80 and Pluronic F108, E. time for samples fabricated with no surfactant and no internal phase and with Span 80 and 4% w/o internal phase all with polymers PCL, PLGA, PLA, and 7:3 PLA: PLGA. Figure D replotted from data provided by Hu et al. <sup>10</sup> The other figures were reproduced with permission and originally published by A. Li et al. in <i>Colloids and Surfaces B: Biointerfaces</i> , B. Vasita et al. in <i>Polymer</i> , C. Beigmoradi et al. in <i>Polymer</i> , E. Coimbra et al. in <i>Material Science &amp; Engineering C</i> , F. Johnson et al. in <i>Biomaterials Science</i> . <sup>4,6,8,30,31</sup> .....	94



Figure 3.4: Chemical structures of non-ionic surfactants with increasing HLB values drawn with ChemDraw software. General non-polar regions are colored in pink and general polar regions are shaded in blue. Brackets indicate potentially repeating groups. .... 97

Figure 3.5: Representative SEM images showing the topography of electrospun fibers fabricated with CHCl<sub>3</sub> solvent at high (50% ± 10%) and low (10% ± 10%) relative humidity. Electrospun fibers show the effect of increasing internal phase volume fraction through fibers fabricated with no surfactant and 0% w/o internal phase control and with surfactant at volume fractions of 0, 2, 4, and 8% w/o internal phase. Scale bars are different sizes to visually display representative surface topography given the difference in fiber diameter scale..... 104

Figure 3.6: SEM images depicting the surface topography of electrospun fibers fabricated with CHCl<sub>3</sub> solvent, Span 80 surfactant, and no internal phase at a relative humidity of 11, 17, 43, 51, and 54%. Surface topography transitions as the surface of the polymer jet is saturated with water at higher relative humidity..... 105

Figure 3.7: Fiber volume fraction of electrospun mesh fabricated with CHCl<sub>3</sub> solvent without surfactant and with surfactant at internal phase volume fractions of 0, 2, 4, and 8% w/o at A. high relative humidity and B. low relative humidity. \* p ≤ 0.05; \*\* p ≤ 0.01; \*\*\* p ≤ 0.001; \*\*\*\*p ≤ 0.0001 ..... 107

Figure 3.8: Contact angle of water droplets over 2 minutes when placed on top of electrospun mesh fabricated in CHCl<sub>3</sub> without surfactant and with surfactant at internal phase volume fractions of 0, 2, 4, and 8% w/o at A. high relative humidity and B. low relative humidity. .... 109

Figure 3.9: Images of representative contact angle captured for electrospun mesh fabricated with CHCl<sub>3</sub> at high relative humidity and containing no surfactant and surfactant with internal phase volume fractions of 0, 2, 4, and 8% w/o internal phase. .... 110

Figure 3.10: Images of representative contact angle captured for electrospun mesh fabricated with CHCl<sub>3</sub> at low relative humidity and containing no surfactant and surfactant with internal phase volume fractions of 0, 2, 4, and 8% w/o internal phase. .... 112

Figure 3.11: Representative SEM images showing the topography of electrospun fibers fabricated with 3:1 CHCl<sub>3</sub>: DMF solvent at high (50% ± 10%) and low (10% ± 10%) relative humidity. Electrospun fibers show the effect of increasing internal phase volume fraction through fibers fabricated with no surfactant and 0% w/o internal phase control and with surfactant at volume fractions of 0, 2, 4, and 8% w/o internal phase. .... 113

Figure 3.12: Fiber volume fraction of electrospun mesh fabricated with 3:1 CHCl<sub>3</sub>: DMF solvent without surfactant and with surfactant at internal phase volume fractions of 0, 2, 4, and 8% w/o at A. high relative humidity and B. low relative humidity. \* p ≤ 0.05; \*\* p ≤ 0.01; \*\*\* p ≤ 0.001; \*\*\*\*p ≤ 0.0001 ..... 114

Figure 3.13: Contact angle of water droplets over 2 minutes when placed on top of electrospun mesh fabricated with 3:1 CHCl<sub>3</sub>: DMF solvent without surfactant and with surfactant at internal phase volume fractions of 0, 2, 4, and 8% w/o at A. high relative humidity and B. low relative humidity..... 115

Figure 3.14: Images of representative contact angle captured for electrospun mesh fabricated with 3:1 CHCl<sub>3</sub>: DMF at high relative humidity and containing no surfactant, and surfactant with internal phase volume fractions of 0, 2, 4, and 8% w/o internal phase. .... 117

Figure 3.15: Images of representative contact angle captured for electrospun mesh fabricated with 3:1 CHCl<sub>3</sub>: DMF at low relative humidity and containing no surfactant, and surfactant with internal phase volume fractions of 0, 2, 4, and 8% w/o internal phase. .... 119

Figure 3.16: Representative SEM images showing the topography of electrospun fibers fabricated with 3:1 CHCl<sub>3</sub>: MeOH solvent at high (50% ± 10%) and low (10% ± 10%) relative humidity. Electrospun fibers show the effect of increasing internal phase volume fraction through fibers fabricated with no surfactant and 0% w/o internal phase control and with surfactant at volume fractions of 0, 2, 4, and 8% w/o internal phase. .... 120

Figure 3.17: Fiber volume fraction of electrospun mesh fabricated with 3:1 CHCl<sub>3</sub>: MeOH solvent without surfactant, and with surfactant at internal phase volume fractions of 0, 2, 4, and 8% w/o at A. high relative humidity and B. low relative humidity. \* p ≤ 0.05; \*\* p ≤ 0.01; \*\*\* p ≤ 0.001; \*\*\*\*p ≤ 0.0001 ..... 121

Figure 3.18: Contact angle of water droplets over 2 minutes when placed on top of electrospun mesh fabricated with 3:1 CHCl<sub>3</sub>: MeOH solvent without surfactant and with surfactant at internal phase volume fractions of 0, 2, 4, and 8% w/o at A. high relative humidity and B. low relative humidity..... 123

Figure 3.19: Images of representative contact angle captured for electrospun mesh fabricated with 3:1 CHCl<sub>3</sub>: MeOH at high relative humidity and containing no surfactant, and surfactant with internal phase volume fractions of 0, 2, 4, and 8% w/o internal phase. .... 124

Figure 3.20: Images of representative contact angle captured for electrospun mesh fabricated with 3:1 CHCl<sub>3</sub>: MeOH at low relative humidity and containing no surfactant, and surfactant with internal phase volume fractions of 0, 2, 4, and 8% w/o internal phase. .... 125

Figure 3.21: Comparison of fiber volume fraction of electrospun mesh fabricated with CHCl<sub>3</sub>, 3:1 CHCl<sub>3</sub>: DMF, and 3:1 CHCl<sub>3</sub>: MeOH solvent without surfactant, and with surfactant at internal phase volume fractions of 0, 2, 4, and 8% w/o at A. high relative humidity and B. low relative humidity. Surface topography of porous (P), rough or wrinkled (R), and smooth (S) for each sample is marked in the data point. .... 127

Figure 3.22: Comparison of contact angle of water droplets over 2 minutes when placed on top of electrospun mesh fabricated at high relative humidity with CHCl<sub>3</sub>, 3:1 CHCl<sub>3</sub>: DMF, and 3:1 CHCl<sub>3</sub>: MeOH solvent without surfactant, and with surfactant at internal phase volume fractions of 0, 2, 4, and 8% w/o at A. 0 seconds after droplet release B. 5 seconds after droplet release C. 10 seconds after droplet release and D. 120 seconds after droplet release. All samples were fabricated at high relative humidity..... 129

Figure 3.23: Comparison of contact angle of water droplets over 2 minutes when placed on top of electrospun mesh fabricated at low relative humidity with CHCl<sub>3</sub>, 3:1 CHCl<sub>3</sub>: DMF, and 3:1 CHCl<sub>3</sub>: MeOH solvent without surfactant, and with surfactant at internal phase volume fractions of 0, 2, 4, and 8% w/o at A. 0 seconds after droplet release B. 5 seconds after droplet release C. 10 seconds after droplet release and D. 120 seconds after droplet release. All samples were fabricated at low relative humidity..... 130

Figure 3.24: Images of 30% w/w surfactant in a CHCl<sub>3</sub> PCL solution with no surfactant as control and Span 85, Span 80, PGPR, Span 40, and Pluronic F108 mixed with 8% w/o water dyed blue. Images were captured at time points of 0, 10, 20, 30, 40, 50 minutes, 1 hour, 2 hours, 3 hours, 24 hours, and 48 hours. Pictures highlighted with a black border indicate that phase separation has occurred. .... 138

Figure 3.25: Images of a 3:1 CHCl<sub>3</sub>: DMF control and Span 85, Span 80, PGPR, Span 40, and Pluronic F108 mixed with 3:1 CHCl<sub>3</sub>: DMF over two weeks. All samples had an internal phase of 4% w/o. Images were captured at 0 minutes, 2 minutes, 30 minutes, 1 hour, 2 hours, 3 hours, 24 hours, 48 hours, 1 week, and 2 weeks. Pictures highlighted with a black border indicate that phase separation is present. .... 141

Figure 3.26: Representative micrographs of emulsions of 3:1 CHCl<sub>3</sub>: DMF with 8% w/o internal phase and surfactants Span 85, Span 80, PGPR, Span 40, and Pluronic F108 at 0 and 3 hours after mixing. .... 142

Figure 3.27: Droplet diameters of emulsions made with 3:1 CHCl<sub>3</sub>: DMF solvent without surfactant, with Span 85, with Span 80, with PGPR, with Span 40, and with Pluronic F108 at A. 0 hours after mixing and B. 3 hours after mixing. \*  $p \leq 0.05$ ; \*\*  $p \leq 0.01$ ; \*\*\*  $p \leq 0.001$ ; \*\*\*\* $p \leq 0.0001$  ..... 143

Figure 3.28: A. Shear stress with increasing shear rate for solutions made with CHCl<sub>3</sub> solvent without surfactant, with Span 85, with Span 80, with PGPR, with Span 40, and with Pluronic F108. B. Viscosity data subset focused on shear rates near the expected values experienced at an electrospinning needle tip. .... 145

Figure 3.29: Representative SEM images showing the morphology and average fiber diameter of electrospun fibers fabricated with CHCl<sub>3</sub> solvent and Span 85, Span 80, PGPR, Span 40, and Pluronic F108 with and without 8% w/o internal phase as an emulsion. Emulsions SEMs are shown at a higher magnification because they are smaller fibers than monolithic fibers. .... 146

Figure 3.30: Fiber diameters of electrospun mesh fabricated with CHCl<sub>3</sub> solvent without surfactant, with Span 85, Span 80, PGPR, Span 40, and Pluronic F108 with A. no internal phase and B. with 8% w/o internal phase. Span 40 without internal phase was unable to fabricate continuous fibers and was omitted from plot A. \*  $p \leq 0.05$ ; \*\*  $p \leq 0.01$ ; \*\*\*  $p \leq 0.001$ ; \*\*\*\* $p \leq 0.0001$  ..... 147

Figure 3.31: Pairwise comparisons of the fiber diameters of electrospun mesh fabricated with CHCl<sub>3</sub> and A. Span 85 with and without 8% w/o internal phase B. Span 80 with and without 8% w/o internal phase, C. PGPR with and without 8% w/o internal phase, D. Span 40 with and without 8% w/o internal phase, and E. Pluronic F108 with and without 8% w/o internal phase. \*  $p \leq 0.05$ ; \*\*  $p \leq 0.01$ ; \*\*\*  $p \leq 0.001$ ; \*\*\*\* $p \leq 0.0001$  ..... 150

Figure 3.32: Representative SEM images showing the topography of electrospun fibers fabricated with CHCl<sub>3</sub> solvent and Span 85, Span 80, PGPR, Span 40, and Pluronic F108 with and without 8% w/o internal phase. .... 151

Figure 3.33: Original micrographs of emulsions of 3:1 CHCl<sub>3</sub>: DMF with 8% w/o internal phase and surfactants Span 85, Span 80, PGPR, Span 40, and Pluronic F108 at 0 and 3 hours after mixing. .... 157

- Figure 4.1: A. Schematic representing emulsion coalescence into the center of the fiber during the electrospinning process. B. CLSM image of core shell fiber fabricated with emulsion electrospinning and aqueous phase loaded with PEO-FITC to demonstrate coalescence of internal phase within the core of the fiber. Figures originally published by Xu et al. in *Macromolecular Rapid Communications* and reproduced with permission.<sup>4</sup> ..... 159
- Figure 4.2: A. SEM cross-sections of emulsion electrospun fibers and B. corresponding drug release of fluorescein for samples fabricated with surfactant concentrations of a.2.5% w/w (black squares), 7.5% w/w (red circles), and 15% w/w (blue triangles) all electrospun at 10% relative humidity. C. SEM cross-sections of emulsion electrospun fibers and B. corresponding drug release of fluorescein for samples fabricated with ambient relative humidity of a.10% w/w (black squares), 35% w/w (red circles), and 60% w/w (blue triangles) all in emulsions with 2.5% surfactant. Figures originally published by Yazgan et al. in *Polymer* and reproduced with permission.<sup>7</sup> ..... 160
- Figure 4.3: A. Elongation of internal phase droplets over time with applied electric field. B. Schematic describing the evolution of emulsion internal phase droplets during the electrospinning process. Figures originally published by Wang et al. in *Materials Letters* and reproduced with permission.<sup>8</sup> ..... 161
- Figure 4.4: Representative SEM images demonstrating morphology of electrospun fibers fabricated with  $\text{CHCl}_3$  solvent at  $50\% \pm 10\%$  relative humidity with no surfactant, and with surfactant at volume fractions of 0%, 2%, 4%, and 8% w/o internal phase. Non-emulsion samples are shown at a lower magnification for better visualization of morphology because fibers were larger. .... 165
- Figure 4.5: Representative SEM images of close-up selected fiber morphology in electrospun fibers fabricated with  $\text{CHCl}_3$  solvent at  $50\% \pm 10\%$  relative humidity with no surfactant and with surfactant at volume fractions of 0%, 2%, 4%, and 8% w/o internal phase. Setup was standardized for monolithic solution control. .... 167
- Figure 4.6: Representative SEM images demonstrating morphology of electrospun fibers fabricated with  $\text{CHCl}_3$  solvent at  $10\% \pm 10\%$  relative humidity with no surfactant, and with surfactant at volume fractions of 0%, 2%, 4%, and 8% w/o internal phase. .... 172
- Figure 4.7: Representative SEM images of close-up selected fiber morphology in electrospun mesh fabricated with  $\text{CHCl}_3$  solvent at  $10\% \pm 10\%$  relative humidity with no surfactant, and with surfactant at volume fractions of 0%, 2%, 4%, and 8% w/o internal phase. .... 173
- Figure 4.8. Representative SEM images showing the topography of electrospun fibers fabricated with  $\text{CHCl}_3$  solvent at high ( $50\% \pm 10\%$ ) and low ( $10\% \pm 10\%$ ) relative humidity. Electrospun fibers show the effect of increasing internal phase volume fraction through fibers fabricated with no surfactant and 0% w/o internal phase control, and with surfactant at volume fractions of 0%, 2%, 4%, and 8% w/o internal phase. .... 176
- Figure 4.9: Mechanism depicting at high relative humidity in systems with  $\text{CHCl}_3$  the interaction of ambient water with the electrospun jet during electrospinning. In fibers with surfactant Span 80, water penetrates the core of the fiber. In fibers without Span 80, water droplets only condense on the fiber surface, creating a porous topography. Figure originally published in *Biomaterials Science* by Johnson et al. and reproduced with permission.<sup>13</sup> ..... 177

Figure 4.10: Representative SEM images showing the fiber diameter of electrospun fibers fabricated with  $\text{CHCl}_3$  solvent at high ( $50\% \pm 10\%$ ) and low ( $10\% \pm 10\%$ ) relative humidity. Overall average fiber diameter and fiber diameter distribution represented with histograms for each sample parameter. Electrospun fibers show the effect of increasing internal phase volume fraction through fibers fabricated with no surfactant and 0% w/o internal phase control, and with surfactant at volume fractions of 0%, 2%, 4%, and 8% w/o internal phase. .... 179

Figure 4.11: Box-plot representing average fiber diameter for fibers fabricated with  $\text{CHCl}_3$  solvent and electrospun at high relative humidity ( $50\% \pm 10\%$ ) with no surfactant and 0% w/o surfactant span 80 with internal phase volume fraction of 2% w/o, 4% w/o and 8% w/o. \*  $p \leq 0.05$ ; \*\*  $p \leq 0.01$ ; \*\*\*  $p \leq 0.001$  ..... 180

Figure 4.12: Box-plot representing average fiber diameter for fibers fabricated with  $\text{CHCl}_3$  solvent and electrospun at low relative humidity ( $10\% \pm 10\%$ ) with no surfactant and 0% w/o surfactant span 80 with internal phase volume fraction of 2% w/o, 4% w/o and 8% w/o. \*  $p \leq 0.05$ ; \*\*  $p \leq 0.01$ ; \*\*\*  $p \leq 0.001$  ..... 182

Figure 4.13: Representative SEM images demonstrating morphology of electrospun fibers fabricated with 3:1  $\text{CHCl}_3$ : DMF solvent at  $50\% \pm 10\%$  relative humidity with no surfactant and with surfactant at volume fractions of 0%, 2%, 4%, and 8% w/o internal phase. .... 183

Figure 4.14: Representative SEM images of close-up selected fiber morphology in electrospun fibers fabricated with 3:1  $\text{CHCl}_3$ : DMF solvent at  $50\% \pm 10\%$  relative humidity with no surfactant, and with surfactant at volume fractions of 0%, 2%, 4%, and 8% w/o internal phase. .... 185

Figure 4.15: Representative SEM images demonstrating morphology of electrospun fibers fabricated with 3:1  $\text{CHCl}_3$ : DMF solvent at  $10\% \pm 10\%$  relative humidity with no surfactant and with surfactant at volume fractions of 0%, 2%, 4%, and 8% w/o internal phase. .... 187

Figure 4.16: Representative SEM images of close-up selected fiber morphology in electrospun fibers fabricated with 3:1  $\text{CHCl}_3$ : DMF solvent at  $10\% \pm 10\%$  relative humidity with no surfactant, and with surfactant at volume fractions of 0%, 2%, 4%, and 8% w/o internal phase. .... 189

Figure 4.17: Representative SEM images showing the topography of electrospun fibers fabricated with 3:1  $\text{CHCl}_3$ : DMF solvent at high ( $50\% \pm 10\%$ ) and low ( $10\% \pm 10\%$ ) relative humidity. Electrospun fibers show the effect of increasing internal phase volume fraction through fibers fabricated with no surfactant and 0% w/o internal phase control, and with surfactant at volume fractions of 0%, 2%, 4%, and 8% w/o internal phase. .... 193

Figure 4.18: Representative SEM images showing the fiber diameter of electrospun fibers fabricated with 3:1  $\text{CHCl}_3$ : DMF solvent at high ( $50\% \pm 10\%$ ) and low ( $10\% \pm 10\%$ ) relative humidity. Overall average fiber diameter and fiber diameter distribution represented with histograms for each sample parameter. Electrospun fibers show the effect of increasing internal phase volume fraction through fibers fabricated with no

	surfactant and 0% w/o internal phase control, and with surfactant at volume fractions of 0%, 2%, 4%, and 8% w/o internal phase.....	194
Figure 4.19:	Box-plot representing average fiber diameter for fibers fabricated with 3:1 CHCl <sub>3</sub> : DMF solvent and electrospun at high relative humidity (50% ± 10%) with no surfactant and 0% w/o surfactant span 80 with internal phase volume fraction of 2% w/o, 4% w/o and 8% w/o. * p ≤ 0.05; ** p ≤ 0.01; *** p ≤ 0.001.....	195
Figure 4.20:	Box-plot representing average fiber diameter for fibers fabricated with 3:1 CHCl <sub>3</sub> : DMF solvent and electrospun at low relative humidity (10% ± 10%) with no surfactant and 0% w/o surfactant span 80 with internal phase volume fraction of 2% w/o, 4% w/o and 8% w/o. * p ≤ 0.05; ** p ≤ 0.01; *** p ≤ 0.001.....	198
Figure 4.21:	Representative SEM images demonstrating morphology of electrospun fibers fabricated with 3:1 CHCl <sub>3</sub> : MeOH solvent at 50% ± 10% relative humidity with no surfactant and with surfactant at volume fractions of 0%, 2%, 4%, and 8% w/o internal phase. ....	199
Figure 4.22:	Representative SEM images of close-up selected fiber morphology in electrospun fibers fabricated with 3:1 CHCl <sub>3</sub> : MeOH solvent at 50% ± 10% relative humidity with no surfactant, and with surfactant at volume fractions of 0%, 2%, 4%, and 8% w/o internal phase. ....	200
Figure 4.23:	Formation of nanowebbing with increasing internal phase volume fractions of 2%, 4%, and 8% w/o in samples electrospun at high relative humidity (50%± 10%) and solvent 3:1 CHCl <sub>3</sub> :MeOH.....	203
Figure 4.24:	Representative SEM images demonstrating morphology of electrospun fibers fabricated with 3:1 CHCl <sub>3</sub> : MeOH solvent at 10% ± 10% relative humidity with no surfactant and with surfactant at volume fractions of 0%, 2%, 4%, and 8% w/o internal phase. ....	204
Figure 4.25:	Representative SEM images of close-up selected fiber morphology in electrospun fibers fabricated with 3:1 CHCl <sub>3</sub> : MeOH solvent at 10% ± 10% relative humidity with no surfactant, and with surfactant at volume fractions of 0%, 2%, 4%, and 8% w/o internal phase. ....	206
Figure 4.26:	Representative SEM images showing the topography of electrospun fibers fabricated with 3:1 CHCl <sub>3</sub> : MeOH solvent at high (50% ± 10%) and low (10% ± 10%) relative humidity. Electrospun fibers show the effect of increasing internal phase volume fraction through fibers fabricated with no surfactant and 0% w/o internal phase control, and with surfactant at volume fractions of 0%, 2%, 4%, and 8% w/o internal phase. ....	209
Figure 4.27:	Representative SEM images showing the fiber diameter of electrospun fibers fabricated with 3:1 CHCl <sub>3</sub> : MeOH solvent at high (50% ± 10%) and low (10% ± 10%) relative humidity. Overall average fiber diameter and fiber diameter distribution represented with histograms for each sample parameter. Electrospun fibers show the effect of increasing internal phase volume fraction through fibers fabricated with no surfactant and 0% w/o internal phase control, and with surfactant at volume fractions of 0%, 2%, 4%, and 8% w/o internal phase.....	211

Figure 4.28	Box-plot representing average fiber diameter for fibers fabricated with 3:1 CHCl <sub>3</sub> : MeOH solvent and electrospun at high relative humidity (50% ± 10%) with no surfactant and 0% w/o surfactant span 80 with internal phase volume fraction of 2% w/o, 4% w/o and 8% w/o. * p ≤ 0.05; ** p ≤ 0.01; *** p ≤ 0.001 .....	212
Figure 4.29:	Box-plot representing average fiber diameter for fibers fabricated with 3:1 CHCl <sub>3</sub> : MeOH solvent and electrospun at low relative humidity (10% ± 10%) with no surfactant and 0% w/o surfactant span 80 with internal phase volume fraction of 2% w/o, 4% w/o and 8% w/o. * p ≤ 0.05; ** p ≤ 0.01; *** p ≤ 0.001 .....	214
Figure 5.1:	A. Increasing fiber volume fraction of electrospun fibers through increasing the electrospinning time. Representative SEM images and correlating contact angle fabricated with collection times of a. 10 minutes, b. 20 minutes, and c. 60 minutes. Drug release from fibers with increasing volume fraction and control polymer film loaded with d. acetaminophen and e. 5-fluorouracil. B. Fiber alignment of electrospun fibers and alignment shown in representative SEM images of a. aligned fibers and b. nonwoven unaligned fibers with c. corresponding contact angle. Drug release from fibers with increasing volume fraction and control polymer film loaded with d. acetaminophen and e. 5-fluorouracil. Figures originally published by Xu et al. in the Journal of Materials Chemistry B and reproduced with permission. <sup>10</sup> .....	222
Figure 5.2:	Schematic illustrating the effect of electrospun nanofiber density or fiber volume fraction on overall mesh hydrophobicity and subsequent drug release. Figure originally published by Xu et al. in the Journal of Materials Chemistry B and reproduced with permission. <sup>10</sup> .....	223
Figure 5.3:	Fibers loaded with 5-Fluorouracil with fiber diameters of 1.02 μm (c, F-1), 0.73 μm (d, F-2), 0.53 μm (e, F-3), and 0.35 μm (f, F-4). A. Representative SEM images of fibers. B. Burst drug release. C. Release with linear regression after initial burst release. Figures originally published by Chen et al. in Fibers and Polymers and reproduced with permission. <sup>11</sup> .....	224
Figure 5.4:	Chemical structure of model drugs Nile Red and Rhodamine B with their logP values. Chemical structures were drawn with ChemDraw Professional software.....	229
Figure 5.5:	Fluorescence standards for A. Nile Red in 3:1 CHCl <sub>3</sub> : DMF with and without Span 80 and B. Rhodamine B in 3:1 CHCl <sub>3</sub> : DMF with and without Span 80. Only concentrations up to 2 μg/mL are plotted because higher concentrations are outside of the linear region, suggesting that the fluorophores were over saturated. The Pearson coefficient for each standard is at or above 0.98, indicating a good linear fit. ....	233
Figure 5.6:	Representative SEM images of smaller fibers fabricated with high ambient relative humidity and no surfactant and surfactant showing A. fiber morphology, B. fiber surface topography, and C. cross-sections of the fibers showing internal architecture. Some images used in a publication by Johnson et al. in Biomaterials Science and reproduced with permission. <sup>16</sup> .....	236
Figure 5.7:	A. Representative SEM images of electrospun fibers without surfactant (CSN) and with surfactant (CSS) electrospun with parameters to achieve smaller fiber diameters. Average fiber diameter and standard deviation calculated for all fibers in the sample.	

	B. Average fiber diameter and C. average fiber percent volume fraction for each SEM image plotted in a boxplot. * $p \leq 0.05$ ; ** $p \leq 0.01$ ; *** $p \leq 0.001$ ; **** $p \leq 0.0001$	237
Figure 5.8:	A. Amount of Nile Red encapsulated in 8 mm electrospun mesh punch samples and B. Percent relative Nile Red release rate over one hour for samples fabricated with chloroform solvent with smaller fiber diameter and normalized by weight of individual sample mesh. Each symbol in figure A represents the electrospun sample that the specimen was removed from to determine amount of loaded drug. Figures modified from originally published data by Johnson et al. in Biomaterials Science and reproduced with permission. <sup>16</sup> * $p \leq 0.05$ ; ** $p \leq 0.01$ ; *** $p \leq 0.001$ ; **** $p \leq 0.0001$	239
Figure 5.9:	Representative SEM images of larger fibers fabricated with high ambient relative humidity and no surfactant and surfactant showing the A. fiber morphology, B. fiber surface topography, and C. cross-sections of the fibers showing solid and small pore internal architecture.	241
Figure 5.10:	A. Representative SEM images of electrospun fibers without surfactant (CLN) and with surfactant (CLS) electrospun with parameters to achieve larger fiber diameters. Average fiber diameter and standard deviation calculated for all fibers in the sample. B. Average fiber diameter and C. Average fiber percent volume fraction for each SEM image plotted in a boxplot. * $p \leq 0.05$ ; ** $p \leq 0.01$ ; *** $p \leq 0.001$ ; **** $p \leq 0.0001$	243
Figure 5.11:	A. Amount of Nile Red encapsulated in 8 mm electrospun mesh punch samples and B. Percent cumulative Nile Red release rate over one hour for samples fabricated with $\text{CHCl}_3$ and larger fiber diameters. Samples were normalized by weight of individual sample mesh. Each symbol in figure A represents the electrospun sample that the specimen was removed from to determine amount of loaded drug. * $p \leq 0.05$ ; ** $p \leq 0.01$ ; *** $p \leq 0.001$ ; **** $p \leq 0.0001$	244
Figure 5.12:	A. Representative SEM images of electrospun fiber cross sections. B. Representative SEM images of electrospun fiber topography. C. Fiber diameter. D. Fiber volume fraction. E. Amount of Nile Red encapsulated in electrospun mesh samples. F. Percent cumulative Nile Red release rate over one hour for samples fabricated with different processing parameters. Samples were normalized by weight of individual sample mesh. * $p \leq 0.05$ ; ** $p \leq 0.01$ ; *** $p \leq 0.001$ ; **** $p \leq 0.0001$	245
Figure 5.13:	A. Representative SEM images of electrospun fibers loaded with Nile Red without surfactant (DNN), with surfactant (DNS), and with both surfactant and internal phase volume fraction at 8% w/o to form an emulsion (DNE). Average fiber diameter and standard deviation calculated for all fibers in the sample. B. Average fiber diameter and C. average fiber percent volume fraction for each SEM image plotted in a boxplot. D. Topography of electrospun fibers. * $p \leq 0.05$ ; ** $p \leq 0.01$ ; *** $p \leq 0.001$ ; **** $p \leq 0.0001$	248
Figure 5.14:	A. Amount of Nile Red encapsulated in 8 mm electrospun mesh punch samples and B. Percent Nile Red release over one hour for samples fabricated without surfactant (DNN), with surfactant (DNS), and with both surfactant and internal phase volume fraction at 8% w/o to form an emulsion (DNE). Normalized by weight of individual sample mesh. Each symbol in figure A represents the electrospun sample that the	



specimen was removed from to determine amount of loaded drug. \*  $p \leq 0.05$ ; \*\*  $p \leq 0.01$ ; \*\*\*  $p \leq 0.001$ ; \*\*\*\* $p \leq 0.0001$  ..... 250

Figure 5.15: A. Representative SEM images of electrospun fibers loaded with Rhodamine B without surfactant (DRN), with surfactant (DRS), and with both surfactant and internal phase volume fraction at 8% w/o to form an emulsion (DRE). Average fiber diameter and standard deviation calculated for all fibers in the sample. B. Average fiber diameter and C. average fiber percent volume fraction for each SEM image plotted in a boxplot. D. Topography of electrospun fibers. \*  $p \leq 0.05$ ; \*\*  $p \leq 0.01$ ; \*\*\*  $p \leq 0.001$ ; \*\*\*\* $p \leq 0.0001$ ..... 252

Figure 5.16: A. Amount of Rhodamine B encapsulated in 8 mm electrospun mesh punch samples and B. Percent Nile Red release over one hour for samples fabricated without surfactant (DRN), with surfactant (DRS), and with both surfactant and internal phase volume fraction at 8% w/o to form an emulsion (DRE) and normalized by weight of individual sample mesh. Each symbol in figure A represents the electrospun sample that the specimen was removed from to determine amount of loaded drug. \*  $p \leq 0.05$ ; \*\*  $p \leq 0.01$ ; \*\*\*  $p \leq 0.001$ ; \*\*\*\* $p \leq 0.0001$  ..... 253

Figure 5.17: For electrospun samples, DNN, DNS, DNE, DRN, DRS, and DRE, A. fiber diameter, B. fiber volume fraction, C. encapsulated drug showing all groups are statistically different except for DRN and DRE, and D. percent cumulative drug release rate. \*  $p \leq 0.05$ ; \*\*  $p \leq 0.01$ ; \*\*\*  $p \leq 0.001$ ; \*\*\*\* $p \leq 0.0001$ ..... 255

## LIST OF TABLES

Table 2.1: Solvent properties of boiling point, dielectric constant, surface tension, and absolute viscosity from PubChem. PCL solubility in solvents based on the experimental studies by Luo et al. <sup>3</sup> Chemical structures were generated with ChemDraw software.....	55
Table 2.2: Summary table for fiber morphology, topography, diameter, and distribution for electrospun fibers fabricated from CHCl <sub>3</sub> , DCM, 3:1 CHCl <sub>3</sub> : DMF, and 3:1 CHCl <sub>3</sub> : MeOH.....	82
Table 3.1: Summary of fiber topography, diameter, fraction, and contact angle over time for varying solvent systems at high relative humidity.....	131
Table 3.2: Summary of fiber topography, diameter, fraction, and contact angle over time for varying solvent systems at low relative humidity.....	133
Table 3.3: Summary of non-ionic surfactants structure, HLB, LogP, and hydrogen bonding....	136
Table 3.4: Summary of surface topography, fiber diameter, and emulsion stability for Span 85, Span 80, PGPR, Span 40, and Pluronic F108 .....	152
Table 4.1: Summary table of fiber morphology, topography, diameter, and distribution electrospun at high (50% ± 10%) and low (10% ± 10%) relative humidity with control containing no surfactant and increasing internal phase volume fractions of 0% w/o, 2% w/o, 4% w/o, and 8% w/o internal phase volume fraction.....	215
Table 5.1: Sample Parameters for all electrospun mesh fabricated.....	230

## CHAPTER 1: INTRODUCTION AND BACKGROUND

### 1.1 APPLICATIONS OF ELECTROSPINNING

Electrospinning is a versatile process used to fabricate nonwoven mesh with fibers in the diameter range of approximately 10 nm to 10  $\mu\text{m}$ .<sup>1</sup> The range of these sized fibers is significant because most commercially produced synthetic fibers are only able to produce fibers in the diameter range of 10-100  $\mu\text{m}$ .<sup>2,3</sup> This difference in fiber diameter is critical because using electrospinning technology allows further applications of fibrous materials in the nanometer range. The resulting mesh has a high surface area-to-volume ratio, is flexible, is a porous material that allows the flow of fluid through the mesh while excluding solid particles larger than the mesh, and can mimic the native extracellular matrix in tissue.<sup>4</sup> In addition to the ability to create submicron fibers, this technique is popular because it is relatively inexpensive, produced fibers with a high surface area to volume ratio, and has the capability to produce fibers that have a wide range of diameters and porosity. The fibers can be fabricated from a wide variety of materials and can be produced with a hierarchical structure from the shape of individual fibers to the geometry of the overall mesh.<sup>1,5</sup>

These fibers are used in a wide range of applications, including filtration, microreactors, sensors, energy storage, catalysis, textiles, and biotechnology.<sup>5</sup> Within the field of filtration, electrospun fibers can be used because they can allow for high flow through the material without high resistance.<sup>2,6</sup> This allows the mesh to be used to remove small particles in HEPA filters, decompose harmful materials, and recover precious metals.<sup>2,6</sup> Electrospun mesh has been used in sensor technology to respond to applied stimuli such as changes in pH, light, temperature, an electric field, and a magnetic field.<sup>7</sup> Electrospun fibers are also used within the fields of catalysis,

energy, and photonic devices.<sup>2</sup> Fibers are used in these fields because they have a high surface area per volume for catalysis, can be fabricated with conducting materials for energy harvesting, conversion, and storage, and the alignment can be controlled for photonic devices.<sup>2</sup> The remainder of the application discussion will focus on applications within the biomedical field.

Electrospun fibers have been widely used in the biomedical engineering field. The most popular applications within this field are in the areas of tissue modeling for pharmaceutical testing and diagnostics, coatings on biomedical devices, barrier membranes, tissue engineering, and drug delivery.<sup>8-11</sup> One commercial application of electrospun fibers is as a coating for an FDA-approved vascular stent by the company Biotronik. The use of nanofibers on this stent enhanced flexibility during implantation.<sup>12</sup> Further research is focused on stents with fibers loaded with endothelial growth factors and heparin to enhance recovery time and to prevent blood clotting.<sup>13</sup> Barrier membrane applications are also commercially available in products like Healsmart Personalized Wound Care System by PolyRemedy and ReDura and NeoDura by Medprin Regenerative Medical Technologies Co..<sup>2,14</sup> HealSmart is FDA approved dressing used for wound dressings, and NeoDura and ReDura are used to prevent adhesions after surgery.<sup>15</sup>

### **1.1.1 Tissue Engineering**

Within tissue engineering applications, electrospun fibers are used to recapitulate native tissue either through signaling local cells when the scaffold is placed in the body or to create a tissue model. This is because fibrous mesh can mimic the native extracellular matrix of tissues which include fibrous proteins such as collagen.<sup>4,16</sup> Further, because electrospun fibers are porous, they allow the exchange of gas and, in some cases facilitate cells growing through the scaffold.

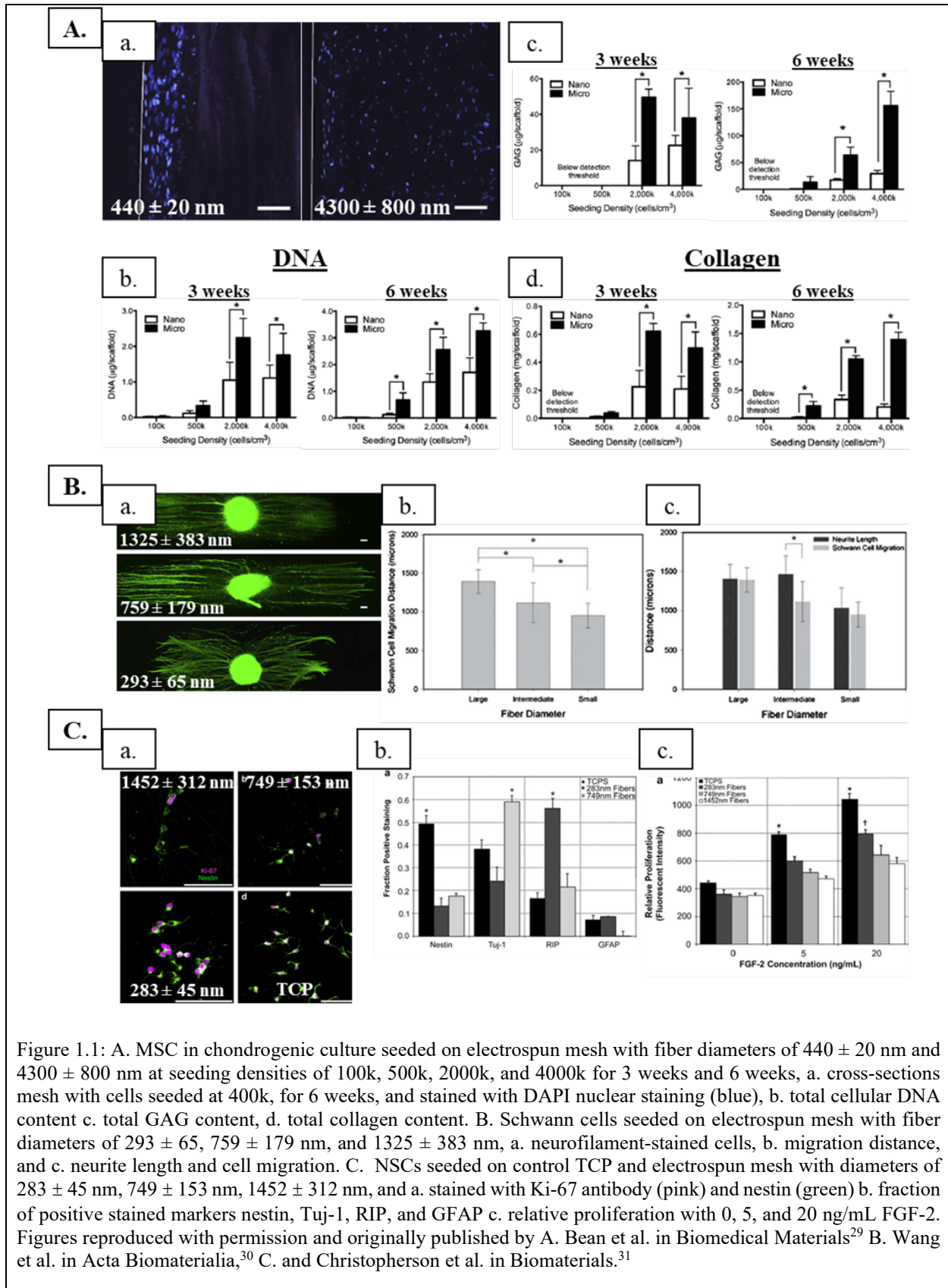
Electrospun mesh that has been fabricated as the scaffolding for tissues have been widely used to create tissue models for diagnostics in cancer.<sup>17</sup> Electrospun fibers have a high surface area

to volume ratio that allows for a high contact area for analytes in/on the fibers and cancer cells, in some cases with sensitivity at the femtomolar levels.<sup>15,17-19</sup> Electrospun scaffolds have also been used to create disease models for drug screening.<sup>20</sup> Using an external tissue model to screen drugs can be a less expensive option and can be done with human cells that can have responses closer to an *in vivo* tissue than animal tissue.<sup>20</sup> Further, these fibers can be loaded with a drug to provide localized delivery or act as a tissue model for drug screening<sup>21-23</sup>.

Cells respond differently to microenvironments created by 3D vs. 2D tissue constructs.<sup>20</sup> In order to recapitulate the native tissue in the body, it is important to create scaffolds that mimic the spatiotemporal geometry through material fabrication. Cells respond differently in terms of proliferation, differentiation, and phenotype to spatiotemporal geometry, fiber diameter, fiber alignment, fiber topography, hydrophobicity, and biomechanical cues.<sup>2,20,24</sup> Ideally, tissue constructs will also be composed of biocompatible materials that will degrade at the same rate as new tissue growth so that the scaffold is seamlessly replaced with native tissue.

Within the biomedical field, electrospun scaffolds are used for applications such as tissue engineering because the structure can mimic the native fiber structure of the extracellular matrix.<sup>25</sup> For example, one of the most abundant structural proteins in the extracellular matrix is collagen, which has nanofibers in the 50 nm- 40+  $\mu\text{m}$  range that are composed of fibrils in the 10-300 nm range.<sup>26,27</sup> This is important because cells will respond differently to cells with different sized fiber diameters. For example, in a study by Bashur et al., fibroblast cells were cultured on PLGA fibers with increasing fiber diameters of 0.14- 3.6  $\mu\text{m}$  with increasing alignment. The morphology of the cells increased with respect to cell area and aspect ratio with increasing fiber diameter and orientation.<sup>28</sup>

In another study by Bean et al., mesenchymal stem cells (MSC) were seeded on PCL fibers with diameters of  $440 \pm 20$  nm or  $4300 \pm 800$  nm for cartilage tissue engineering.<sup>29</sup> MSCs were cultured with transforming growth factor- $\beta$  to induce chondrogenic differentiation. Cells cultured on mesh with microfibers were able to proliferate deeper into the mesh than nanofiber mesh (Figure 1.1A-a). The proliferation of cells, measured by the amount of cellular DNA, was also higher in cells cultured on microfibers compared to nanofibers at higher seeding densities for both 3 weeks and 6 weeks (Figure 1.1A-b). Critical components of cartilage, glycosaminoglycans (GAG), and collagen were measured to evaluate the ability to produce critical components of cartilage. Production of GAG was higher for cells cultured on microfibers compared to nanofibers at higher seeding densities for both 3 weeks and 6 weeks (Figure 1.1A-c). Production of collagen was higher for cells cultured on microfibers compared to nanofibers at higher seeding densities for both 3 weeks and 6-weeks (Figure 1.1A-d). When normalized for cellular DNA, collagen and GAG trends were only significant at 6 weeks.



In another study by Wang et al., Schwann cells were cultured on PLLA electrospun mesh with fiber diameters of  $1325 \pm 383$ ,  $759 \pm 179$ , and  $293 \pm 65$  nm. The alignment of cells increased with increasing fiber diameter, and the neurite length increased and then decreased with increasing fiber diameter (Figure 1.1B-a, Figure 1.1B-c). Cell migration increased with increasing fiber diameter (Figure 1.1B-b, Figure 1.1B-c).

Christopherson et al. cultured neural progenitor/stem cells (NSCs) on laminin coated polyethersulfone (PES) electrospun mesh with fiber diameters of  $1452 \pm 312$ ,  $749 \pm 153$ , and  $283 \pm 45$  nm and tissue cultured polystyrene.<sup>31</sup> Proliferation of cells, measured qualitatively with Ki-67 antibody stained cells, increased with decreasing fiber diameters (Figure 1.1C-a). Differentiation of cells was evaluated with immunofluorescence staining to characterize the expression of Nestin (NSCs marker), Tuj-1 (neuronal marker), RIP (oligodendrocyte marker), and GFAP (astrocyte marker). Nestin and GFAP were not statistically different between fibers with diameters of 283 nm and 749 nm, Tuj-1 was higher in larger fiber diameters, RIP was higher in smaller fiber diameters (Figure 1.1C-b). Differences in immunofluorescence staining between samples with different fiber diameters indicate that fiber diameter may be able to influence the differentiation of cells. Relative proliferation was quantified with Nestin, and the proliferation on the 283 nm diameter fibers cultured with 20 ng/mL of FGF-2 was statistically higher than the proliferation of cells on fibers with larger fiber diameters (Figure 1.1C-c). The mechanism for cell proliferation rate dependence on fiber diameter has not been fully explored, and therefore, it is crucial to reproducibly control mesh characteristics such as fiber diameter in order to determine downstream effects on cell response.



Interestingly, fiber surface topography has also been shown to affect cell adherence, proliferation, differentiation, and gene expression.<sup>32-34</sup> In a study by Liu et al., smooth fiber topography was compared to fibers with increasing shish kebob topography size for bone tissue engineering applications (Figure 1.2A).<sup>32</sup> Higher mineralization of  $\beta$ -tricalcium phosphate was seen in the shish kebob topography and with larger shish kebob size (Figure 1.2B). The proliferation of bone marrow derived MSC (BMSC) on scaffolds shish kebob fibers was higher than smooth fibers, and larger shish kebob size also resulted in higher proliferation (Figure 1.2C, E). Differentiation of BMSC cultured in an osteogenic induction medium was evaluated by measuring the fluorescence intensity of osteocalcin (OCN), a late-stage marker of osteogenic differentiation, and activity of alkaline phosphatase (ALP), an early-stage marker of osteogenic differentiation. Differentiation was higher for shish kebob fibers compared to smooth fibers and for 338 nm compared to 153 nm shish kebobs (Figure 1.2D, F).

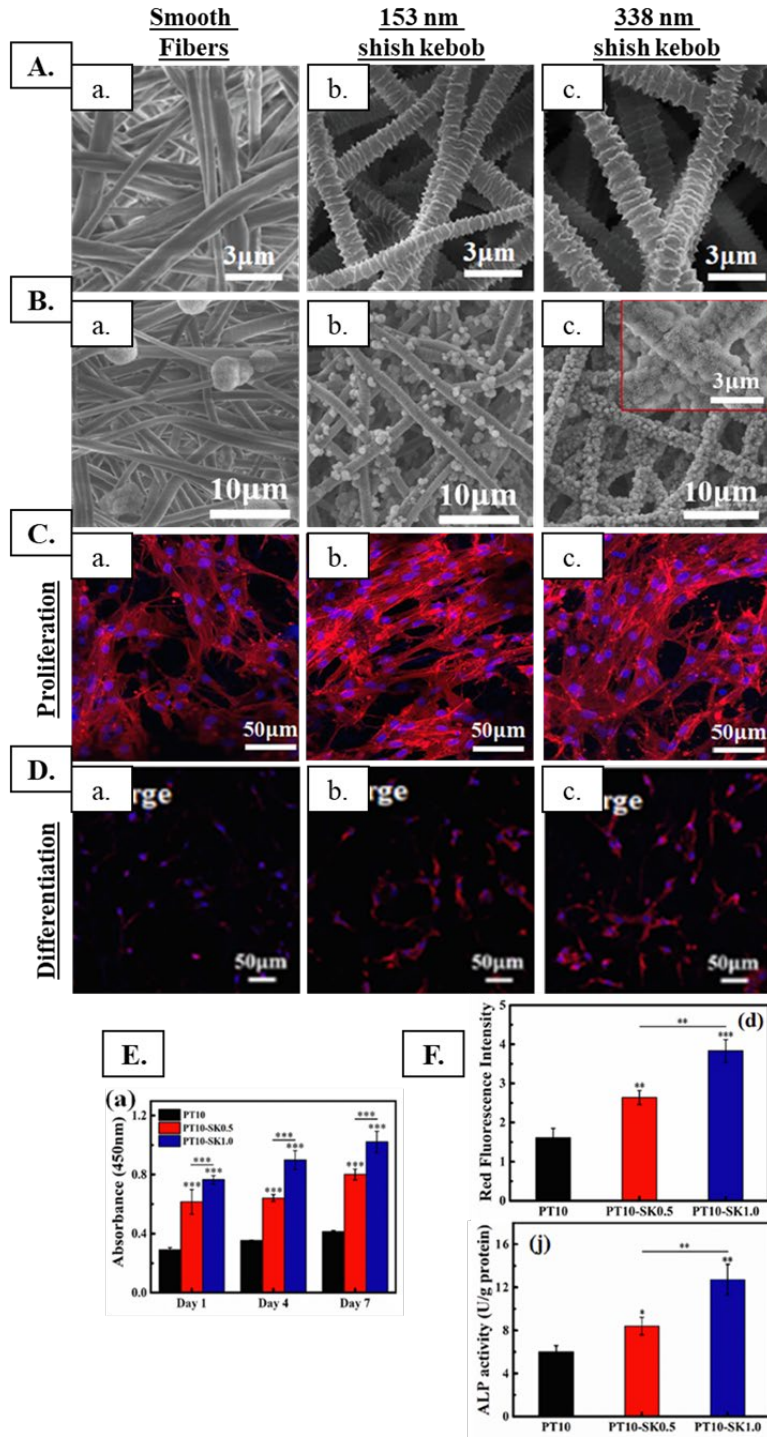
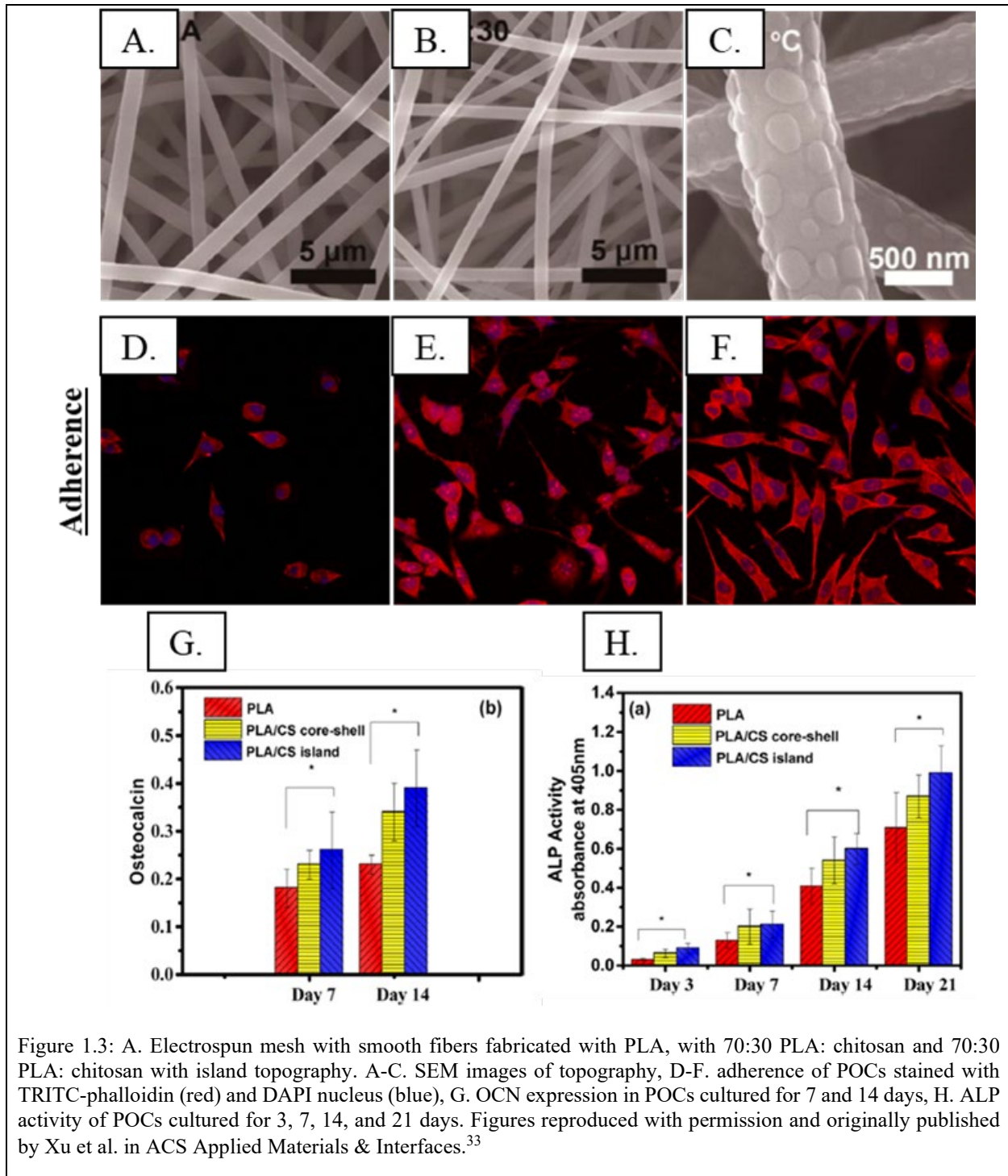


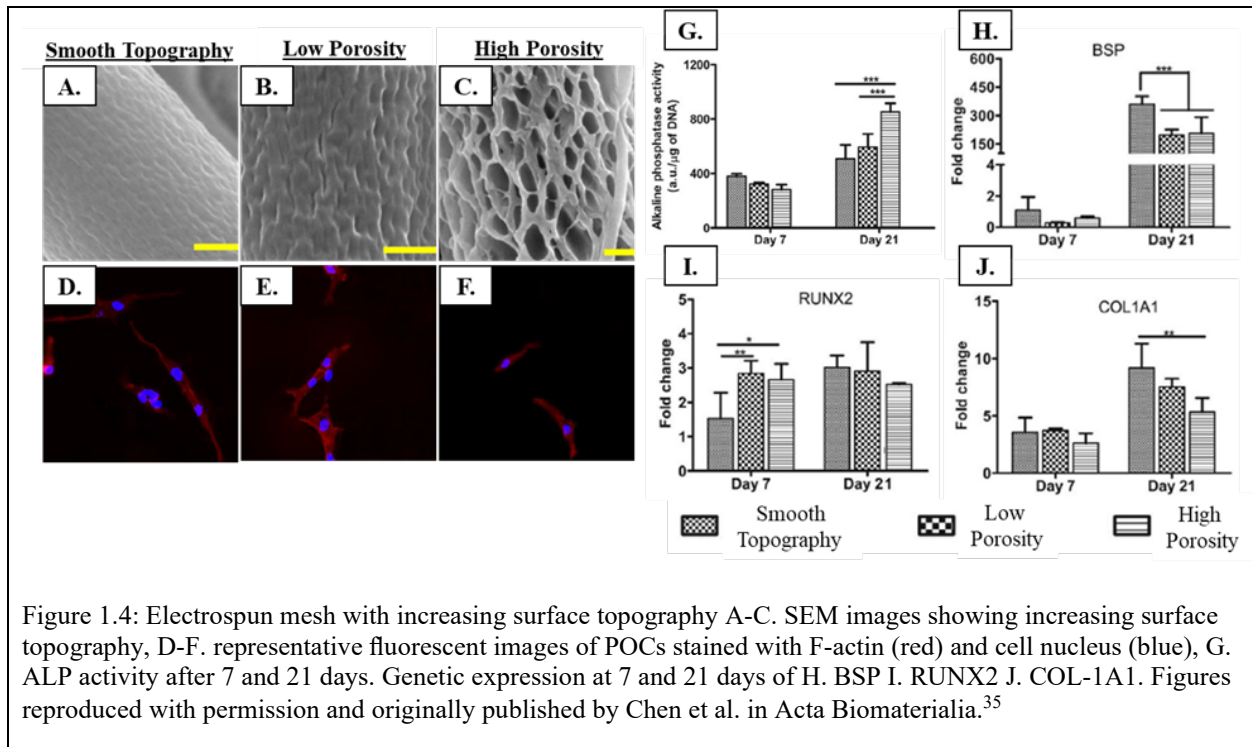
Figure 1.2: Electrospun fibers with smooth topography, 153 nm shish kebob topography and 338 nm shish kebob topography A. SEM images of fiber topography B. SEM images of TCP mineralization C. BMSC with F-actin stain (red) and nucleus stain (blue) D. BMSC cultured in osteogenic induction medium and stained for OCN (red) and nuclei (blue) E. proliferation of BMSC after 1, 4, and 7 days F. differentiation of BMSC in osteogenic induction medium measured by OCN and ALP biomarkers. Figures originally published by Liu et al. in European Polymer Journal and reproduced with permission.<sup>32</sup>

In another study conducted by Xu et al., island-like fiber topography was compared to smooth PLA and 7:3 PLA: chitosan fibers also for bone tissue engineering applications (Figure 1.3A-a).<sup>33</sup> Adherence of mouse pre-osteoblast cells (POC) was greater on fibers with island topography compared to smooth fiber topography (Figure 1.3A-C). Differentiation of POCs, as measured by OCN and ALP levels, was higher for fibers with island like topography (Figure 1.3B, C). OCN and ALP are late and early-stage markers for osteoblast differentiation, and, therefore, differentiation occurred and was likely enhanced by the topography.



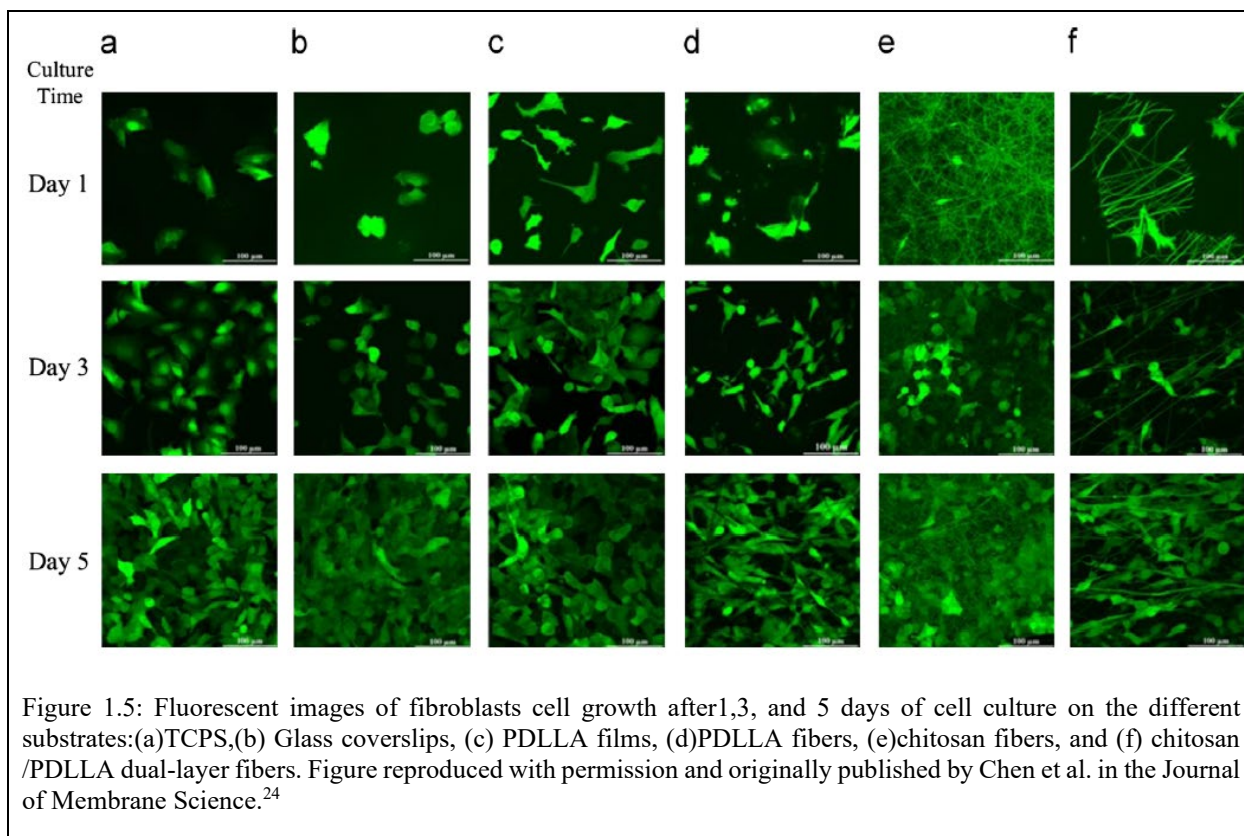
In a study by Chen et al., electrospun fibers with increasing surface porosity were compared for skeletal tissue engineering applications (Figure 1.4A-C).<sup>35</sup> Human MSC (hMSC) were seeded

on these fibers, and ALP activity and gene expression were evaluated (Figure 1.4D-F). ALP activity indicating osteoblast differentiation increased with increasing surface porosity (Figure 1.4G). Genetic expression of BSP and COL-1A1 was higher for smooth fibers at 21 days of culture, and RUNX2 expression was higher for porous fibers after 7 days of culture (Figure 1.4H-J). The impact of specific genetic markers and chondrogenic differentiation was not described in detail other than the observation that surface topography appears to be influenced by genetic expression.



Finally, cells will respond differently to the hydrophobicity of an electrospun mesh. In a study by Chen et al., fibroblast cells were cultured on treated polystyrene, glass coverslips, hydrophobic PDLLA films, hydrophobic PDLLA electrospun fibers, hydrophilic chitosan electrospun fibers, and the combination of chitosan and PDLLA electrospun fibers.<sup>24</sup> The cells were imaged at time points of one, three, and five days (Figure 1.5). Cells cultured on the more hydrophilic chitosan electrospun fibers have exhibited higher confluency compared to cells

cultured on the more hydrophobic PDLLA electrospun fibers indicating that hydrophobicity of the scaffold may play a role in cell response (Figure 1.5). The phenotype of cells cultured on fibers also demonstrated a more elongated shape compared to those on film and glass coverslips controls, further confirming cell response to 3D fibers.



### 1.1.2 Drug Delivery

Electrospun fibers have been used to deliver antibiotics, anticancer drugs, DNA, RNA, living cells, growth factors, small molecules, antibiotics, enzymes, and proteins.<sup>8,36</sup> Electrospun fibers have a high surface area, allowing for more contact with a diffusive media for drug release.<sup>8,10</sup> The electrospinning process also includes a rapidly evaporating solvent, which has the potential for preventing recrystallization of drug. Electrospun fibers offer a wide variety of tunability, which has been used to achieve controlled drug release profiles, including immediate,

delayed, smooth, pulsated, and biphasic.<sup>37,38</sup> Several different materials can be used to fabricate fibers and, therefore, control the rate of release of encapsulated drugs. Relative to other techniques, loading drug in electrospun fibers allows for high loading capacity and a high encapsulation efficiency at a relatively low cost of fabrication.<sup>36</sup> Encapsulation of drug and growth factors within electrospun fibers is particularly exciting for tissue engineering applications. Encapsulating drugs within fibers allows localized delivery to the tissue when implanted in the human body and often requires a lower overall amount of drug, reducing the potential for adverse side effects. Furthermore, in electrospun fibers used for wound dressings and other applications where mesh directly interfaces with the human body, antibacterial drugs can be encapsulated to prevent infection. Within tissue engineering applications, bioactive molecules such as protein, growth factors, DNA, and RNA have been incorporated within electrospun fibers. Bioactive molecules are important in tissue engineering scaffolds in order to encourage cells to differentiate into appropriate lineages, promote or inhibit proliferation, and turn on/off metabolic pathways.<sup>2,36</sup>

One of the challenges in encapsulating bioactive molecules within electrospun fibers is maintaining bioactivity during the electrospinning process.<sup>36</sup> This is because the use of traditional single-solvent electrospinning of hydrophobic polymers often requires the use of harsh solvents that can negatively affect the bioactivity of molecules and can kill cells.<sup>39-42</sup> A reduction in the bioactivity of bioactive molecules can lead to lowered therapeutic effects and loss of controlled release. Additionally, bioactive molecules and hydrophilic drugs are not compatible with many hydrophobic polymers and will separate during the electrospinning process and move to the fiber surface, which can both reduce bioactivity and result in a burst release of drug.<sup>39,43</sup>

Common methods to overcome these issues are to use coaxial or emulsion electrospinning techniques.<sup>39,41,44</sup> Coaxial electrospinning is a process through which concentric needles are used

to electrospin the polymer solution with the inner core generally loaded with the bioactive molecules to protect it from harsh solvents used to formulate the core of the shell.<sup>39</sup> Coaxial electrospinning is a popular method because it is effective in reducing burst effects, and multiple concentric needles can be used to tune the rate of drug release. One of the disadvantages of using coaxial electrospinning to encapsulate drug is that, in some cases, the release rate from nanofibers is controlled by desorption of molecules from the surface directly interfacing with release media and not by solid-state diffusion.<sup>45</sup> In these cases, diffusion from the core will not occur until it is exposed to surrounding media, such as through hydrolytic degradation of polymer or through shell imperfections where water is able to enter the core of the fiber. One method employed to allow faster penetration of water into the core of electrospun fibers is through adding porogens that are specifically designed to dissolve in specific solvents to the shell. After electrospinning, the porogens are removed by postprocessing to allow contact of their release media with the core of the fiber.

Another method to introduce porosity into fibers without using a sacrificial added material while still maintaining the protection of bioactive molecules is through emulsion electrospinning.<sup>45</sup> Emulsion electrospinning uses two immiscible liquids with one liquid suspended within the other liquid and often stabilized at the interface with a surfactant.<sup>41</sup> This two-phase polymer solution allows for the natural formation of pores through templating of the internal phase. In some cases, emulsions are able to maintain their internal phase pores resulting in fibers with internal porosity, while in other cases, water droplets coalesce to the center of the electrospun fiber creating a hollow core.<sup>45-48</sup> Emulsion electrospinning also requires a simpler setup because it only needs one needle to electrospin, potentially making it an easier candidate for scale-up production of commercial electrospun fibers encapsulating a bioactive molecule.



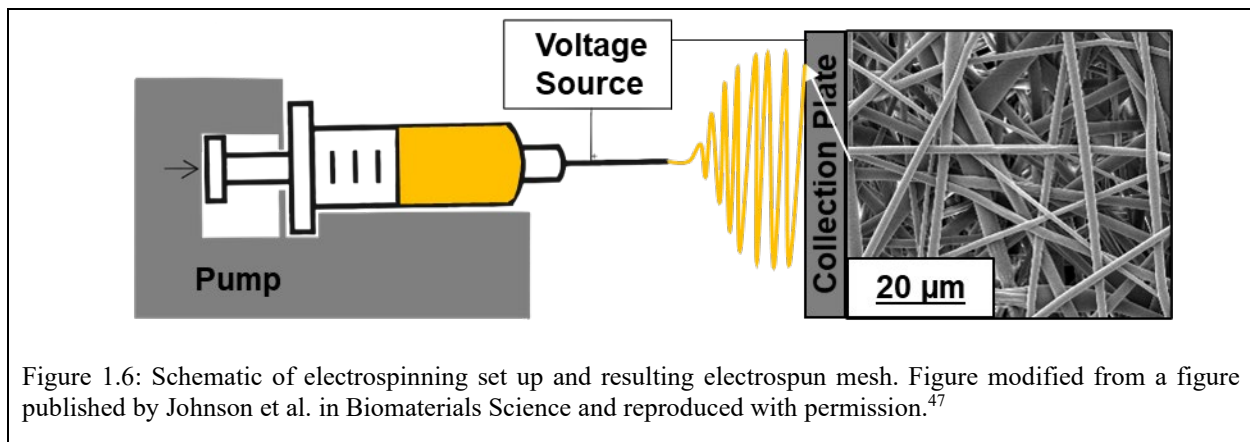
## 1.2 HISTORY OF ELECTROSPINNING

One of the earliest records of the technology underlying the electrospinning process was conducted by William Gilbert in the 1600s, who observed the deformation of a water droplet into a cone like shape when in an electric field.<sup>49</sup> This work was further developed in the 1700s when George Mathias Bose described aerosols under high electric potential.<sup>49</sup> He was a professor of philosophy in Wittenberg, Germany, and demonstrated his understanding of this material by performing demonstrations. One of these demonstrations included standing female subjects inside an insulated platform and inviting men from the audience to kiss the female. When they kissed, both parties would receive a shock. This demonstrated that the water droplets in the air could be charged<sup>49</sup>. The first commercial application of electrospinning is in a patent filed by George Audemars in 1855, who developed a method for spinning collodion, which is synthesized from cellulose extracted from a Mulberry tree. This was likely developed as a less expensive version of silk because Mulberry silkworms were used to create silk at the time. In this process, he extruded the collodion from a needle in a liquid concentrated form, which would solidify during the process. However, the material developed was too flammable for clothing.

The understanding of how interrelated parameters affect the electrospinning process first started around 1971 when Peter Karl Baumgarten while working for Du Pont Nemours, developed a method of photographing electrospun fibers in flight.<sup>49</sup> Imaging continued to play a large role in understanding, and when the electron microscope became more accessible in the 1990s, imaging of resulting fibers in mesh was enabled. Imaging fibers at the nanoscale allowed further understanding of fiber morphology and topography of fibers. Imaging fibers also lead to a more robust theoretical understanding of the electrospinning process, and pioneering work was conducted by Alexander Yarin, Darrell Reneker, and Gregory Rutledge.<sup>50-54</sup>

### 1.3 ELECTROSPINNING MECHANISM

In the electrospinning process, a polymer solution or polymer dope is extruded from a syringe attached to a voltage source, creating an electric field (Figure 1.6).<sup>2</sup> The solvent in the needle is charged from the applied voltage, and electrostatic repulsion eventually overcomes surface tension to eject a column of liquid in the form of a fiber which collects on the grounded collection plate. As the column of liquid moves from the needle tip to the collection plate, it whips back and forth due to bending instabilities, facilitating the evaporation of solvent, and allows dry fibers to collect on either a stagnant collection plate or a rotating cylindrical collector.



#### 1.3.1 Taylor Cone

The polymer solution is pumped out of the needle tip at a predetermined and controlled rate. Initially, this polymer solution takes the form of a spherical droplet because surface tension favors a minimal surface area and free energy of the droplet.<sup>55</sup> As voltage is applied to the spinneret, electrostatic repulsion favors increased surface area and deforms the spherical shape into a cone like shape called a Taylor Cone. The electrostatic pressure ( $\rho_e$ ) acting on the surface of the droplet can be characterized by Equation 1.1.<sup>2</sup>

$$\rho_e = \frac{\epsilon E^2}{2} \quad (\text{Eq. 1.1})$$

Where  $\epsilon$  is the dielectric constant and  $E$  is the intensity of the electric field. The opposing capillary pressure ( $\rho_c$ ) caused by surface tension is defined by the Young-Laplace equation (Equation 1.2).<sup>2</sup>

$$\rho_c = \frac{2\gamma}{r} \quad (\text{Eq. 1.2})$$

In this case,  $\gamma$  is the surface tension, and  $r$  is the radius of the curvature of the jet. When the electrostatic pressure exceeds the capillary pressure, surface tension is overcome, and the droplet forms a column of fluid. An additional force acts within the Taylor cone in the form of viscoelastic force of the liquid. Generally, polymer solutions are used to electrospin fibers, and the chain entanglement of the polymer also resists electrostatic pressure. Therefore, as viscosity increases, the applied voltage will also need to increase to achieve an electrostatic pressure that is able to overcome both capillary pressure and the viscoelastic force. In cases with insufficient chain entanglement of the polymer to maintain the column structure of the injected liquid, the column will break up into droplets, and particles will be collected instead of fibers. This process is called electrospaying.

### 1.3.2 Bending Instability

The elongated Taylor cone is followed by a linear region of the electrospinning jet, also known as the near-field region.<sup>2</sup> This length can vary based on multiple parameters in the system, and as it ends, the bending instability starts. The near field region has been characterized by Equations 1.3 and 1.4.

$$L = \frac{4kQ^3}{\pi\rho^2I^2} \left( \frac{1}{R_0^2} - \frac{1}{r_0^2} \right) \quad (\text{Eq. 1.3})$$

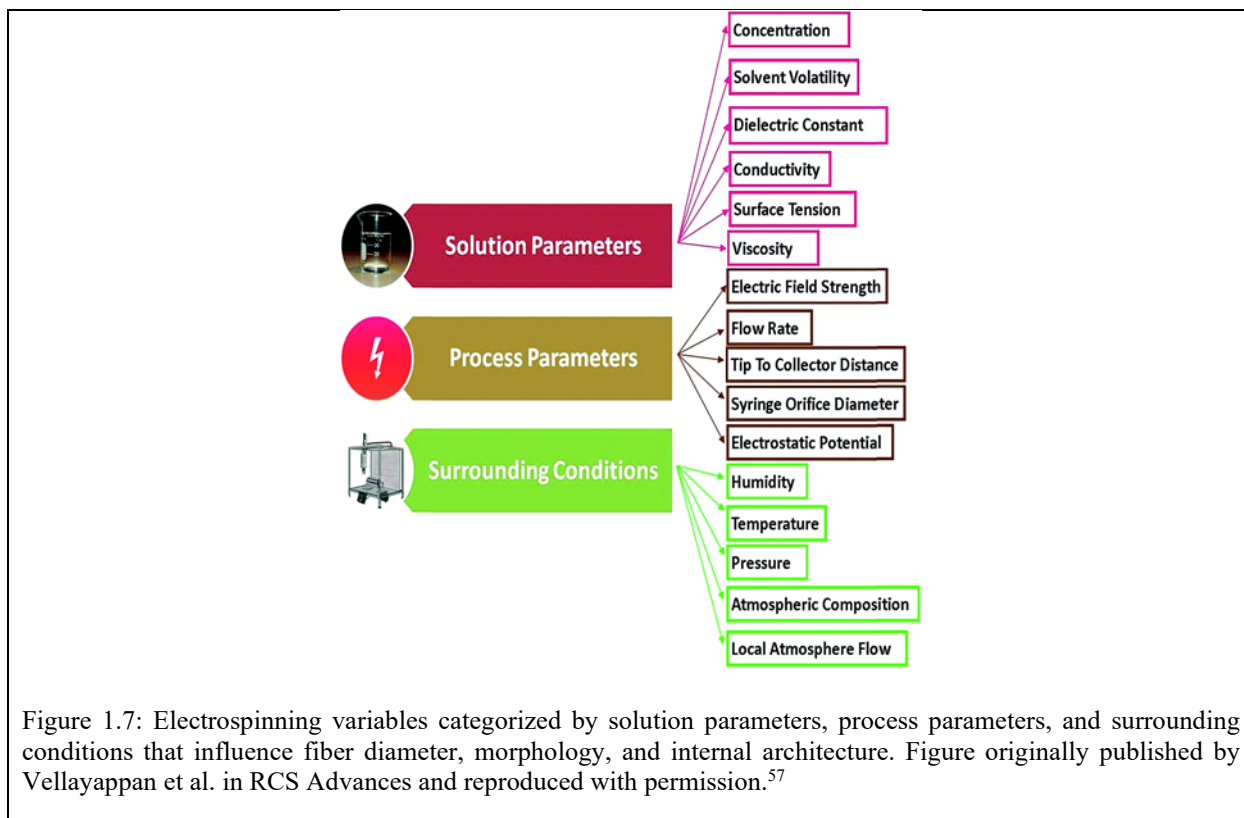
$$R_0 = \left( \frac{2\sigma Q}{\pi k\rho E} \right)^{\frac{1}{3}} \quad (\text{Eq. 1.4})$$

In this case, the near-field region length is  $L$ ,  $R_0$  is the final radius of the jet,  $Q$  is the flow rate,  $k$  is the electrical conductivity of the fluid,  $\rho$  is the density of the fluid,  $I$  is the current passing through the jet,  $E$  is the strength of the electric field, and  $r_0$  is the initial radius of the jet. In general, this means that at low flow rates and low electrical conductivity of the fluid, the near field region is relatively short.

As the polymer jet in this region moves further away from the needle tip, acceleration slowly decreases, and the diameter of the jet decreases in a monotonic function.<sup>51,54</sup> Small perturbations caused by this change create an onset of instability and lead to bending of the fibers. This bending is caused by a lateral force caused by electrostatic repulsion of surface charges. Whipping in this region is critical to stretch the fibers. Some estimate that the elongation of the jet in this region can achieve up to 10,000 times elongation.<sup>51,56</sup> Solvent evaporates during the whipping process, often enabling fibers to collect dry or mostly dry on the collection plate.

#### **1.4 PARAMETERS AFFECTING THE COLLECTION OF ELECTROSPUN MESH**

Several variables play key roles in how the fiber collects on the plate and influence the resulting fiber diameter, morphology, and internal architecture. These variables are categorized as solution parameters, processing parameters, and environmental surrounding conditions (Figure 1.7)<sup>57,58</sup>.



### 1.4.1 Processing Parameters

Processing parameters in electrospinning specifically are focused on equipment-based setups. Processing parameters include the applied voltage, the distance from the needle tip to the collection in plate, the flow rate of the extruded polymer solution from the pump, and the needle inner diameter.<sup>57,59</sup> Voltage is applied to the needle of the syringe in a traditional electrospinning set up from a high voltage power supply. In general, the increasing voltage in the electrospinning system will first result in a decrease in fiber diameter until excess voltage occurs in the Taylor cone, which results in multiple jets of polymer from the Taylor cone (Figure 1.8).<sup>60</sup> When multiple jets occur in electrospinning, applied voltage will actually increase in fiber diameter because the jet velocity will increase for the same flow rate used.<sup>57,59</sup> Insufficient applied voltage and excessive applied voltage can also result in beaded morphology in nanofibers.

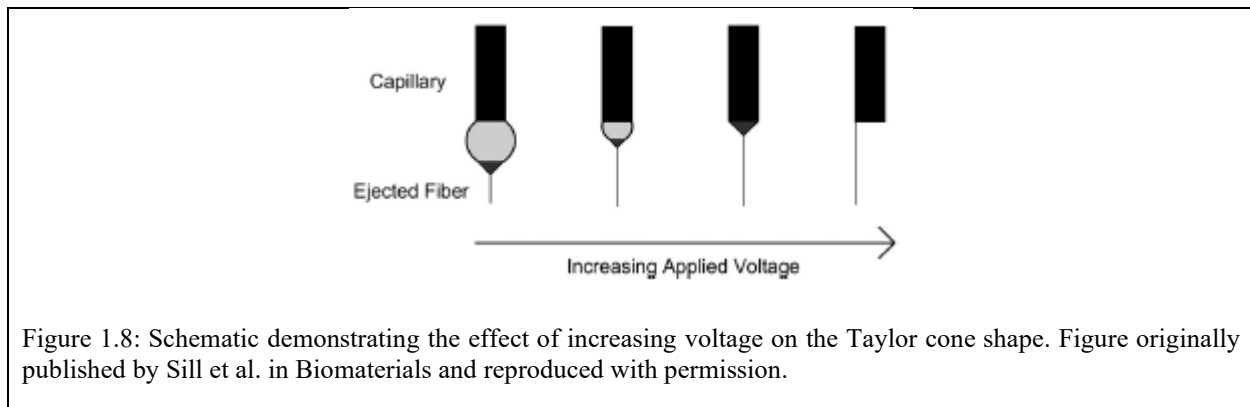


Figure 1.8: Schematic demonstrating the effect of increasing voltage on the Taylor cone shape. Figure originally published by Sill et al. in *Biomaterials* and reproduced with permission.

Generally, increasing the distance between the needle tip in the collection plate will result in a decrease in fiber diameter because the jets have a longer flight time to stretch before hitting the collection plate.<sup>59,60</sup> Very short distances from the needle tip to the collection plate can end up decreasing the fiber diameter; however, as the increased electric field strength causes an increase in fiber whipping and stretching. Although, these conditions are not often used as they can lead to incomplete solvent evaporation and wet fiber collection. Studies by Theron et al. suggest that the electrostatic charge on the surface of the electrospinning jet decreases with distance from the needle tip.<sup>60,61</sup> Therefore, as the surface charge on the surface of the jet decreases, surface tension can dominate and result in beaded morphology. Decreases in the electric field at a further distance from the needle tip can also result in an increase in fiber diameter due to the viscoelastic forces of the polymer in the jet.<sup>62</sup>

Increasing the flow rate, in general, leads to increases in fiber diameter and increased fiber volume fractions.<sup>60</sup> Excessive flow rate can result in beading and ribbon morphology because fibers do not have enough time to dry prior to hitting the collection plate. At flow rates that are too low for the given system, receded jets, jet that form from inside the needle with no Taylor cone forming, will form.<sup>59</sup> Receded jets are not stable and therefore can result in a wide distribution of fiber diameters. Increasing the flow rate can increase the elongation of the Taylor cone and also result in increased fiber diameter (Figure 1.9).<sup>63</sup>

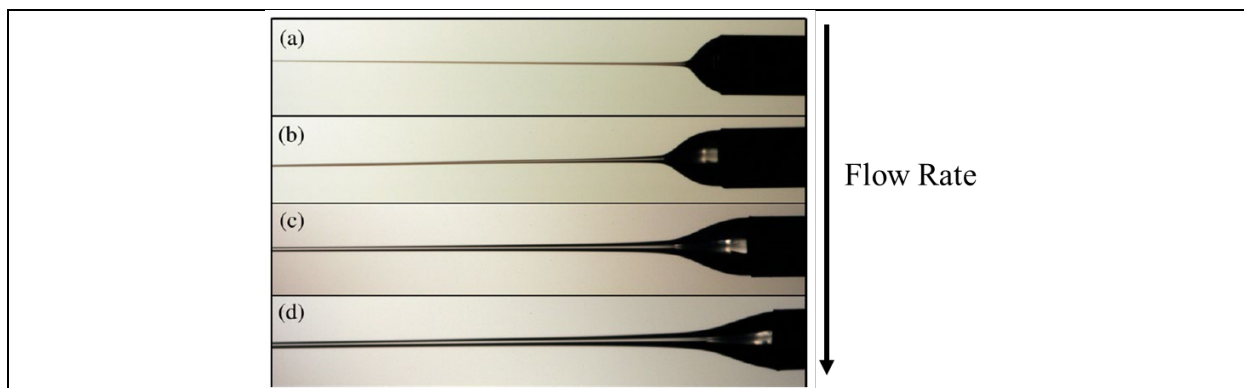


Figure 1.9: Taylor cone shape change with increasing flow rate. Figure originally published in *Advanced Drug Delivery Reviews* by Rutledge et al. and reproduced with permission.<sup>63</sup>

Increasing the needle inner diameter has been shown to increase the diameter of the resulting fibers.<sup>64</sup> Increased fiber diameter is primarily attributed to increased volume of fluid in the Taylor cone, resulting in a larger starting diameter for electrospinning. Larger inner diameters are also shown to favor multiple jets formation.<sup>65</sup> This is due to a larger surface area of the droplet at the needle tip allowing for uneven distribution of surface charges to allow multiple jets to form from one droplet. Fiber diameter distribution can also increase with an increasing inner diameter of the needle use because of this instability and multiple jets formations.

### 1.4.2 Solution Chemistry

The solvent selected for electrospinning fibers is important because it can affect fibers due to the solvent evaporation rate, conductivity, viscosity, surface tension, and ability to solubilize polymer. To obtain dry cylindrical fibers, a solvent with optimal volatility must be selected for the system.<sup>66</sup> This optimal evaporation rate must be rapid enough that solvent is able to evaporate prior to fibers hitting the collection plate yet not too rapid as to cause clogging of the needle tip.<sup>66</sup> A solvent that evaporates quickly can also cause clogging or intermittent “spitting” or large clumps of polymer in chunks hitting the collection plate sometimes between periods of normal

collection.<sup>2,67</sup> This is caused by a polymer film growing at the needle tip that eventually chokes off the polymer jet causing it to ‘spit’. Polymer solutions fabricated with solvents that do not evaporate fast enough can result in wet fibers, fused fibers, ribbon morphology, and surface pores.<sup>60,66,68</sup> Ribbon morphology occurs in systems with a highly volatile solvent because rapid evaporation creates a skin or glassy shell of solidified polymer on the outside of the fiber that later collapses once on the collector due to Maxwell forces.<sup>68,69</sup> Haider et al. has suggested that boiling point is a good indication of the volatility of solvents.<sup>59</sup>

Conductivity is also an important parameter in electrospun solutions.<sup>54</sup> When selecting a solvent for electrospinning, it is critical that the solvent is conductive enough that it will allow electrons to propagate through the electrospinning jet within the electric field to form a continuous fiber. The conductivity of the solution is also an important factor in dictating the shape of the Taylor cone.<sup>2</sup> Solutions with a greater ability to hold charge will have a higher charge density and, therefore, greater electrostatic repulsion. Without sufficient conductivity, the jet may not form a liquid column. An optimal range also exists within individual systems for ideal solvent conductivities and low conductivity that can form beaded fibers while high conductivity can cause multiple jets.<sup>70,71</sup> One of the challenges with selecting a solvent for hydrophobic polymers is that they generally are most soluble in organic solvents. Organic solvents often have low conductivity due to their composition and, therefore, may be insufficiently conductive on their own to be used for electrospinning. Therefore, organic solvents are often blended with solvents with higher conductivity, conductive elements are added, or plasma treatment is added.

Surface tension is also an important parameter in solution chemistry for electrospinning. Surface tension is one of the factors that dictates the shape of the Taylor cone, and higher surface tension can result in beading morphology.<sup>2,50</sup> Cationic and anionic surfactants are the most



common type of surfactant added to electrospun fibers because they increase conductivity and can improve the morphology of the system in addition to decreasing surface tension.<sup>72,73</sup>

Finally, viscosity plays a major role in solution chemistry used for electrospinning fibers. At high viscosity levels, the charge repulsion may be insufficient to stretch the droplet at the needle tip into fibers.<sup>59</sup> Similarly, at low viscosity, surface tension dominates, and the viscoelastic forces are insufficient to overcome surface tension resulting in an elector spraying of droplets instead of fibers. At lower solution viscosities, multiple jets are more likely to form at the Taylor cone due to insufficient polymer chain entanglement. The deposition area of fibers on a collection plate is generally smaller for more viscous fibers because higher chain entanglement resists bending instability.<sup>66</sup> This reduction in bending also results in larger fiber diameters with higher levels of viscosity. Shenoy et al. evaluated polymer chain entanglement of polymer for electrospinning solutions fabricated with polystyrene (PS), polylactic acid (PLA), and polyethylene oxide (PEO) based on the calculated entanglement number ( $n_e$ ) (Equation 1.5).<sup>74</sup>

$$(n_e)_{soln} = \frac{M_w}{(M_e)_{soln}} = \frac{(\Phi_p M_w)}{M_e} \quad (\text{Eq. 1.5})$$

Where  $M_w$  is the weight average molecular weight of the polymer,  $M_e$  is a solution entanglement molecular weight, and  $\Phi_p$  is a polymer volume fraction in solvent. Shenoy found that smooth cylindrical fibers were produced for entanglement numbers greater than 3.5, and no fibers were formed below entanglement numbers of 2. This was true for solutions each containing polymers polylactic acid, polyethylene oxide, and polystyrene.

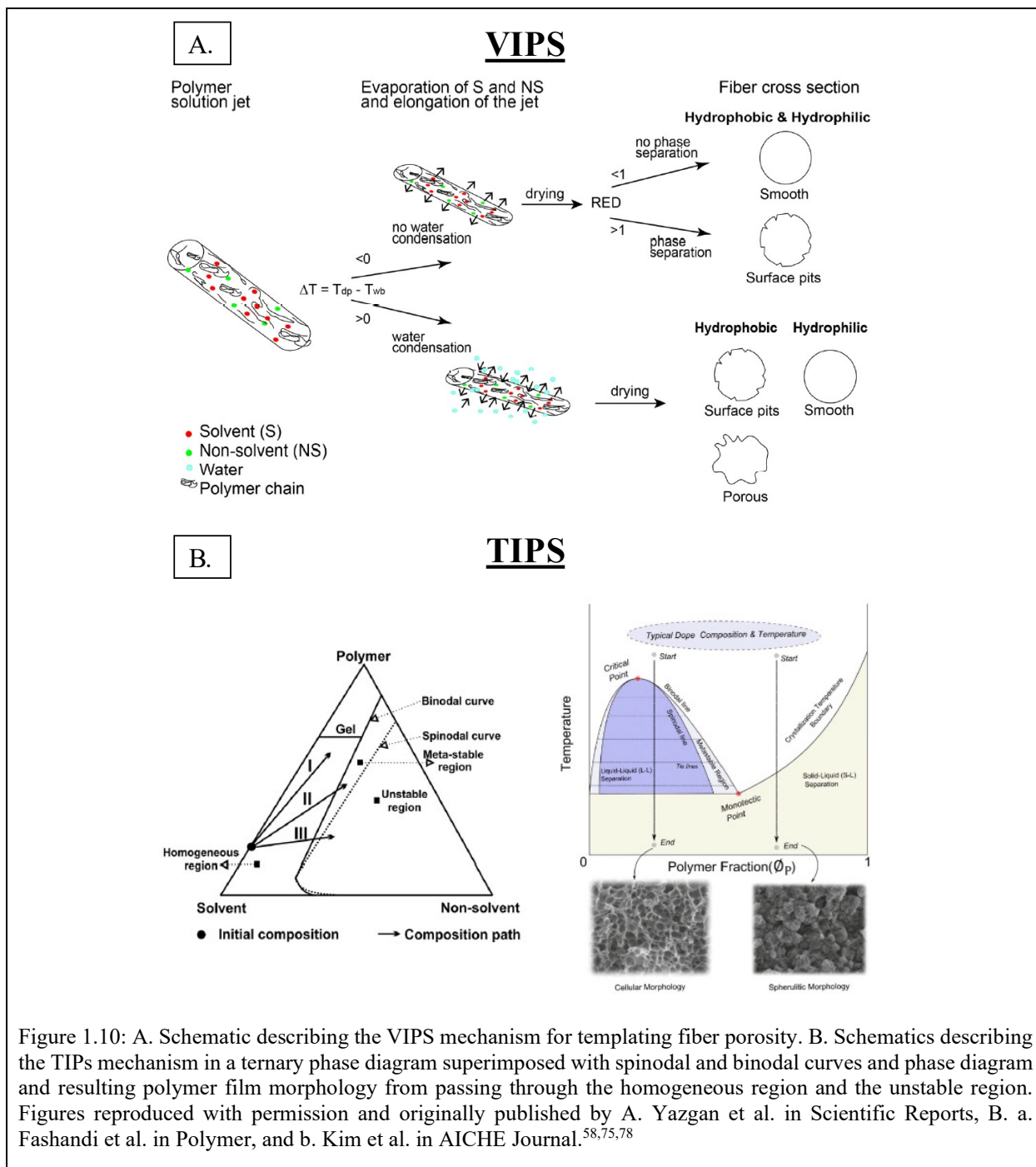
#### *1.4.2.1 Phase Separation*

Phase separation is a common phenomenon in electrospinning, and in this process, the polymer solution separates into polymer-rich and polymer-poor regions due to vapor-induced

phase separation (VIPS), thermally induced phase separation (TIPS), and non-solvent induced phase separation (NIPS).

#### *1.4.2.2 Vapor Induced Phase Separation*

VIPS can occur when ambient water droplets either condense on the surface of the fiber or are able to penetrate into electrospun fibers during the electrospinning process.<sup>58,75-77</sup> In systems with hydrophobic polymer particularly, this phenomenon results in phase separation into polymer-rich and polymer-poor sections. In general, higher relative humidity causes more VIPS, resulting in fibers with porous surfaces and sometimes porous internal architectures. Yazgan et al. developed a model for when water condenses on the outside of fibers by first comparing the wet-bulb temperature of the polymer jet to the dew point temperature of the ambient air (Figure 1.10).<sup>75</sup> In fibers where the dew point temperature is greater than the wet-bulb temperature, condensation will occur, and pores will form at least on the surface of the fiber for hydrophobic polymers.



### 1.4.2.3 Thermally Induced Phase Separation (TIPS)

TIPS is a phenomenon that is commonly hypothesized as a potential mechanism for pore formation in electrospun fibers but is not well described and often misused in the field. TIPS

originates in studies performed on thin films or membranes resulting in pores.<sup>79</sup> TIPS creates pores by dissolving a semi-crystalline polymer in solution and removing thermal energy from the solution. As thermal energy is removed from the system, the polymer solution moves into a metastable region in which liquid-liquid separation can occur given nucleation or activation energy. In electrospinning, two solvents with different volatility are often used to electrospin fibers. When the solvent with higher volatility evaporates out of the fiber first, the surface of the fiber undergoes evaporative cooling.<sup>58,80-82</sup> This reduction of temperature can force the remaining solution from a heterogeneous solution into either an unstable region of liquid-liquid phase separation or into a metastable region of liquid-liquid phase separation with nucleation. In both cases, the gelation of polymer following this process allows the microstructure formed in liquid-liquid phase separation to retain porosity (Figure 1.10). Megelski et al. argues that in the absence of high relative humidity, pores on the surface of electrospun fibers and not within the fiber indicate that this process only occurs at the surface of electrospun fibers where evaporative cooling occurs.<sup>80</sup> However, this method of phase separation has yet to be fully explored independently of high relative humidity where the effects of VIPs are controlled for.

#### *1.4.2.4 Non-Solvent Induced Phase (NIPS)*

NIPS can occur in electrospinning systems having two or more solvents and at least one polymer.<sup>75,79,81</sup> As previously discussed, it is common to put a second solvent into the electrospinning solution to increase conductivity, especially in cases where a less conductive solvent is used as the main solvent in the system. In this system, however, the polymer is soluble or highly favors one of the solvents resulting in polymer-rich and polymer-poor regions. This type of phase separation is different from thermally induced phase separation in that the liquid regions are separated prior to starting the electrospinning process. Katsogiannis et al. argues that using

systems with NIPS phase separation is easier to control and can increase reproducibility in samples.<sup>81</sup>

### 1.4.3 Ambient Conditions

The ambient relative humidity can play a major role in fiber morphology, diameter, topography, and internal architecture.<sup>75-77</sup> This is because relative humidity can alter the rate of evaporation of the solvent and can interact with the solvent(s) in the system. In general, increasing relative humidity will increase the surface porosity of hydrophobic polymers. Internal porosity of fibers with hydrophobic polymers at high relative humidity depends on the fiber diameter and miscibility of the polymer and solvent(s).<sup>2</sup> Relative humidity has been shown to both increase and decrease fiber diameter.<sup>83-85</sup> At higher levels of relative humidity in systems using hydrophobic polymer, fiber diameter may increase due to precipitation of polymer with water when the polymer is particularly water insoluble.<sup>83,84</sup> Other studies have found that fiber diameter decreases with increasing relative humidity due to slower solvent evaporation.<sup>75,86</sup> Ghobeira et al. also hypothesized that water may be acting as a plasticizer and facilitating stretching of PCL fibers.<sup>86</sup> Studies using hydrophilic polymer have shown a decrease in fiber diameter due to water absorption leading to a reduced concentration of polymer in solvent, therefore allowing for greater stretching of the polymer chains during the whipping phase of electrospinning and also may result in broken fibers.<sup>77,87</sup> At low levels of relative humidity, fiber diameter may increase due to rapid solvent evaporation reducing polymer chain mobility and therefore less stretching during the electrospinning process.<sup>58,75</sup> Other studies found that at low relative humidity, the fiber diameter decreased due to reduced precipitation effects when polymer came into contact with ambient water droplets at high relative humidity.<sup>84</sup>

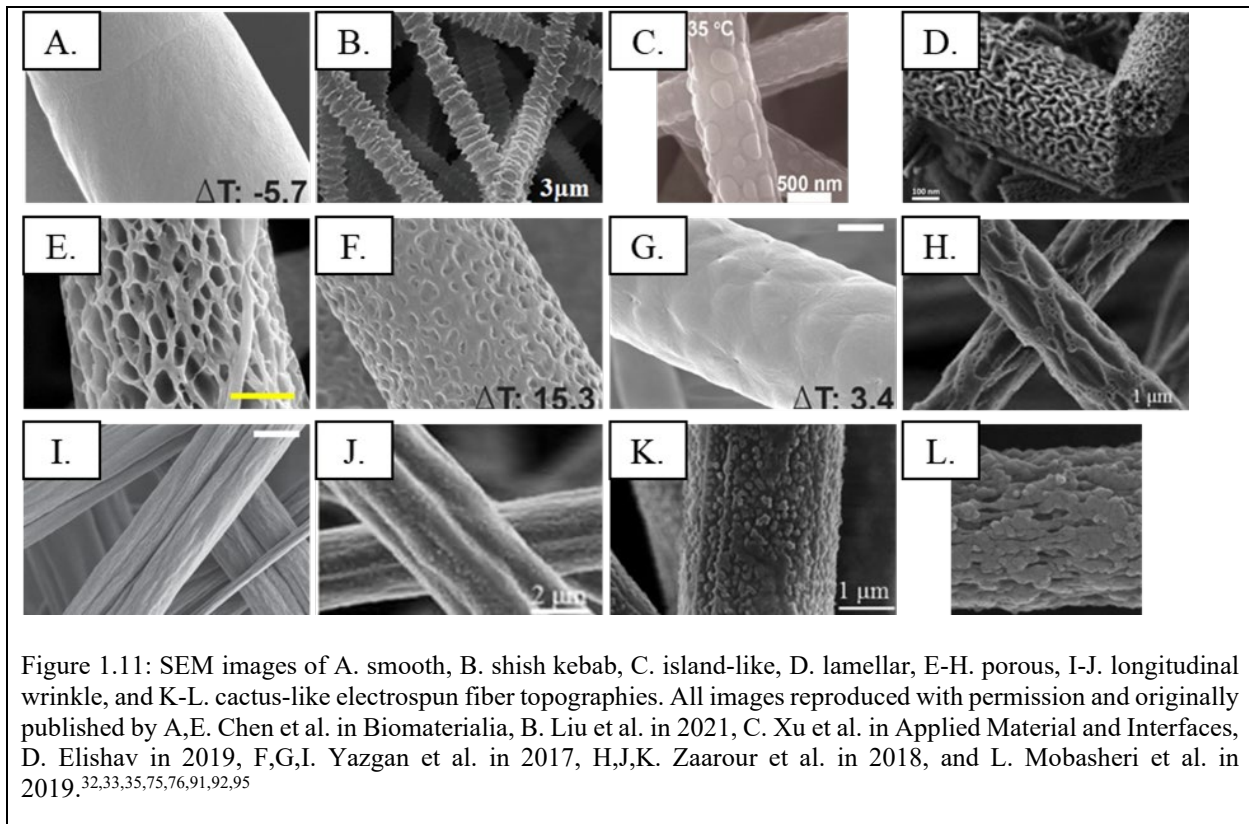
Temperature may also affect the electrospinning fiber morphology, topography, and fiber diameter.<sup>58</sup> Increasing the temperature of the environment in the electrospinning generally will accelerate solvent evaporation, alter polymer solubility, and decrease viscosity. Therefore, increasing temperature generally leads to smaller fiber diameters.<sup>83,84</sup> Higher temperature effects on solution chemistry also result in fiber morphology of branching, multiple jets formation, beading, and increase in fiber distribution.<sup>58,88,89</sup> Faster vaporization of solvent at higher temperatures can also decrease the crystallinity because the polymer does not have as much time to self-associate.

## **1.5 ELECTROSPUN MESH CHARACTERISTICS**

### **1.5.1 Fiber Surface Topography**

Fiber surface topography can be created in electrospun fibers either by creating the topography during the electrospinning process or after the electrospinning process through postprocessing of the mesh. Typical electrospinning fibers with no phase separation and no postprocessing have a smooth fiber topography (Figure 1.11A).<sup>75</sup> Some postprocessing methods involve bathing the polymer in a solution to alter crystallinity, electrospinning with a sacrificial component that is later dissolved out to create topography, and annealing fibers. Liu et al. created shish kebab topography of fibers by bathing mesh in solution to create recrystallization of the polymer in lateral ridges (Figure 1.11B).<sup>32</sup> Xu et al. electrospun fibers with a sacrificial component in the electrospinning solution that was then dissolved out in postprocessing to create island like topography (Figure 1.11C).<sup>90</sup> Elishay et al. used an annealing process to create lamellar topography on the surface of fibers (Figure 1.11D).<sup>91</sup> Chen et al., Yazgan et al., Liu et al., and Zaarour et al. have all demonstrated that fiber surface porosity can also be tuned with relative humidity to create a wide variety of porous surface structures depending on solvents and polymer it is used (Figure

1.11E-H).<sup>35,75,76,92</sup> Zaarour et al., Yazgan et al., and Wang et al. have also reported that humidity can also be templated into longitudinal wrinkles from elongation of ambient water condensing on the surface of the fiber and from buckling of the fiber, causing it to collapse in on itself when drying (Figure 1.11I,J).<sup>75,93,94</sup> Zaarour et al. has created fibers with a cactus like surface topography and hypothesizes that this topography is due to pressure differences in evaporating solvents (Figure 1.11K).<sup>92</sup> Mobasheri et al. created an even more prominent protrusion covered fiber through a similar mechanism as the cactus fibers (Figure 1.11L).<sup>95</sup>



## 1.5.2 Fiber Morphology

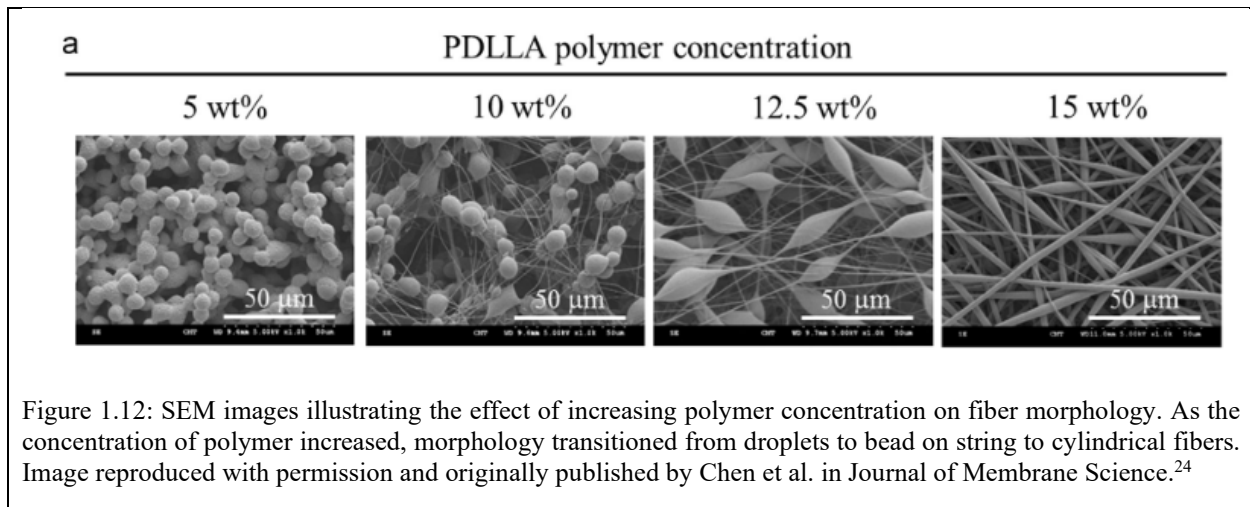
### 1.5.2.1 Beading Morphology

Beading morphology of electrospun fibers is generally undesirable because they usually reduce the mechanical properties of the mesh and are difficult to control in order to create

reproducible samples.<sup>96</sup> Some of the primary mechanisms involved in the formation of beading morphology include solution viscosity, net charge density in the electrospinning jet, and surface tension of polymer solution. In general, the formation of beading morphology in electrospinning occurs in cases where the solution has low polymer molecular weight, concentration, or viscosity, high polymer solution surface tension, and low charge density.<sup>50</sup> During the electrospinning process, sufficient charge density is needed to elongate the liquid polymer jet to form fibers. Factors that oppose this elongation into a cylindrical jet include surface tension, where the liquid will favor a smaller surface area per unit mass which is a spherical shape (Rayleigh instability). Therefore, when a polymer solution has a high surface tension or insufficient charge density to overcome the surface tension, beading morphology may occur.<sup>50,54</sup> Polymer within the solution also plays a major role in opposing the Raleigh instability through the viscoelasticity and chain entanglement opposing surface tension deformation.

One of the first studies to investigate the change in beading morphology with solution viscosity, solution surface tension, and the solution's ability to propagate charge was Fong and Reneker in 1999.<sup>50</sup> In this study when solution viscosity was increased, the formation of beads was less likely to occur. In cases where beading did occur, the diameter of the beads became larger, the average distance between the beads became longer, and the shape turned more spindle-like with increasing viscosity, indicating a transition from bead on string morphology to cylindrical fibers. This transition was also observed in a study by Chen et al. where increasing the polymer concentration of PDLLA resulted in fiber morphology that ranged from droplets to bead on string to cylindrical fibers (Figure 1.12).<sup>24</sup>





### 1.5.2.2 Branching Morphology

Branching of smaller fibers from the primary electrospinning jet can occur during the electrospinning process. There are several factors that can affect branching morphology, including charge in charge distribution, solution concentration, the radius of the electrospinning jet, and the surface area of the jet.<sup>2,97</sup> One of the popular explanations for the cause of branching occurring during the electrospinning flight was described in the model by Yarin, Kataphinan, and Reneker.<sup>97</sup> This model was based on experimental data where high-speed cameras were used to capture the branching phenomenon occurring during the electrospinning process (Figure 1.13).

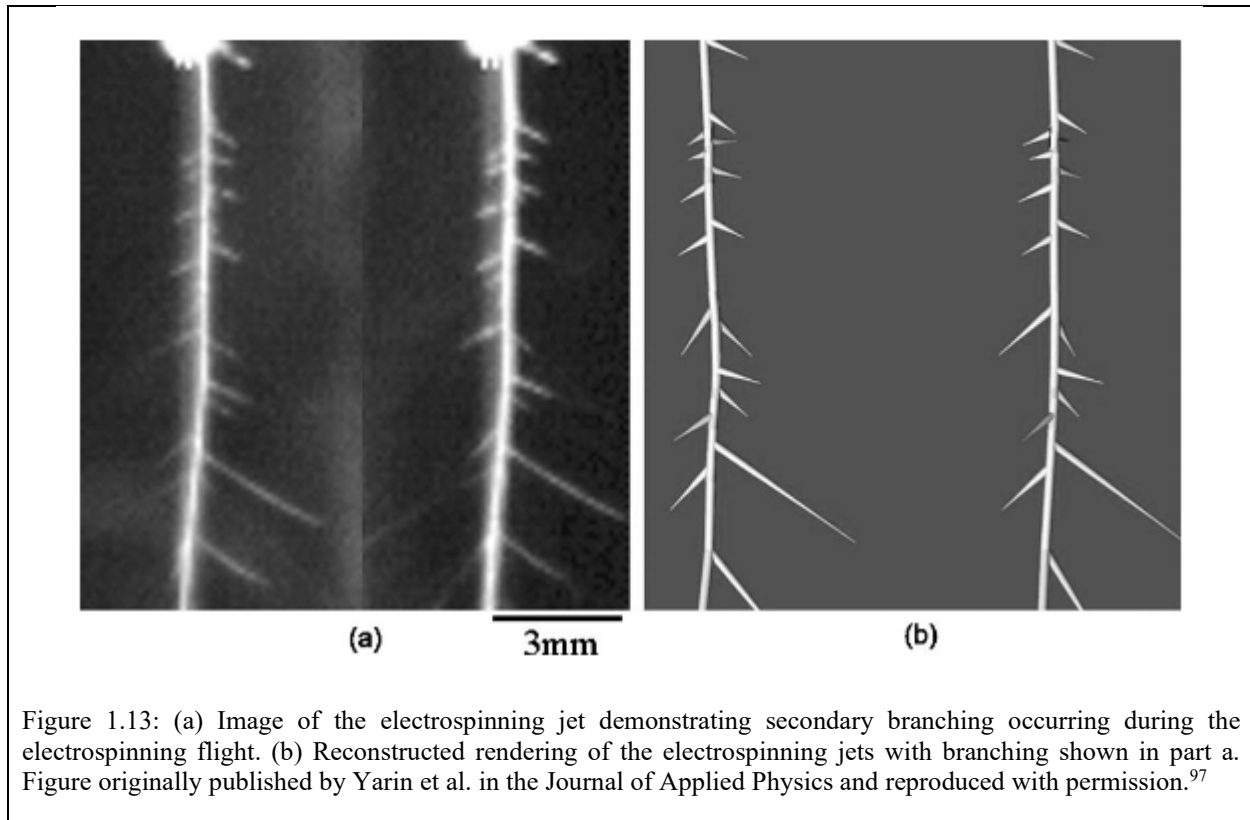
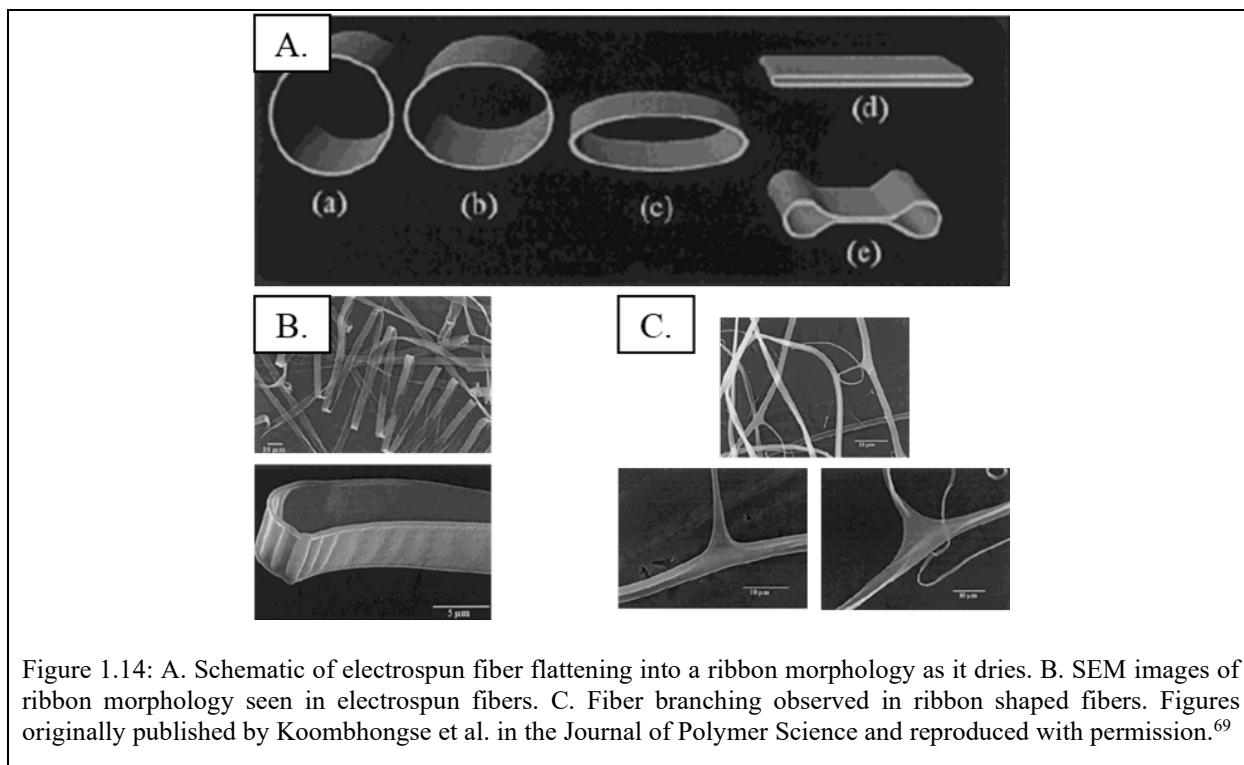


Figure 1.13: (a) Image of the electrospinning jet demonstrating secondary branching occurring during the electrospinning flight. (b) Reconstructed rendering of the electrospinning jets with branching shown in part a. Figure originally published by Yarin et al. in the Journal of Applied Physics and reproduced with permission.<sup>97</sup>

### 1.5.2.3 Flat/Ribbon Morphology

Ribbon or flat fibers can occur when the electrospinning jet hits the collector before completely drying. This often occurs in systems that have a rapid formation of a solid skin or shell, such as in systems that use highly volatile solvents.<sup>54,69</sup> This initial shell traps solvent in the fiber and minimizes jet elongation, and therefore, the center of the jet is wet upon collection on the collection plate. As the solvent begins to evaporate through the shell of the fiber after collection, the repulsive Coulomb forces in the plane of the ribbon are sufficient to pull the ribbon apart laterally (Figure 1.14A, B). Ribbon morphology is also often seen in fibers with branches because repulsive forces on the skin of a ribbon can pull the jet apart to create a split branch (Figure 1.14C).



Ribbon morphology can also occur with other parameters such as polymer concentration, viscosity, and polymer molecular weight.<sup>98-100</sup> Dhanalakshmi et al. demonstrated the formation of ribbon fibers when the polymer concentration increased from 5% w/v to 10% w/v in systems with 20kV applied voltage.<sup>100</sup> Koski et al. demonstrated that for the same concentration of polymer (25 wt. %) when the molecular weight was increased from 13,000 -23,000 g/mol to 31,000, 50,000 g/mol fiber morphology changed from cylindrical fibers to flat ribbon fibers.<sup>98</sup> In a study conducted by Amiraliyan et al., flat ribbon fibers were observed when the temperature was increased from 25° C to 50°C.<sup>88</sup> Chen et al. also showed ribbon morphology when the solution feed rate was increased from 1 mL/h to 1.5 mL/h.<sup>24</sup>

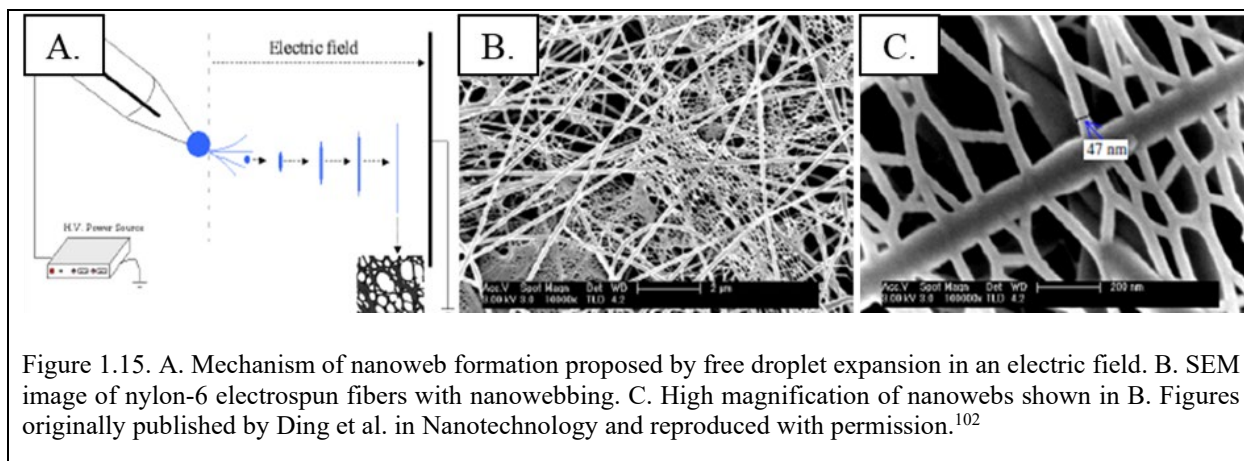
#### 1.5.2.4 Garland Fibers

Garland fibers are fibers that have wound around each other or entangled during electrospinning to form a column of electrospun fibers.<sup>2,53,54,101</sup> Studies from Darrell Reneker's lab

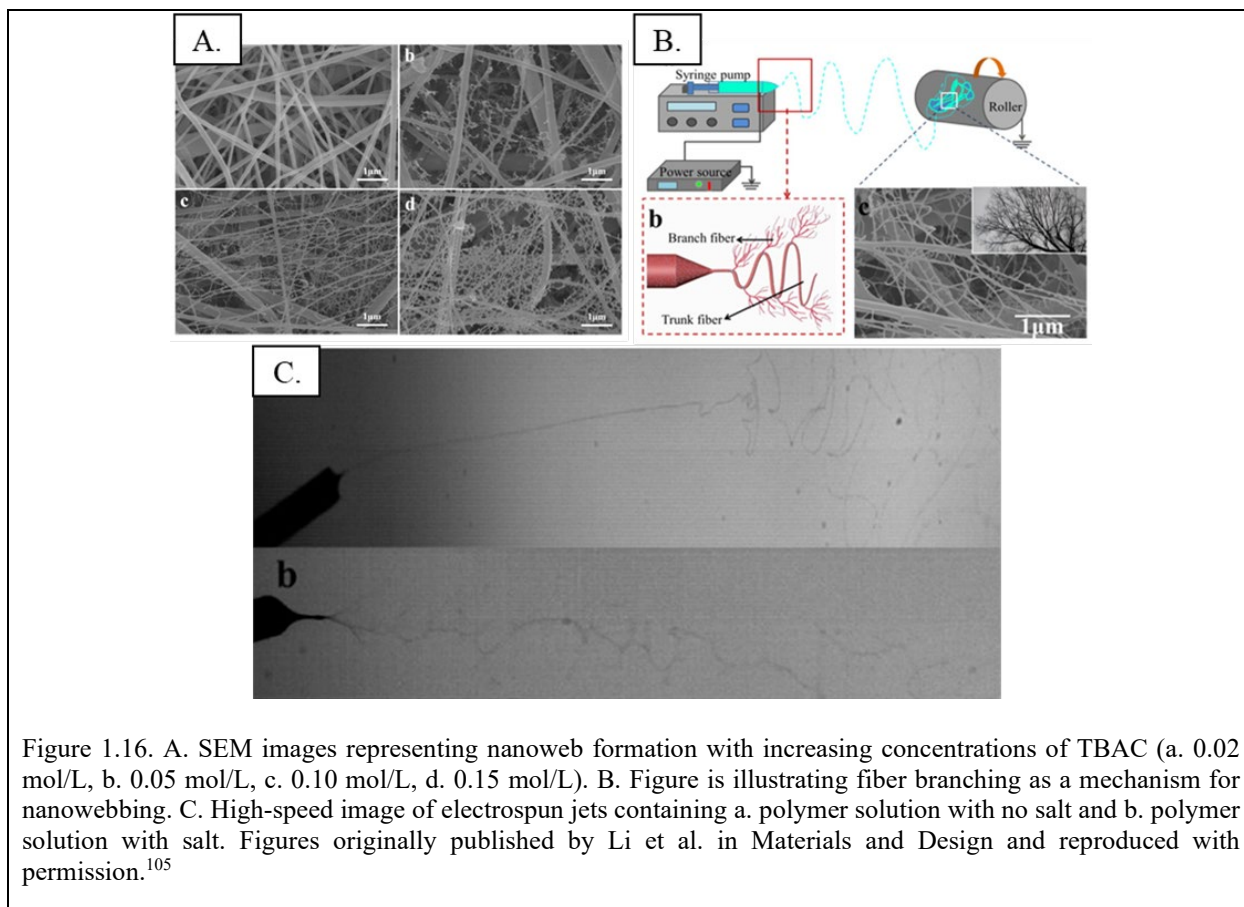
have shown that garland fibers occur when polymer jets intersect during the electrospinning process, conglutinate, and form a column of fibers. This column of fibers generally has larger overall fiber diameters because whipping is reduced due to fibers being interwoven. Garlands generally form when either the jet experiences branching, multiple jets are formed, or higher order bending instabilities cause fibers to intersect.

#### *1.5.2.5 Nanowebs*

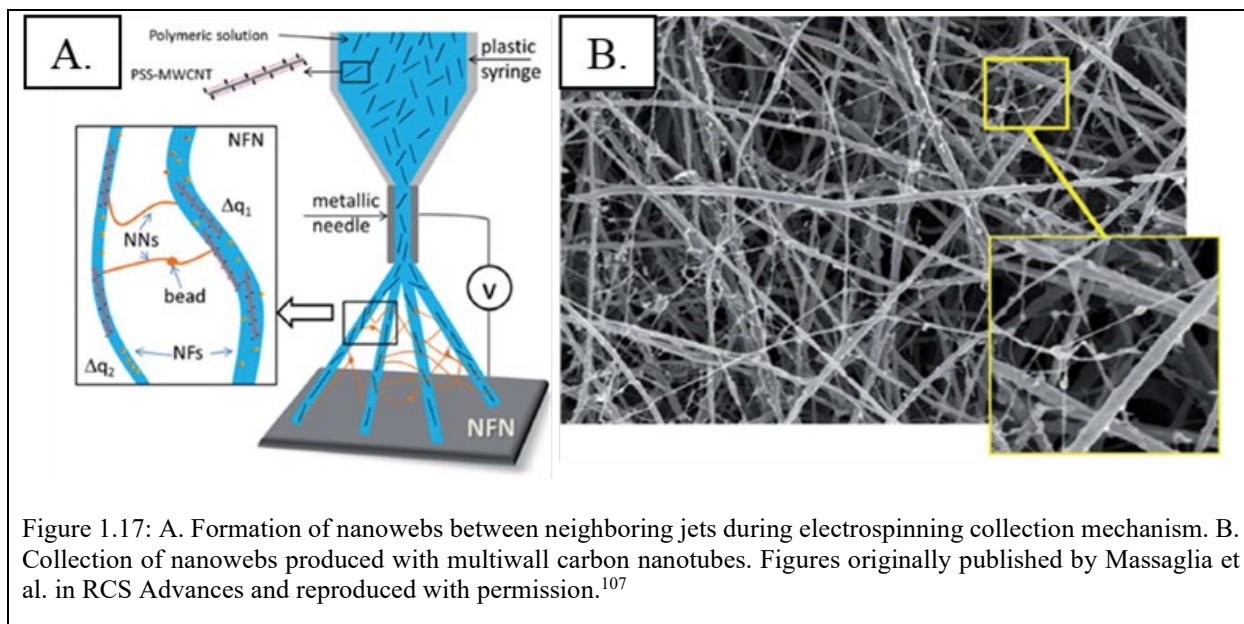
Nanowebs are nanofibers in the tens of nanometer diameter range that form between larger electrospinning fibers. These fibers are often at least one order of magnitude smaller than the other electrospun fibers collected.<sup>102</sup> One of the earliest publications of nanowebs was by Ding et al., where nanowebs were fabricated using poly(acrylic acid) in ethanol and Nylon-6 in formic acid (Figure 1.15B, C).<sup>102</sup> Ding hypothesized that nanowebs are formed when droplets of polymer are ejected from the needle tip and under conditions of a high electric field, phase separation and rapid solvent evaporation, the droplets expand to form a nonwoven web (Figure 1.15A). Interestingly, in this study, webs did not form in conditions when the relative humidity was under 45% and when the applied voltage was less than 20 kV. The droplet expansion method was also hypothesized by Pant et al. in a study where increasing concentrations of a methoxy poly(ethylene glycol) (MPEG oligomer in a nylon-6 electrospun system encouraged nanonet formation.<sup>103</sup>



Li et al. produced nanowebbs in systems with polyvinylidene fluoride (PVDF) and increasing concentrations of tetrabutylammonium chloride (TBAC), and different types of salts added to the system.<sup>104,105</sup> As the concentration of salt increased, the amount of nanowebbing present in the SEM collection increased (Figure 1.16A). Nanowebbs were produced with the salts TBAC, TBAB, TEAC, LiCl, AlCl<sub>3</sub>, and CaCl<sub>2</sub> in the system used. Li proposed that nanowebbs in this system were produced by fiber branching near the needle tip (Figure 1.16B). The fiber branching mechanism, in part, was supported by high-speed images of the electrospinning jet during electrospinning showing no branching in electrospinning collection with no salt and branching in electrospinning systems with salt (Figure 1.16C). The high-speed imaging evidence for branching mechanism should be considered in view of fiber branching mechanisms described by Yarin and Reneker where branching occurs when there are perturbations in charge on the surface of an electrospinning jet, and this can occur with the addition of ionic compounds such as salts.<sup>54,97</sup>



A third mechanism in achieving nanowebbing morphology was proposed in studies by Barakat et al. and Massaglia et al..<sup>106,107</sup> In the study by Massaglia et al., nanowebbing was produced by incorporating multiwall carbon nanotubes with sodium polystyrene sulfonate as electrically conductive elements to induce nanowebbing.<sup>107</sup> Barakat et al. demonstrated the effect of solution mixing time in Nylon-6 systems with added salt and the effect of different kinds of salt (Figure 1.17A).<sup>106</sup> Interestingly, both Massaglia and Barakat proposed a mechanism of unbalanced concentrations of electrically charged salts inducing the formation of nanowebbs due to the localized charge between two neighboring multiple jets or branches during the electrospinning process (Figure 1.17B).



## 1.6 KNOWLEDGE GAP

A detailed and thorough understanding of electrospinning parameters have been developed to relate the processing parameters and the resulting mesh morphology, topography, and fiber diameter. Electrospun fibers have been tested and are a promising material in the fields of tissue engineering and drug delivery. Within these two fields, there are many applications in which encapsulation of bioactive molecules or drugs is beneficial. Hydrophobic polymers are often used to create tissue engineering scaffolds and constructs for drug delivery because they have slower hydrolytic degradation rates and, therefore, can release drug for a longer period of time.

Incorporating bioactive molecules and hydrophilic drugs can be challenging within hydrophobic polymer solutions used for electrospinning because phase separation causes these compounds to relocate to the surface of the fibers, thus resulting in a burst release of drug and often a reduction in bioactivity. Furthermore, many of the organic solvents used to electrospin hydrophobic polymers into fibers are harsh and can cause a reduction in the bioactivity of encapsulated biomolecules. One method employed to encapsulate hydrophilic drugs and bioactive

molecules is emulsion electrospinning. Emulsion electrospinning also provides the advantage of a tunable internal structure to create a drug release profile optimized for the application. Emulsion electrospinning is a relatively new area of research, and while it has been used to create fibers for drug delivery applications, the mechanistic understanding of how emulsion components affect the resulting electrospun mesh has not been fully explored.

## **1.7 APPROACH**

This work focuses on evaluating individual components of emulsions in emulsion electrospinning to determine the resulting effects on electrospun mesh properties. Specifically, single solvent systems are first compared to systems using a second solvent that is miscible with both the first solvent and ambient water. A second comparison is made to a system employing an immiscible solvent with a polymer compatible solvent. Solvents and solvent blends were selected to compare the effects of evaporation rate and conductivity. All samples are compared at high and low relative humidity, and the resulting effects on fiber morphology, diameter, and surface topography are determined.

Next, the additional effects of surfactant in systems containing no aqueous internal phase and internal phase are compared. Although some work has been done to evaluate surfactants in emulsion and non-emulsion systems, these have primarily focused on cationic and anionic surfactants. The work detailed here will focus on non-ionic surfactants and specifically surfactant chemistry as characterized by hydrophobic lipophilic balance (HLB). Furthermore, some studies have hypothesized that surfactant relocates to the surface of the fibers during the electrospinning process. Surfactant relocation is further explored in systems containing no surfactant, surfactant, and internal phase creating an emulsion within increasing internal phase volume fractions of 2%, 4%, and 8% w/o. Surfactant relocation in electrospun fibers is compared at high and low relative



humidity to understand how vapor induced phase separation may further influence the resulting mesh characteristics.

Although emulsions have been generated with many different solution chemistries, the effect of internal phase volume fraction on electrospun fibers with appropriate controls containing surfactant only and no surfactant is explored in this body of work. Emulsion solution chemistry is also evaluated by using water-in-oil emulsions with continuous phase consisting of a single relatively hydrophobic solvent, a blend of solvents containing a continuous phase miscible and internal phase miscible solvent, and a blend of solvents containing an internal phase miscible solvent that is immiscible with the other continuous phase. Solution chemistry is important to understand how solvent affects emulsion chemistry and the resulting mesh morphology, surface topography, fiber diameter, and fiber diameter distribution. All of these meshes are also compared at high and low relative humidity to understand the effects of ambient water droplets on the emulsion electrospinning process.

Finally, using the tunability described above, a model for hydrophilic and hydrophobic drugs are encapsulated within fibers containing no surfactant, surfactant only, and in an emulsion to determine resulting burst drug release effects. Importantly, these systems are developed to control fiber diameter, fiber fraction, and fiber surface topography to minimize confounding variables. Although eliminating confounding variables may seem obvious due to the complexity of emulsion electrospinning and interrelated parameters, another study that has successfully controlled for all of these parameters and model the drug release rates of a hydrophilic and hydrophobic model drug is not found in the literature. Drug release from fibers containing porous internal architectures with smooth topography and porous topography with solid interiors were compared using a hydrophobic drug model drug for release rates. Additionally, larger fiber

diameters containing surface porosity with solid internal architecture were compared to fibers containing intermittent cores and primarily solid cores with smooth topography. This is important because surface roughness, fiber diameter, and internal porosity all play a role in drug release rates and cell interactions with tissue scaffolds. Overall, this work on emulsion electrospinning defines how solution chemistry dictates fiber morphology, surface topography, and fiber diameter for controlled electrospun fibrous meshes with tunable properties.

## 1.8 BIBLIOGRAPHY

- 1 Fridrikh, S. V., Yu, J. H., Brenner, M. P. & Rutledge, G. C. Controlling the fiber diameter during electrospinning. *Phys Rev Lett* **90**, 144502, doi:10.1103/PhysRevLett.90.144502 (2003).
- 2 Xue, J., Wu, T., Dai, Y. & Xia, Y. Electrospinning and Electrospun Nanofibers: Methods, Materials, and Applications. *Chem Rev* **119**, 5298-5415, doi:10.1021/acs.chemrev.8b00593 (2019).
- 3 Luo, C. J., Stoyanov, S. D., Stride, E., Pelan, E. & Edirisinghe, M. Electrospinning versus fibre production methods: from specifics to technological convergence. *Chemical Society reviews* **41**, 4708-4735, doi:10.1039/c2cs35083a (2012).
- 4 Ramakrishna, S. *et al.* Electrospun nanofibers: solving global issues. *Mater Today* **9**, 40-50, doi:10.1016/s1369-7021(06)71389-x (2006).
- 5 Ding, B., Wang, X. & Yu, J. *Electrospinning: Nanofabrication and Applications*. (Elsevier Science & Technology Books, 2018).
- 6 Matulevicius, J. *et al.* Design and Characterization of Electrospun Polyamide Nanofiber Media for Air Filtration Applications. *J Nanomater* **2014**, 1-13, doi:10.1155/2014/859656 (2014).
- 7 Stuart, M. A. C. *et al.* Emerging applications of stimuli-responsive polymer materials. *Nature Materials* **9**, 101-113, doi:10.1038/nmat2614 (2010).
- 8 Sun, Y. *et al.* Electrospun fibers and their application in drug controlled release, biological dressings, tissue repair, and enzyme immobilization. *RSC Advances* **9**, 25712-25729, doi:10.1039/c9ra05012d (2019).
- 9 Lu, W., Sun, J. & Jiang, X. Recent advances in electrospinning technology and biomedical applications of electrospun fibers. *J Mater Chem B* **2**, 2369, doi:10.1039/c3tb21478h (2014).
- 10 Goh, Y.-F., Shakir, I. & Hussain, R. Electrospun fibers for tissue engineering, drug delivery, and wound dressing. *J Mater Sci* **48**, 3027-3054, doi:10.1007/s10853-013-7145-8 (2013).
- 11 Wang, X., Ding, B. & Li, B. Biomimetic electrospun nanofibrous structures for tissue engineering. *Mater Today* **16**, 229-241, doi:10.1016/j.mattod.2013.06.005 (2013).
- 12 *PK Papyrus*, <<https://www.biotronik.com/en-de/products/coronary/pk-papyrus>> (

- 13 Wang, J. *et al.* Heparin and Vascular Endothelial Growth Factor Loaded Poly(L-lactide-co-caprolactone) Nanofiber Covered Stent-Graft for Aneurysm Treatment. *Journal of biomedical nanotechnology* **11**, 1947-1960 (2015).
- 14 Pickering, J. *POLYREMEDY LAUNCHES HEALSMART HYALURONIC ACID DRESSING ENHANCEMENT*, <<https://polyremedy.com/polyremedy-launches-healsmart-hyaluronic-acid-dressing-enhancement/>> (2013).
- 15 Ali, M. A. *et al.* Microfluidic Immuno-Biochip for Detection of Breast Cancer Biomarkers Using Hierarchical Composite of Porous Graphene and Titanium Dioxide Nanofibers. *Acs Appl Mater Inter* **8**, 20570-20582, doi:10.1021/acsami.6b05648 (2016).
- 16 Lannutti, J., Reneker, D., Ma, T., Tomasko, D. & Farson, D. Electrospinning for tissue engineering scaffolds. *Materials Science and Engineering: C* **27**, 504-509, doi:<https://doi.org/10.1016/j.msec.2006.05.019> (2007).
- 17 Chen, Z. *et al.* Electrospun nanofibers for cancer diagnosis and therapy. *Biomater Sci-Uk* **4**, 922-932, doi:10.1039/C6BM00070C (2016).
- 18 Yang, G. *et al.* From nano to micro to macro: Electrospun hierarchically structured polymeric fibers for biomedical applications. *Progress in Polymer Science* **81**, 80-113, doi:<https://doi.org/10.1016/j.progpolymsci.2017.12.003> (2018).
- 19 Paul, K. B., Singh, V., Vanjari, S. R. K. & Singh, S. G. One step biofunctionalized electrospun multiwalled carbon nanotubes embedded zinc oxide nanowire interface for highly sensitive detection of carcinoma antigen-125. *Biosens Bioelectron* **88**, 144-152, doi:10.1016/j.bios.2016.07.114 (2017).
- 20 Mohammadi, M. H., Obregon, R., Ahadian, S., Ramon-Azcon, J. & Radisic, M. Engineered Muscle Tissues for Disease Modeling and Drug Screening Applications. *Current pharmaceutical design* **23**, 2991-3004, doi:10.2174/1381612823666170215115445 (2017).
- 21 Meinel, A. J., Germershaus, O., Luhmann, T., Merkle, H. P. & Meinel, L. Electrospun matrices for localized drug delivery: current technologies and selected biomedical applications. *Eur J Pharm Biopharm* **81**, 1-13, doi:10.1016/j.ejpb.2012.01.016 (2012).
- 22 Hartman, O. *et al.* Microfabricated Electrospun Collagen Membranes for 3-D Cancer Models and Drug Screening Applications. *Biomacromolecules* **10**, 2019-2032, doi:10.1021/bm8012764 (2009).
- 23 Braghirolli, D. I., Steffens, D. & Pranke, P. Electrospinning for regenerative medicine: a review of the main topics. *Drug Discov Today* **19**, 743-753, doi:10.1016/j.drudis.2014.03.024 (2014).
- 24 Chen, S.-H., Chang, Y., Lee, K.-R. & Lai, J.-Y. A three-dimensional dual-layer nano/microfibrous structure of electrospun chitosan/poly(d,l-lactide) membrane for the improvement of cytocompatibility. *J Membrane Sci* **450**, 224-234, doi:10.1016/j.memsci.2013.08.007 (2014).
- 25 Agarwal, S., Wendorff, J. H. & Greiner, A. Use of electrospinning technique for biomedical applications. *Polymer* **49**, 5603-5621, doi:<https://doi.org/10.1016/j.polymer.2008.09.014> (2008).
- 26 Bancelin, S. *et al.* Determination of collagen fibril size via absolute measurements of second-harmonic generation signals. *Nature Communications* **5**, 4920, doi:10.1038/ncomms5920 (2014).

- 27 Puetzer, J. L., Ma, T., Sallent, I., Gelmi, A. & Stevens, M. M. Driving Hierarchical Collagen Fiber Formation for Functional Tendon, Ligament, and Meniscus Replacement. *Biomaterials* **269**, 120527, doi:10.1016/j.biomaterials.2020.120527 (2021).
- 28 Bashur, C. A., Dahlgren, L. A. & Goldstein, A. S. Effect of fiber diameter and orientation on fibroblast morphology and proliferation on electrospun poly(D,L-lactic-co-glycolic acid) meshes. *Biomaterials* **27**, 5681-5688, doi:10.1016/j.biomaterials.2006.07.005 (2006).
- 29 Bean, A. C. & Tuan, R. S. Fiber diameter and seeding density influence chondrogenic differentiation of mesenchymal stem cells seeded on electrospun poly( $\epsilon$ -caprolactone) scaffolds. *Biomedical Materials* **10**, 015018, doi:10.1088/1748-6041/10/1/015018 (2015).
- 30 Wang, G., Hu, X., Lin, W., Dong, C. & Wu, H. Electrospun PLGA-silk fibroin-collagen nanofibrous scaffolds for nerve tissue engineering. *In Vitro Cell Dev Biol Anim* **47**, 234-240, doi:10.1007/s11626-010-9381-4 (2011).
- 31 Christopherson, G. T., Song, H. & Mao, H. Q. The influence of fiber diameter of electrospun substrates on neural stem cell differentiation and proliferation. *Biomaterials* **30**, 556-564, doi:10.1016/j.biomaterials.2008.10.004 (2009).
- 32 Liu, L. *et al.* Regulating surface roughness of electrospun poly( $\epsilon$ -caprolactone)/ $\beta$ -tricalcium phosphate fibers for enhancing bone tissue regeneration. *Eur Polym J* **143**, 110201, doi:10.1016/j.eurpolymj.2020.110201 (2021).
- 33 Xu, T., Yang, H., Yang, D. & Yu, Z.-Z. Polylactic Acid Nanofiber Scaffold Decorated with Chitosan Islandlike Topography for Bone Tissue Engineering. *Acs Appl Mater Inter* **9**, 21094-21104, doi:10.1021/acsami.7b01176 (2017).
- 34 Chen, H. *et al.* Tailoring surface nanoroughness of electrospun scaffolds for skeletal tissue engineering. *Acta Biomaterialia* **59**, 82-93, doi:10.1016/j.actbio.2017.07.003 (2017).
- 35 Chen, H. *et al.* Tailoring surface nanoroughness of electrospun scaffolds for skeletal tissue engineering. *Acta Biomater* **59**, 82-93, doi:10.1016/j.actbio.2017.07.003 (2017).
- 36 Hu, X. *et al.* Electrospinning of polymeric nanofibers for drug delivery applications. *Journal of controlled release : official journal of the Controlled Release Society* **185**, 12-21, doi:10.1016/j.jconrel.2014.04.018 (2014).
- 37 Prabakaran, M., Jayakumar, R. & Nair, S. V. in *Biomedical Applications of Polymeric Nanofibers* (eds Rangasamy Jayakumar & Shantikumar Nair) 241-262 (Springer Berlin Heidelberg, 2012).
- 38 Zhang, Y., Lim, C. T., Ramakrishna, S. & Huang, Z. M. Recent development of polymer nanofibers for biomedical and biotechnological applications. *J Mater Sci Mater Med* **16**, 933-946, doi:10.1007/s10856-005-4428-x (2005).
- 39 Abdullah, M. F., Nuge, T., Andriyana, A., Ang, B. C. & Muhamad, F. Core-Shell Fibers: Design, Roles, and Controllable Release Strategies in Tissue Engineering and Drug Delivery. *Polymers-Basel* **11**, 2008, doi:10.3390/polym11122008 (2019).
- 40 Sperling, L. E., Reis, K. P., Pranke, P. & Wendorff, J. H. Advantages and challenges offered by biofunctional core-shell fiber systems for tissue engineering and drug delivery. *Drug Discov Today* **21**, 1243-1256, doi:10.1016/j.drudis.2016.04.024 (2016).
- 41 Zhang, C., Feng, F. & Zhang, H. Emulsion electrospinning: Fundamentals, food applications and prospects. *Trends in Food Science & Technology* **80**, 175-186, doi:10.1016/j.tifs.2018.08.005 (2018).

- 42 Frizzell, H., Ohlsen, T. J. & Woodrow, K. A. Protein-loaded emulsion electrospun fibers optimized for bioactivity retention and pH-controlled release for peroral delivery of biologic therapeutics. *Int J Pharm* **533**, 99-110, doi:10.1016/j.ijpharm.2017.09.043 (2017).
- 43 Chou, S. F., Carson, D. & Woodrow, K. A. Current strategies for sustaining drug release from electrospun nanofibers. *Journal of controlled release : official journal of the Controlled Release Society* **220**, 584-591, doi:10.1016/j.jconrel.2015.09.008 (2015).
- 44 McClellan, P. & Landis, W. J. Recent Applications of Coaxial and Emulsion Electrospinning Methods in the Field of Tissue Engineering. *Biores Open Access* **5**, 212-227, doi:10.1089/biores.2016.0022 (2016).
- 45 Yarin, A. L. Coaxial electrospinning and emulsion electrospinning of core-shell fibers. *Polym Advan Technol* **22**, 310-317, doi:10.1002/pat.1781 (2011).
- 46 Yazgan, G. *et al.* Tunable release of hydrophilic compounds from hydrophobic nanostructured fibers prepared by emulsion electrospinning. *Polymer* **66**, 268-276, doi:10.1016/j.polymer.2015.04.045 (2015).
- 47 Johnson, P. M. *et al.* Surfactant location and internal phase volume fraction dictate emulsion electrospun fiber morphology and modulate drug release and cell response. *Biomater Sci-Uk*, doi:10.1039/D0BM01751E (2021).
- 48 Xu, X. *et al.* Preparation of Core-Sheath Composite Nanofibers by Emulsion Electrospinning. *Macromol Rapid Comm* **27**, 1637-1642, doi:10.1002/marc.200600384 (2006).
- 49 Tucker, N., Stanger, J. J., Staiger, M. P., Razzaq, H. & Hofman, K. The History of the Science and Technology of Electrospinning from 1600 to 1995. *J Eng Fiber Fabr* **7**, 155892501200702S155892501200710, doi:10.1177/155892501200702S10 (2012).
- 50 Fong, H., Chun, I. & Reneker, D. H. Beaded nanofibers formed during electrospinning. *Polymer* **40**, 4585-4592, doi:10.1016/s0032-3861(99)00068-3 (1999).
- 51 Reneker, D. H., Yarin, A. L., Fong, H. & Koombhongse, S. Bending instability of electrically charged liquid jets of polymer solutions in electrospinning. *J Appl Phys* **87**, 4531-4547, doi:10.1063/1.373532 (2000).
- 52 Yarin, A. L., Koombhongse, S. & Reneker, D. H. Bending instability in electrospinning of nanofibers. *J Appl Phys* **89**, 3018-3026, doi:10.1063/1.1333035 (2001).
- 53 Reneker, D. H., Kataphinan, W., Theron, A., Zussman, E. & Yarin, A. L. Nanofiber garlands of polycaprolactone by electrospinning. *Polymer* **43**, 6785-6794, doi:10.1016/s0032-3861(02)00595-5 (2002).
- 54 Reneker, D. H. & Yarin, A. L. Electrospinning jets and polymer nanofibers. *Polymer* **49**, 2387-2425, doi:10.1016/j.polymer.2008.02.002 (2008).
- 55 Reneker, D. H. & Fong, H. in *Acs Sym Ser Vol. 918 ACS Symposium Series* Ch. 1, 1-6 (American Chemical Society, 2006).
- 56 Liu, F., Guo, R., Shen, M., Wang, S. & Shi, X. Effect of Processing Variables on the Morphology of Electrospun Poly[(lactic acid)-co -(glycolic acid)] Nanofibers. *Macromol Mater Eng* **294**, 666-672, doi:10.1002/mame.200900110 (2009).
- 57 Vellayappan, M. V. *et al.* Electrospinning applications from diagnosis to treatment of diabetes. *RSC Advances* **6**, 83638-83655, doi:10.1039/C6RA15252J (2016).
- 58 Fashandi, H. & Karimi, M. Pore formation in polystyrene fiber by superimposing temperature and relative humidity of electrospinning atmosphere. *Polymer* **53**, 5832-5849, doi:<https://doi.org/10.1016/j.polymer.2012.10.003> (2012).

- 59 Haider, A., Haider, S. & Kang, I.-K. A comprehensive review summarizing the effect of electrospinning parameters and potential applications of nanofibers in biomedical and biotechnology. *Arabian Journal of Chemistry* **11**, 1165-1188, doi:10.1016/j.arabjc.2015.11.015 (2018).
- 60 Sill, T. J. & von Recum, H. A. Electrospinning: applications in drug delivery and tissue engineering. *Biomaterials* **29**, 1989-2006, doi:10.1016/j.biomaterials.2008.01.011 (2008).
- 61 Theron, S. A., Zussman, E. & Yarin, A. L. Experimental investigation of the governing parameters in the electrospinning of polymer solutions. *Polymer* **45**, 2017-2030, doi:10.1016/j.polymer.2004.01.024 (2004).
- 62 Bosworth, L. A. & Downes, S. Acetone, a Sustainable Solvent for Electrospinning Poly( $\epsilon$ -Caprolactone) Fibres: Effect of Varying Parameters and Solution Concentrations on Fibre Diameter. *Journal of Polymers and the Environment* **20**, 879-886, doi:10.1007/s10924-012-0436-3 (2012).
- 63 Rutledge, G. C. & Fridrikh, S. V. Formation of fibers by electrospinning. *Advanced drug delivery reviews* **59**, 1384-1391, doi:10.1016/j.addr.2007.04.020 (2007).
- 64 Thompson, C. J., Chase, G. G., Yarin, A. L. & Reneker, D. H. Effects of parameters on nanofiber diameter determined from electrospinning model. *Polymer* **48**, 6913-6922, doi:10.1016/j.polymer.2007.09.017 (2007).
- 65 Kong, C. S. *et al.* Multi-jet ejection and fluctuation in electrospinning of polyvinyl alcohol with various nozzle diameters. *Polymer Engineering & Science* **49**, 2286-2292, doi:10.1002/pen.21528 (2009).
- 66 Mit-Uppatham, C., Nithitanakul, M. & Supaphol, P. Ultrafine Electrospun Polyamide-6 Fibers: Effect of Solution Conditions on Morphology and Average Fiber Diameter. *Macromol Chem Phys* **205**, 2327-2338, doi:10.1002/macp.200400225 (2004).
- 67 Knopf, J. A. *Investigation of Linear Electrospinning Jets* Bachelor of Science thesis, University of Delaware, (2009).
- 68 Celebioglu, A. & Uyar, T. Electrospun porous cellulose acetate fibers from volatile solvent mixture. *Mater Lett* **65**, 2291-2294, doi:<https://doi.org/10.1016/j.matlet.2011.04.039> (2011).
- 69 Koombhongse, S., Liu, W. & Reneker, D. H. Flat polymer ribbons and other shapes by electrospinning. *Journal of Polymer Science Part B: Polymer Physics* **39**, 2598-2606, doi:10.1002/polb.10015 (2001).
- 70 Xue, N. *et al.* Rapid patterning of 1-D collagenous topography as an ECM protein fibril platform for image cytometry. *PLoS One* **9**, e93590, doi:10.1371/journal.pone.0093590 (2014).
- 71 Wu, Y.-K. *et al.* Multi-Jet Electrospinning with Auxiliary Electrode: The Influence of Solution Properties. *Polymers-Basel* **10**, 572, doi:10.3390/polym10060572 (2018).
- 72 Lin, Y.-M. & Rutledge, G. C. Separation of oil-in-water emulsions stabilized by different types of surfactants using electrospun fiber membranes. *J Membrane Sci* **563**, 247-258, doi:10.1016/j.memsci.2018.05.063 (2018).
- 73 Lin, T., Wang, H., Wang, H. & Wang, X. The charge effect of cationic surfactants on the elimination of fibre beads in the electrospinning of polystyrene. *Nanotechnology* **15**, 1375-1381, doi:10.1088/0957-4484/15/9/044 (2004).
- 74 Shenoy, S. L., Bates, W. D., Frisch, H. L. & Wnek, G. E. Role of chain entanglements on fiber formation during electrospinning of polymer solutions: good solvent, non-specific

- polymer–polymer interaction limit. *Polymer* **46**, 3372-3384, doi:10.1016/j.polymer.2005.03.011 (2005).
- 75 Yazgan, G. *et al.* Steering surface topographies of electrospun fibers: understanding the mechanisms. *Sci Rep-Uk* **7**, doi:ARTN 158 10.1038/s41598-017-00181-0 (2017).
- 76 Zaarour, B., Zhu, L., Huang, C. & Jin, X. Controlling the Secondary Surface Morphology of Electrospun PVDF Nanofibers by Regulating the Solvent and Relative Humidity. *Nanoscale Research Letters* **13**, 285, doi:10.1186/s11671-018-2705-0 (2018).
- 77 Nezarati, R. M., Eifert, M. B. & Cosgriff-Hernandez, E. Effects of humidity and solution viscosity on electrospun fiber morphology. *Tissue Eng Part C Methods* **19**, 810-819, doi:10.1089/ten.TEC.2012.0671 (2013).
- 78 Kim, J. F., Kim, J. H., Lee, Y. M. & Drioli, E. Thermally induced phase separation and electrospinning methods for emerging membrane applications: A review. *Aiche J* **62**, 461-490, doi:10.1002/aic.15076 (2016).
- 79 Jung, J. T. *et al.* Understanding the non-solvent induced phase separation (NIPS) effect during the fabrication of microporous PVDF membranes via thermally induced phase separation (TIPS). *J Membrane Sci* **514**, 250-263, doi:<https://doi.org/10.1016/j.memsci.2016.04.069> (2016).
- 80 Megelski, S., Stephens, J. S., Chase, D. B. & Rabolt, J. F. Micro- and Nanostructured Surface Morphology on Electrospun Polymer Fibers. *Macromolecules* **35**, 8456-8466, doi:10.1021/ma020444a (2002).
- 81 Katsogiannis, K. A. G., Vladislavljevic, G. T. & Georgiadou, S. Porous electrospun polycaprolactone (PCL) fibres by phase separation. *Eur Polym J* **69**, 284-295, doi:10.1016/j.eurpolymj.2015.01.028 (2015).
- 82 Conoscenti, G., Carrubba, V. L. & Brucato, V. A Versatile Technique to Produce Porous Polymeric Scaffolds: The Thermally Induced Phase Separation (TIPS) Method. *Archives in Chemical Research* **01**, doi:10.21767/2572-4657.100012 (2017).
- 83 Icoglu, H. I. & Ogulata, R. T. Effect of Ambient Parameters on Morphology of Electrospun Poly (Trimethylene Terephthalate) (Ptt) Fibers. *Tekst Konfeksiyon* **27**, 215-223 (2017).
- 84 Icoglu, H. I. & Ogulata, R. T. Effect of Ambient Parameters on Morphology of Electrospun Polyetherimide (Pei) Fibers. *Tekst Konfeksiyon* **23**, 313-318 (2013).
- 85 Ogulata, R. T. & Icoglu, H. I. Interaction between effects of ambient parameters and those of other important parameters on electrospinning of PEI/NMP solution. *J Text I* **106**, 57-66, doi:10.1080/00405000.2014.902561 (2015).
- 86 Ghobeira, R. *et al.* Wide-ranging diameter scale of random and highly aligned PCL fibers electrospun using controlled working parameters. *Polymer* **157**, 19-31, doi:10.1016/j.polymer.2018.10.022 (2018).
- 87 Htike, H. H., Long, C. & Sukigara, S. The Effect of Relative Humidity on Electrospinning of Poly-(vinyl alcohol) with Soluble Eggshell Membrane. *Journal of Textile Engineering* **58**, 9-12, doi:10.4188/jte.58.9 (2012).
- 88 Amiraliyan, N., Nouri, M. & Kish, M. H. Effects of some electrospinning parameters on morphology of natural silk-based nanofibers. *J Appl Polym Sci* **113**, 226-234, doi:10.1002/app.29808 (2009).
- 89 Hardick, O., Stevens, B. & Bracewell, D. G. Nanofibre fabrication in a temperature and humidity controlled environment for improved fibre consistency. *J Mater Sci* **46**, 3890-3898, doi:10.1007/s10853-011-5310-5 (2011).

- 90 Xu, T., Yang, H., Yang, D. & Yu, Z. Z. Polylactic Acid Nanofiber Scaffold Decorated with Chitosan Islandlike Topography for Bone Tissue Engineering. *ACS Appl Mater Interfaces* **9**, 21094-21104, doi:10.1021/acsami.7b01176 (2017).
- 91 Elishav, O. *et al.* Lamellar-like Electrospun Mesoporous Ti-Al-O Nanofibers. *Materials* **12**, 252, doi:10.3390/ma12020252 (2019).
- 92 Zaarour, B., Zhu, L., Huang, C. & Jin, X. Fabrication of a polyvinylidene fluoride cactus-like nanofiber through one-step electrospinning. *RSC Advances* **8**, 42353-42360, doi:10.1039/c8ra09257e (2018).
- 93 Pai, C. L., Boyce, M. C. & Rutledge, G. C. Morphology of Porous and Wrinkled Fibers of Polystyrene Electrospun from Dimethylformamide. *Macromolecules* **42**, 2102-2114, doi:10.1021/ma802529h (2009).
- 94 Wang, L., Pai, C.-L., Boyce, M. C. & Rutledge, G. C. Wrinkled surface topographies of electrospun polymer fibers. *Appl Phys Lett* **94**, 151916, doi:10.1063/1.3118526 (2009).
- 95 Mobasheri, M., Valipouri, A. & Ravandi, S. A. H. Developing porous fibers by electrocentrifuge spinning system. *J Appl Polym Sci* **136**, doi:ARTN 47513  
10.1002/app.47513 (2019).
- 96 Gaharwar, A. K. *et al.* Amphiphilic beads as depots for sustained drug release integrated into fibrillar scaffolds. *Journal of Controlled Release* **187**, 66-73, doi:10.1016/j.jconrel.2014.04.035 (2014).
- 97 Yarin, A. L., Kataphinan, W. & Reneker, D. H. Branching in electrospinning of nanofibers. *J Appl Phys* **98**, 064501, doi:10.1063/1.2060928 (2005).
- 98 Koski, A., Yim, K. & Shivkumar, S. Effect of molecular weight on fibrous PVA produced by electrospinning. *Mater Lett* **58**, 493-497, doi:10.1016/s0167-577x(03)00532-9 (2004).
- 99 Holzmeister, A., Yarin, A. L. & Wendorff, J. H. Barb formation in electrospinning: Experimental and theoretical investigations. *Polymer* **51**, 2769-2778, doi:10.1016/j.polymer.2010.04.005 (2010).
- 100 Dhanalakshmi, M., Lele, A. K. & Jog, J. P. Electrospinning of Nylon11: Effect of processing parameters on morphology and microstructure. *Materials Today Communications* **3**, 141-148, doi:10.1016/j.mtcomm.2015.01.002 (2015).
- 101 Xin, Y. & Reneker, D. H. Garland formation process in electrospinning. *Polymer* **53**, 3629-3635, doi:10.1016/j.polymer.2012.05.060 (2012).
- 102 Ding, B., Li, C. R., Miyauchi, Y., Kuwaki, O. & Shiratori, S. Formation of novel 2D polymer nanowebs via electrospinning. *Nanotechnology* **17**, 3685-3691, doi:10.1088/0957-4484/17/15/011 (2006).
- 103 Pant, H. R. Biomimetic Spider-web like Electrospun Nanofibrous Membrane of Nylon-6 for Future Air Filtration. *Journal of the Institute of Engineering* **11**, 108-115, doi:10.3126/jie.v11i1.14702 (2016).
- 104 Li, Z., Xu, Y., Fan, L., Kang, W. & Cheng, B. Fabrication of polyvinylidene fluoride tree-like nanofiber via one-step electrospinning. *Mater Design* **92**, 95-101, doi:10.1016/j.matdes.2015.12.037 (2016).
- 105 Li, Z. *et al.* A Novel Polyvinylidene Fluoride Tree-Like Nanofiber Membrane for Microfiltration. *Nanomaterials (Basel)* **6**, doi:10.3390/nano6080152 (2016).
- 106 Barakat, N. A. M., Kanjwal, M. A., Sheikh, F. A. & Kim, H. Y. Spider-net within the N6, PVA and PU electrospun nanofiber mats using salt addition: Novel strategy in the electrospinning process. *Polymer* **50**, 4389-4396, doi:10.1016/j.polymer.2009.07.005 (2009).



- 107 Massaglia, G. *et al.* Defining the role of nanonetting in the electrical behaviour of composite nanofiber/nets. *RSC Advances* **7**, 38812-38818, doi:10.1039/c7ra05573k (2017).

## CHAPTER 2: DETERMINING THE ROLE THAT SOLVENT VOLATILITY, CONDUCTIVITY, SOLUBILITY, AND MISCIBILITY PLAY IN ELECTROSPUN FIBER DIAMETER AND MORPHOLOGY.

### 2.1 INTRODUCTION

Controlling fiber morphology, topography, and diameter is essential in creating reproducible electrospun meshes with consistent mechanical, spatial, drug release, and cell response characteristics. Optimizing processing parameters, ambient conditions, and solution chemistry can be used to control mesh characteristics.<sup>1,2</sup> Focusing on the solution chemistry used in electrospinning, the interaction between the polymer and solvent(s) plays a significant role in dictating fiber morphology, topography, and diameter. In solution electrospinning, a polymer is dissolved in one or more solvents and used to fabricate fibers in an electric field. Within the field of tissue engineering and drug delivery, using hydrophobic polymers can be desirable because their degradation rate can be tuned to match the rate of tissue repair. Moreover, they are less susceptible to hydrolytic degradation due to fewer hydrolytically cleavable functional groups, facilitating stability *in vivo*.

However, the use of hydrophobic polymers can create additional challenges. Polymer solubility can be an issue in electrospinning systems as nonpolar or organic solvents are generally superior in their ability to solubilize hydrophobic polymers. Organic solvents, due to their chemical composition, are usually less dielectric compared to polar solvents. The electrospinning process relies on propagating electrons through a fluid jet to achieve cylindrical fibers. Within the electrospinning process, organic solvents can sometimes have insufficient conductivity to maintain cylindrical jets throughout the entire electrospinning process.<sup>3</sup>

Researchers have altered solution chemistry by adding conductive particles such as salts, plasma treating solvents, and adding a second, more conductive solvent to the electrospinning process to overcome this reduced solvent conductivity.<sup>1-4</sup> Adding conductive particles such as salts to polymer solutions is an effective method of increasing overall solution conductivity but complicates the electrospinning parameters by altering solution conductivity, distribution of charge, viscosity, polymer solubility, and surface tension.<sup>5-9</sup> Furthermore, the addition of salts into the electrospun fibers can create potential downstream challenges, especially in loading drugs within the fibers for drug release, cell response in tissue engineering, and Food and Drug Administration approval for a product used as a medical device or in food science. Another recently developed strategy to increase the conductivity of organic solvents for electrospinning is plasma treating the polymer solution. For example, in a study by Fasano et al., several different hydrophobic polymers were dissolved in DCM solvent treated with cold atmospheric pressure plasma and ionized gas dissolved within the solvent.<sup>4</sup> The resulting electrospun fibers demonstrated a reduction in beading morphology when the polymer solution was plasma-treated, potentially indicating an increase in solution conductivity. This study failed to report the ambient relative humidity during the electrospinning process, affecting the fiber morphology. Plasma treatment is an exciting potential new area of research. However, it remains untested in terms of overall system effects on fiber morphology, topography, and diameter and the effects on drug release and, in particular, burst release of drugs.

Another strategy used to improve the conductivity of the polymer solution for electrospinning is adding a second, more conductive solvent.<sup>10</sup> Dual solvent systems are popular in studies where a hydrophilic drug is encapsulated within a hydrophobic polymer mesh.<sup>11,12</sup> This is because an organic solvent is needed to dissolve the hydrophobic polymer, while a polar solvent

is necessary to dissolve the hydrophilic drug. However, introducing a second solvent into the system can affect the solubility of the polymer with each of the solvents, and this difference in solvent miscibility can create NIPS.<sup>12</sup> Phase separation of solvents can affect the distribution of charge within the polymer jet during electrospinning, and unequal solvation of polymer in different solvents can develop regions of different viscosity during electrospinning.<sup>1</sup>

Relative humidity can also influence phase separation through VIPS. The relative ratios of non-conductive polymer solvent to conductive polymer insoluble or lower soluble non-solvent can affect resulting mesh characteristics due to solvent properties. Luo et al. described the effects of both singular and dual solvents used to electrospin fibers at high relative humidity.<sup>3,13</sup> In general, the addition of a second, more conductive solvent at low ratios relative to the non-conductive solvent improved the ability to electrospin smooth fibers. In contrast, high ratios of a conductive solvent prevented electrospinning due to poor polymer solubility. In a study by Liu et al., fibers electrospun with a hydrophobic polymer at high relative humidity and increasing volume fractions of a conductive solvent reduced the presence of beading morphology until the jet became unstable (Figure 2.1).<sup>14</sup> Interestingly, lower proportions of conductive solvent also increased the surface topography of fibers. Surface topography, in this case, was attributed to water condensing on the surface of the fibers at high relative humidity and inducing phase separation and polymer precipitation. A similar effect of reduced beading was also observed by Konstantinos et al. at medium relative humidity.<sup>15</sup>

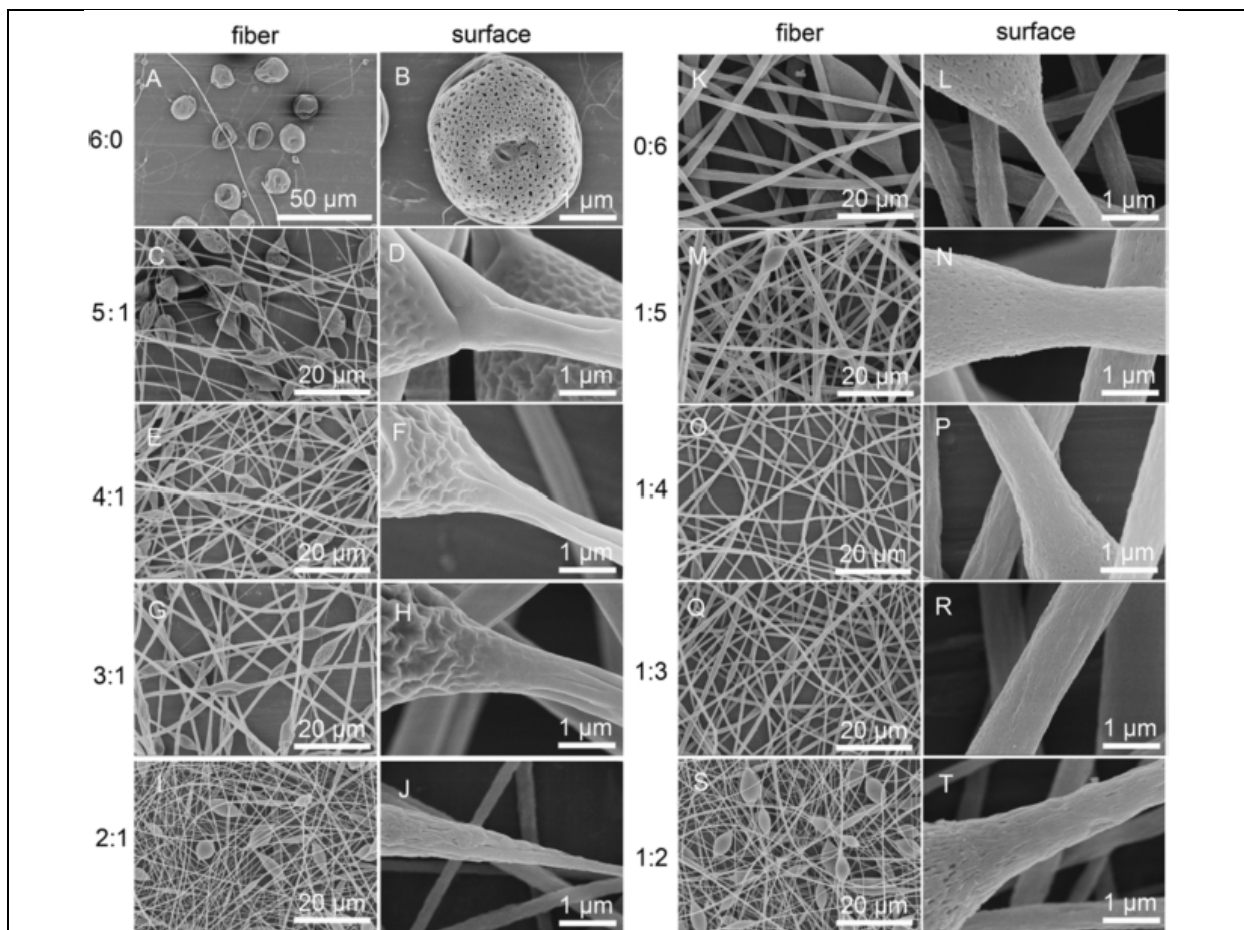


Figure 2.1: Polystyrene electrospun fibers fabricated with increasing ratios of solvents THF: DMF demonstrating the topographical and morphological effects of solvent volatility and conductivity. Figure originally published by Liu et al. and reproduced with permission.<sup>14</sup>

Increasing solvent conductivity often can improve fiber uniformity by reducing morphology and fiber diameter.<sup>16</sup> Uniformity of fibers is improved because higher conductivity solvents increase the charge repulsion acting in opposition to the capillary forces reducing surface area to conserve surface area in spherical shapes. Increased charge repulsion from more conductive solvents is also responsible for decreases in fiber diameter because of the increased bending instability whipping of the fibers.<sup>17-19</sup> In systems where the solvent evaporation rate is held relatively consistent, the solution conductivity is directly correlated to fiber diameter.<sup>20,21</sup>

Evaporation rate is an essential parameter in electrospinning solution chemistry and, in some cases, may dominate the effect on resulting mesh characteristics. During the electrospinning process, a polymer solution is extruded from a needle and, due to the electric field, is pulled in a column towards the electrospinning plate. When the polymer solution is between the needle tip and collection plate, whipping of the fiber occurs, causing evaporation of the solvent and allowing for dry, solid fibers to collect on the collection plate. The solvent evaporation rate can also play a major role in fiber morphology, topography, and diameter because as the solvent evaporates from the electrospinning jet, the fiber solidifies. This solidification reduces the stretching of the jet due to polymer chain entanglement. Mit-Uppatham et al. demonstrated that using solvents with low volatility resulted in film collection on the collection plate, wet fibers, and fused fibers.<sup>22</sup> This study also revealed that using solvents with high volatility resulted in clogging or solidification at the needle tip. Knopf found that using poly(ethylene oxide) dissolved in  $\text{CHCl}_3$ , rapid evaporation of solvent at the Taylor cone could cause the intermittent formation of a skin or shell around the Taylor cone, which was periodically expelled with occasional formation of multiple jets.<sup>23</sup> In some cases, as the film grows off the needle tip, it may eventually cause clogs at the needle tip, which are dislodged and collected on the collection plate as polymer globs. During this polymer film formation, jets can split or form multiple jets, affecting overall fiber collection (Figure 2.2).

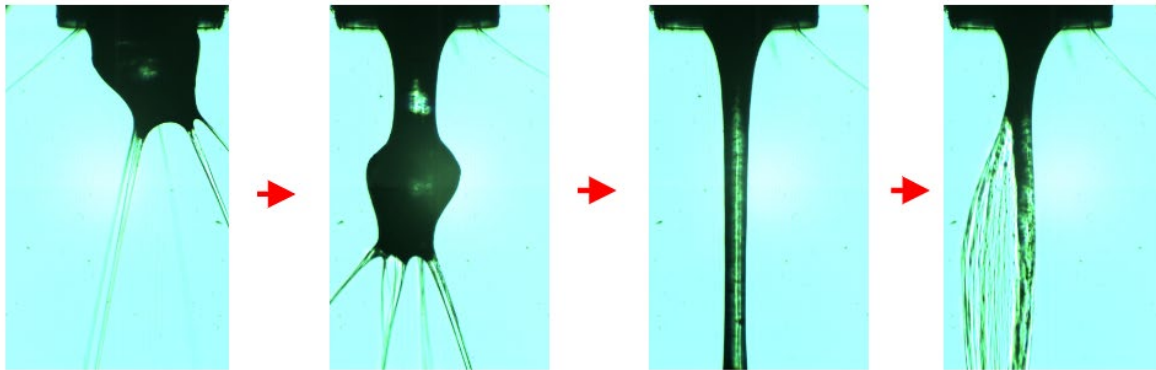


Figure 2.2: Formation of clogging at the needle tip over time caused by rapid evaporation of the solvent. Figure reproduced from the thesis of Knopf 2009 with permission.<sup>23</sup>

The rate of evaporation and the subsequent effect on electrospun fibers can be affected by relative humidity.<sup>24-26</sup> The impact of relative humidity is highly dependent on the solvent miscibility with ambient water droplets and polymer solubility in water. In systems electrospun at high relative humidity and fabricated with a hydrophobic polymer, fiber diameter increases due to polymer precipitation at the surface of the jet as ambient water droplets condense on this surface during electrospinning.<sup>27,28</sup> This early precipitation of polymer creates a solid outer shell of the polymer jet which reduces the ability for stretching of the fiber during the bending instability. High relative humidity can also result in decreased fiber diameter due to ambient water droplets penetrating into the fiber, reducing the viscosity of the jet, and allowing for greater stretching of the fiber.<sup>29</sup> This reduction of fiber diameter has also been hypothesized to be due to a decrease in the rate of evaporation of native solvents due to water condensation on the surface of the jet.<sup>26</sup> Interestingly, low levels of relative humidity can also cause a reduction in fiber diameter due to reduced polymer precipitation and faster evaporation of the solvent.<sup>25,27</sup>

Although previous literature has shown some effects of solvent conductivity, solvent evaporation, relative humidity, polymer solubility, and solvent miscibility on electrospun fibers, a holistic understanding of how each of these interdependent parameters interacts in electrospun fibers has still not fully explored. Processing parameters can be altered to achieve smooth, continuous fibers with different solvents. Thus the effect of solvents with each of these parameters, especially on fiber morphology, is often unreported. It is essential to understand the impact of solvents within a solvent system to create tunable, controlled, and reproducible fibers in a mesh.

The long-term research objective is to control fiber morphology by systematically choosing solvents that will yield desired fiber properties and incorporate hydrophilic and hydrophobic drugs. It is crucial to understand solvent evaporation, conductivity, solubility, and miscibility in both single solvent and dual solvent systems because dual solvents are often used to incorporate drugs that are insoluble in typical organic single solvent systems required for biodegradable polymers used in biomedical applications.

In this study, a range of solvent systems that compare electrospun fibers prepared with both single and two- solvent systems at a range of different dielectric constants, volatility, solvent miscibility, and polymer solubility was developed. Each of the solvent systems was electrospun at high and low relative humidity to determine the additional interdependent effect on electrospun fiber collection. The electrospun fibrous mesh was characterized by fiber morphology, fiber surface topography, fiber diameter, and the distribution of fiber diameters with each parameter.

## **2.2 MATERIALS AND METHODS**

### **2.2.1 Materials**

PCL (50,000  $M_w$ ) was purchased from CAPA lot # 120625. N, N-Dimethylformamide (DMF) anhydrous with 99.8% purity was purchased from Sigma Aldrich lot # SHBJ7641.



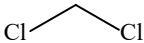
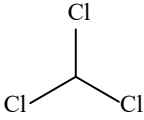
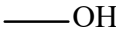
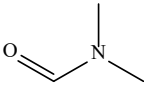
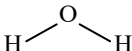
Chloroform ( $\text{CHCl}_3$ ) with  $\geq 99.5\%$  purity was purchased from Sigma Aldrich lot # SHBL1580.

Methanol with 99.9% purity was purchased from Sigma Aldrich lot # 065112.

## 2.2.2 Polymer Solution Fabrication

Polymer solutions were fabricated with 20% w/v PCL dissolved in single solvent systems of DCM and  $\text{CHCl}_3$ , and the dual solvent systems of 3:1  $\text{CHCl}_3$ : DMF and 3:1  $\text{CHCl}_3$ : MeOH. Properties of each of these solvents can be seen in Table 2.1 below. Each solution was mixed for at least one hour on a stir plate with a stir bar spinning at a rate of 250 rpm, after which no solid polymer was visible in the solution. All solutions used to confirm effects of conductivity and volatility with processing parameters were 20 % w/v PCL in  $\text{CHCl}_3$ .

Table 2.1: Solvent properties of boiling point, dielectric constant, surface tension, and absolute viscosity from PubChem. PCL solubility in solvents based on the experimental studies by Luo et al. <sup>3</sup> Chemical structures were generated with ChemDraw software.

Solvents	Structure	Boiling Point (°C)	Vapor Pressure at 25 °C (kPa)	Dielectric Constant	Surface Tension at 20 °C	Absolute Viscosity at 25 °C (mPa·s)	PCL Solubility
DCM		40	53.33	9	28	0.4	High
$\text{CHCl}_3$		61	26.26	5	27	0.6	Partial to High
Methanol		65	16.93	33	23	0.1	Insoluble
DMF		153	0.52	37	35	0.8	Poor
Water		100	3.17	80	73	0.9	Insoluble

### 2.2.3 Electrospun Scaffold Fabrication

Polymer solution electrospinning parameters were held constant with a Harvard Apparatus pump flow rate of 0.5 mL/h, a distance between the needle tip to collection plate of 25 cm, an applied voltage of 15kV from a Gamma High Voltage Source, and a blunted 21-gauge needle. Samples were electrospun at high and low relative humidity of  $50\% \pm 10\%$  and  $10\% \pm 10\%$ , respectively, to evaluate the influence of ambient water moisture on fiber collection. At high relative humidity, specimens were electrospun directly onto the copper collection plate, which was grounded both to the voltage source and to the fume hood. After each specimen was collected, it was carefully peeled off the collection plate and left to dry in the fume hood overnight. The collection plate was wiped down with chloroform followed by water before thoroughly drying between each specimen collection. Previous studies had demonstrated that delamination of the electrospun mesh and partial sticking to the collection plate could occur at low relative humidity. Therefore, at low relative humidity, the collection plate was covered in aluminum foil with the grounding alligator clip wire attached to the collection plate over the foil. Specimens were further dried in a vacuum chamber before further characterization. At least three samples were fabricated per group of parameters.

Samples electrospun to confirm effects of solution chemistry with processing parameters were all electrospun in environmental conditions of  $12\% \pm 1\%$  relative humidity and  $24\text{ }^{\circ}\text{C} \pm 1\text{ }^{\circ}\text{C}$ . Each sample was electrospun for 10 minutes with a 21-gauge blunted needle and a 15 mL/h flow rate. Collection distance was systematically increased at distances of 15, 20, 25, and 30 cm. For each collection distance, the applied voltage was increased at levels of 12, 15, 18, 21, and 24 kV. One specimen was collected for each set pair of collection distance and applied voltage. The relative humidity fell out of range for the 15 cm and 24 kV sample so it was not collected.

#### 2.2.4 Fiber Characterization

Mesh was analyzed using a Phenom Pro Desktop scanning electron microscope (SEM) to capture fiber morphology, surface topography, diameter, and fiber diameter distribution. All samples were coated with 8 nm of iridium before imaging. Fiber morphology was characterized by imaging each specimen in at least five different locations to capture morphological effects using 10 kV accelerating voltage, a backscatter detector, and a magnification appropriate to observe the fiber morphology. Locations were selected for each of the four corners of the square specimen and the center. The overall morphology of the fibers was qualitatively analyzed for morphological evidence of round fibers, ribbon-like fibers, wet indistinct fibers, beading, fiber splitting, and garlands. Fiber topography was characterized by imaging with 10 kV accelerating voltage, a secondary electron detector, and a magnification of 25,000x.

Fiber diameter was determined by imaging each sample specimen in five different locations using 10 kV of accelerating voltage and a backscatter detector. Mesh fabricated with the solvents  $\text{CHCl}_3$  and DCM had larger fibers. Therefore, to get a sufficient sampling of fibers for analysis, SEM images were captured at a magnification of 1,000x. Mesh fabricated with solvents 3:1  $\text{CHCl}_3$ : DMF and 3:1  $\text{CHCl}_3$ : MeOH had smaller fibers than mesh fabricated with  $\text{CHCl}_3$  solvent, and therefore SEM images were captured at a magnification of 5,000x. Each image was subsequently analyzed with the software ImageJ using the plugin DiameterJ. From this initial segmentation, binary-colored segmented images produced with the algorithms M3, M5, M7, S2, S3, and S7 were used to determine fiber diameter and fiber diameter distribution using DiameterJ. In a few rare cases, DiameterJ was unable to process a segmented image, in which case a segmented image produced with an un-used algorithm that was judged to be the most representative of the original image was substituted for further analysis. Un-used algorithms were

named M1, M2, M4, M6, M8, S1, S4, S5, S6, and S8, and only one was used to replace standard algorithms in the rare cases where the image was unable to proceed with the segmentation process.

The average fiber diameter for each algorithm was used to determine the average fiber diameter per SEM image. These fiber diameters for each image were further statistical comparison between groups. For each overall set of sample parameters, fiber distribution histogram raw data, mean of fiber diameters, fiber diameters standard deviation, fiber skewness, and fiber kurtosis were also determined using DiameterJ.

Skewness is a statistical measure of asymmetry in a population of data distributed in a symmetrical bell curve. A perfectly balanced distribution with even distribution of samples deviating above and below the center of the distribution would have a skew value of zero. A positive skew occurs when more samples lie on the left-hand side of the center, and a negative skew occurs when more samples lie to the right-hand side of the distribution. This will indicate if the fiber distribution favors smaller or larger fibers. Kurtosis is the measure of the degree of a tail in a symmetrical bell curve distribution. According to the DiameterJ source code, the calculated kurtosis used for all measured kurtosis in this body of work was normalized to zero.<sup>30</sup> This means that values above zero indicate more outliers in the population data than a standard normal curve. In comparison, a value below zero means fewer outliers than in a standard normal curve.

Raw fiber diameter histogram data were replotted using Graphpad Prism. Fiber diameter with standard deviation listed was generated for all samples in a sample parameter group. DiameterJ does not output all the raw data because each sample has millions of data points. Therefore, statistical analysis and graphing of data were performed with the average diameter output for each segmentation.

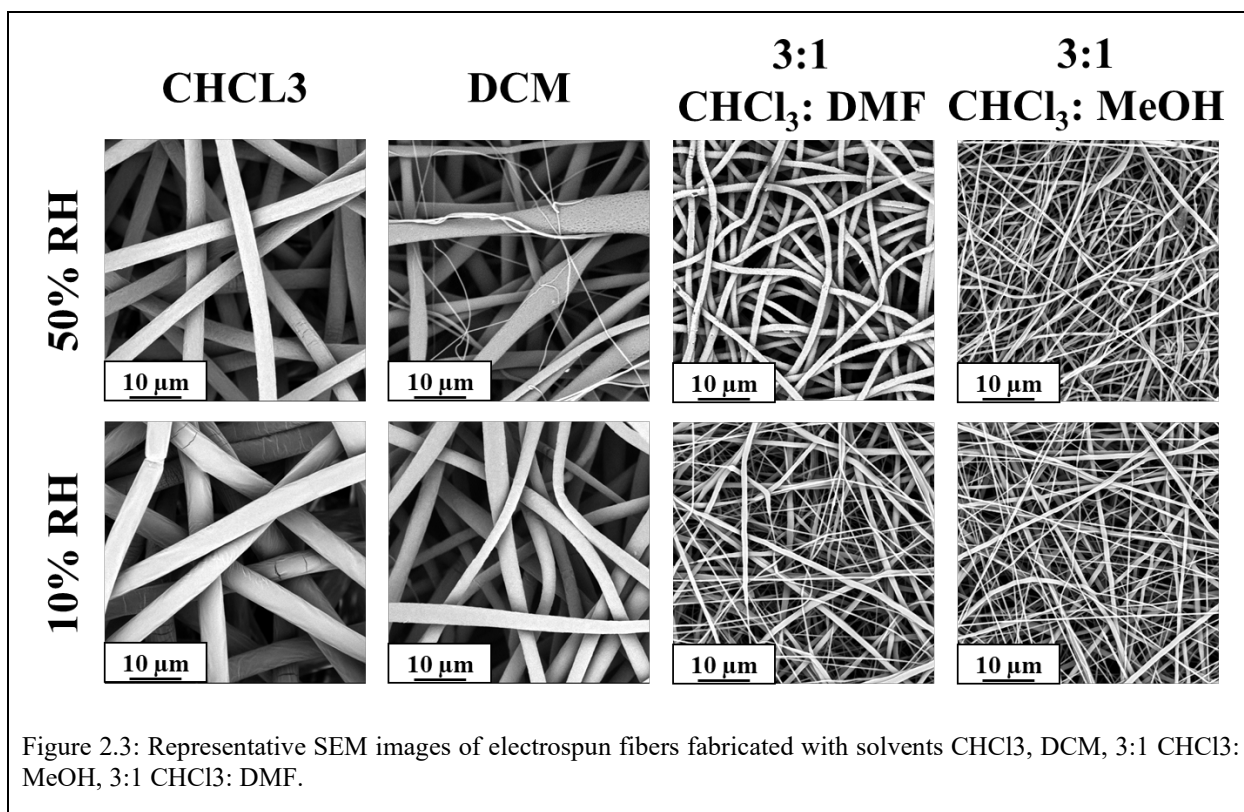
### **2.2.5 Statistical Analysis**

The average fiber diameter for each set of sample parameters was determined from the average of each segmentation produced by ImageJ and plugin DiameterJ described above (n=15). First, a one-way ANOVA with Brown-Forsythe and Welch's tests was performed on each set of sample parameters to determine if the electrospun samples were statistically different. This was followed up with Dunnett's post hoc test. Within the same solvent systems, the effect of relative humidity on fiber diameter was determined using Welch's t-test and a 95% confidence level. The effect of solvent systems was determined using a one-way Brown-Forsythe and Welch's ANOVA with Dunnett's multiple comparison post hoc and a 95% confidence interval. This test was performed at both high and low relative humidity, respectively. All statistical tests and graphing were performed using Prism Graphpad software.

## **2.3 RESULTS AND DISCUSSION**

### **2.3.1 Fiber Morphology**

The  $\text{CHCl}_3$  fibers at both high and low relative humidity were cylindrical in shape and homogeneous in terms of relative fiber size (Figure 2.3). This is because  $\text{CHCl}_3$  is a good solvent for PCL, and therefore phase separation would not be expected during the electrospinning process. Increasing the relative humidity was not observed to have major effects on the morphology of the fibers.



The DCM fibers at low relative humidity had predominantly uniform cylindrical morphology and beading morphology at high relative humidity (Figure 2.3). Yazgan et al. modeled DCM and CHCl<sub>3</sub> from PCL solutions which showed that DCM evaporates at a much faster rate than CHCl<sub>3</sub>.<sup>25</sup> As a result of this evaporation, latent heat loss due to evaporative cooling created a minimum surface temperature (wet-bulb temperature) of -13.7 °C and -4.6 °C for DCM and CHCl<sub>3</sub> respectively. When comparing the wet-bulb temperature to the temperature at which air can be cooled down to achieve full saturation (dew-point temperature), which is approximately 10.7 °C at 55% relative humidity, condensation will readily occur on the surface of the jet. Water condensing on the surface of polymer jets using hydrophobic polymers has been shown to create rapid polymer precipitation.<sup>28,31</sup>

DCM may have beading morphology because of intermittent film formation at the Taylor cone. In this system, as DCM rapidly evaporates, water condenses on the surface of the jet at a faster rate than at low relative humidity. DCM's evaporation rate is also faster than that of  $\text{CHCl}_3$ , so this rapid evaporation paired with condensation caused surface precipitation. This precipitation is likely to occur because PCL is insoluble in water.<sup>3</sup> If precipitation occurs at the Taylor cone, then a thin film may form in a bead-like shape due to surface tension. Knopf observed that this formation of the film could be intermittent, and as the shape forms, jet instability in the form of multiple jets can occur.<sup>23</sup> Multiple jets cause a rapid decrease in fiber diameter.<sup>32-34</sup> A minority morphology seen in this morphology is also thin fibers consistent with the proposed mechanism.

Precipitation of polymer at the surface of electrospinning jets can also cause a film-like layer of solid polymer, preventing significant stretching during the whipping phase in these areas.<sup>27,28</sup> Simultaneously, water coating the outside of a polymer jet would slow down the evaporation of the solvent, allowing the center to be liquid for a longer period.<sup>35</sup> This allows for the initial sections solidified by polymer precipitation to form the larger diameter center portions of the bead. Through stretching, the center of the fiber can elongate through the whipping process to form thin strings connecting the beads. At low relative humidity, water does not condense as rapidly on the surface of the fibers, and the solvent evaporates relatively quickly. This reduces the beading effects and instead creates cylindrical morphology (Figure 2.4).

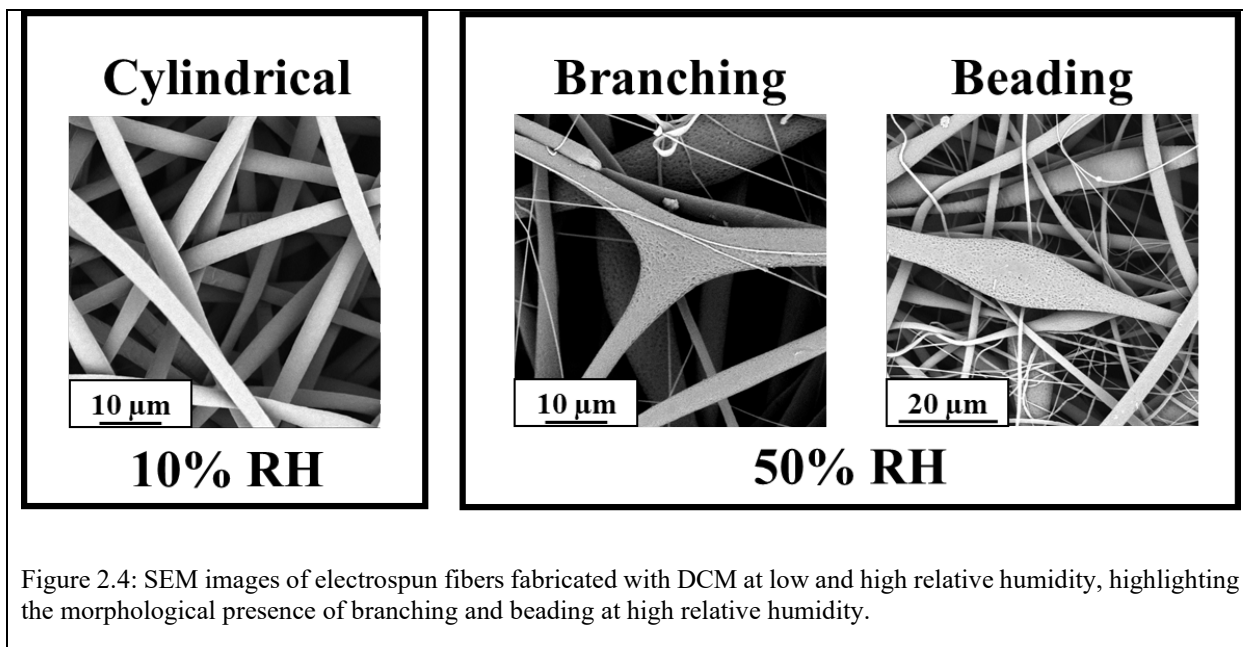


Figure 2.4: SEM images of electrospun fibers fabricated with DCM at low and high relative humidity, highlighting the morphological presence of branching and beading at high relative humidity.

In the 3:1  $\text{CHCl}_3$ : DMF samples, fibers are cylindrical and approximately the same diameter in homogeneity at high relative humidity. At low relative humidity, the samples demonstrate severe bead on string morphology with some breaking of the fibers and the presence of jet splitting (Figure 2.5). At high relative humidity, water condenses on the surface of the jet, and some of the electric charge is transferred to this water. Water is a conductive solvent, and as it coats the polymer jet evenly and absorbs into the fiber, it creates a more evenly distributed charge, thus encouraging the cylindrical fiber formation. Fashandi et al. described this same effect with a hydrophobic polymer demonstrating fewer morphological defects at high relative humidity. They attributed this to water absorbing into the jet from the air to increase overall viscosity.<sup>28</sup> Breaking morphology is observed when fibers have discontinuous areas that clearly were previously attached to an adjacent fiber during the electrospinning process. Beading morphology is observed when there is a wider curved area than the majority of the fiber that is next to sections of a continuous fiber containing thin sections.



However, at low relative humidity, the polymer jet does not have the water condensation on the outside of the fiber to evenly distribute charge. This creates an issue because PCL is more soluble in  $\text{CHCl}_3$  than DMF, and DMF has a higher charge. In addition to differences in solubility causing a certain degree of NIPS, differences in dielectric constant indicate that the ability of the solvent to propagate charge generating electrostatic repulsion differs greatly between  $\text{CHCl}_3$  and DMF (Table 2.1). This uneven distribution of charge in the polymer jet when in an electric field can encourage jet branching formation, as seen at low relative humidity (Figure 2.5). Furthermore, the solubility of PCL in  $\text{CHCl}_3$  and DMF also differs. PCL is more soluble in  $\text{CHCl}_3$  than DMF, and therefore, both solvents could encourage NIPS, contributing to the bead on string fiber morphology.

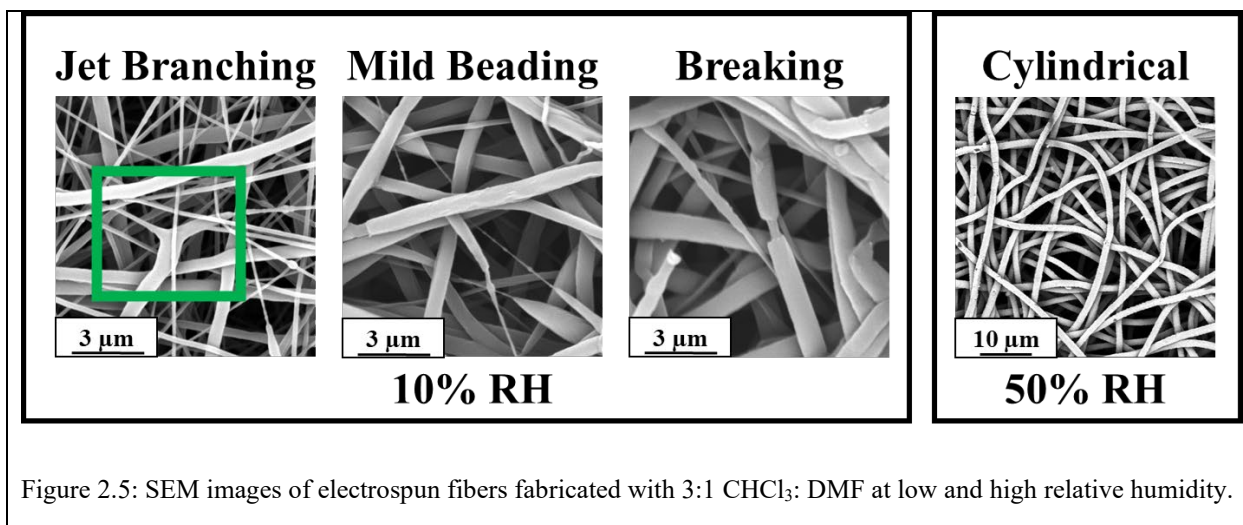


Figure 2.5: SEM images of electrospun fibers fabricated with 3:1  $\text{CHCl}_3$ : DMF at low and high relative humidity.

In the 3:1  $\text{CHCl}_3$ : MeOH solvent samples, fibers did not have homogeneous fiber sizes (Figure 2.3). At high relative humidity, long elongated bead morphology and the presence of garlands were observed (Figure 2.6). At low relative humidity, fibers remain cylindrical with some bead on string morphology and some broken fibers (Figure 2.6). This morphology is likely due to methanol being a highly conductive solvent that is immiscible with chloroform and provides low

solubility to PCL polymer. The additional conductivity of methanol likely caused the polymer jet to split into multiple jets at the needle tip.

At high relative humidity, ambient water in the air would have slowed down the evaporation of the solvent, allowing the polymer jets to remain liquid for a more extended period. This is important because when multiple jets form and the jets remain liquid for longer, the jets can touch while still wet, causing conglutination and subsequent formation of garlands.<sup>36</sup> Garlands can act as a single column consisting of many fibers in the electrospinning process and generally undergo less stretching than individual jets. This reduction in the whipping of the jet may have contributed to the less severe beading morphology observed at high relative humidity.

At low relative humidity with no ambient moisture, if the multiple jets interacted, they did so without observed conglutination and garland formation. This would allow for each jet to individually go through more whipping during the electrospinning process. At low relative humidity, the preference of PCL for the  $\text{CHCl}_3$  solvent could have created MeOH regions with a lower concentration of PCL. The regions with reduced polymer concentration could result in less polymer viscoelastic resistance to stretching during the bending instability and, therefore, very thin string sections to the point of breaking. Breaking also may have been attributed to the viscoelastic contraction of the polymer when drying due to increased acceleration with a more conductive solvent. This mechanism is described in greater detail in Chapter 4.

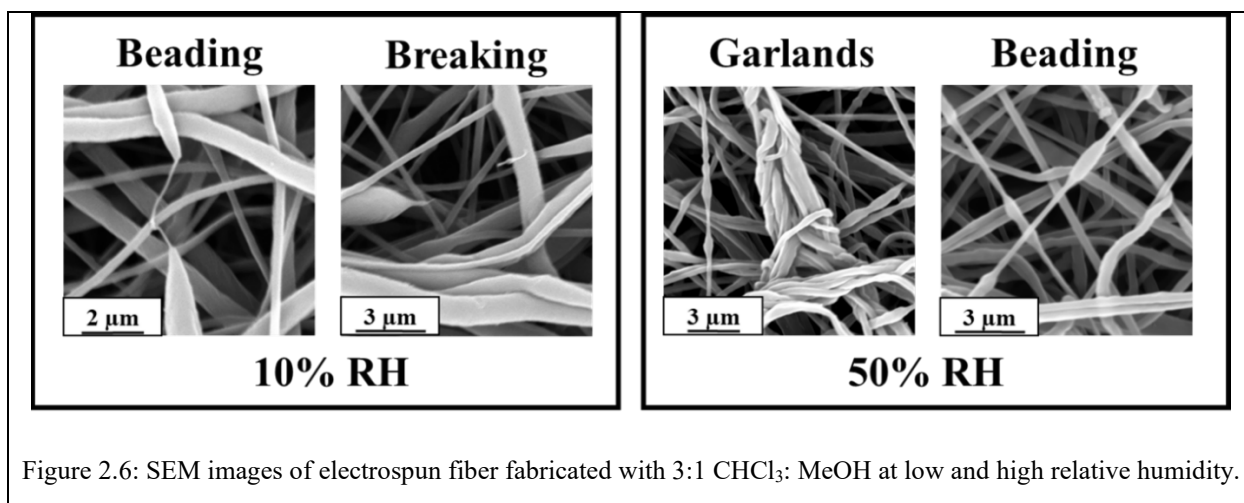
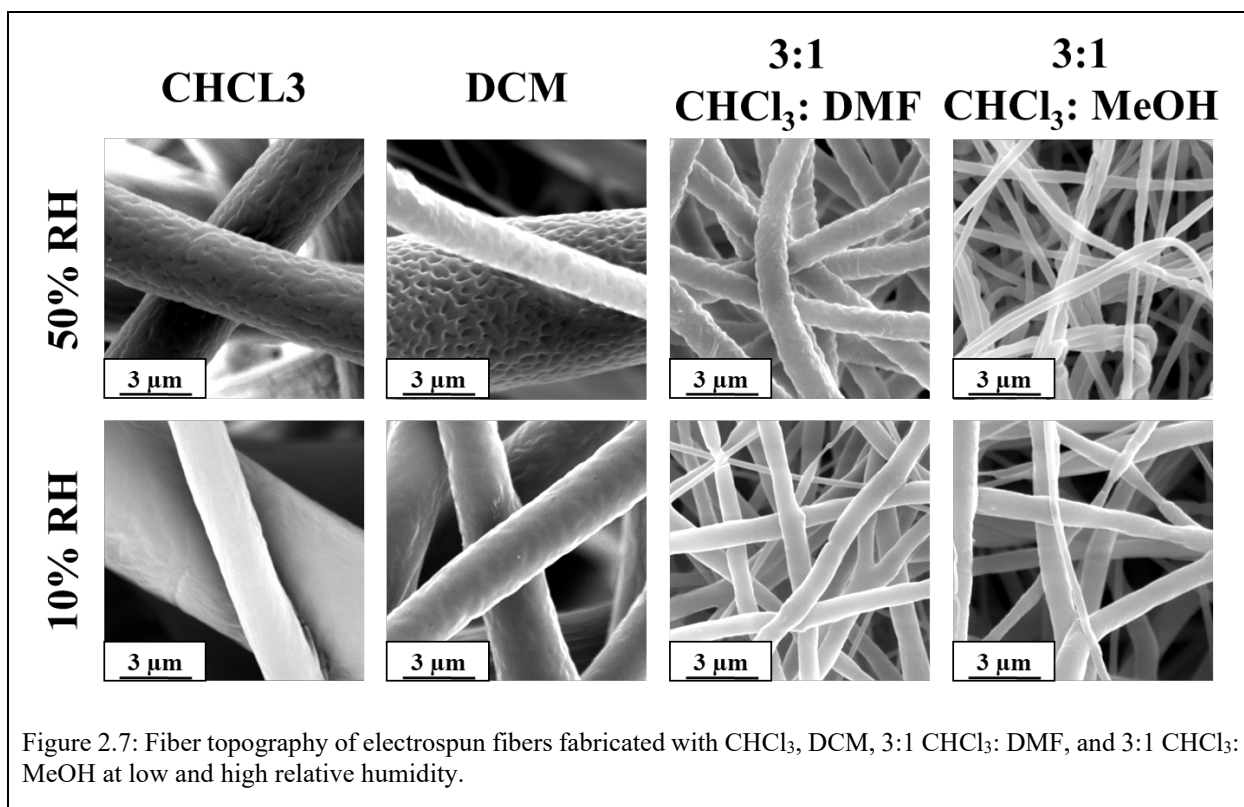


Figure 2.6: SEM images of electrospun fiber fabricated with 3:1 CHCl<sub>3</sub>: MeOH at low and high relative humidity.

### 2.3.2 Fiber Topography

In the CHCl<sub>3</sub> solvent system, the topography of fibers at low relative humidity was smooth, and the topography of fibers at high relative humidity was porous (Figure 2.7). Fibers were porous at high relative humidity because ambient water droplets condense on the surface of fibers and create pores. In the location where the water droplets contacted the fiber, phase separation occurred because water is a poor solvent for PCL. PCL was precipitated out on the surface of the fiber, allowing the fiber to retain the porous topography when solidified. At low relative humidity, the surfaces of the fibers were smooth because the water was not present in the ambient air and therefore could not condense on the outside of the fibers.



In the DCM system, fibers were smooth at low relative humidity and had a porous surface topography on the surface of beads at high relative humidity (Figure 2.7). At high relative humidity, the strings interconnecting beads were smooth in topography. The porous structure on the surface of the beads was caused by water condensing on the surface of the polymer jet during the electrospinning process. When water condensed on the surface of the jets, it caused phase separation because water and DCM are not miscible, and water is a poor solvent for PCL. This caused precipitation of polymer at the surface of the jet, allowing the beaded structure to maintain its porous topography as the fibers collected on the collection plate rather than becoming stretched. Yazgan et al. also saw porous topography using similar solution chemistry and ambient relative humidity.<sup>25</sup>

The thinner string sections connecting the beads formed due to the elongation of the liquid polymer jet during the whipping process. Therefore, any pores on the surface were stretched out to the point that the fibers were smooth and did not maintain the porous structure. Evaporation rate would also be different for a different volume fraction of polymer, which would be unlikely to produce the same evaporative cooling effects. At low relative humidity, the fibers remained smooth because there was no ambient water vapor to condense on the surface of the polymer jet.

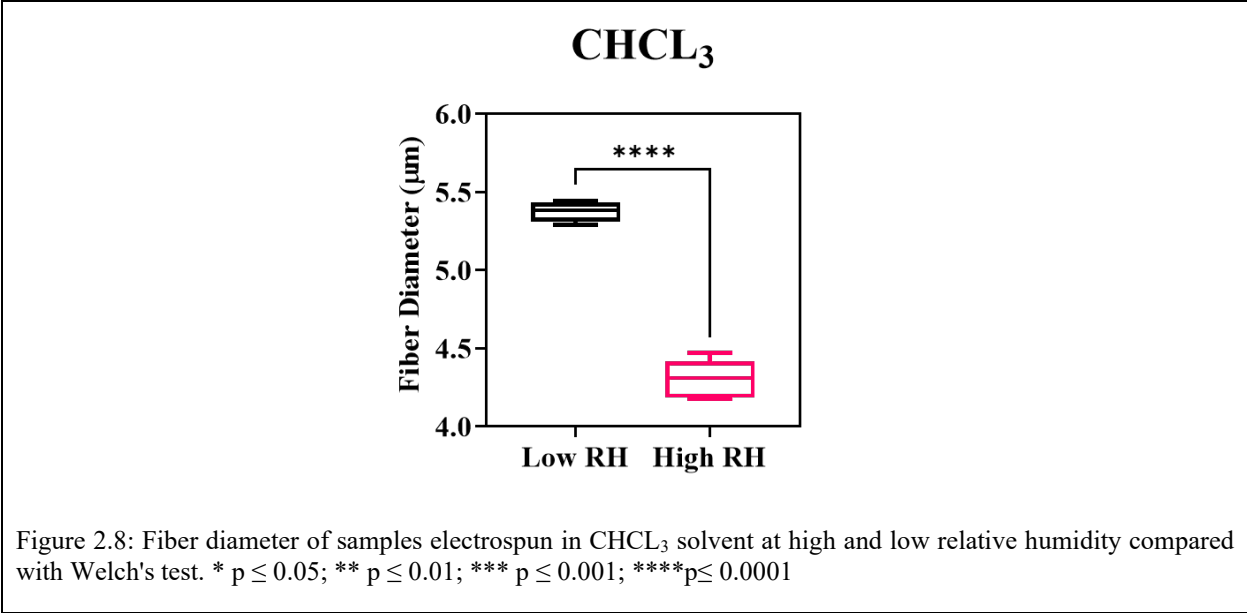
In the 3:1  $\text{CHCl}_3$ : DMF solvent system, fibers were smooth at low relative humidity and wrinkled at high relative humidity (Figure 2.7). The wrinkled morphology seen at high relative humidity may be due to the initial surface precipitation from water condensation. This caused a glassy polymer layer at the surface that shrinks and forms wrinkles when the remaining solvent evaporated out. The absence of pores on the surface of the fibers indicates that due to the miscibility of DMF with water, condensed water on the surface of the jet may have been able to penetrate into the fiber. This would slow the evaporation rate from the polymer jet and allow for more stretching due to the solvent's ability to enable polymer chains to slip past each other while still in a solvent. It is also possible that the slower evaporation caused any pores that initially formed on the surface of these fibers to stretch out into a wrinkled morphology. At low relative humidity, the fibers were smooth because there was very little ambient water in the surrounding environment to condense on the surface of the fibers.

In the 3:1  $\text{CHCl}_3$ : MeOH solvent system, fibers were smooth at high and low relative humidity (Figure 2.7). This smooth topography was because, at high relative humidity, ambient water would likely have been able to mix with the methanol solvent in the polymer jet and thus penetrate into the fiber, not just condense on the surface of the fiber. Additionally, the increased conductivity from methanol caused fibers to become much smaller and likely undergo more

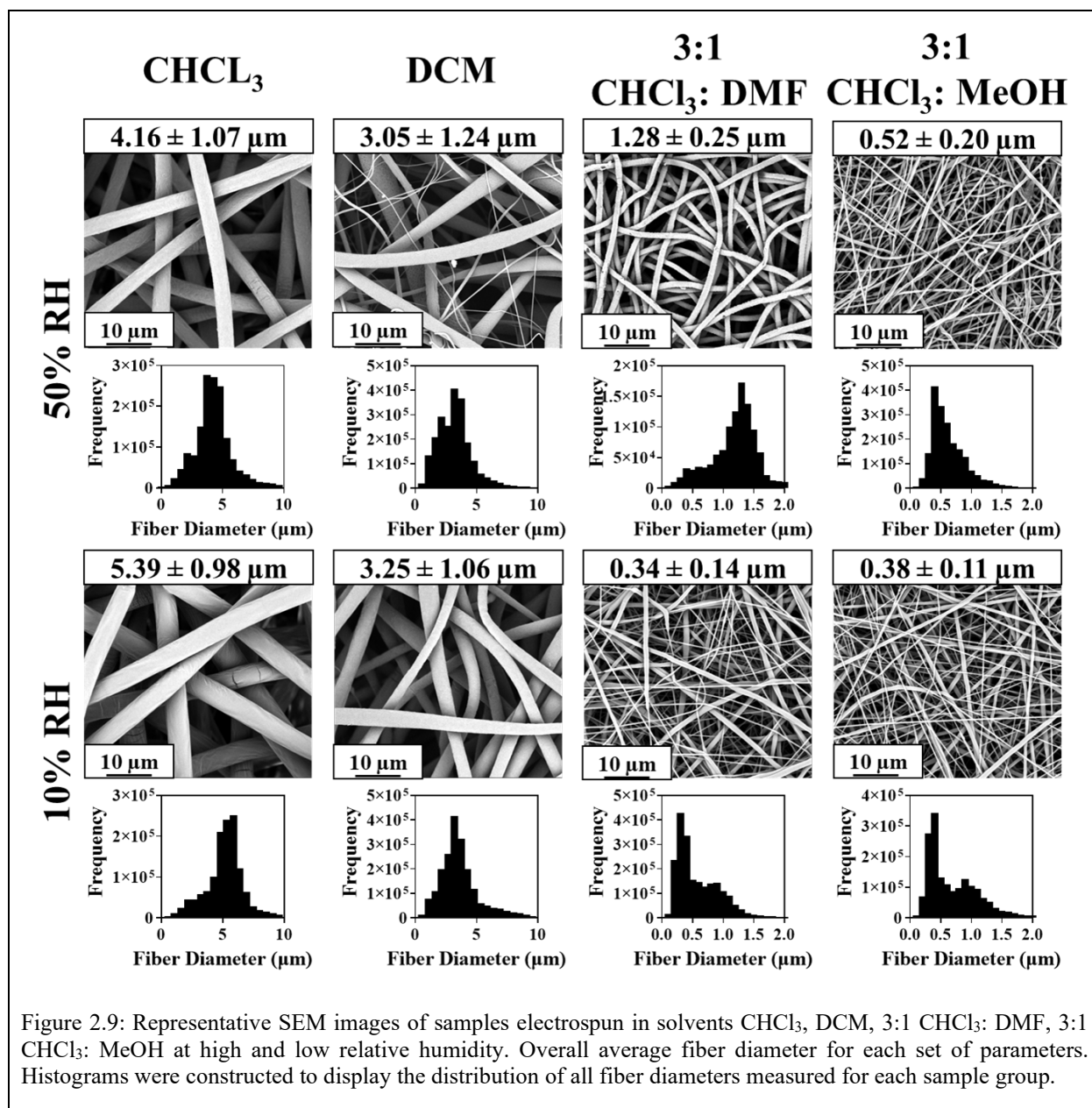
whipping than in other solvent systems. This increased whipping allowed fibers to be further stretched, reducing potential initial surface topography due to ambient water droplets. At low relative humidity, fibers were smooth for the same reasons they were smooth at high relative humidity. Also, there would be very little moisture available to condense on the surface of the fibers to cause surface topography.

### **2.3.3 Fiber Diameter and Distribution**

In the  $\text{CHCl}_3$  solvent system, the average fiber diameter at high relative humidity was  $4.16 \pm 1.07 \mu\text{m}$  and  $5.39 \pm 0.98 \mu\text{m}$  at low relative humidity. Fiber diameter significantly decreased with increasing relative humidity (Figure 2.8). The decrease in fiber diameter with increasing relative humidity was likely due to faster polymer precipitation when the ambient water droplets condense on the surface of the fibers. This precipitation of polymer on the surface of the fiber would have created a polymer film-like layer that would reduce the rate of solvent evaporation allowing increased stretching of the polymer jet during the electrospinning process and thus create a smaller fiber diameter. This decrease in fiber diameter in PCL fibers with increasing relative humidity is consistent with studies by Ghobeira et al. and Yazgan et al.<sup>25,37</sup> Ghoberia et al. also suggests that condensed water on the surface of the PCL fibers could also be acting as a plasticizer to facilitate stretching of the fiber which also could be true in this case.<sup>37</sup>



The distribution of fibers at both high and low relative humidity was narrow with a unimodal distribution (Figure 2.9). The unimodal fiber distribution further supports the qualitative SEM observation. All fibers appear to be approximately the same fiber diameter for samples electrospun at both high and low relative humidity with this solvent system.

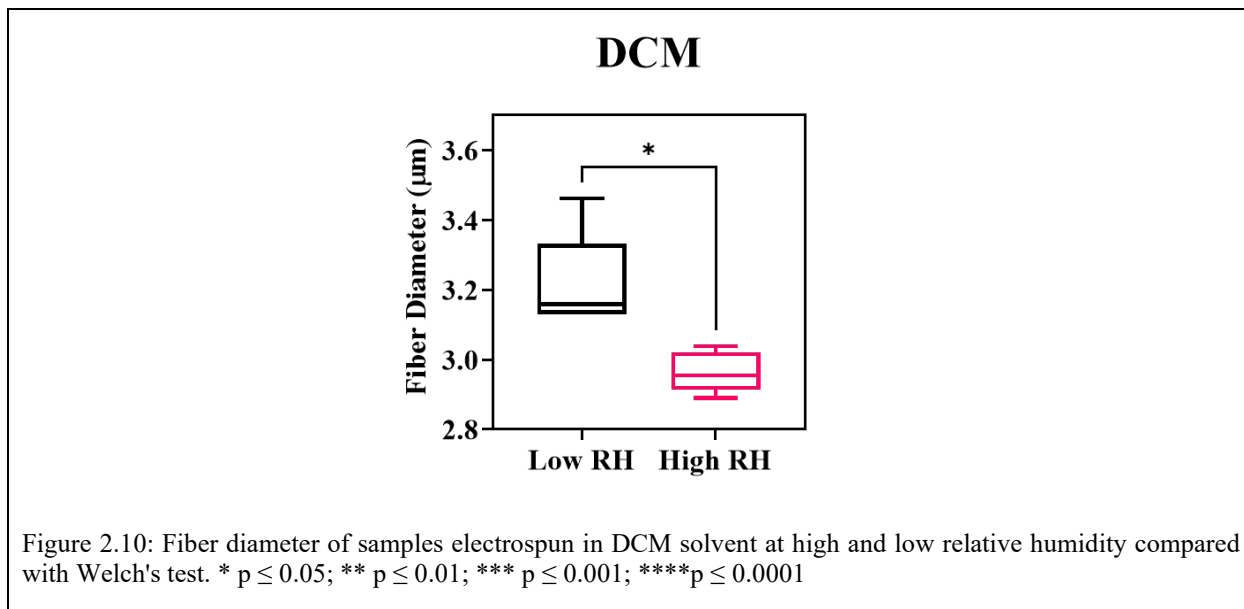


5

In the DCM solvent system, the average fiber diameter at high relative humidity was  $3.05 \pm 1.24 \mu\text{m}$  and at low relative humidity was  $3.25 \pm 1.06 \mu\text{m}$ . Fiber diameter significantly decreased with increasing relative humidity (Figure 2.10). The decrease in fiber diameter with increasing relative humidity is due to the beading morphology creating smaller fiber diameters and, on average, a smaller fiber diameter, in addition to the mechanism listed for CHCl<sub>3</sub>. The distribution



of fibers at high relative humidity had a bimodal distribution, while the distribution of fibers at low relative humidity had a unimodal distribution that was slightly positive skew (Figure 2.9).



In the 3:1  $\text{CHCl}_3$ : DMF solvent system, the average fiber diameter at high relative humidity was  $1.28 \pm 0.25 \mu\text{m}$  and at low relative humidity was  $0.34 \pm 0.14 \mu\text{m}$  (Figure 2.9). The average fiber diameter statistically increased with increasing relative humidity (Figure 2.11). This may be due to rapid precipitation of the sheath at high relative humidity preventing further stretching in a higher conductive solvent. Fibers at high relative humidity had a negative skew with a bimodal-like distribution with a smaller peak representing smaller fibers and the larger peak representing larger fiber diameters (Figure 2.9). The shorter secondary peak in the fiber distribution was due to the beading morphology of the fibers at low relative humidity. The bimodal fiber diameter distribution at low relative humidity is due to fiber branching creating smaller fibers.

### 3:1 CHCl<sub>3</sub>: DMF

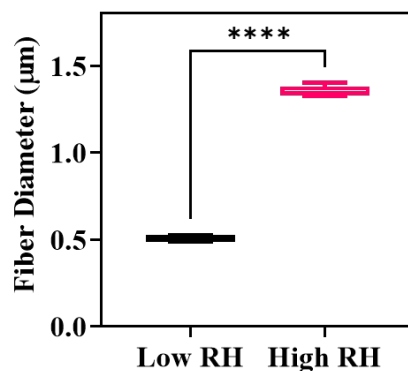


Figure 2.11: Fiber diameter of samples electrospun in 3:1 CHCl<sub>3</sub>: DMF solvent at high and low relative humidity compared with Welch's test. \*  $p \leq 0.05$ ; \*\*  $p \leq 0.01$ ; \*\*\*  $p \leq 0.001$ ; \*\*\*\*  $p \leq 0.0001$

In the 3:1 CHCl<sub>3</sub>: MeOH solvent system, the average fiber diameter at high relative humidity was  $0.52 \pm 0.20 \mu\text{m}$  and at low relative humidity was  $0.38 \pm 0.11 \mu\text{m}$  (Figure 2.9). Although this trend was seen in the shift in distribution peaks of fiber diameter, the change in fiber diameter was not statistically significant (Figure 2.12). This may be because the larger and smaller fibers present in the beading morphology were averaged together.

**3:1  
CHCl<sub>3</sub>: MeOH**

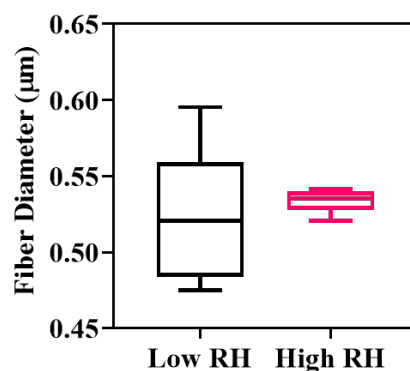
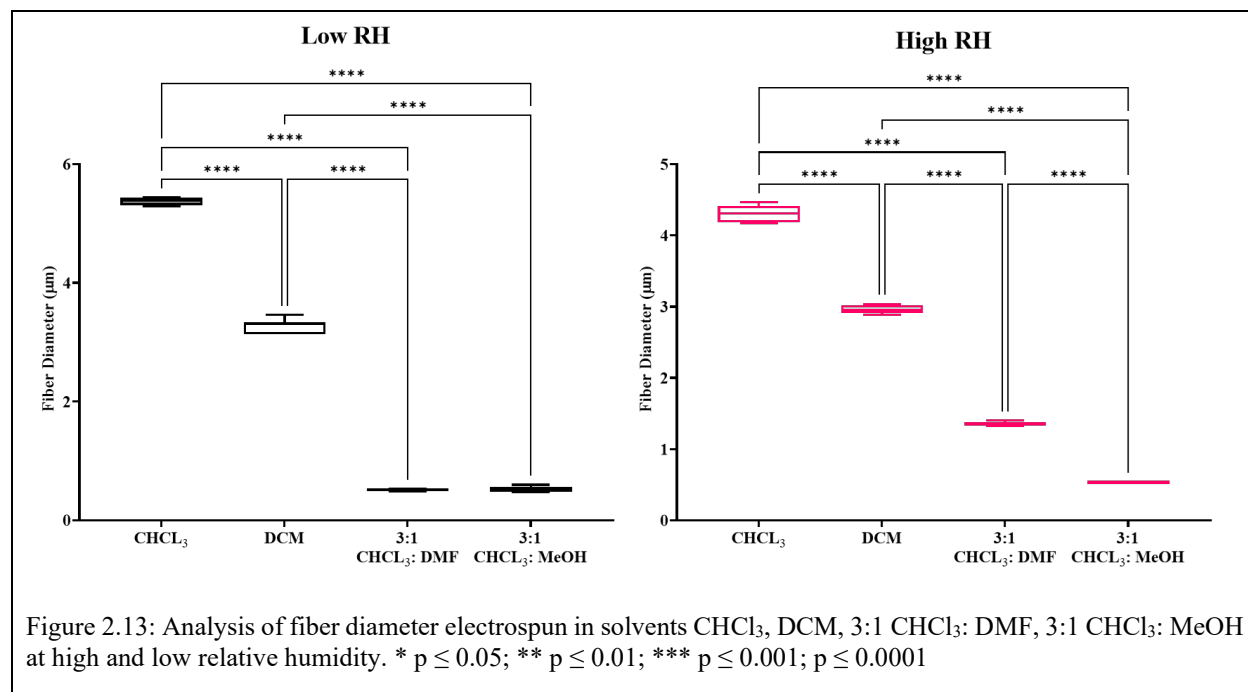


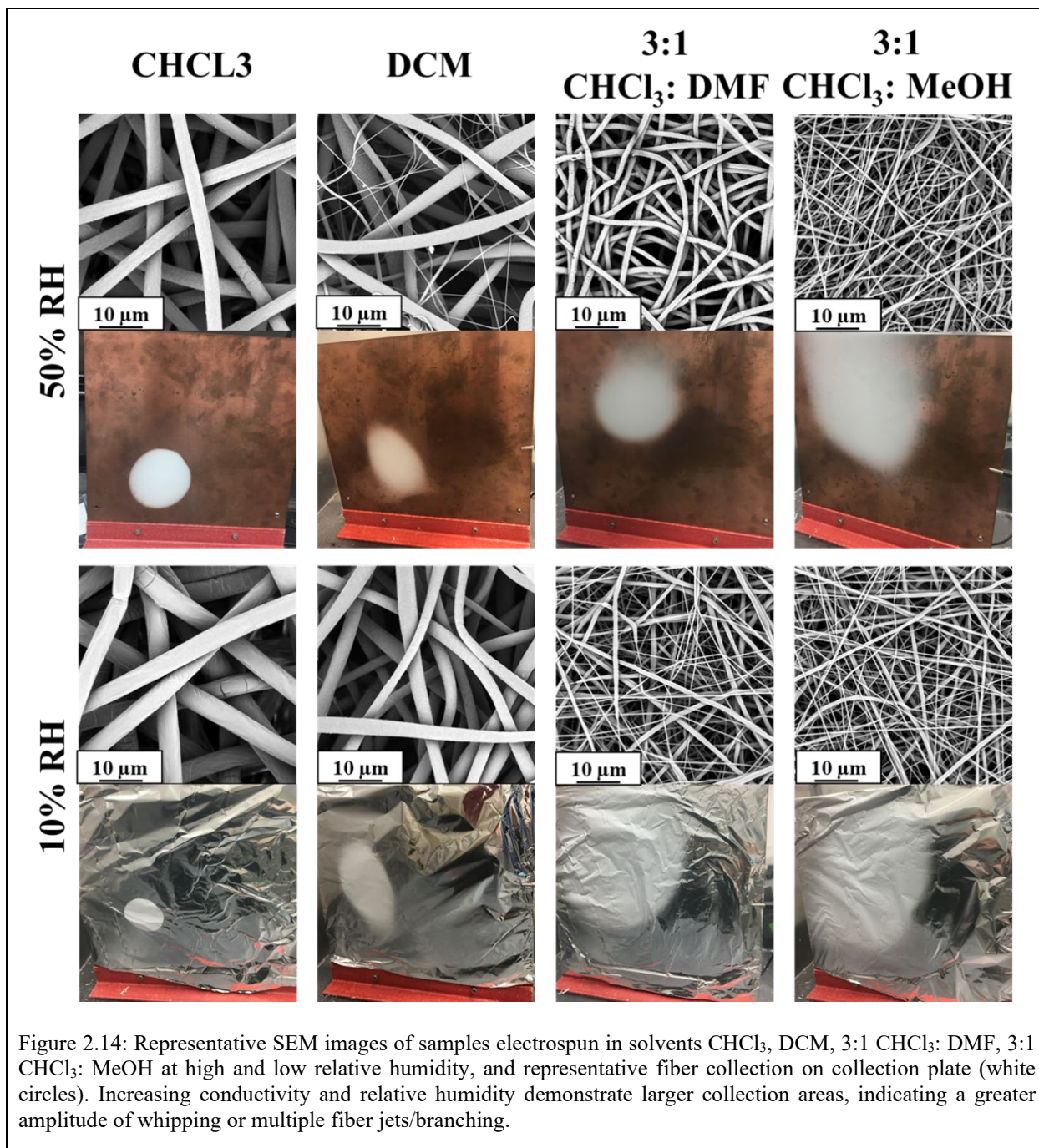
Figure 2.12: Fiber diameter of samples electrospun in 3:1 CHCl<sub>3</sub>: MeOH solvent at high and low relative humidity compared with Welch's test. \*  $p \leq 0.05$ ; \*\*  $p \leq 0.01$ ; \*\*\*  $p \leq 0.001$ ;  $p \leq 0.0001$

The distribution of fiber diameter at high relative humidity had a unimodal distribution with a positive skew, while the fiber diameter distribution at low relative humidity also had a positive skew but with a bimodal distribution (Figure 2.9). The bimodal distribution of fibers at low relative humidity was probably due to humidity preventing the formation of garlands and, therefore, multiple jets unable to form conglutination. MeOH has high conductivity, is immiscible with CHCl<sub>3</sub>, and is a poor solvent for PCL. The immiscible and poor solvent properties contributed to a degree of phase separation, while the increase in conductivity enhanced the overall conductivity of the system and encouraged multiple jets formation. This occurred in part because polymer and polymer solubility between the two solvents led to regions of polymer-rich and polymer-poor electrospun jets. The regions with less polymer had less resistance to whipping due to decreased chain entanglement of the polymer and therefore increased stretching leading to smaller fiber diameters. In contrast, areas with higher concentrations of PCL in chloroform led to larger fiber diameters.

The fiber diameter of DCM was smaller and statistically different from the CHCl<sub>3</sub> fibers at both high and low relative humidity (Figure 2.13). Smaller fibers found in the DCM mesh were because DCM solvent is a more conductive solvent and, consequently, has higher electrostatic charge repulsion and ability to propagate electrons through the polymer jet, allowing for more whipping stretching during the electrospinning process.

The increased whipping is supported by the larger collection area on the electrospinning collection plate, demonstrating a larger whipping amplitude (Figure 2.14). Increasing relative humidity decreased collection area in the single solvent systems and increased collection area in the dual solvent systems.





When comparing the average fiber diameter in this solvent system to fibers fabricated with CHCl<sub>3</sub> or DCM, the fibers are smaller and statistically different at high and low relative humidity (Figure 2.13). This decrease fiber diameter is due to the DMF component in the system having higher conductivity and increasing the overall conductivity of the solvent system. Higher

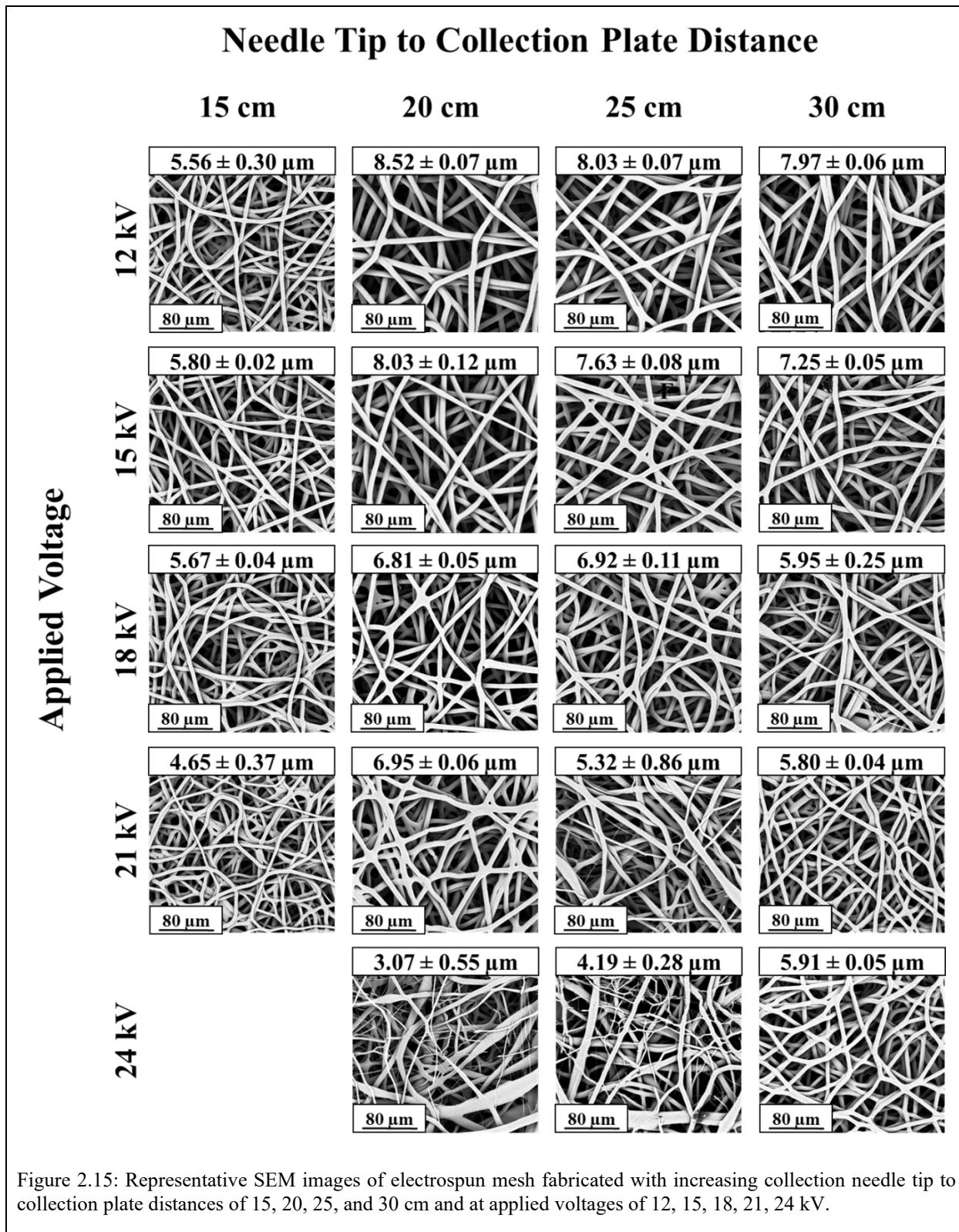
conductivity in solvent systems allows for increased whipping and subsequent stretching of the fibers, resulting in smaller fiber diameters. This increased stretching can be seen in the increased diameter of fiber collection, indicating an increased amplitude of whipping, or branching of fibers covering a larger area of the collection plate (Figure 2.14)

The fibers, fabricated with the 3:1 CHCl<sub>3</sub>: MeOH solvent, were statistically different compared to all other solvent systems at both high and low relative humidity (Figure 2.13). At high relative humidity, fibers fabricated in this system were smaller than in all other systems. This decrease in fiber diameter was likely due to multiple jets formation at the needle tip. The formation of multiple jets and the increased whipping of the fibers was seen in the diameter of fiber collection on the collection plate, which was larger than in any other solvent system (Figure 2.14).

#### **2.3.4 Confirming Solvent Evaporation and Conductivity Effects with Processing Parameters**

The electrospun mesh was fabricated with varying processing parameters to compare known effects of processing parameters to effects seen with increasing conductivity and volatility caused by solution chemistry. All samples were collected using the CHCl<sub>3</sub> solvent system to compare the effects to fibers optimized to produce uniform cylindrical fibers. Studies were conducted at a lower relative humidity to minimize the potential impacts of VIPS.

The effects of systematically altering applied voltage and distance between the needle tip and collection plate were determined by analyzing the resulting fiber morphology and fiber diameter. The needle tip distance was ranged from 15cm to 30cm, with every 5 cm in between. The applied voltage ranged from 12kV to 24kV, with every 3kV in between. Representative SEM images of each processing parameter combination are shown below (Figure 2.15).



Increasing applied voltage in systems with a single jet drawn from the Taylor cone will decrease fiber diameter because the fiber will undergo more stretching in the bending instability region.<sup>38</sup> Increasing voltage also increases electrostatic repulsion at the surface of the jet, and increased electric field favors a larger amplitude of whipping.<sup>1,19,39</sup> Increased velocity and bending within the electric field can also create branching and the presence of smaller fibers.<sup>17,40</sup> Increasing applied voltage beyond this threshold has been shown to initiate multiple jets. Once multiple jets have formed, studies have demonstrated that fiber diameter can increase because of the increased velocity of individual jets.<sup>2,41</sup> Increasing the applied voltage can also change the shape of the Taylor cone because higher electrostatic repulsive forces can overcome capillary forces earlier, which causes the Taylor cone to narrow towards the needle tip.<sup>38,42</sup> Deitzel et al. found that as Taylor cone narrows, bead morphology has been observed.<sup>42</sup>

Based on the mechanisms described above, as applied voltage increases, fiber diameter decreases due to increased stretching in the bending region (Figure 2.16). Smaller fibers were observed in samples with 25 cm and 21 kV, 20 cm and 24 kV, and 25 cm and 24 kV (Figure 2.15). These tiny fibers indicate that the 24 kV jets experienced branching due to high whipping caused by the high voltage. This was not seen in the sample with a 30 cm collection distance because the weaker electric field tempered the whipping. The transition from fused fiber morphology to small fiber morphology at 21 kV indicates that a transition in drying occurred between 20 to 25 centimeters. Beading morphology was also observed at 20 cm collection distance, and 25 kV applied voltage, potentially indicating a Taylor cone transition to a reeded jet.



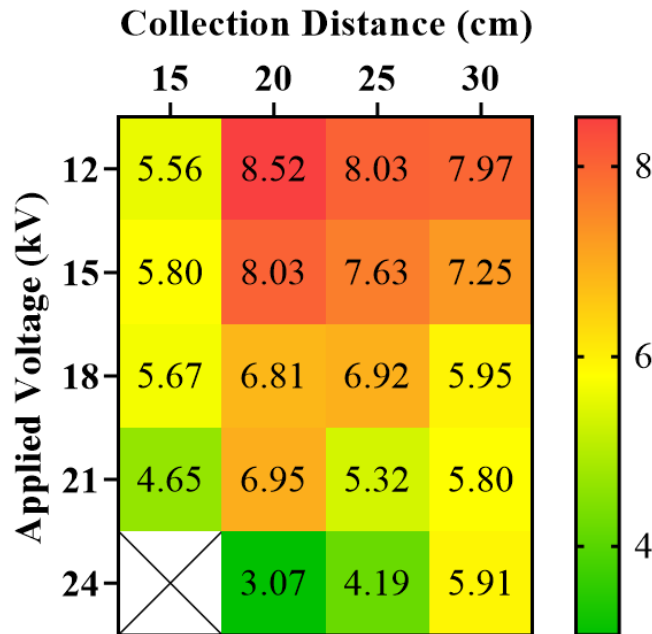


Figure 2.16: Heat map of average fiber diameters in  $\mu\text{m}$  illustrating the effects of collection distance and applied voltage.

The trend in fiber diameter decreased as the applied voltage increased (Figure 2.16). For samples fabricated at a 15 cm collection gap, the fiber diameters were  $5.56 \pm 0.30$ ,  $5.80 \pm 0.02$ ,  $5.67 \pm 0.04$ , and  $4.65 \pm 0.37 \mu\text{m}$  for samples that used 12, 15, 18, and 21 kV applied voltage, respectively. Samples fabricated at a 20 cm collection gap had fiber diameters of  $8.52 \pm 0.07$ ,  $8.03 \pm 0.12$ ,  $6.81 \pm 0.05$ ,  $6.95 \pm 0.06$ , and  $3.07 \pm 0.55 \mu\text{m}$  for samples that used 12, 15, 18, 21, and 24 kV applied voltage, respectively. Samples fabricated at a 25 cm collection gap had fiber diameters of  $8.03 \pm 0.07$ ,  $7.63 \pm 0.08$ ,  $6.92 \pm 0.11$ ,  $5.32 \pm 0.86$ , and  $4.19 \pm 0.28 \mu\text{m}$  for samples that used 12, 15, 18, 21, and 24 kV applied voltage, respectively. Finally, samples fabricated at a 30 cm collection gap had fiber diameters of  $7.97 \pm 0.06$ ,  $7.25 \pm 0.05$ ,  $5.95 \pm 0.25$ ,  $5.80 \pm 0.04$ , and  $5.91 \pm 0.05 \mu\text{m}$  for samples that used 12, 15, 18, 21, and 24 kV applied voltage, respectively. A heat

map of the fiber diameters at the different processing conditions was generated to aid in visualization (Figure 2.16).

At shorter distances between the needle tip and the collection plate, fibers are generally larger in fiber diameter and have been shown to increase fiber diameter because less evaporation of solvent occurs.<sup>39,40,43</sup> After the fibers have had an adequate amount of time to dry, which can be achieved by altering processing parameters such as increasing collection distance, fiber diameter generally decreases with increased collection distance. Fiber diameter decreases because the solvent can evaporate further and undergo more stretching in the bending instability. At the far range of collection distance, fiber has also been shown to increase because the charge on the surface of the fiber decreases with increasing distance from the collection plate.<sup>44</sup> The electric field strength also influences the amount of whipping in the bending instability. This electric field strength increases with increased distance between the needle tip and the collection plate.<sup>39,40,43</sup> Stronger electric fields can also increase the acceleration of the jet delaying the onset of the bending instability.<sup>18,39</sup>

Based on the studies and theoretical models above, at shorter collection distances, as collection distances increase, the electric field increases and acceleration increases and delays the bending instability, and the fiber diameter increases. At further collection distances, as collection distance increases, stretching of the fiber in the bending region increases, and fiber diameter decreases. This is consistent with the fiber diameter data measured with increasing distance (Figure 2.16). Between 20 to 30 centimeters in collection distance, the stretching of the jet dominates fiber diameter, and at 15 centimeters, the jet is dominated by electric field strength. Shorter distances in collection distance also resulted in more fused fiber morphology due to less time solvent to evaporate and fibers to dry.

## 2.4 CONCLUSION

Understanding the role that solvent plays in electrospun systems is crucial to controlling the fiber morphology, topography, and fiber diameter. Fiber morphology was cylindrical for fibers electrospun in  $\text{CHCl}_3$ , DCM at low relative humidity, and 3:1  $\text{CHCl}_3$ : DMF at high relative humidity. Beading morphology was present in DCM samples at high relative humidity, 3:1  $\text{CHCl}_3$ : DMF at low relative humidity, and 3:1  $\text{CHCl}_3$ : MeOH at high and low relative humidity. In single solvent systems, the surface topography of fibers was porous at high relative humidity and smooth at low relative humidity. Fibers electrospun with 3:1  $\text{CHCl}_3$ : DMF were wrinkled at high relative humidity and smooth at low relative humidity. Fibers electrospun with 3:1  $\text{CHCl}_3$ : MeOH were smooth at both high and low relative humidity. Overall, using solvents with increasing conductivity resulted in decreased fiber diameter at both high and low relative humidity due to increased stretching of the fibers within the whipping phase of electrospinning. In single solvent systems, increasing the relative humidity led to a decrease in fiber diameter. In the dual solvent system, fiber diameter either increased with increasing relative humidity or did not statistically change. Fiber distribution had a unimodal distribution for fibers with primarily cylindrical fibers and bimodal for fibers with beading morphology. Increased solvent conductivity coupled with phase separation also led to the formation of multiple jet fibers, further decreasing the average fiber diameter. Summarized results of solvent chemistry can be seen in Table 2.2.

Overall, fiber diameter decreased with increasing applied voltage. The fiber diameter also decreased with collection distances greater than 20 cm because of increased stretching. Fiber diameter increased with increasing collection distance before 20 cm because bending instability attributed to delayed onset of bending instability, causing less whipping through stretching.

Understanding the interdependent parameters in electrospinning with a particular focus on solvent volatility and conductivity allows for further control of the electrospinning fiber diameters and morphologies. This is important because it can create possibilities to control fiber diameter and morphology for tissue engineering and drug delivery applications. Understanding the effects of solution chemistry and critical processing parameters independently can allow fiber characteristics like diameter and morphology to be tuned to achieve maximum therapeutic benefit while maintaining the integrity of the surfactant, internal phase, or drug they encapsulate.

Table 2.2: Summary table for fiber morphology, topography, diameter, and distribution for electrospun fibers fabricated from CHCl<sub>3</sub>, DCM, 3:1 CHCl<sub>3</sub>: DMF, and 3:1 CHCl<sub>3</sub>: MeOH.

Table 2.2. Summary of Fiber Morphology, Topography, Diameter, and Distribution for CHCl <sub>3</sub> , DCM, 3:1 CHCl <sub>3</sub> : DMF, and 3:1 CHCl <sub>3</sub> : 1MeOH						
Solvent(s)	Fiber Morphology	Fiber Topography	Relative Humidity	Average Fiber Diameter (μm)	Cumulative Diameter Skewness	Cumulative Diameter Kurtosis
CHCl <sub>3</sub>	Cylindrical	Porous	50%	4.16 ± 1.07	1.84	9.59
CHCl <sub>3</sub>	Cylindrical	Smooth	10%	5.39 ± 0.98	0.76	5.14
DCM	Branching, Beading	Porous	50%	3.05 ± 1.24	0.97	1.18
DCM	Cylindrical	Smooth	10%	3.25 ± 1.06	0.84	1.01
3:1 CHCl <sub>3</sub> : DMF	Cylindrical	Wrinkled	50%	1.28 ± 0.25	0.31	1.87
3:1 CHCl <sub>3</sub> : DMF	Branching, Mild Beading, Breaking	Smooth	10%	0.34 ± 0.14	1.18	1.58
3:1 CHCl <sub>3</sub> : MeOH	Garlands, Beading	Smooth	50%	0.52 ± 0.20	1.77	5.39
3:1 CHCl <sub>3</sub> : MeOH	Beading, Breaking	Smooth	10%	0.38 ± 0.11	1.57	4.28

Understanding the influence of solution chemistry on fiber formation mechanism during electrospinning will give researchers the ability to create more finely tuned and reproducible

meshes. In tissue engineering, this knowledge could lead to selecting an ideal solvent that would encapsulate the needed drug into the mesh while producing fiber morphology that can elicit desired cell responses.

## 2.5 BIBLIOGRAPHY

- 1 Abutaleb, A. *et al.* Effects of Surfactants on the Morphology and Properties of Electrospun Polyetherimide Fibers. *Fibers* **5**, 33, doi:10.3390/fib5030033 (2017).
- 2 Lin, T., Wang, H., Wang, H. & Wang, X. The charge effect of cationic surfactants on the elimination of fibre beads in the electrospinning of polystyrene. *Nanotechnology* **15**, 1375-1381, doi:10.1088/0957-4484/15/9/044 (2004).
- 3 Aykut, Y., Pourdeyhimi, B. & Khan, S. A. Effects of surfactants on the microstructures of electrospun polyacrylonitrile nanofibers and their carbonized analogs. *J Appl Polym Sci* **130**, 3726-3735, doi:10.1002/app.39637 (2013).
- 4 Johnson, P. M. *et al.* Surfactant location and internal phase volume fraction dictate emulsion electrospun fiber morphology and modulate drug release and cell response. *Biomater Sci-Uk*, doi:10.1039/D0BM01751E (2021).
- 5 Zhang, C., Feng, F. & Zhang, H. Emulsion electrospinning: Fundamentals, food applications and prospects. *Trends in Food Science & Technology* **80**, 175-186, doi:10.1016/j.tifs.2018.08.005 (2018).
- 6 Beigmoradi, R., Samimi, A. & Mohebbi-Kalhor, D. Fabrication of polymeric nanofibrous mats with controllable structure and enhanced wetting behavior using one-step electrospinning. *Polymer* **143**, 271-280, doi:<https://doi.org/10.1016/j.polymer.2018.04.025> (2018).
- 7 Li, X., Su, Y., Zhou, X. & Mo, X. Distribution of Sorbitan Monooleate in poly(L-lactide-co-epsilon-caprolactone) nanofibers from emulsion electrospinning. *Colloids Surf B Biointerfaces* **69**, 221-224, doi:10.1016/j.colsurfb.2008.11.031 (2009).
- 8 Vasita, R., Mani, G., Agrawal, C. M. & Katti, D. S. Surface hydrophilization of electrospun PLGA micro-/nano-fibers by blending with Pluronic® F-108. *Polymer* **51**, 3706-3714, doi:<https://doi.org/10.1016/j.polymer.2010.05.048> (2010).
- 9 Zheng, J.-Y. *et al.* The Effect of Surfactants on the Diameter and Morphology of Electrospun Ultrafine Nanofiber. *J Nanomater* **2014**, 1-9, doi:10.1155/2014/689298 (2014).
- 10 Hu, J., Prabhakaran, M. P., Ding, X. & Ramakrishna, S. Emulsion electrospinning of polycaprolactone: influence of surfactant type towards the scaffold properties. *Journal of Biomaterials Science, Polymer Edition* **26**, 57-75, doi:10.1080/09205063.2014.982241 (2015).
- 11 Yazgan, G. *et al.* Tunable release of hydrophilic compounds from hydrophobic nanostructured fibers prepared by emulsion electrospinning. *Polymer* **66**, 268-276, doi:10.1016/j.polymer.2015.04.045 (2015).
- 12 Wang, S.-Q., He, J.-H. & Xu, L. Non-ionic surfactants for enhancing electrospinnability and for the preparation of electrospun nanofibers. *Polym Int* **57**, 1079-1082, doi:10.1002/pi.2447 (2008).

- 13 Kriegel, C., Kit, K. M., McClements, D. J. & Weiss, J. Nanofibers as carrier systems for antimicrobial microemulsions. Part I: fabrication and characterization. *Langmuir* **25**, 1154-1161, doi:10.1021/la803058c (2009).
- 14 Xue, J., Wu, T., Dai, Y. & Xia, Y. Electrospinning and Electrospun Nanofibers: Methods, Materials, and Applications. *Chem Rev* **119**, 5298-5415, doi:10.1021/acs.chemrev.8b00593 (2019).
- 15 Jia, L. & Qin, X.-h. The effect of different surfactants on the electrospinning poly(vinyl alcohol) (PVA) nanofibers. *Journal of Thermal Analysis and Calorimetry* **112**, 595-605, doi:10.1007/s10973-012-2607-9 (2013).
- 16 Kriegel, C., Kit, K. M., McClements, D. J. & Weiss, J. Influence of Surfactant Type and Concentration on Electrospinning of Chitosan–Poly(Ethylene Oxide) Blend Nanofibers. *Food Biophysics* **4**, 213-228, doi:10.1007/s11483-009-9119-6 (2009).
- 17 Talwar, S., Krishnan, A. S., Hinestroza, J. P., Pourdeyhimi, B. & Khan, S. A. Electrospun Nanofibers with Associative Polymer–Surfactant Systems. *Macromolecules* **43**, 7650-7656, doi:10.1021/ma1013447 (2010).
- 18 Nilsson, S., Thuresson, K., Hansson, P. & Lindman, B. Mixed Solutions of Surfactant and Hydrophobically Modified Polymer. Controlling Viscosity with Micellar Size. *The Journal of Physical Chemistry B* **102**, 7099-7105, doi:10.1021/jp9812379 (1998).
- 19 Yu, D.-G., Chatterton, N. P., Yang, J.-H., Wang, X. & Liao, Y.-Z. Coaxial Electrospinning with Triton X-100 Solutions as Sheath Fluids for Preparing PAN Nanofibers. *Macromol Mater Eng* **297**, 395-401, doi:10.1002/mame.201100258 (2012).
- 20 Griffin, W. C. Calculation of HLB Values of Non-ionic surfactants. *Journal of The Society of Cosmetic Chemists*, 249-256 (1954).
- 21 Griffin, W. C. Classification of Surface-Active Agents by "HLB". *Journal of the Society of Cosmetic Chemists* **1**, 311-326 (1949).
- 22 Davies, T. J. in *International Congress Surface Activity*. 426-438.
- 23 Nakama, Y. in *Cosmetic Science and Technology* (eds Kazutami Sakamoto, Robert Y. Lochhead, Howard I. Maibach, & Yuji Yamashita) 231-244 (Elsevier, 2017).
- 24 Kunieda, H. & Ishikawa, N. Evaluation of the hydrophile-lipophile balance (HLB) of nonionic surfactants. II. Commercial-surfactant systems. *J Colloid Interf Sci* **107**, 122-128, doi:10.1016/0021-9797(85)90155-9 (1985).
- 25 Li, X. *et al.* Encapsulation of proteins in poly(L-lactide-co-caprolactone) fibers by emulsion electrospinning. *Colloids Surf B Biointerfaces* **75**, 418-424, doi:10.1016/j.colsurfb.2009.09.014 (2010).
- 26 Yazgan, G. *et al.* Steering surface topographies of electrospun fibers: understanding the mechanisms. *Sci Rep-Uk* **7**, doi:ARTN 15810.1038/s41598-017-00181-0 (2017).
- 27 Zaarour, B., Zhu, L., Huang, C. & Jin, X. Controlling the Secondary Surface Morphology of Electrospun PVDF Nanofibers by Regulating the Solvent and Relative Humidity. *Nanoscale Research Letters* **13**, 285, doi:10.1186/s11671-018-2705-0 (2018).
- 28 Nezarati, R. M., Eifert, M. B. & Cosgriff-Hernandez, E. Effects of humidity and solution viscosity on electrospun fiber morphology. *Tissue Eng Part C Methods* **19**, 810-819, doi:10.1089/ten.TEC.2012.0671 (2013).
- 29 Szewczyk, P. *et al.* Roughness and Fiber Fraction Dominated Wetting of Electrospun Fiber-Based Porous Meshes. *Polymers-Basel* **11**, 34, doi:10.3390/polym11010034 (2018).

- 30 Li, X., Su, Y., Zhou, X. & Mo, X. Distribution of Sorbitan Monooleate in poly(l-lactide-co-ε-caprolactone) nanofibers from emulsion electrospinning. *Colloids and Surfaces B: Biointerfaces* **69**, 221-224, doi:<https://doi.org/10.1016/j.colsurfb.2008.11.031> (2009).
- 31 Coimbra, P., Freitas, J. P., Goncalves, T., Gil, M. H. & Figueiredo, M. Preparation of gentamicin sulfate eluting fiber mats by emulsion and by suspension electrospinning. *Mater Sci Eng C Mater Biol Appl* **94**, 86-93, doi:10.1016/j.msec.2018.09.019 (2019).
- 32 Szewczyk, P. K. *et al.* Roughness and Fiber Fraction Dominated Wetting of Electrospun Fiber-Based Porous Meshes. *Polymers (Basel)* **11**, doi:10.3390/polym11010034 (2018).
- 33 Wang, L., Pai, C.-L., Boyce, M. C. & Rutledge, G. C. Wrinkled surface topographies of electrospun polymer fibers. *Appl Phys Lett* **94**, 151916, doi:10.1063/1.3118526 (2009).
- 34 Zaarour, B., Zhu, L., Huang, C. & Jin, X. Fabrication of a polyvinylidene fluoride cactus-like nanofiber through one-step electrospinning. *RSC Advances* **8**, 42353-42360, doi:10.1039/c8ra09257e (2018).
- 35 Naraghi, M., Chasiotis, I., Kahn, H., Wen, Y. & Dzenis, Y. Mechanical deformation and failure of electrospun polyacrylonitrile nanofibers as a function of strain rate. *Appl Phys Lett* **91**, 151901, doi:10.1063/1.2795799 (2007).
- 36 Zhang, X., Shi, X., Gautrot, J. E. & Peijs, T. Nanoengineered electrospun fibers and their biomedical applications: a review. *Nanocomposites* **7**, 1-34, doi:10.1080/20550324.2020.1857121 (2021).
- 37 Wang, C., Wang, L. & Wang, M. Evolution of core-shell structure: From emulsions to ultrafine emulsion electrospun fibers. *Mater Lett* **124**, 192-196, doi:<https://doi.org/10.1016/j.matlet.2014.03.086> (2014).
- 38 Sy, J. C., Klemm, A. S. & Shastri, V. P. Emulsion as a Means of Controlling Electrospinning of Polymers. *Advanced Materials* **21**, 1814-1819, doi:10.1002/adma.200701630 (2009).
- 39 Santhanalakshmi, J. & Maya, S. Solvent effects on reverse micellisation of Tween 80 and Span 80 in pure and mixed organic solvents. *Proc. Intian Acad. Sci.* **109**, 22=38 (1997).
- 40 Griffin, W. C. Classification of Surface-Active Agents By "HLB". *Journal of the Society of Cosmetic Chemists*, 311-326 (1949).
- 41 Fong, H., Chun, I. & Reneker, D. H. Beaded nanofibers formed during electrospinning. *Polymer* **40**, 4585-4592, doi:10.1016/s0032-3861(99)00068-3 (1999).
- 42 Rutledge, G. C. & Fridrikh, S. V. Formation of fibers by electrospinning. *Advanced drug delivery reviews* **59**, 1384-1391, doi:10.1016/j.addr.2007.04.020 (2007).
- 43 Xu, D., Liu, C.-Y. & Craig, S. L. Divergent Shear Thinning and Shear Thickening Behavior of Supramolecular Polymer Networks in Semidilute Entangled Polymer Solutions. *Macromolecules* **44**, 2343-2353, doi:10.1021/ma2000916 (2011).
- 44 Zheng, J., He, A., Li, J., Xu, J. & Han, C. C. Studies on the controlled morphology and wettability of polystyrene surfaces by electrospinning or electro spraying. *Polymer* **47**, 7095-7102, doi:10.1016/j.polymer.2006.08.019 (2006).
- 45 Reneker, D. H. & Yarin, A. L. Electrospinning jets and polymer nanofibers. *Polymer* **49**, 2387-2425, doi:10.1016/j.polymer.2008.02.002 (2008).
- 46 Ding, B., Li, C. R., Miyauchi, Y., Kuwaki, O. & Shiratori, S. Formation of novel 2D polymer nanowebs via electrospinning. *Nanotechnology* **17**, 3685-3691, doi:10.1088/0957-4484/17/15/011 (2006).

## CHAPTER 3: DETERMINING THE ROLE OF NON-IONIC SURFACTANT LOCATION AND CHEMISTRY IN ELECTROSPINNING

### 3.1 INTRODUCTION

Surfactants are powerful components in an electrospinning solution, altering the characteristics of the solution and stabilizing immiscible components. Surfactants are amphiphilic molecules containing both a hydrophilic and a hydrophobic region, allowing them to reside at the interface of two fluids and will generally lower surface tension or interfacial tension depending on phase composition. Surfactants are added to electrospinning solutions for a variety of reasons, such as controlling fiber morphology<sup>1-3</sup>, surface topography<sup>4,5</sup> and hydrophobicity<sup>6-8</sup>, diameter<sup>9,10</sup>, internal architecture<sup>4,11</sup>, to increase solution conductivity<sup>12,13</sup>, and to stabilize emulsions<sup>5,10</sup>.

Establishing the mechanism of electrospinning is key to understanding the effects of surfactant within the system. During electrospinning, a polymer solution is extruded out of a needle tip from a syringe. The droplet remains at this needle tip until sufficient voltage is applied to the polymer solution to overcome the surface tension of the droplet and create a continuous, cylindrical polymer jet. Surface tension on the outside of the fiber during electrospinning remains, and without sufficient voltage to elongate the cylindrical jet or polymer to maintain the shape, the polymer jet will form droplets due to surface tension conserving energy in the most thermodynamically stable shape, which is a sphere. This can result in either electrospaying droplets towards the electric field or beading morphology along the electrospun fibers. Beads within electrospun fibers are generally undesirable because they are difficult to reproduce, reduce encapsulation efficiency, and produce mesh with lower mechanical properties.<sup>14</sup>



Surfactants will impact the fundamental force balance the fiber experiences, as well as its geometry during electrospinning. When surfactant is added to a polymer solution used in electrospinning, it will generally reduce the surface tension. In addition to potentially reducing beading morphology in fibers, this also affects fiber diameter and other morphological characteristics. These effects can be understood based on general principles described by Wang et al.<sup>12</sup> Focusing on the droplet of polymer solution at the needle tip, Newton's second law can be applied (Equation 3.1):

$$F_E - F_S = ma \quad (\text{Eq. 3.1})$$

Where  $F_E$  is the electric force from the applied voltage,  $F_S$  is the surface tension in the droplet,  $m$  is the mass of the solution in the droplet, and  $a$  is the acceleration of the droplet. When surfactant is added to the system, it reduces surface tension. When the applied voltage in a system is held constant, the  $F_E$  term and the mass does not change. Therefore the reduction in surface tension increases the acceleration of the jet. This increase may then reduce flight time of the jet, thus resulting in less time for solvent to evaporate. Increased acceleration may also influence the diameter. According to conservation of mass during electrospinning (Equation 3.2):

$$\pi r^2 \rho \mu = Q \quad (\text{Eq. 3.2})$$

where  $r$  is the radius of droplet leaving the needle,  $\rho$  is the density,  $\mu$  is the velocity of the jet, and  $Q$  is the flow rate of the extruded polymer solution. A correlation between the radius of the fiber and the velocity can be made in a system where the flow rate, density, and geometry of the needle remain constant (Equation 3.3).

$$r \propto \mu^{-\frac{1}{2}} \quad (\text{Eq. 3.3})$$

Since acceleration is the rate of change of velocity, the radius is anticipated to decrease as acceleration increases. The decrease in radius is likely a result of thinning of the jet at the Taylor Cone.

This relationship is generally true for surfactants that do not affect the charge of the polymer solution. Surfactants are chemically categorized as cationic, anionic, or non-ionic. Cationic surfactants have a positive charge, anionic surfactants have a negative charge, and non-ionic surfactants have no charge. Therefore, surfactant is sometimes added to electrospun systems to reduce the surface tension and reduce beading effects or alter the conductivity of an electrospinning solution. Surfactants that increase overall solution conductivity may also lead to an increase in charge and potentially more stretching of the fiber and greater resistance to beading morphology.<sup>2</sup>

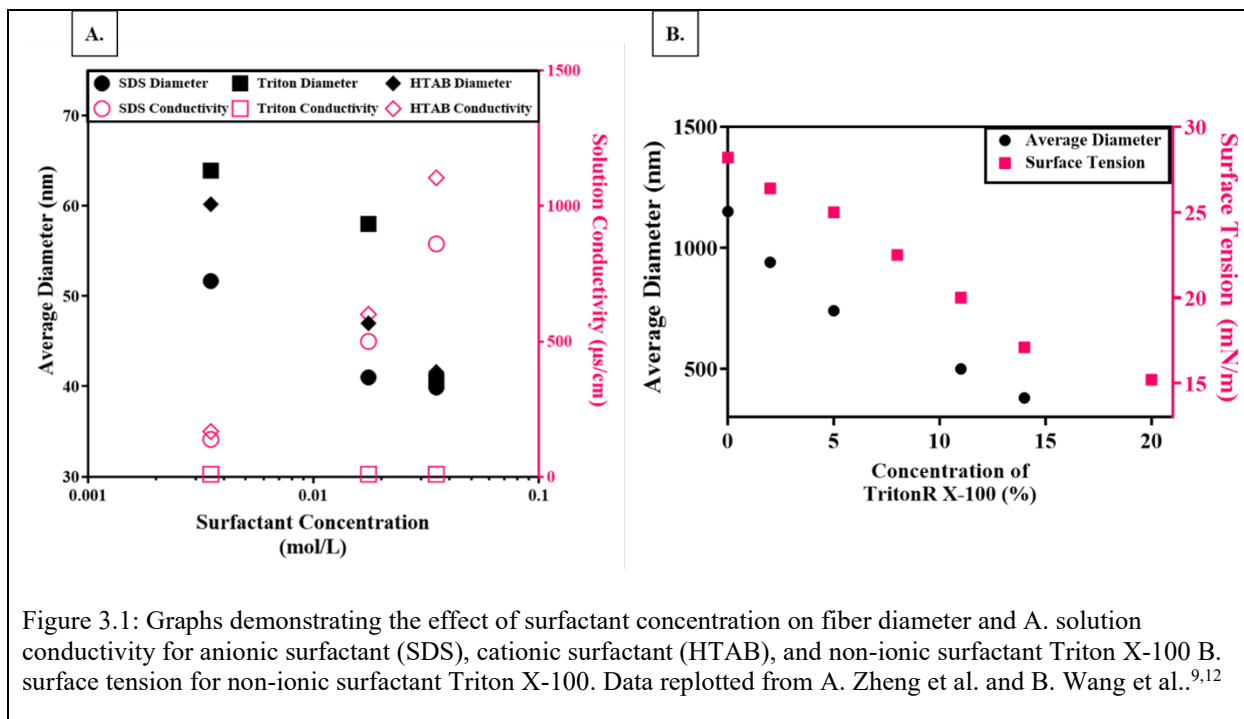
In a study by Lin et al., cationic and non-ionic surfactants were added to PS solutions and electrospin fibers.<sup>2</sup> This study found that cationic surfactants increased the overall conductivity of the system and eliminated bead morphology. This study also showed that non-ionic surfactants at the concentrations used reduced but did not eliminate beading morphology. In a similar study by Aykut et al., cationic surfactant was added to a polymer solution containing PAN for electrospinning and found that a cationic surfactant resulted in increased beading morphology.<sup>3</sup> Aykut attributed this increase in beading morphology to a decrease in solution viscosity with surfactant addition. However, in a study by Jia et al., increasing the concentration of cationic, anionic, and non-ionic surfactants in a PVA solution resulted in either an increase or no change in

solution viscosity.<sup>15</sup> The increase or no change in solution viscosity was also seen in other polymer solutions such as Kriegel et al. with Chitosan, Talwar with PEO, and Nilsson with HMHEC.<sup>16-18</sup>

The data from Aykut is helpful because it also offers an alternative explanation that the charge of the cationic surfactant increased the overall conductivity of the system into an unstable region that resulted in jet expulsion of droplets. This indicates that the chemistry of the surfactant, independent of surface tension, may play a critical role in fiber diameter and morphology of fibers fabricated with surfactants.

Zheng et al. studied the effects of the concentration of a cationic surfactant HTAB, anionic surfactant SDS, and non-ionic surfactant Triton X-100 on polyvinylidene fluoride electrospun fibers.<sup>9</sup> When increasing concentrations of each type of surfactant were added to the system, fiber diameter decreased (Figure 3.1A). Solution conductivity also increased with increasing cationic and anionic surfactants while remaining the same for the non-ionic surfactant. This study further supports that surfactant addition still results in a decreased fiber diameter in the absence of charge effects.

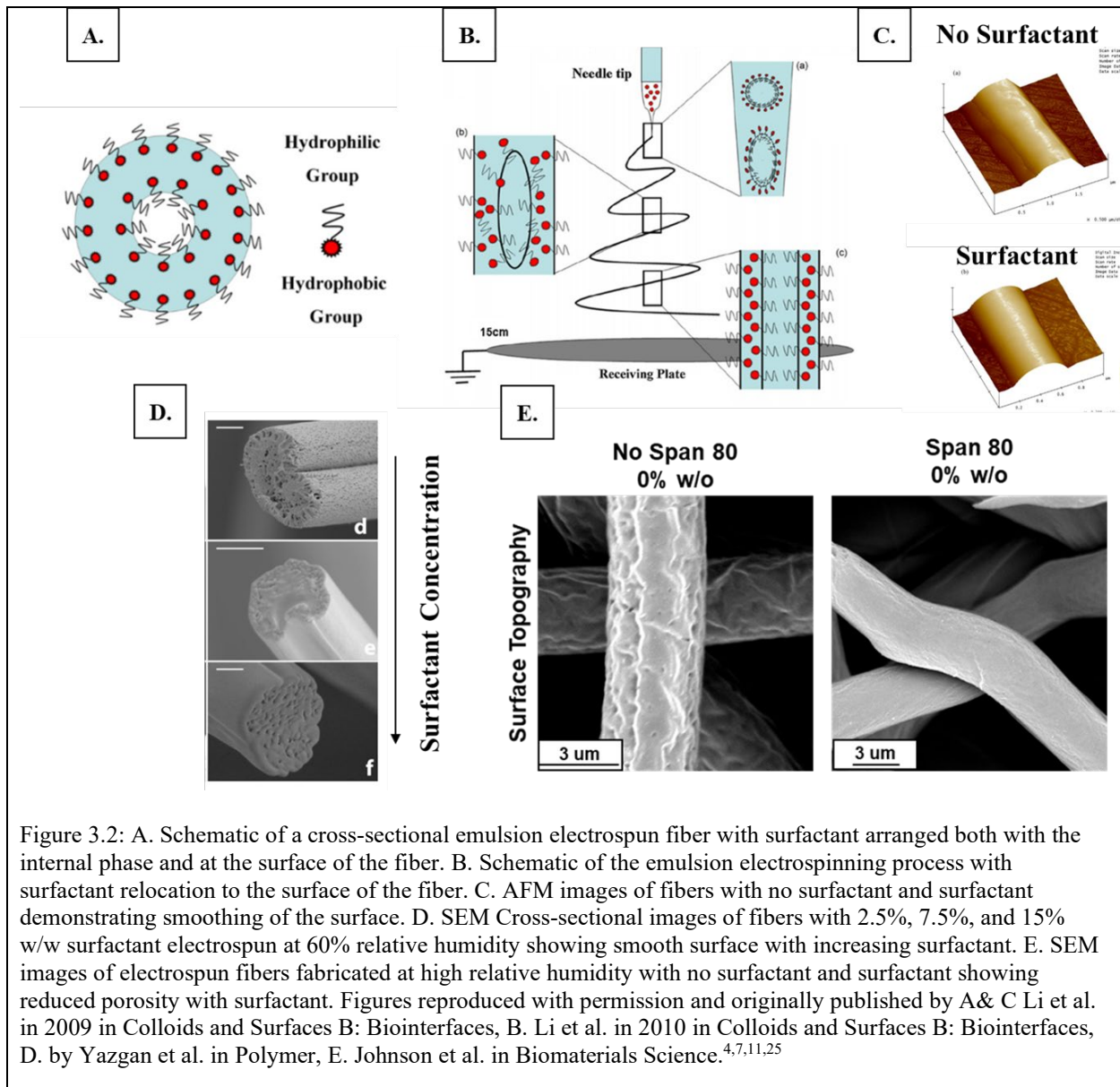
This relationship is further supported by a study conducted by Wang et al. demonstrating the relationship between non-ionic surfactant Triton X-100 concentration, solution surface tension, and mesh average fiber diameter in fibers fabricated with PVDF (Figure 3.1B).<sup>12</sup> This trend in fiber diameter and surface tension with increasing concentration of Triton X-100 was also seen in coaxial fibers electrospun with polyacrylonitrile by Yu et al.<sup>19</sup> Decreases in both fiber diameter and surface tension with increasing concentrations of surfactant may support a correlating relationship between decreasing surface tension and decreasing fiber diameter.



Surfactants have been classified by their hydrophobic lipophilic balance (HLB), first described by William Griffin.<sup>20,21</sup> The HLB for an individual surfactant is calculated by the strength and size of chemical species within a surfactant molecule. The HLB value ranges from 0-30, with molecules containing more hydrophilic species calculated as higher HLB numbers. Griffin and Davies categorized surfactants with HLB ranges 3.5-6 as w/o emulsifiers, 7-9 as wetting agents, 8-18 as o/w emulsifiers, 13-15 as detergents, and 15-18 as solubilizers.<sup>21,22</sup> HLB is a good preliminary indicator for non-ionic surfactant behavior and has been correlated to coalescence and emulsification that can be used for more rigorous formulation studies.<sup>22-24</sup>

Surfactants are amphiphilic molecules and therefore are often found at the interface of two fluids with different polarities. Interestingly, adding surfactant to solvent and emulsion solutions used for electrospinning can alter the surface topography, hydrophobicity, and internal architecture of the resultant fibers, potentially due to surfactant relocating to the solvent-air interface.<sup>4,6,7,10,11,25</sup>

Li et al. was one of the first to publish this phenomenon and hypothesized that in emulsion electrospun fibers containing poly(L-lactide-co-ε-caprolactone) (PLLACL) and the surfactant Span 80, the surfactant relocated to the surface of the fibers in addition to the water-oil interface (Figure 3.2A-B).<sup>7,25</sup> This study also mapped the surface of individual fibers with atomic force microscopy (AFM), which showed that fibers containing surfactant had a more smooth surface compared to fibers without surfactant (Figure 3.2C).<sup>7</sup> Li, however, fails to disclose the relative humidity, which is known to play a prominent role in the surface topography of fibers, used to fabricate all samples.<sup>26-28</sup> Yazgan et al. was one of the first to publish the shift in surface topography of emulsion electrospun fibers with increasing surfactant concentration.<sup>11</sup> This study showed that at 60% relative humidity with non-ionic surfactant Span 80, surface topography transitions from porous to smooth with increasing surfactant concentrations (Figure 3.2D). Published studies from this body of work show clear images of the surface topography of monolithic electrospun fibers with and without surfactant Span 80 at 50% relative humidity.<sup>4</sup> This study showed that the porous topography of fibers could be eliminated to create smooth fibers with surfactant addition (Figure 3.2E).



Li et al. further showed that surfactant was relocating to the surface of the fiber by measuring the contact angle of water droplets on the surface of mesh with and without surfactant.<sup>7</sup> This is because surfactants decrease surface tension through contact with the water droplet. Water droplets placed on fibers without surfactant decreased in size marginally within the first eight seconds, while fibers with surfactant absorbed the water droplet within eight seconds (Figure 3.3A). This work was continued by Vasita et al., who showed that increasing the concentration of

non-ionic surfactant, Pluronic F-108, in a PLGA monolithic electrospun fibers increased the rate of absorption of water droplets shown through contact angle (Figure 3.3B).<sup>8</sup> PLGA fibers containing no surfactant remained approximately constant at a contact angle of 120° for at least 140 seconds (Figure 3.3B). Beigmoradi et al. further demonstrated that hydrophobicity of the overall mesh could be controlled with surfactant concentration, and fiber surface roughness and mesh porosity could be altered through the use of different solvents (Figure 3.3C).<sup>6</sup> Similar to Vasita's results, contact angle decreases with increasing concentration of surfactant, further supporting the hypothesis that surfactant is present at the surface of the fibers. Beigmoradi also shows mesh porosity and fiber porosity, or roughness, also play a role in the contact angle of fibers. This can be controlled using different solvents when electrospinning. Mesh porosity is directly correlated to mesh volume fraction, and its relationship with contact angle in electrospun fibers is thoroughly discussed in a paper by Szewczyk et al.<sup>29</sup>

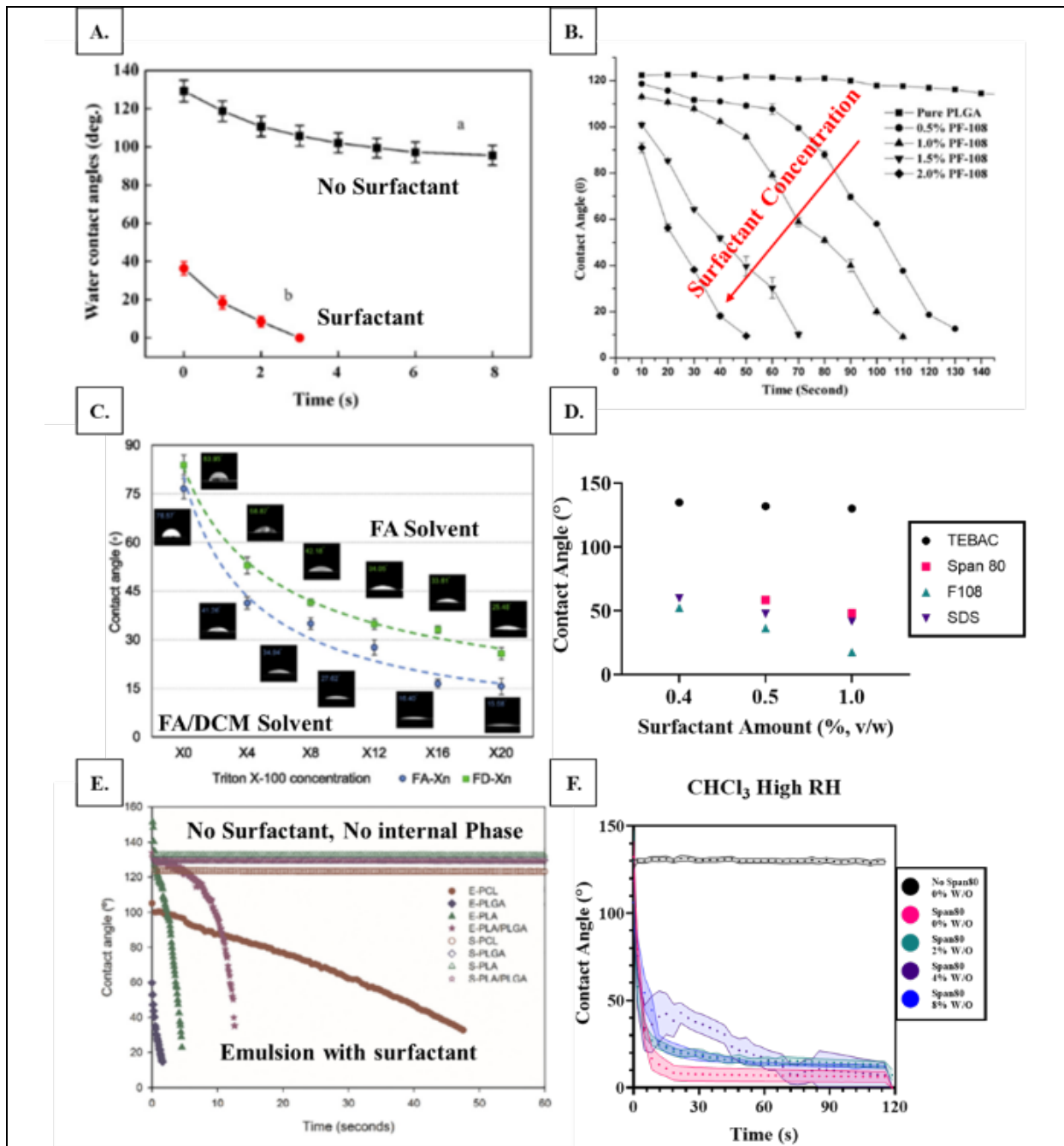


Figure 3.3: Graphs of water droplet contact angle on electrospun fibers versus A. time for samples with and without surfactant, B. time for increasing concentration of surfactant, C. concentration of non-ionic surfactant Triton-X fabricated with solvents formic acid (FA) and 2:1 FA: DCM, D. concentration of cationic surfactant TEBAC, anionic surfactant SDS, and non-ionic surfactants Span 80 and Pluronic F108, E. time for samples fabricated with no surfactant and no internal phase and with Span 80 and 4% w/o internal phase all with polymers PCL, PLGA, PLA, and 7:3 PLA: PLGA. Figure D replotted from data provided by Hu et al.<sup>10</sup> The other figures were reproduced with permission and originally published by A. Li et al. in Colloids and Surfaces B: Biointerfaces, B. Vasita et al. in Polymer, C. Beigmoradi et al. in Polymer, E. Coimbra et al. in Material Science & Engineering C, F. Johnson et al. in Biomaterials Science.<sup>4,6,8,30,31</sup>



Hu et al. studied the effect of surfactant concentration in emulsion electrospun systems with anionic, cationic, and non-ionic surfactants. Except for surfactant TBAC, which only marginally decreased contact angle, increasing surfactant concentration lowered the initial contact angles for all surfactant types (Figure 3.3D).<sup>10</sup> Coimbra et al. continued this work comparing contact angle over time in systems with no surfactant and no internal phase to systems with internal phase and surfactant with different polymer types.<sup>31</sup> All fibers electrospun with no surfactant and no internal phase did not show water absorption within one minute, while all samples electrospun as an emulsion with internal phase and a surfactant absorb the water droplet within one minute (Figure 3.3E). Interestingly, the rate of absorption of the water droplet changed with different types of polymer, despite control samples having similar contact angles. This suggests that surfactant interaction with polymer may affect the concentration at the surface of the fiber. All emulsion electrospun samples also had different fiber diameters indicating that the surface area of the fibers was different, and this potentially could have affected the rate of water absorption into the mesh. Fiber volume fraction and trapping of air can also affect contact angle absorption.<sup>32</sup> Published studies included in this chapter show the effect of internal phase volume fraction on samples containing no surfactant and surfactant-containing internal phase volume fractions of 0, 2, 4, and 8% w/o electrospun at 50% relative humidity.<sup>4</sup> This study further supports that within emulsion electrospinning systems, location of surfactant at the surface of the fibers may be reduced as surfactant prefers the internal water-oil interface compared to the surface oil-air interface (Figure 3.3F).

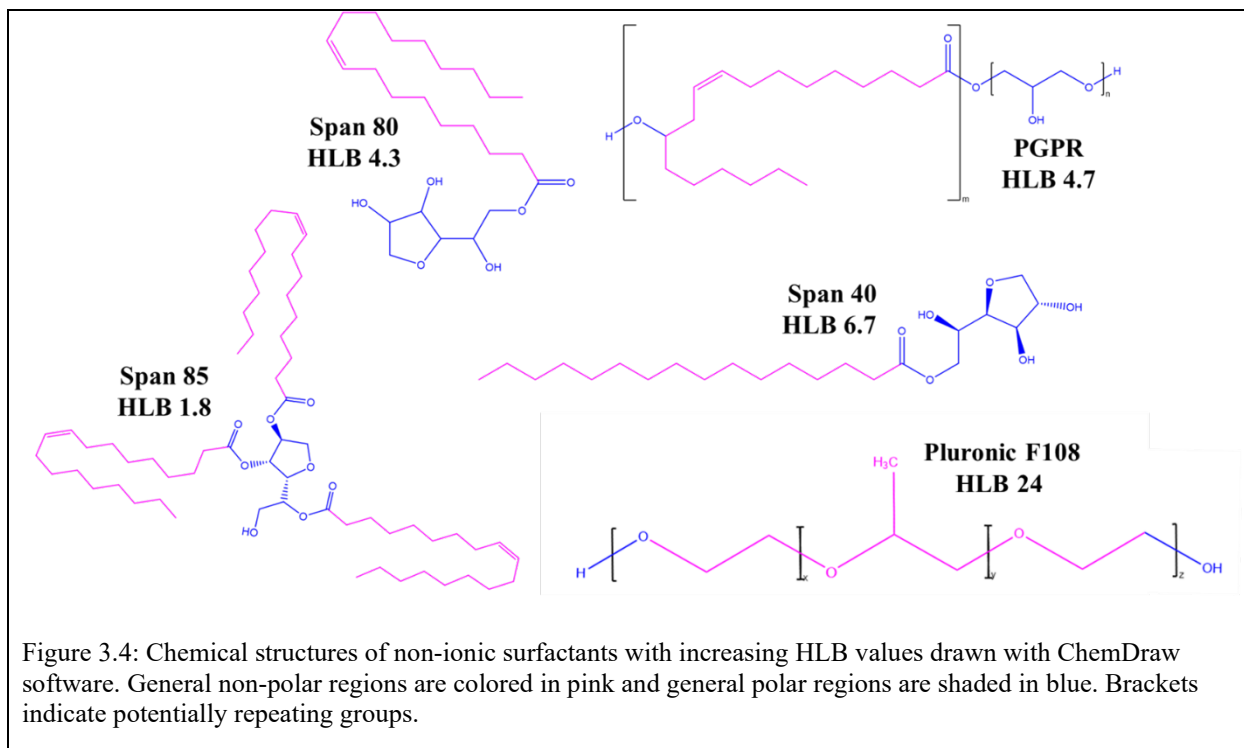
Altering the overall mesh hydrophobicity with surfactants has focused on systems with a single solvent or within emulsion systems at a set internal phase volume fraction. The relocation

of surfactant in systems with different solvents has not been fully explored. Furthermore, the relocation of surfactant with increasing volume fractions of the internal phase competing for surfactant saturation at high and low relative humidity had not been fully considered until the recently published study from the Robinson Lab.<sup>4</sup> This work is further expanded upon in this chapter. Further, while many previously published studies focus on effects of surfactants with different charges such as cationic, anionic, and non-ionic surfactant comparisons, the chemistry of non-ionic surfactants is an area for further discovery. This study also evaluates how changes in non-ionic surfactant chemistry, as characterized by HLB, affect monolithic and emulsion electrospun fiber properties. The goal is to understand the effects that surfactant plays in monolithic and emulsion electrospinning and control mesh characteristics with solution chemistry.

## **3.2 MATERIALS AND METHODS**

### **3.2.1 Materials**

PCL (50,000  $M_w$ ) was purchased from CAPA lot # 120625. Sorbitan monooleate (Span 80) was purchased from Sigma Aldrich lot # MKCF4138. Poly(ethylene glycol)-block-poly(propylene glycol)-block-poly(ethylene glycol) (Pluronic-F108) was purchased from Sigma Aldrich lot # MKBV1257V. Sorbitan monopalmitate (Span 40) was purchased from TCI Chemicals lot # FJTHK-IQ. Polyglycerol polyricinoleate 4125 (PGPR) was donated from Palsgaard batch # 31076104. Sorbitan trioleate (Span 85) was purchased from Sigma Aldrich lot # MKCF1009. Solvent N, N-Dimethylformamide anhydrous with 99.8% purity was purchased from Sigma Aldrich lot # SHBJ7641. Chloroform solvent with  $\geq 99.5\%$  purity was purchased from Sigma Aldrich lot # SHBL1580. Methanol with 99.9% purity was purchased from Sigma Aldrich lot # 065112. Red and blue food coloring from McCormick was used for bulk emulsion stability studies. The chemical structures for all surfactants used in these studies can be found in Figure 3.4.



### 3.2.2 Polymer Solution Fabrication

#### 3.2.2.1 Surfactant Location Studies

For studies on surfactant location within the fiber, 20% w/v PCL was dissolved in  $\text{CHCl}_3$ , 3:1  $\text{CHCl}_3$ : DMF, or 3:1  $\text{CHCl}_3$ : MeOH. Polymer solutions were mixed on the stir plate for at least an hour at a mixing rate of 250 rpm. After this hour, no solid polymer was observed in the solution. Each solution was also prepared with controls containing 30% w/w Span 80. To understand the relocation of surfactant in emulsions systems with increasing internal phase, the internal phase was added to the solutions at internal phase volume fractions of 2, 4, and 8% w/o. Internal phase was added in increments of 20  $\mu\text{L}$ , and after each addition, the emulsion was mixed with a FlackTek Speed Mixer DAC 150.1FVZ-K for 30 seconds at a speed of 2500 RPM.

### 3.2.2.2 HLB studies

Polymer solution used for bulk stability studies had 20% w/v PCL dissolved in either  $\text{CHCl}_3$  or 3:1  $\text{CHCl}_3$ : DMF solvent. Internal phase was added to the  $\text{CHCl}_3$  solution at 8% w/o and added to the 3:1  $\text{CHCl}_3$ : DMF at an internal phase volume fraction of 4% w/o. Polymer solutions used for viscosity studies and electrospinning studies had 20% w/v PCL dissolved in  $\text{CHCl}_3$  with no surfactant as a control and 30% w/w surfactant Span 85, Span 80, PGPR, Span 40, and Pluronic F108. Polymer solutions used for emulsion electrospinning had 20% w/v PCL dissolved in  $\text{CHCl}_3$  with 30% w/w surfactant Span 85, Span 80, PGPR, Span 40, and Pluronic F108 and 8% w/o internal phase as water. Internal phase was added in increments of 20  $\mu\text{L}$ , and after each addition, the emulsion was mixed with a FlackTek Speed Mixer DAC 150.1FVZ-K for 30 seconds at a speed of 2500 RPM.

### 3.2.3 HLB Emulsion Stability Studies

Polymer solutions with 8% w/o in  $\text{CHCl}_3$  were analyzed by bulk analysis for visual separation of water and oil by taking pictures of the emulsions at time points of 0 mins, 10 mins, 20 mins, 30 mins, 40 mins, 50 mins, 1 hour, 2 hours, 3 hours, and 24 hours. Internal phase was dyed with blue food coloring for clear visualization. Emulsion stability was also assessed for samples containing solvent 3:1  $\text{CHCl}_3$ : DMF with 4% w/o internal phase dyed red to visualize separation. Samples with this composition were imaged at time points of 0 mins, 2 mins, 30 mins, 1 hour, 2 hours, 3 hours, 24 hours, 48 hours, 1 week, and 2 weeks. Emulsions fabricated with 3:1  $\text{CHCl}_3$ : DMF with 4% w/o internal phase were also imaged with a Zeiss microscope at 20x magnification to determine emulsification of internal phase and coalescence over three hours. To better visualize the emulsion droplets, images were processed with ImageJ to split color for red (the internal phase), and then the brightness and contrast were adjusted. Original images are

included in Figure 3.33 of the appendix. All studies were performed in triplicate and conducted with no surfactant as a control and with surfactants Span 85, Span 80, PGPR, Span 40, and Pluronic F-108.

### 3.2.4 Viscosity

Viscosity was measured for solutions containing surfactants Span 85, Span 80, PGPR, Span 40, and Pluronic F-108. A TA Instruments AR-2000 rheometer was used to measure viscosity with a 40 mm flat plate, shear ramp-up rate of 0.1-50 s<sup>-1</sup>, and gap distance of 1000 μm. The theoretical shear rate at the needle tip was calculated with Equation 3.4.

$$Shear\ Rate = \frac{Q}{(\pi r^2)L} \quad (Eq. 3.4)$$

Where  $Q$  is the flow rate,  $r$  is the radius, and  $L$  is the length of the needle.

### 3.2.5 Electrospun Scaffold Fabrication

#### 3.2.5.1 Surfactant Location Studies

Electrospinning parameters were held constant with a Harvard Apparatus pump flow rate of 0.5 mL/h, a needle tip to collection plate of 25 cm, an applied voltage of 15 kV from a Gamma High Voltage Research power supply model number ES30P-SW, and a blunted 21-gauge needle. Samples were electrospun at high and low relative humidity of 50% ± 10% and 10% ± 10%, respectively, to evaluate the influence of ambient water moisture on fiber collection. At high relative humidity, specimens were electrospun directly onto the copper collection plate, which was grounded both to the voltage source and to the fume hood. After each specimen was collected, it was carefully removed from the collection plate and left to dry fully in the fume hood overnight. The collection plate was wiped down with chloroform followed by water before thoroughly drying between each specimen collection. Previous studies had demonstrated that delamination of the

electrospun mesh and partial sticking to the collection plate could occur at low relative humidity. Therefore, the collection plate was covered in aluminum foil at low relative humidity with the grounding alligator clip wire attached to the collection plate over the foil. Specimens were further dried in a vacuum chamber before further characterization. Fibers with cross-sections were analyzed by freezing mesh in liquid nitrogen and fracturing to image cross-sections. Cross-sections were also coated with 8 nm of iridium. At least three specimens were fabricated per sample group.

#### *3.2.5.2 HLB Studies*

Electrospinning parameters were held constant with a Harvard Apparatus pump flow rate of 1.8 mL/h, a distance needle tip to collection plate of 33 cm, an applied voltage of 18 kV from a Gamma High Voltage Research power supply model number ES30P-SW, and a blunted 21-gauge needle. Samples were electrospun at lower relative humidity of  $20\% \pm 5\%$  to minimize the effect of vapor induced phase separation. Samples were electrospun for 20 minutes. After each sample was collected, it was left to fully dry in the fume hood overnight on the aluminum foil. At least three specimens were fabricated per sample group.

#### **3.2.6 Fiber Characterization**

Mesh was analyzed using a Phenom Pro Desktop scanning electron microscope (SEM) to capture fiber morphology, surface topography, and diameter. All samples were coated with 8 nm of iridium before imaging. Fiber morphology was assessed for overall homogeneity and appearance of wet fibers. Fiber topography was determined through visual assessment and captured for samples electrospun at high relative humidity by imaging with 10 kV accelerating voltage, a backscatter detector, and at a magnification of 25,000x.

Fiber diameter and fiber volume fraction or mesh porosity was determined by imaging each sample specimen in five different locations using 10 kV of accelerating voltage and a backscatter

detector. Locations were selected for each of the four corners of the square specimen and the central location.

Each image was then analyzed with the software ImageJ using the plugin DiameterJ. From this initial segmentation, binary-colored segmented images produced with the algorithms M3, M5, M7, S2, S3, and S7 were used to determine fiber diameter and fiber diameter distribution using DiameterJ. In a few rare cases, DiameterJ was unable to process a segmented image, in which case a segmented image produced with an un-used algorithm that was judged to be most representative of the original image was substituted for further analysis.

The average fiber diameter for each algorithm was then used to determine the average fiber diameter per SEM image. These fiber diameters were then used for further statistical comparison between groups. For each overall set of sample parameters, fiber distribution histogram raw data, mean of fiber diameters, fiber diameters standard deviation, fiber skewness, and fiber kurtosis were also determined using DiameterJ.

These same, binary-colored, segmented images from ImageJ were used to calculate the fiber volume fraction, based on Szewczyk et al.. This equation is written out in Equation 3.5.<sup>32</sup> Each image had all of its white pixels, representing the fiber area, and all of the black pixels, which represent the void area, counted. The number of pixels representing fibers was divided by the total number of pixels and multiplied by 100 to calculate the percent fiber fraction.

$$Fiber\ Fraction = \frac{Fiber\ Area}{(Fiber\ Area + Void\ Area)} * 100 \quad (Eq. 3.5)$$

### 3.2.7 Contact Angle Analysis

Water contact angle was conducted on all groups to assess the effect of mesh properties on wettability. Mesh fabricated with no surfactant and surfactant with 0, 2, 4, and 8% water internal phase were used to determine contact angle over time. This was repeated for groups electrospun at high and low relative humidity and with solvents  $\text{CHCl}_3$ , 3:1  $\text{CHCl}_3$ : DMF, and 3:1  $\text{CHCl}_3$ : MeOH. Specimens were cut from the center of the mesh in approximately 1 cm  $\times$  2 cm rectangles and loaded with minimal wrinkles onto glass slides with double-sided tape. A Biolin Scientific Theta Lite 101 optical tensiometer was used to determine contact angle over 2 minutes at 30 frames per second. A droplet of ultra-pure water was placed on each of the dry mesh samples using a sessile drop technique, a glass syringe, and a blunted needle. The contact angle was analyzed using OneAttension software. For each run, time zero was determined at the time when the water droplet was released from the needle tip. Contact angle data across nine trials per sample parameter were pruned by averaging groups of one hundred measurements, equating to 3.33 seconds of collection time. Below 15°, the contact angle measurement software could not consistently resolve the difference between the baseline and the sample droplet, routinely producing large, erroneous spikes in measured contact angle. Therefore, after fifteen consecutive contact angle measurements below 15°, the droplet was considered fully absorbed, and the contact angle was set to 0° for the remainder of the two-minute collection.

### 3.2.8 Statistical Analysis

Fiber volume fraction per SEM image was determined with ImageJ and the plugin DiameterJ, as described above. Five images from each of three meshes fabricated with the same parameters were analyzed to give a total of fifteen data points per sample parameter. A one-way ANOVA with Brown-Forsythe and Welch tests was performed on each set of parameters,



respectively, to determine any statistical differences between the samples. This method was used for samples fabricated at high and low relative humidity.

Internal phase droplet size was performed by tracing ten internal phase droplets from microscope images at 20x magnification with ImageJ. Each emulsion was fabricated three times, and each was imaged and traced with ImageJ. The ferret diameter was determined from these tracings, and all droplet measurements for each set of parameters at 0 and 3 hours (n=30) were compared using a one-way ANOVA with Brown-Forsythe and Welch tests.

Fiber diameter per SEM image was also determined using ImageJ and DiameterJ, in the same way that fiber volume fraction was determined. A one-way ANOVA with Brown-Forsythe and Welch tests was performed on each set of parameters, respectively, to determine any statistical differences between the samples. Pairwise comparisons between fiber diameters of surfactant loaded samples with and without internal phase were also conducted. These comparisons used Welch's t-tests to determine statistical differences between samples with and without internal phase. All statistical tests and graphing were performed using Prism GraphPad software.

### **3.3 RESULTS AND DISCUSSION**

#### **3.3.1 Span 80 Relocation with Increasing Internal Phase Volume Fraction**

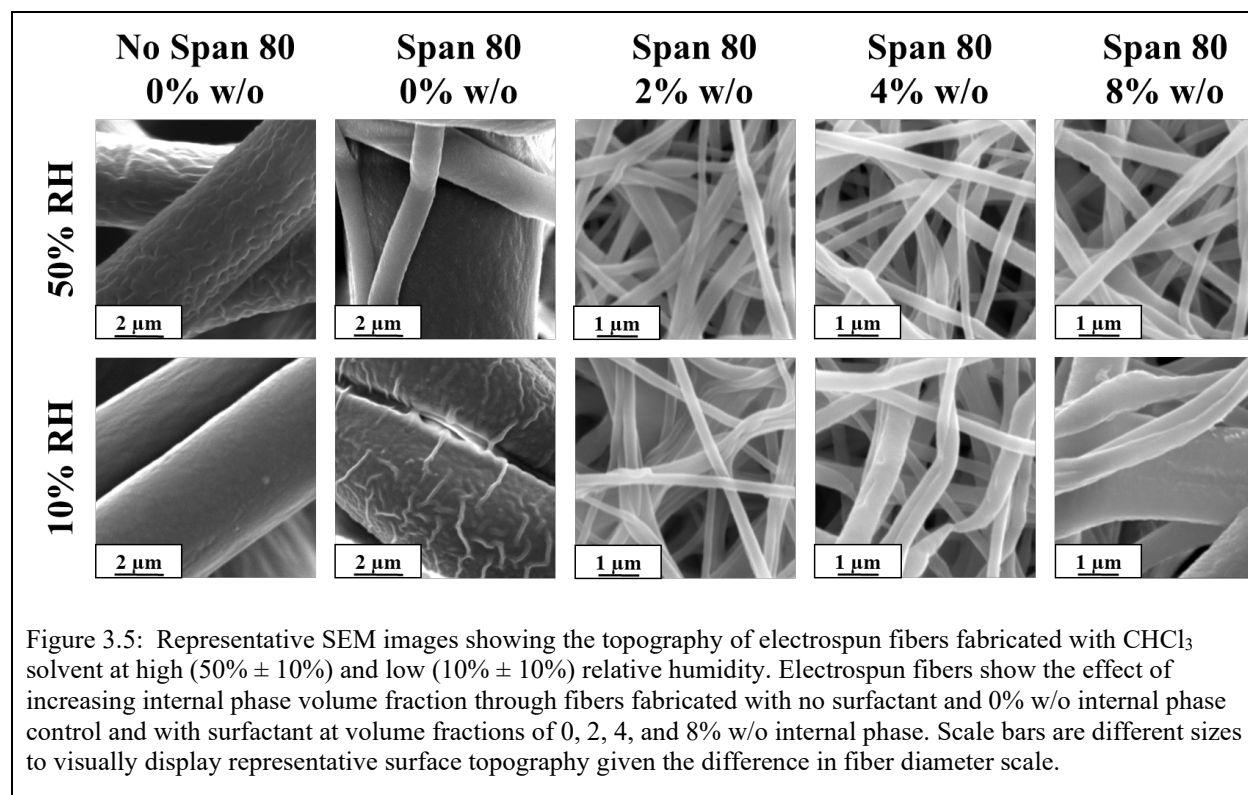
Surfactants were loaded into emulsion electrospun fibers with increasing internal phase volume fractions of 0, 2, 4, and 8% w/o to determine if surfactant relocation at the air interface changes with internal phase volume fraction and solvents used. In theory, as the internal phase volume fraction increases, more surfactant would relocate from the air-oil interface to the water-oil interface. This is because liquid water has a higher saturation of water than water droplets in the air, making it thermodynamically more favorable. This relocation may change with the solvent system used and in environments with high and low relative humidity. Surfactant relocation at the

surface of the fibers influences surface energy, and, therefore, when water droplets are placed on top of a surface, the surface tension decreases in the presence of the surfactant, causing the water droplet to absorb into the mesh. This is often seen in contact angle measurement studies.

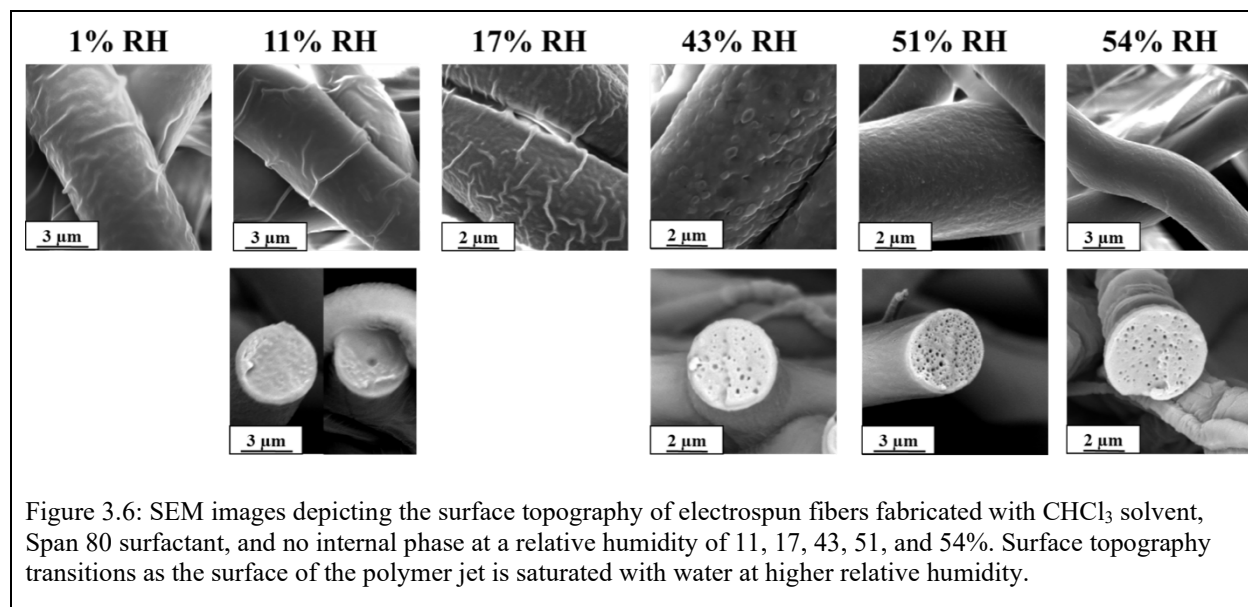
### 3.3.1.1 $\text{CHCl}_3$ Solvent System

#### 3.3.1.1.1 Surface Topography

Surface topography can change with different solvents evaporating at different rates, a single solvent evaporating at a rate that causes the shell of the fiber to contract or buckle inwards as it dries and as ambient water vapor interacts with the surface of the jet.<sup>26,27,33</sup> Fibers fabricated in  $\text{CHCl}_3$  were imaged with a SEM to determine surface topography. The surface topographies of samples fabricated with no surfactant and with surfactant at internal phase volume fractions of 0, 2, 4, and 8% w/o at both high and low relative humidity can be seen in Figure 3.5.



The topography of samples electrospun with  $\text{CHCl}_3$  solvent with surfactant and no internal phase exhibited an unexpected range of fiber topography within the bounds of high and low relative humidity depending on the exact relative humidity used to electrospin individual samples (Figure 3.6). During the electrospinning process, the surfactant likely relocated to the surface of the fiber at the oil-saturated air interface.<sup>4</sup> The system was fabricated with a hydrophobic polymer and a relatively hydrophobic solvent which would cause the surfactant to orient such that the hydrophilic head would be facing out of the fiber towards saturated air. This hydrophilic head oriented outward at the surface of the fiber would serve as an attractive surface to facilitate the condensation of water on the surface of the fiber.



At 43% relative humidity, fibers have a rough cactus-like surface topography (Figure 3.6). Zaarour et al. proposed a mechanism for cactus-like surface topography due to the formation of a strong sheath layer on the outside of the fiber.<sup>34</sup> This was followed by large differences in vapor pressure within the fiber of two different solvents, causing the solvent with higher vapor pressure to escape the fiber. This was followed by the solvent with the higher vapor pressure “erupting”

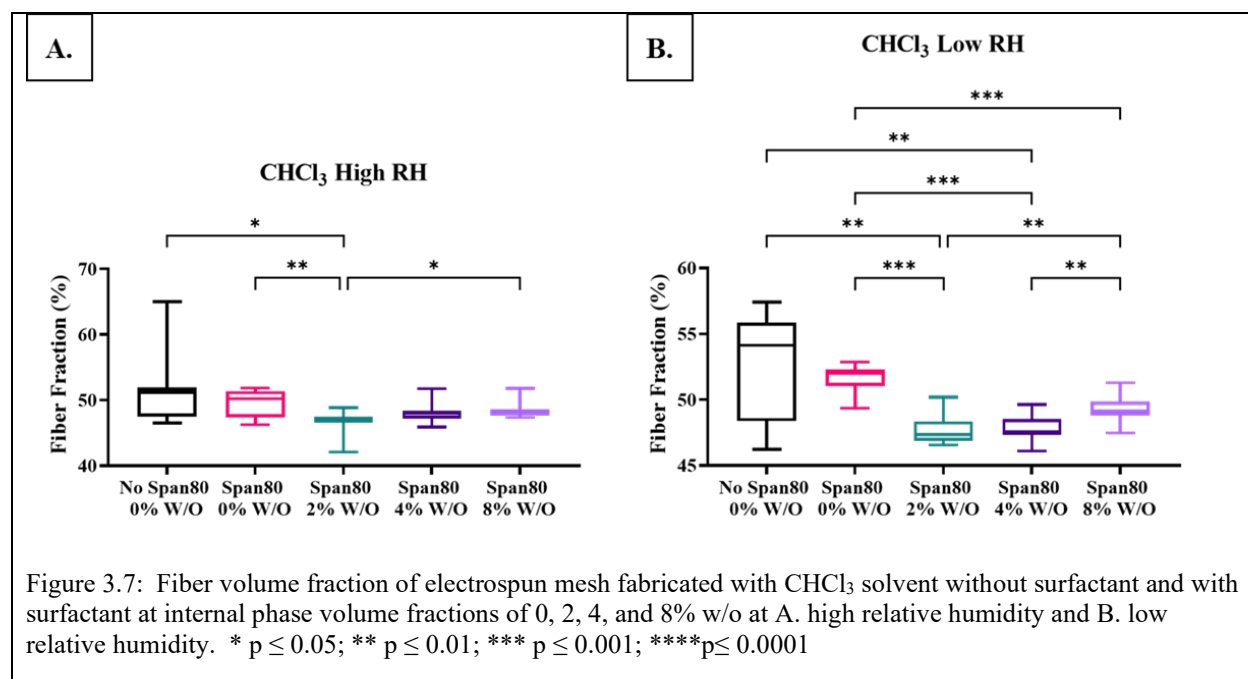
from weak points in the solid sheath, and the eruption points immediately precipitating into a cactus-like structure.<sup>34</sup>

At high relative humidity, the porous topography in the control sample with no surfactant and no internal phase was likely due to ambient water vapor condensing on the surface of the fiber, causing precipitation of polymer upon contact and templating the porous architecture via VIPS. As discussed in Chapter 2, chloroform is a hydrophobic solvent and, therefore, would provide more of a barrier preventing ambient hydrophilic water vapor from penetrating into the fiber. The smooth surface topography observed in samples with surfactant was likely due to both ambient water vapor encouraging surfactant to relocate at the oil-air interface at the surface of the fibers and surfactant allowing water vapor to penetrate into the fiber. Samples that were electrospun at a relative humidity of 1, 11, and 17% with surfactant and no internal phase had wrinkles or neck sections perpendicular to the longitudinal axis of the fiber. One potential mechanism to explain this phenomenon is at low relative humidity, solvent evaporates quickly from the fibers creating a solid outer shell. Surfactant in the system lowers surface tension which increases the jet's acceleration rate towards the plate. During this flight to the collection plate, a high strain rate is applied to the fiber with the solid shell resulting in some stretching and necking on the surface of the fiber creating the lateral wrinkle morphology. A similar lateral wrinkled morphology has been observed in electrospun fibers after undergoing mechanical strain rates.<sup>35,36</sup> Surface roughness plays a major role in mesh wettability, so it is crucial to understand and characterize surface roughness to create fibers with tunable roughness.

#### 3.3.1.1.2 Fiber Volume Fraction

In addition to surface roughness, the mesh porosity or fiber volume fraction plays an essential role in the wettability of an electrospun mesh. Within fiber meshes fabricated with  $\text{CHCl}_3$

solvent at high relative humidity, there were not major differences in the fiber fraction (Figure 3.7A). A few samples, however, were statistically different. The fiber fraction of meshes with no surfactant and no internal phase, with surfactant and no internal phase, and with surfactant and 8% w/o internal phase were all significantly different from meshes with surfactant and 2% w/o internal phase. Differences in fiber fraction may be due to differences in conductivity and solvent evaporation rate as discussed further in Chapter 4.

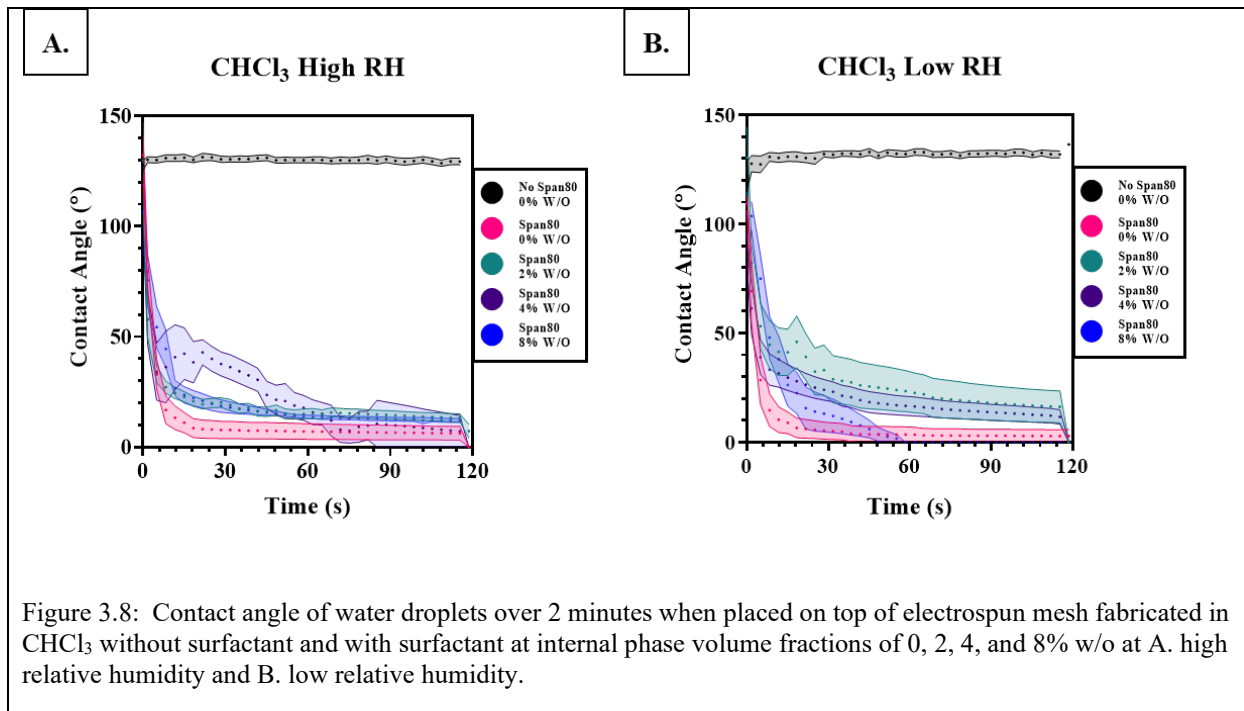


Among groups fabricated with CHCl<sub>3</sub> at low relative humidity, there were more significant differences between fiber volume fractions (Figure 3.7B). Meshes with no surfactant or internal phase were significantly different from meshes with surfactant and both 0% and 4% w/o internal phase. Meshes with surfactant and no internal phase showed significant difference from all other meshes fabricated with surfactant, while meshes with surfactant and 8% w/o internal phase were significantly different from those with surfactant and 2% and 4% w/o internal phase. In addition to the factors discussed above, differences in fiber fraction at low relative humidity may be from

a lack of interactions with water in the ambient air. This is because trapping of air between fibers can increase contact angle.<sup>32</sup>

#### 3.3.1.1.3 Contact Angle

To determine the effect of surfactant relocation to the oil-air interface during electrospinning, contact angle measurements were evaluated for each mesh fabricated with  $\text{CHCl}_3$  solvent. The contact angle of water on dry mesh fabricated at high relative humidity was determined for all groups over two minutes (Figure 3.8A). The PCL control meshes remained approximately constant at a contact angle of  $130^\circ$  due to the hydrophobicity of the polymer. The samples with Span 80 but no aqueous internal phase exhibited a rapidly decreasing contact angle within the first 30 seconds as the water droplet absorbed into the scaffold. The droplets on the samples with surfactant and internal phase also absorbed into the scaffold within the first 30 seconds, but at a slower rate than the sample without internal phase. The rapid decrease in contact angle when surfactant was present in the samples supports the hypothesis that surfactant is likely relocating to the surface of the fibers during electrospinning.



In samples with internal phase, surfactant is at the interior oil-water interface, lowering the surfactant concentration on the surface of the fibers. This is supported by the slower absorption of water into the mesh relative to the sample with surfactant and no internal phase. There is less moisture in the air at lower relative humidity, so the concentration of surfactant at the surface would not be expected to be as high as at high relative humidity, where it is thermodynamically favorable for surfactants to be at the oil-air interface. Representative images for samples electrospun at high relative humidity are shown in Figure 3.9.

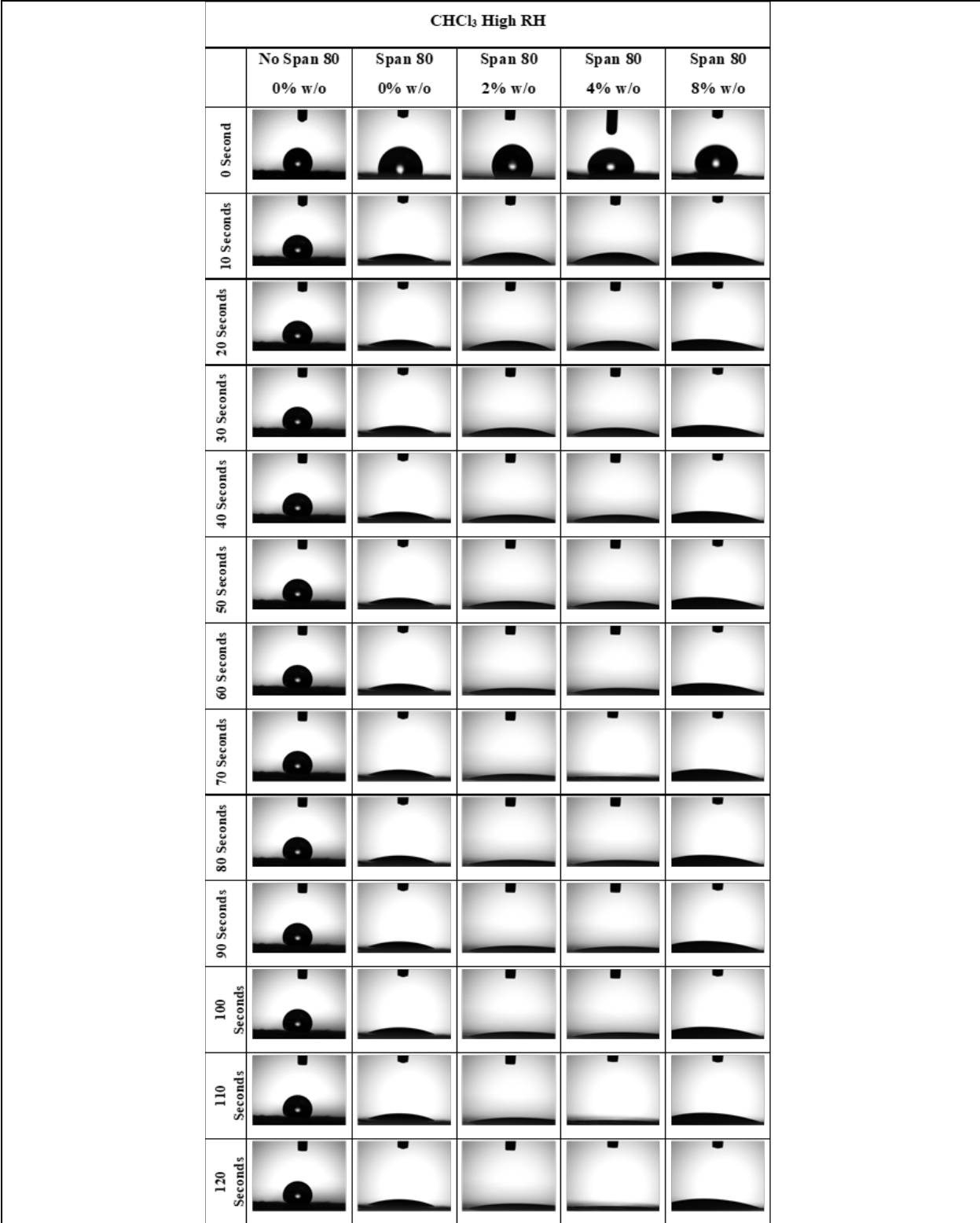


Figure 3.9: Images of representative contact angle captured for electrospun mesh fabricated with CHCl<sub>3</sub> at high relative humidity and containing no surfactant and surfactant with internal phase volume fractions of 0, 2, 4, and 8% w/o internal phase.



The contact angle of samples fabricated at low relative humidity exhibited similar behavior to those fabricated at high relative humidity (Figure 3.8B). The sample with no surfactant or internal phase did not absorb the water droplet within the two minutes, while samples absorbed the droplet with surfactant. Meshes with surfactant and internal phase did not absorb the droplet as quickly as the sample with surfactant and no internal phase. These results support the hypothesis that the surfactant is relocating to the surface of the fibers during electrospinning. Representative images of samples electrospun at low relative humidity are shown below (Figure 3.10).

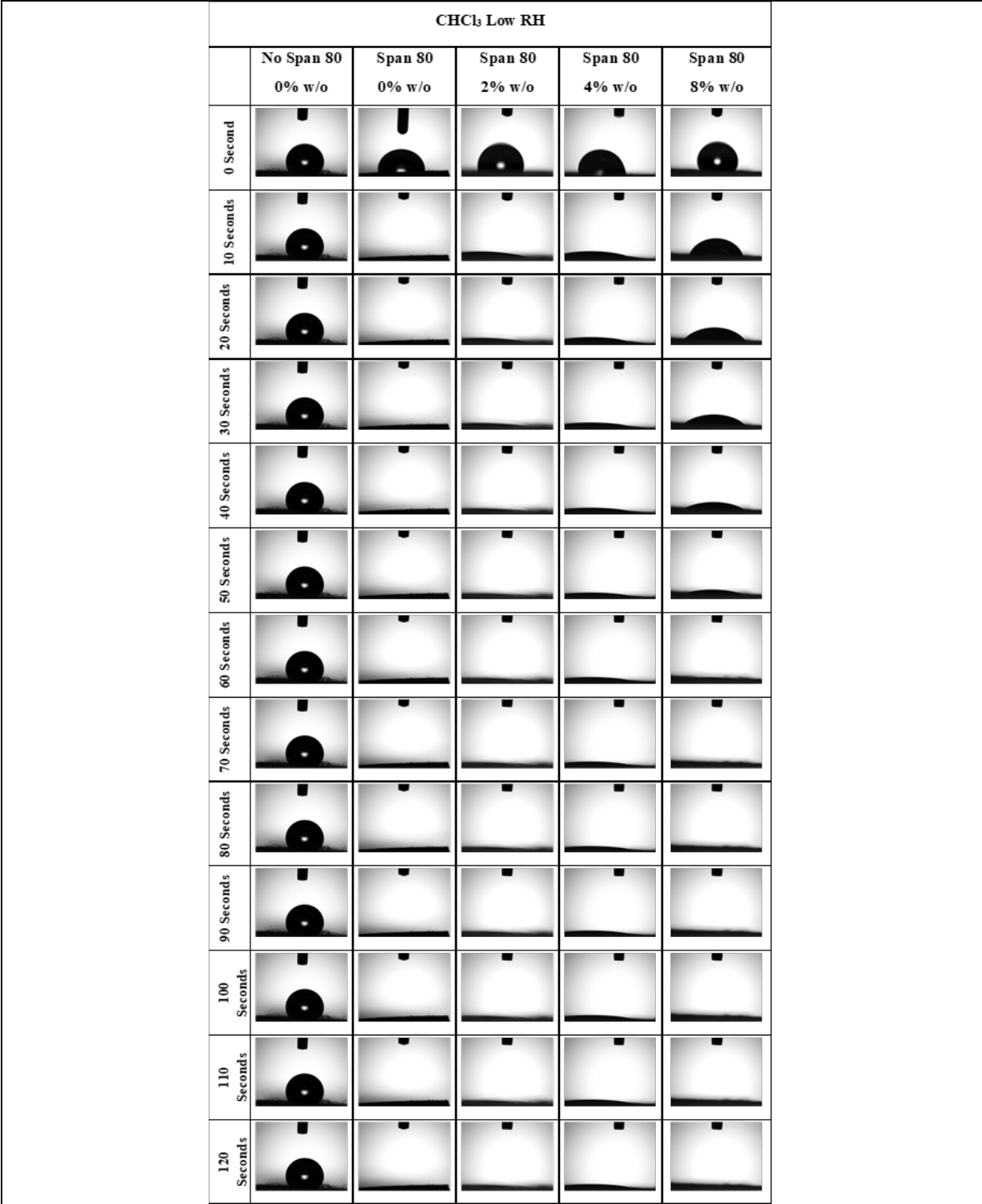
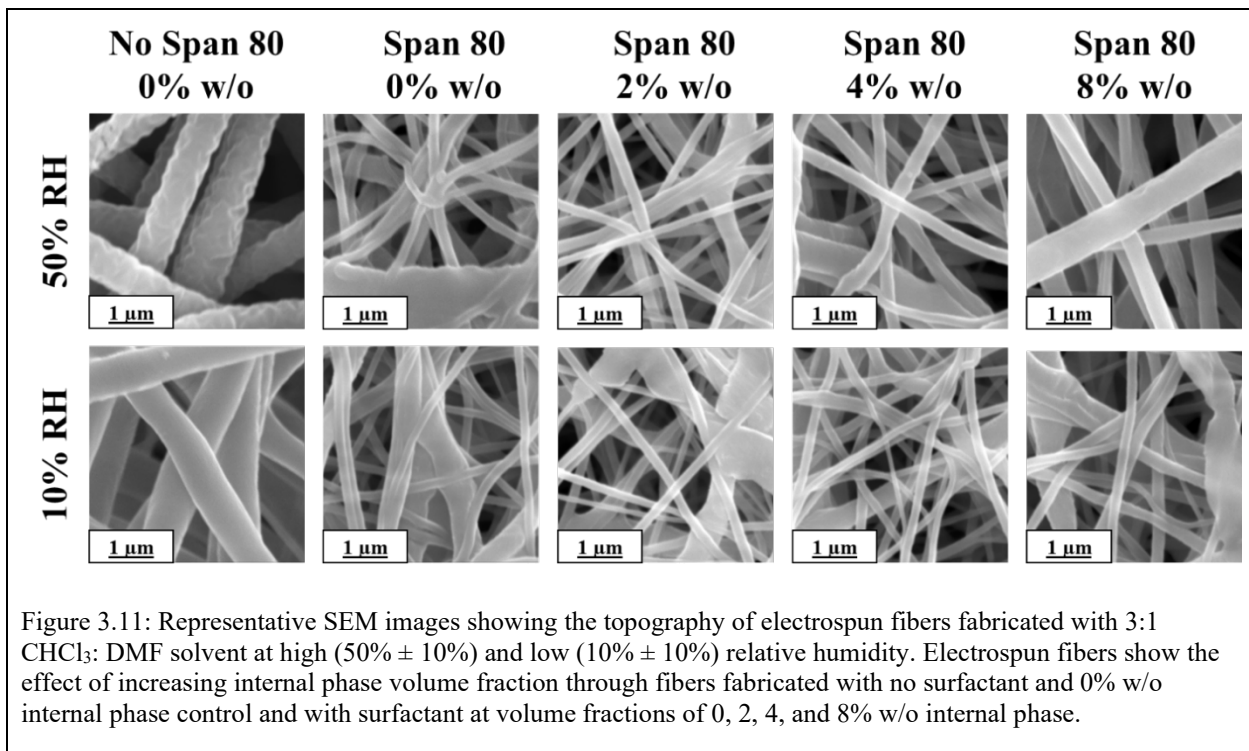


Figure 3.10: Images of representative contact angle captured for electrospun mesh fabricated with CHCl<sub>3</sub> at low relative humidity and containing no surfactant and surfactant with internal phase volume fractions of 0, 2, 4, and 8% w/o internal phase.

### 3.3.1.2 3:1 CHCl<sub>3</sub>: DMF Solvent System

#### 3.3.1.2.1 Surface Topography

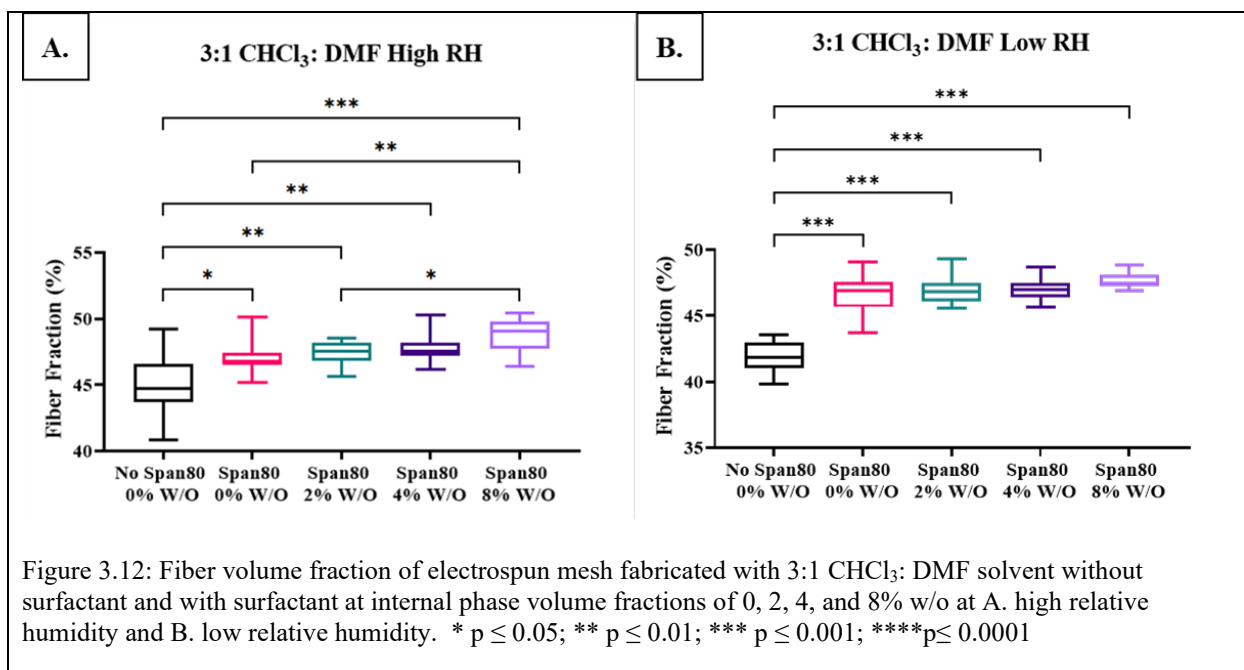
Surface topography for electrospun samples fabricated with 3:1 CHCl<sub>3</sub>: DMF at high and low relative humidity was assessed with SEM images (Figure 3.11). At high relative humidity, samples with no surfactant and no internal phase were wrinkled. Adding Span 80 resulted in smooth surface fibers by reducing phase separation that otherwise leads to water vapor condensation at the surface of the jet leading to the wrinkled phenomenon. At low relative humidity, the surface topography of fibers was smooth for samples fabricated without surfactant, with surfactant, and at internal phase volume fractions of 0, 2, 4, and 8% w/o.



#### 3.3.1.2.2 Fiber Fraction

Within samples fabricated with 3:1 CHCl<sub>3</sub>: DMF solvent at high relative humidity, the fiber fraction of the sample without surfactant or internal phase was significantly lower than the

fiber fractions of the samples with surfactant and internal phase (Figure 3.12A). There were also significant differences between the sample with surfactant and 8% w/o internal phase and the samples with surfactant and 0% and 4% w/o internal phase. These differences could be explained by potential stabilization of the core of the electrospun fibers as increasing amounts of internal phase were added. Studies conducted by others support this emulsion core stabilization.<sup>11,37,38</sup>



Similar behavior was observed in the samples fabricated at low relative humidity (Figure 3.12B). The sample without surfactant or internal phase was significantly lower than all other samples. This behavior could be explained by the same factors discussed in samples fabricated at high relative humidity.

### 3.3.1.2.3 Contact Angle

Contact angle measurements for the samples fabricated with 3:1 CHCl<sub>3</sub>: DMF solvent were evaluated to determine the effect of surfactant relocation to the oil-air interface during electrospinning. In samples fabricated at high relative humidity, the mesh without surfactant or

internal phase did not absorb the water droplet within two minutes (Figure 3.13A). The hydrophobicity of the PCL polymer could explain this.

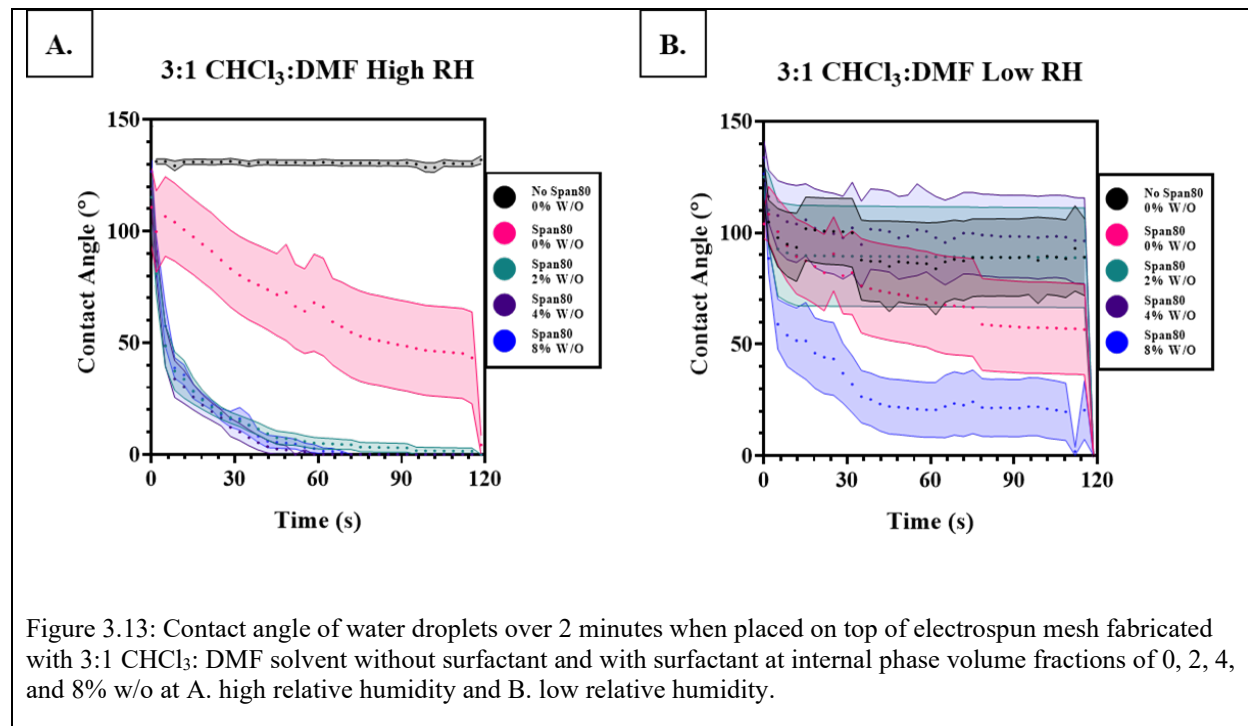


Figure 3.13: Contact angle of water droplets over 2 minutes when placed on top of electrospun mesh fabricated with 3:1 CHCl<sub>3</sub>: DMF solvent without surfactant and with surfactant at internal phase volume fractions of 0, 2, 4, and 8% w/o at A. high relative humidity and B. low relative humidity.

Contact angle absorption rate also changed between solvent systems. In particular, the samples containing surfactant and no internal phase absorbed faster in the CHCl<sub>3</sub> system than in the 3:1 CHCl<sub>3</sub>: DMF. One possible explanation for this increased aggregation of Span 80 in the system containing DMF. Santhanalakshmi et al. found that reverse micellization of Tween 80 was higher in mixtures of CHCl<sub>3</sub> and DMF than in the pure solvents alone.<sup>39</sup> A higher aggregation of surfactants into reverse micelles would account for a lower concentration of surfactant at the surface of the jet. This could also possibly explain the slower absorption rate of water onto fibers with surfactant and no internal phase. As water is added to the system, DMF will phase separate from the CHCl<sub>3</sub> phase into the water phase. This concentration would create a lower concentration of DMF in the CHCl<sub>3</sub> phase, which may decrease aggregation. As a result, the concentration of

surfactant at the surface of the fibers may be higher in samples with an internal phase. Representative images of samples electrospun at high relative humidity are shown below (Figure 3.14).

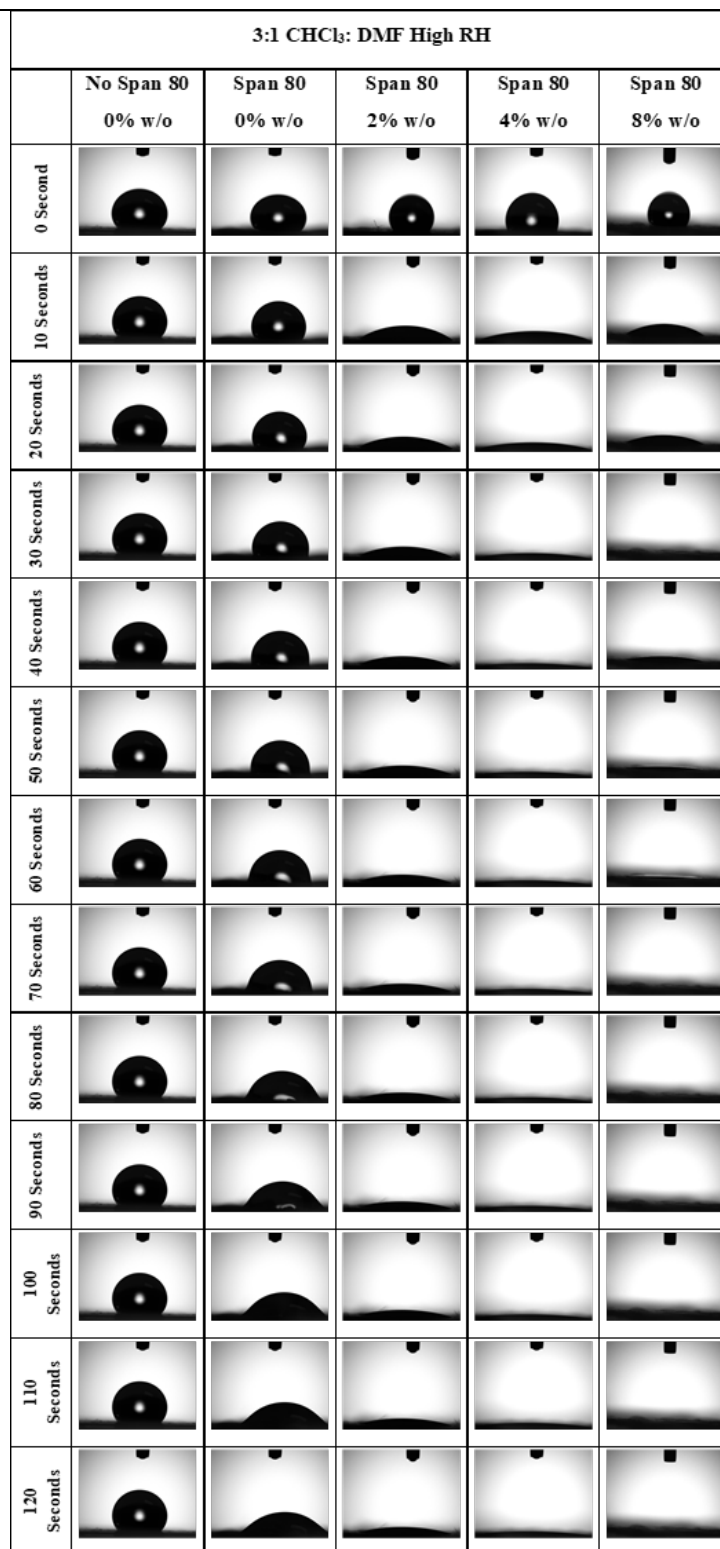


Figure 3.14: Images of representative contact angle captured for electrospun mesh fabricated with 3:1 CHCl<sub>3</sub>: DMF at high relative humidity and containing no surfactant, and surfactant with internal phase volume fractions of 0, 2, 4, and 8% w/o internal phase.

The contact angle measurements for samples fabricated at low relative humidity share some similar behaviors to the samples fabricated at high relative humidity and have unusually high variability (Figure 3.13B). The sample with no surfactant or internal phase still did not absorb the water droplet, and the sample with surfactant and 8% w/o internal phase still absorbed the water droplet faster relative to the sample with just surfactant. The samples with surfactant and 2% and 4% w/o internal phase not absorbing the water droplet was unexpected. This behavior, paired with the wide error bands, suggests that there could have been underlying data collection errors that disrupted the complete analysis of the results. Representative images of samples electrospun at low relative humidity are shown below (Figure 3.15).



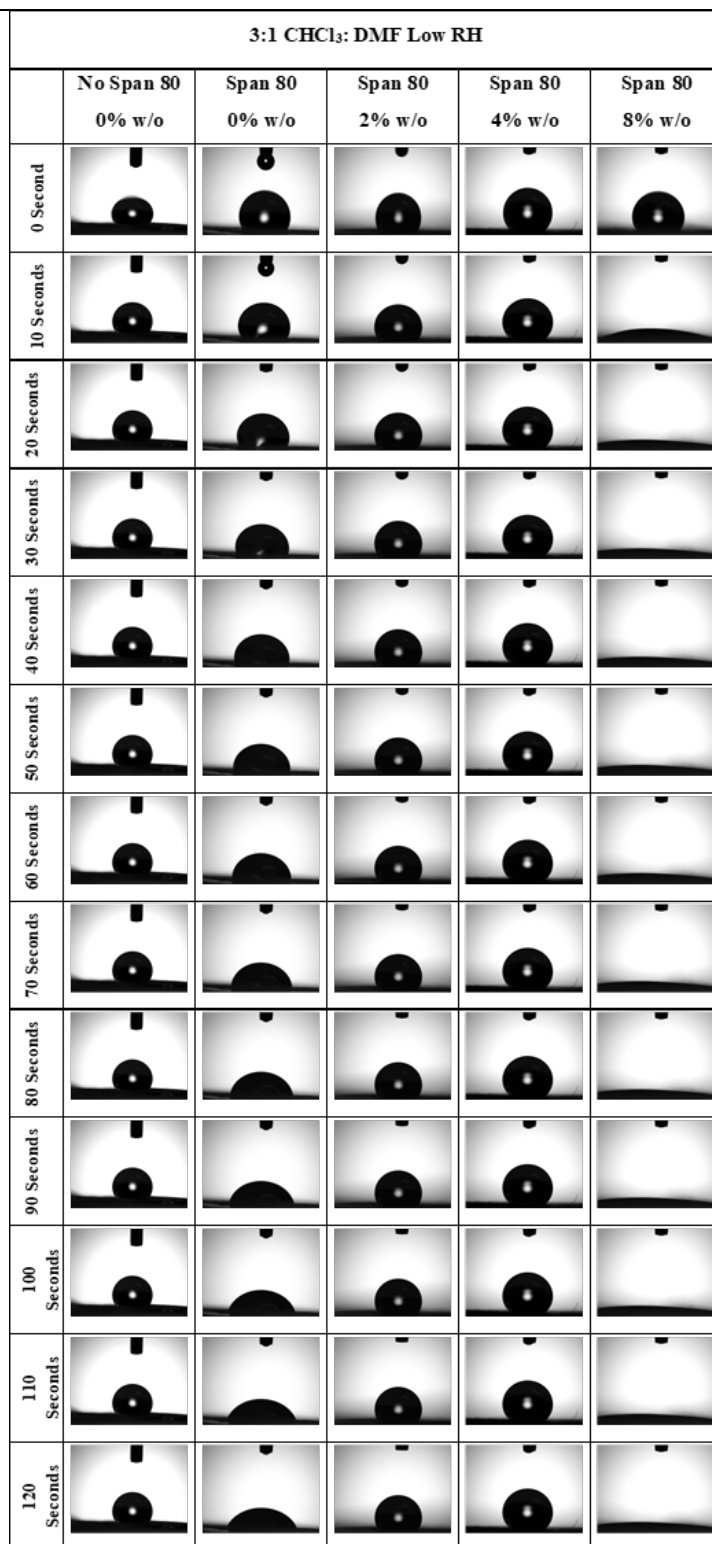
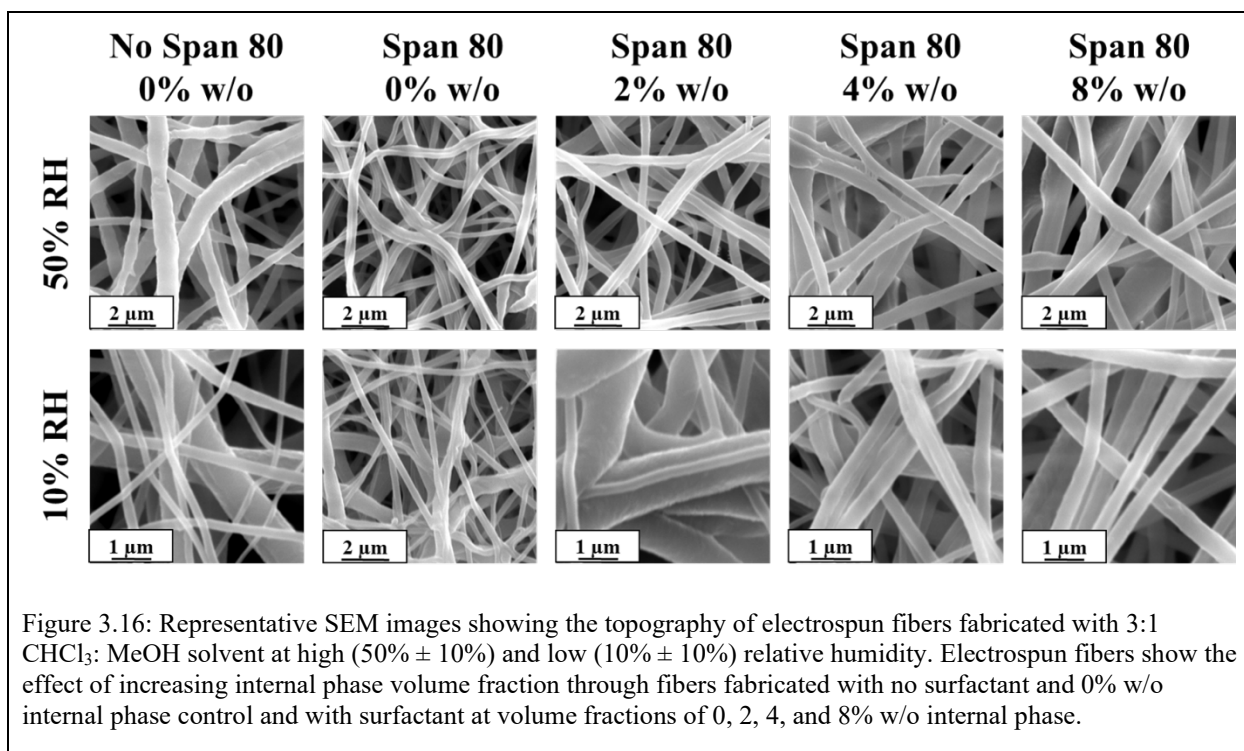


Figure 3.15: Images of representative contact angle captured for electrospun mesh fabricated with 3:1 CHCl<sub>3</sub>: DMF at low relative humidity and containing no surfactant, and surfactant with internal phase volume fractions of 0, 2, 4, and 8% w/o internal phase.

### 3.3.1.3 3:1 CHCl<sub>3</sub>: MeOH Solvent System

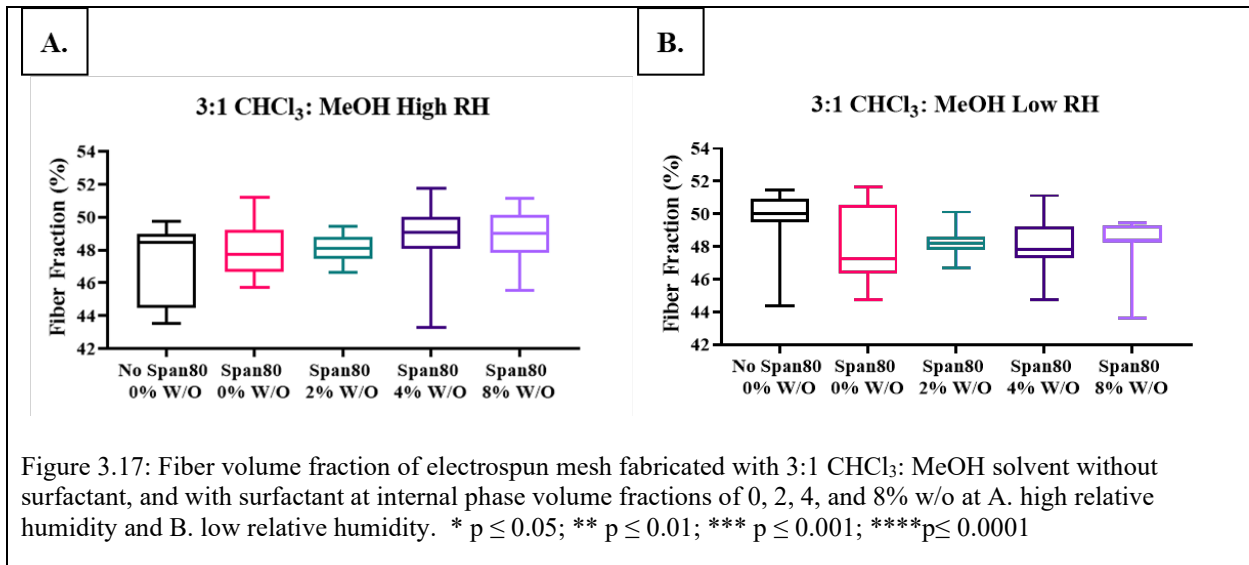
#### 3.3.1.3.1 Surface Topography

The surface topography of fibers electrospun at both high and low relative humidity had smooth surface topography for samples electrospun with no surfactant and samples with surfactant at internal phase volume fractions of 0, 2, 4, and 8% w/o (Figure 3.16). The samples electrospun with 3:1 CHCl<sub>3</sub>: MeOH solvent had smooth topography where samples fabricated with CHCl<sub>3</sub> and DMF had porous surface topography in the absence of surfactant electrospun at high relative humidity. This may be attributed to the increased conductivity of MeOH increasing the whipping of these samples to eliminate porosity and phase separation with MeOH facilitating ambient water penetrating into the fiber.



### 3.3.1.3.2 Fiber Fraction

Within samples electrospun with 3:1  $\text{CHCl}_3$ : MeOH at high relative humidity, no significant fiber fraction differences were observed for any samples (Figure 3.17A). In samples using this solvent system, the added conductivity and immiscibility of the MeOH solvent likely increased the conductivity of the system overall so that multiple jets or substantial branching occurred, as discussed further in Chapter 4. The resulting fibers had smaller fiber diameters and were not statistically different. This resulted in porosity that was not statistically different because the polymer jet(s) had similar flight paths and stretching behavior as they evaporated. The same behavior was observed between samples that were electrospun at low relative humidity (Figure 3.17B). The fact that fiber fraction is not statistically different and that the surface topography appears uniformly smooth indicates that the primary differences in contact angle may be attributed to surfactant at the surface of the fibers.



### 3.3.1.3.3 Contact Angle

Contact angle measurements were evaluated to determine the effect of surfactant relocation to the oil-air interface during electrospinning. Samples fabricated at high relative humidity

exhibited similar behavior as samples fabricated with other solvent systems (Figure 3.18A). The mesh with no surfactant or internal phase failed to absorb the water droplet within two minutes, predominantly due to the hydrophobicity of the PCL polymer. All meshes fabricated with surfactant absorbed the water droplet. This behavior could be explained by the surfactant relocating to the surface of the fibers during electrospinning, creating a more hydrophilic surface so that the droplet can absorb into the mesh. Meshes electrospun at low relative humidity behaved similarly to those fabricated at high relative humidity (Figure 3.18B). Similar behavior can be explained by the same phenomena described above. Wide error bands throughout the contact angle measurements depict a large amount of variability between measurement trials. This could be from user error in the experimental procedure, and additional trials may be beneficial to understand differences between groups containing surfactant fully. Representative images from samples fabricated at high relative humidity (Figure 3.19) and low relative humidity (Figure 3.20) are shown below.

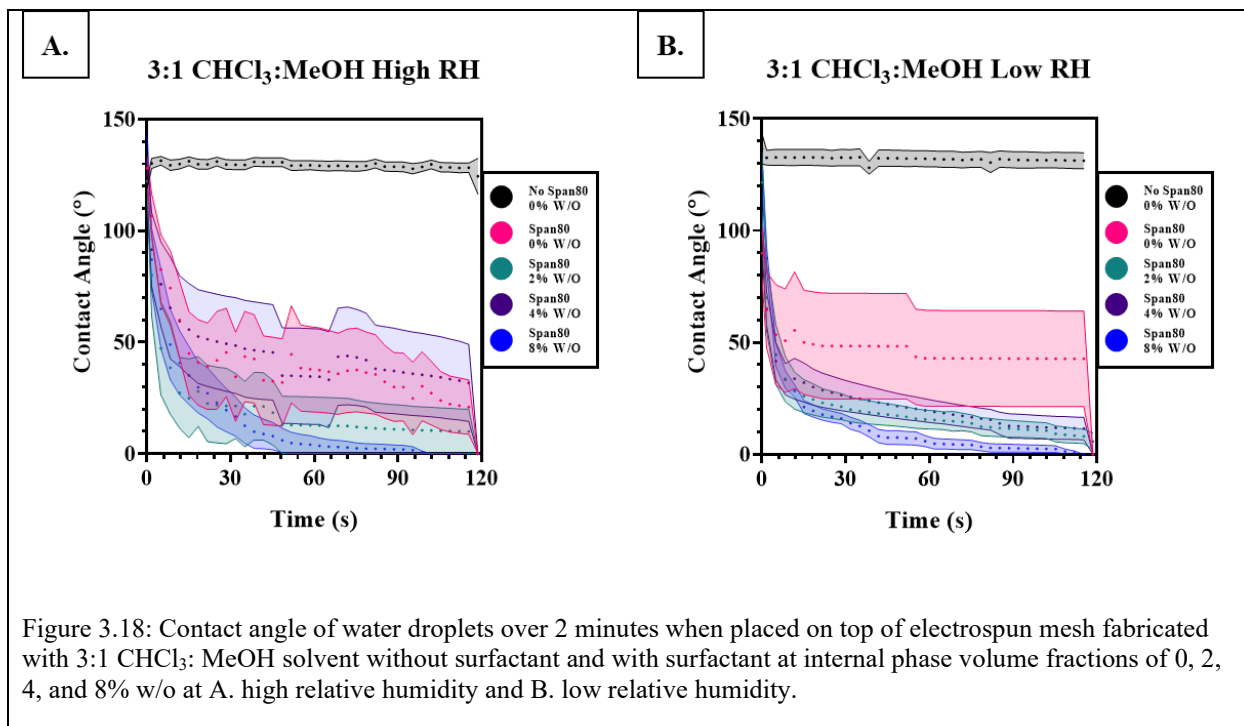


Figure 3.18: Contact angle of water droplets over 2 minutes when placed on top of electrospun mesh fabricated with 3:1 CHCl<sub>3</sub>: MeOH solvent without surfactant and with surfactant at internal phase volume fractions of 0, 2, 4, and 8% w/o at A. high relative humidity and B. low relative humidity.

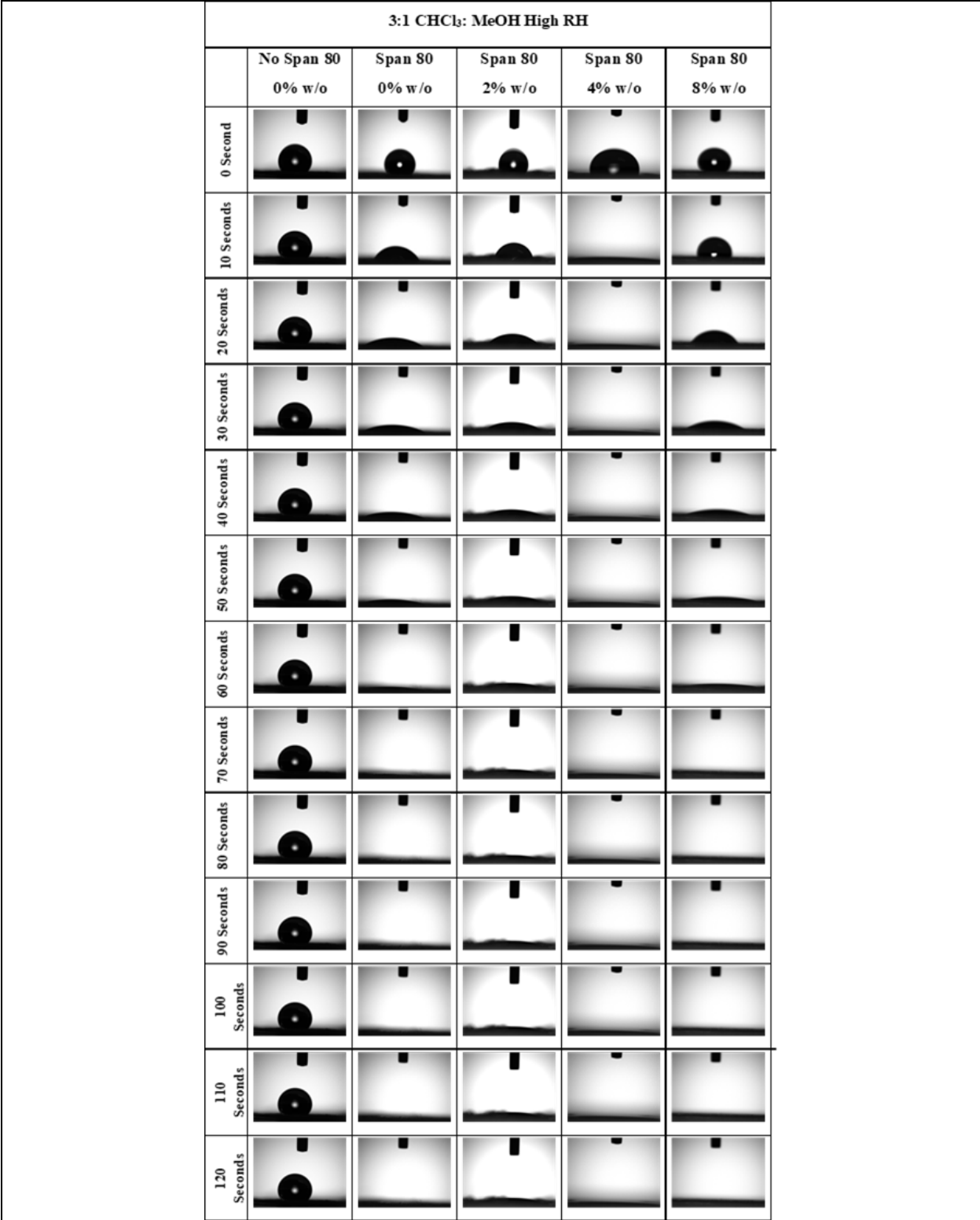


Figure 3.19: Images of representative contact angle captured for electrospun mesh fabricated with 3:1 CHCl<sub>3</sub>: MeOH at high relative humidity and containing no surfactant, and surfactant with internal phase volume fractions of 0, 2, 4, and 8% w/o internal phase.

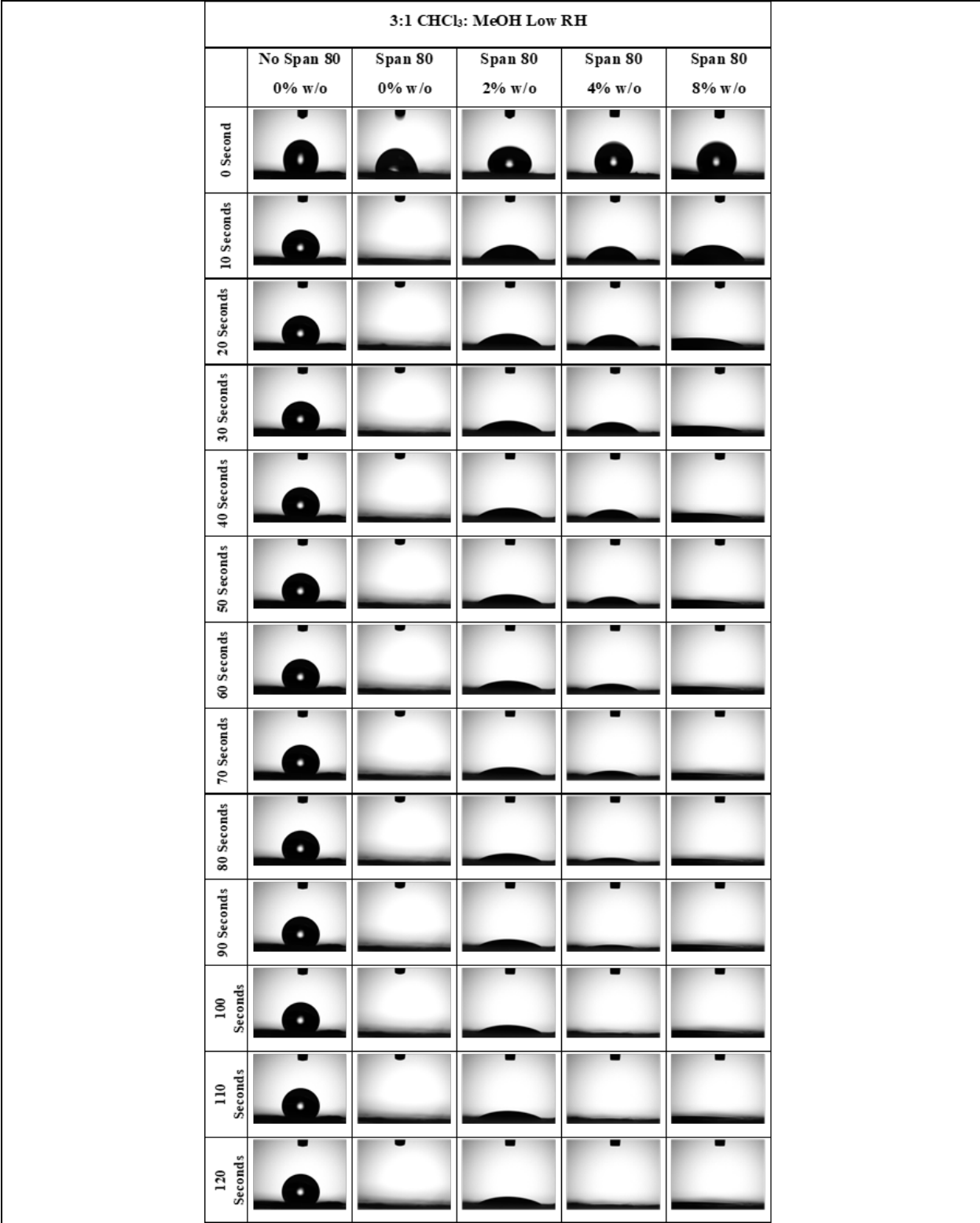
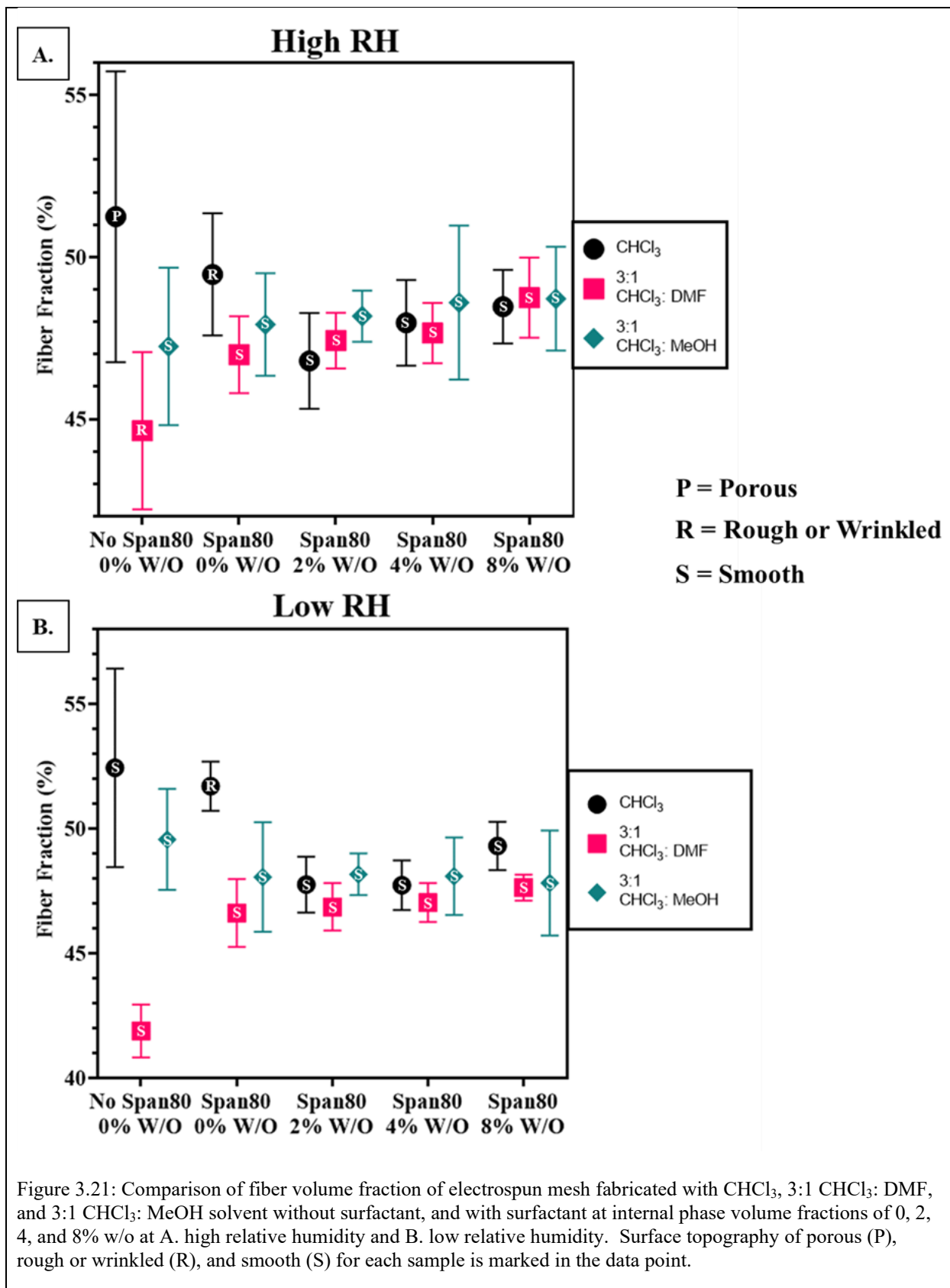


Figure 3.20: Images of representative contact angle captured for electrospun mesh fabricated with 3:1 CHCl<sub>3</sub>: MeOH at low relative humidity and containing no surfactant, and surfactant with internal phase volume fractions of 0, 2, 4, and 8% w/o internal phase.

Beigmoradi et al. showed that using different solvents in samples with surfactant can result in different contact angles and attributed this to differences in fiber porosity and roughness caused by different solvent evaporation rates.<sup>6</sup> Therefore, comparing the fiber fraction and surface roughness and porosity of these samples, we can further expand this work by comparing contact angle for different solvent systems and the characterized surface roughness and fiber volume fraction. For samples containing internal phase at both high and low relative humidity, fiber fraction was relatively similar for each solvent system, and all fibers had a porous structure (Figure 3.21A-B). Differences in these samples are more likely due to surfactant effects. No surfactant samples fabricated with 3:1 CHCl<sub>3</sub>: DMF fibers exhibited lower fiber fractions than the other solvent systems at both high and low relative humidity (Figure 3.21A-B). This was reflected in a comparatively lower contact angle at low relative humidity (Figure 3.23A-D). This trend was not observed at high relative humidity, potentially because the roughness of the fiber counterbalanced the reduced fiber volume fraction (Figure 3.21A-B, Figure 3.22A-D).





The surfactant used in the system is Span 80, which, according to PubChem, has a logP value of 6, indicating that once the interface is saturated with surfactant, excess surfactant will likely be located in the oil phase. In samples containing  $\text{CHCl}_3$ , this would likely not affect the surfactant relocation to the oil-air interface. Comparing  $\text{CHCl}_3$  samples to samples fabricated with 3:1  $\text{CHCl}_3$ : DMF, DMF is a relatively more polar solvent compared to  $\text{CHCl}_3$ , which would likely mean that Span 80 would prefer  $\text{CHCl}_3$  to DMF solvent. Additionally, intermolecular interactions between  $\text{CHCl}_3$  and DMF have been shown to cause increased aggregation of surfactant.<sup>39</sup> This preference would likely be even more extreme in samples containing 3:1  $\text{CHCl}_3$ : MeOH because MeOH is an even more polar solvent and immiscible with  $\text{CHCl}_3$  facilitating phase separation. In cases where an immiscible non-solvent is used to fabricate samples, surfactant may be located at the solvent-non-solvent interface. If this location is preferred to the solvent-air interface, then less surfactant would be expected at the surface of the fibers resulting in a slower absorption of the water droplet. This trend is generally observed with the solvent systems used in this study, but because of the high variability of data, additional trials need to be run to confirm this trend (Figure 3.22A-D, Figure 3.23A-D).

As the internal phase volume fraction is added to the system, the internal emulsion surface area of organic to polar solvent would likely increase, leading to more surfactant located at the internal interface and less at the surface interface because water is more polar and higher in saturation than air. This trend is expected until full coalescence occurs, which would cause an internal core of liquid and, therefore, the polar solvent-organic solvent surface area would decrease, and more surfactant would be expected to remain in the organic solvent. This trend is best observed in the  $\text{CHCl}_3$  system at high relative humidity (Figure 3.22A-D).

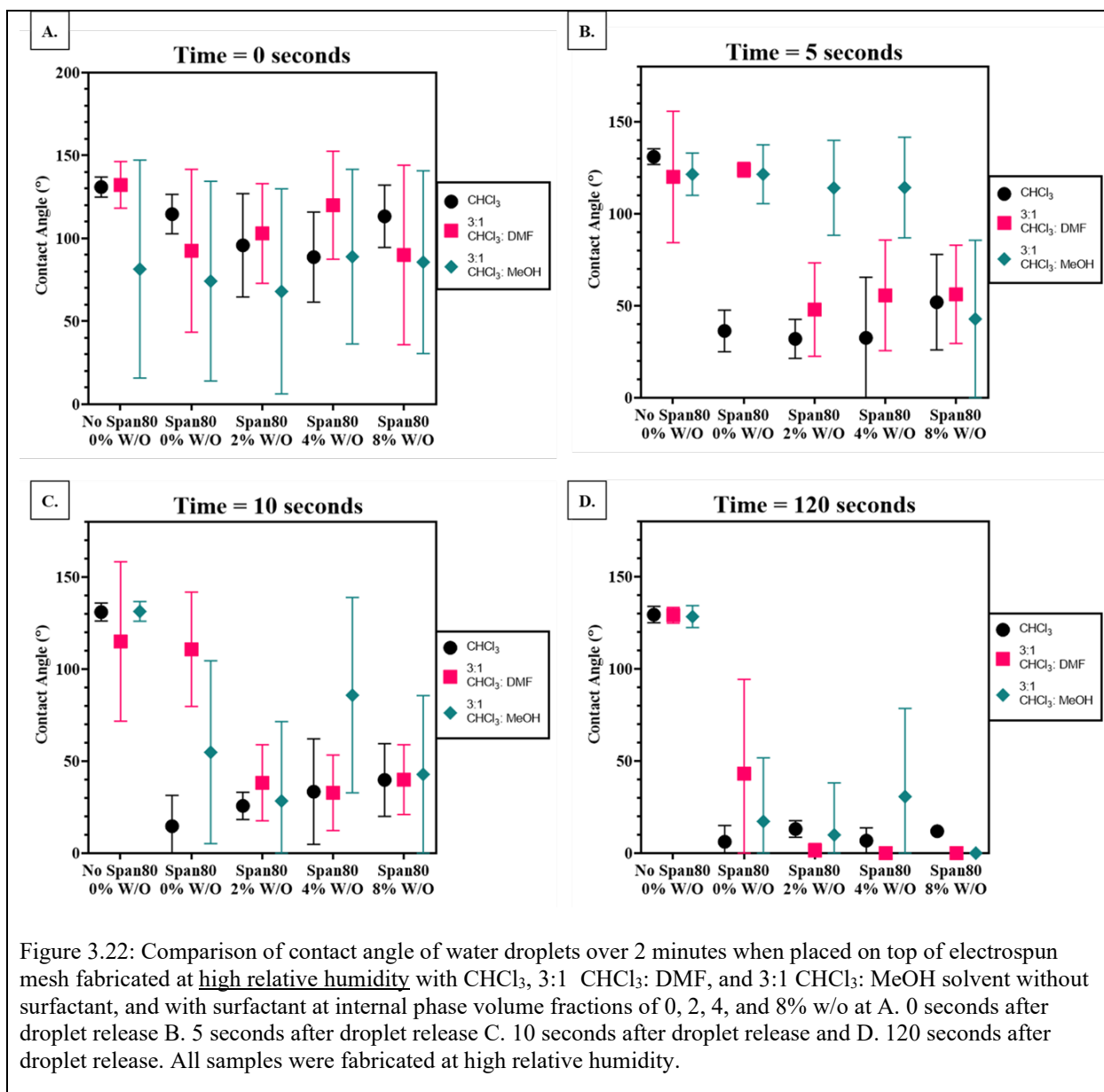


Figure 3.22: Comparison of contact angle of water droplets over 2 minutes when placed on top of electrospun mesh fabricated at high relative humidity with CHCl<sub>3</sub>, 3:1 CHCl<sub>3</sub>: DMF, and 3:1 CHCl<sub>3</sub>: MeOH solvent without surfactant, and with surfactant at internal phase volume fractions of 0, 2, 4, and 8% w/o at A. 0 seconds after droplet release B. 5 seconds after droplet release C. 10 seconds after droplet release and D. 120 seconds after droplet release. All samples were fabricated at high relative humidity.

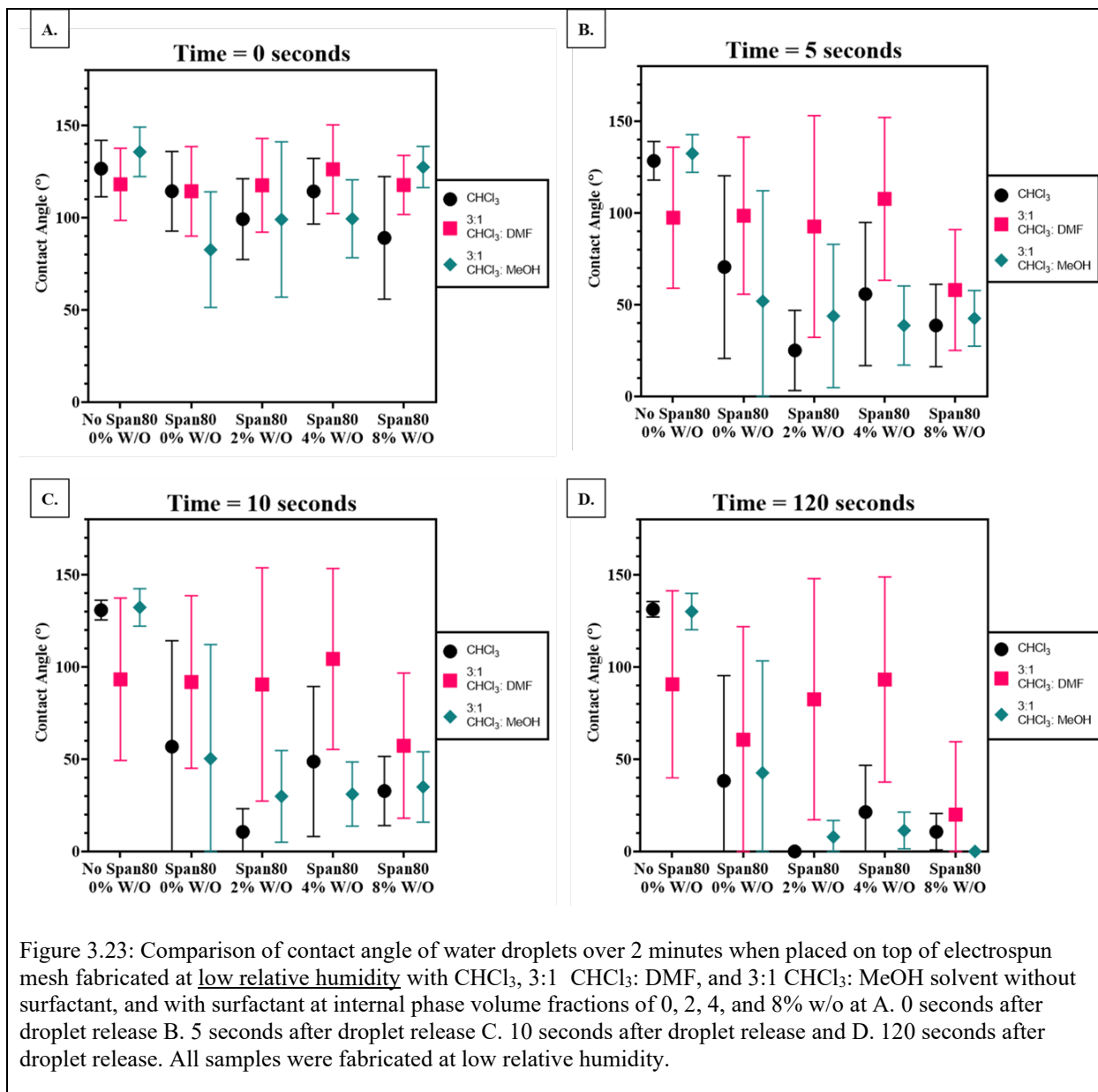


Figure 3.23: Comparison of contact angle of water droplets over 2 minutes when placed on top of electrospun mesh fabricated at low relative humidity with  $\text{CHCl}_3$ , 3:1  $\text{CHCl}_3$ : DMF, and 3:1  $\text{CHCl}_3$ : MeOH solvent without surfactant, and with surfactant at internal phase volume fractions of 0, 2, 4, and 8% w/o at A. 0 seconds after droplet release B. 5 seconds after droplet release C. 10 seconds after droplet release and D. 120 seconds after droplet release. All samples were fabricated at low relative humidity.

Summaries of the surface topography, average fiber diameter, average fiber fraction, and contact angle at time points of 0, 5, 10, and 120 seconds can be seen in Table 3.1 for samples electrospun at high relative humidity and Table 3.2 for samples electrospun at low relative humidity. Fiber diameters are also listed, although fiber diameter has been shown not to correlate with contact angle, it may play a minor role in surfactant location.<sup>29</sup> Fiber diameter was included

instead to understand relative surface area in each of the fibers which may affect the concentration of surfactant at the surface.

Table 3.1: Summary of fiber topography, diameter, fraction, and contact angle over time for varying solvent systems at high relative humidity.

Table 3.1. Summary of Fiber Topography, Diameter, Fraction, and Contact Angle over Time for Varying Solvent Systems at High Relative Humidity

Solvent(s)	Surfactant, Internal Phase Volume Fraction	Surface Topography	Average Fiber Diameter ( $\mu\text{m}$ )	Average Fiber Fraction (%)	Average Contact Angle ( $^\circ$ ), t=0, t=5, t=10, t=120
$\text{CHCl}_3$	No Internal Phase	Porous	$4.16 \pm 1.07$	$51.25 \pm 4.49$	$131.0 \pm 6.1,$ $131.1 \pm 4.3,$ $131.0 \pm 4.9,$ $129.5 \pm 4.4$
$\text{CHCl}_3$	Span 80 0% w/o	Smooth, Cactus, Lateral Wrinkles	$3.65 \pm 1.97$	$49.46 \pm 1.89$	$114.7 \pm 11.8,$ $36.3 \pm 11.3,$ $14.7 \pm 16.7,$ $6.2 \pm 8.9$
$\text{CHCl}_3$	Span 80 2% w/o	Smooth	$0.42 \pm 0.16$	$46.79 \pm 1.48$	$95.9 \pm 31.1,$ $32.0 \pm 10.6,$ $25.7 \pm 7.4,$ $13.1 \pm 4.5$
$\text{CHCl}_3$	Span 80 4% w/o	Smooth	$0.42 \pm 0.16$	$47.97 \pm 1.32$	$88.8 \pm 27.2,$ $32.5 \pm 33.0,$ $33.44 \pm 28.7,$ $6.77 \pm 6.94$
$\text{CHCl}_3$	Span 80 8% w/o	Smooth	$0.45 \pm 0.17$	$48.47 \pm 1.13$	$113.4 \pm 18.8,$ $52.0 \pm 26.0,$ $39.8 \pm 19.8,$ $11.9 \pm 1.3$
3:1 $\text{CHCl}_3$ : DMF	No Internal Phase	Wrinkled	$1.28 \pm 0.25$	$44.64 \pm 2.42$	$132.3 \pm 14.1,$ $120.1 \pm 35.7,$ $115.0 \pm 43.3,$ $129.1 \pm 4.3$
3:1 $\text{CHCl}_3$ : DMF	Span 80 0% w/o	Smooth	$0.37 \pm 0.16$	$46.99 \pm 1.19$	$92.6 \pm 49.1,$ $124.0 \pm 3.9,$ $110.8 \pm 31.0,$ $43.1 \pm 51.2$

Table 3.1. Summary of Fiber Topography, Diameter, Fraction, and Contact Angle over Time for Varying Solvent Systems at High Relative Humidity

Solvent(s)	Surfactant, Internal Phase Volume Fraction	Surface Topography	Average Fiber Diameter ( $\mu\text{m}$ )	Average Fiber Fraction (%)	Average Contact Angle ( $^\circ$ ), t=0, t=5, t=10, t=120
3:1 CHCl <sub>3</sub> : DMF	Span 80 2% w/o	Smooth	0.40 $\pm$ 0.17	47.42 $\pm$ 0.86	103.0 $\pm$ 30.0, 47.9 $\pm$ 25.5, 38.3 $\pm$ 20.7, 1.4 $\pm$ 3.8
3:1 CHCl <sub>3</sub> : DMF	Span 80 4% w/o	Smooth	0.45 $\pm$ 0.18	47.65 $\pm$ 0.93	120.0 $\pm$ 32.5, 55.6 $\pm$ 30.0, 32.9 $\pm$ 20.5, Fully Absorbed
3:1 CHCl <sub>3</sub> : DMF	Span 80 8% w/o	Smooth	0.50 $\pm$ 0.25	48.75 $\pm$ 1.24	90.0 $\pm$ 54.2, 56.2 $\pm$ 26.7, 39.9 $\pm$ 19.0, Fully Absorbed
3:1 CHCl <sub>3</sub> : MeOH	No Internal Phase	Smooth	0.52 $\pm$ 0.20	47.24 $\pm$ 2.43	121.5 $\pm$ 11.5, 131.4 $\pm$ 5.3, 131.4 $\pm$ 5.3, 128.4 $\pm$ 5.9
3:1 CHCl <sub>3</sub> : MeOH	Span 80 0% w/o	Smooth	0.39 $\pm$ 0.18	47.92 $\pm$ 1.58	121.5 $\pm$ 16.0, 69.0 $\pm$ 47.9, 54.9 $\pm$ 49.6, 17.2 $\pm$ 34.5
3:1 CHCl <sub>3</sub> : MeOH	Span 80 2% w/o	Smooth	0.50 $\pm$ 0.20	48.18 $\pm$ 0.79	114.1 $\pm$ 25.8, 36.1 $\pm$ 47.9, 28.7 $\pm$ 43.2, 9.9 $\pm$ 28.3
3:1 CHCl <sub>3</sub> : MeOH	Span 80 4% w/o	Smooth	0.50 $\pm$ 0.18	48.59 $\pm$ 2.37	114.32 $\pm$ 27.33, 76.35 $\pm$ 53.56, 85.86 $\pm$ 53.06, 30.73 $\pm$ 47.84
3:1 CHCl <sub>3</sub> : MeOH	Span 80 8% w/o	Smooth	0.53 $\pm$ 0.26	48.71 $\pm$ 1.6	42.8 $\pm$ 42.8, 56.8 $\pm$ 49.9, 42.8 $\pm$ 42.8, Fully Absorbed

Table 3.2: Summary of fiber topography, diameter, fraction, and contact angle over time for varying solvent systems at low relative humidity.

Table 3.2. Summary of Fiber Topography, Diameter, Fraction, and Contact Angle over Time for Varying Solvent Systems at Low Relative Humidity					
Solvent(s)	Surfactant, Internal Phase Volume Fraction	Surface Topography	Average Fiber Diameter ( $\mu\text{m}$ )	Average Fiber Fraction (%)	Contact Angle ( $^\circ$ ), t=0, t=5, t=10, t=120
$\text{CHCl}_3$	No Internal Phase	Smooth	$5.39 \pm 0.98$	$52.43 \pm 3.98$	$126.6 \pm 15.3$ , $128.5 \pm 10.5$ , $130.8 \pm 5.3$ , $131.3 \pm 4.2$
$\text{CHCl}_3$	Span 80 0% w/o	Lateral Wrinkles	$4.64 \pm 1.57$	$51.7 \pm 0.98$	$114.4 \pm 21.6$ , $70.5 \pm 49.8$ , $56.9 \pm 57.4$ , $38.3 \pm 57.1$
$\text{CHCl}_3$	Span 80 2% w/o	Smooth	$0.43 \pm 0.17$	$47.76 \pm 1.12$	$99.2 \pm 21.9$ , $25.1 \pm 21.9$ , $10.6 \pm 12.6$ , Fully Absorbed
$\text{CHCl}_3$	Span 80 4% w/o	Smooth	$0.45 \pm 0.17$	$47.73 \pm 1$	$114.3 \pm 17.8$ , $55.8 \pm 39.0$ , $48.8 \pm 40.7$ , $21.4 \pm 25.3$
$\text{CHCl}_3$	Span 80 8% w/o	Smooth	$0.65 \pm 0.29$	$49.3 \pm 0.97$	$89.1 \pm 33.2$ , $38.7 \pm 22.4$ , $32.8 \pm 18.8$ , $10.7 \pm 9.9$
3:1 $\text{CHCl}_3$ : DMF	No Internal Phase	Smooth	$0.34 \pm 0.14$	$41.88 \pm 1.06$	$118.1 \pm 19.5$ , $97.4 \pm 38.4$ , $93.3 \pm 44.1$ , $90.7 \pm 50.7$
3:1 $\text{CHCl}_3$ : DMF	Span 80 0% w/o	Smooth	$0.36 \pm 0.16$	$46.61 \pm 1.36$	$114.3 \pm 24.3$ , $98.5 \pm 42.8$ , $91.9 \pm 46.8$ , $60.6 \pm 61.3$

Table 3.2. Summary of Fiber Topography, Diameter, Fraction, and Contact Angle over Time for Varying Solvent Systems at Low Relative Humidity

Solvent(s)	Surfactant, Internal Phase Volume Fraction	Surface Topography	Average Fiber Diameter ( $\mu\text{m}$ )	Average Fiber Fraction (%)	Contact Angle ( $^\circ$ ), t=0, t=5, t=10, t=120
3:1 CHCl <sub>3</sub> : DMF	Span 80 2% w/o	Smooth	0.35 $\pm$ 0.14	46.86 $\pm$ 0.95	117.5 $\pm$ 25.4, 92.6 $\pm$ 60.4, 90.5 $\pm$ 63.2, 82.6 $\pm$ 65.4
3:1 CHCl <sub>3</sub> : DMF	Span 80 4% w/o	Smooth	0.36 $\pm$ 0.14	47.03 $\pm$ 0.78	126.3 $\pm$ 24.0, 107.7 $\pm$ 44.3, 104.3 $\pm$ 49.0, 93.3 $\pm$ 55.6
3:1 CHCl <sub>3</sub> : DMF	Span 80 8% w/o	Smooth	0.40 $\pm$ 0.16	47.64 $\pm$ 0.52	117.8 $\pm$ 16.0, 58.0 $\pm$ 32.9, 57.4 $\pm$ 39.4, 20.0 $\pm$ 39.6
3:1 CHCl <sub>3</sub> : MeOH	No Internal Phase	Smooth	0.38 $\pm$ 0.11	49.57 $\pm$ 2.03	135.7 $\pm$ 13.4, 132.4 $\pm$ 10.3, 132.3 $\pm$ 10.2, 130.1 $\pm$ 9.9
3:1 CHCl <sub>3</sub> : MeOH	Span 80 0% w/o	Smooth	0.35 $\pm$ 0.15	48.06 $\pm$ 2.2	82.7 $\pm$ 31.4, 51.9 $\pm$ 60.2, 50.3 $\pm$ 61.9, 42.6 $\pm$ 60.7
3:1 CHCl <sub>3</sub> : MeOH	Span 80 2% w/o	Smooth	0.46 $\pm$ 0.18	48.17 $\pm$ 0.84	99.0 $\pm$ 42.1, 43.9 $\pm$ 39.0, 29.9 $\pm$ 24.9, 7.9 $\pm$ 9.0
3:1 CHCl <sub>3</sub> : MeOH	Span 80 4% w/o	Smooth	0.54 $\pm$ 0.21	48.09 $\pm$ 1.56	99.4 $\pm$ 21.1, 38.7 $\pm$ 21.6, 31.1 $\pm$ 17.4, 11.3 $\pm$ 10.0
3:1 CHCl <sub>3</sub> : MeOH	Span 80 8% w/o	Smooth	0.56 $\pm$ 0.24	47.82 $\pm$ 2.11	127.4 $\pm$ 11.2, 42.6 $\pm$ 15.1, 35.0 $\pm$ 19.1, Fully Absorbed



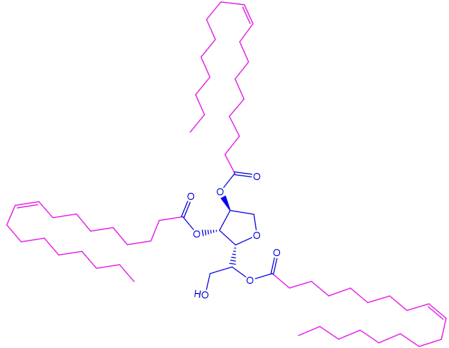
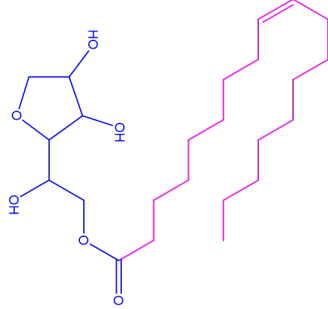
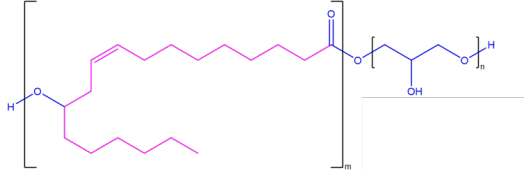

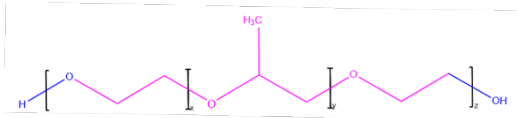
### **3.3.2 Effect of Surfactant HLB Chemistry**

#### *3.3.2.1 Chemical Structure of Non-ionic Surfactants*

Electrospun fiber meshes were fabricated at low relative humidity using five different surfactants of varying HLB value with a single mesh made with  $\text{CHCl}_3$  as a control. Low relative humidity was used to minimize the effect of VIPS as a potentially confounding variable. All surfactants selected were non-ionic and exhibited a range of HLB and logP values as determined by chemical structure. Span 85 (HLB 1.8), Span 80 (HLB 4.3), PGPR (HLB 4.7), Span 40 (HLB 6.7), and Pluronic F108 (HLB 24) were used, and their chemistry with highlighted polar and non-polar regions can be seen in Table 3.3 HLB values were found from Sigma Aldrich, all other values were found from Pubchem.

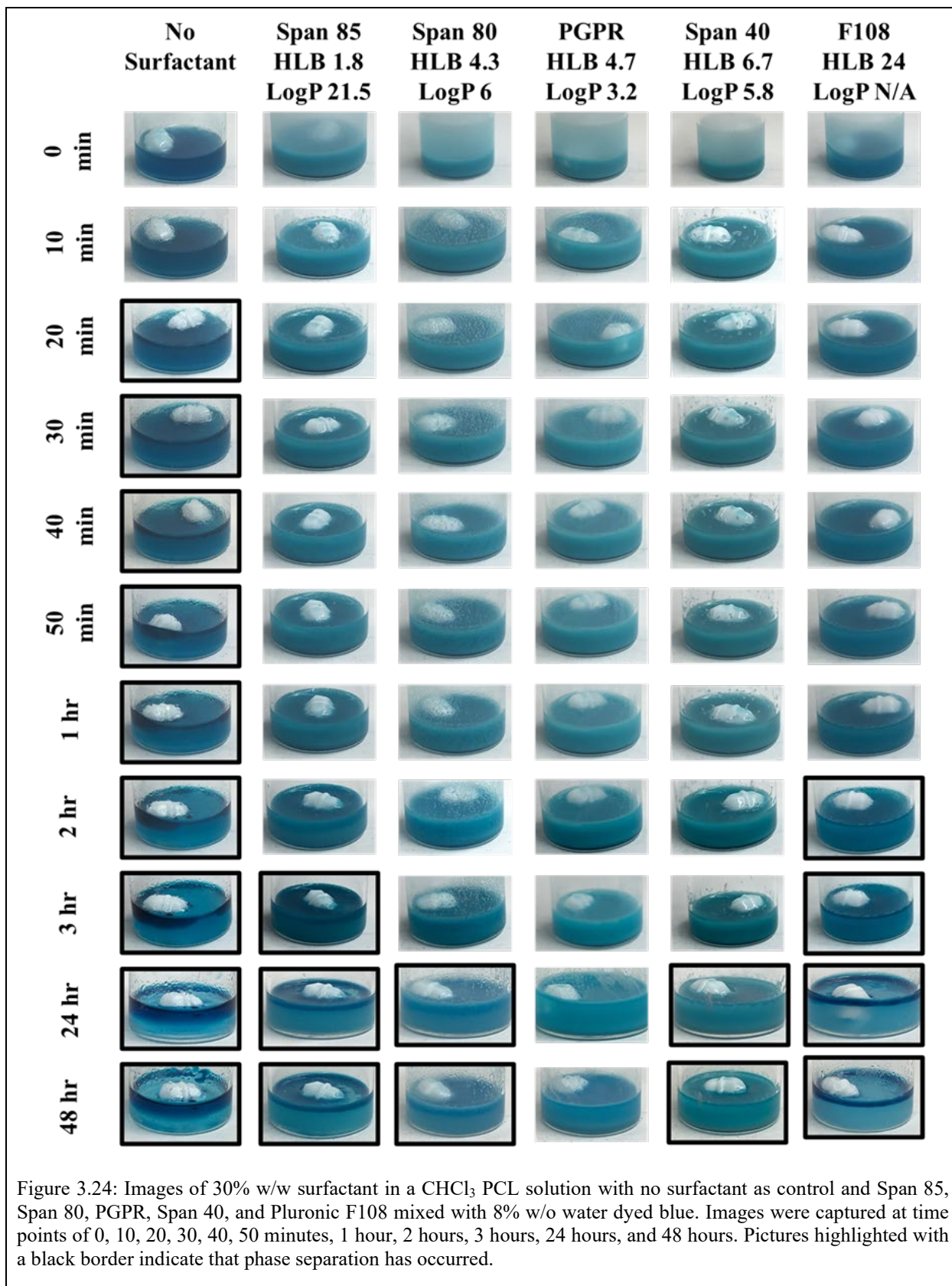
Table 3.3: Summary of non-ionic surfactants structure, HLB, LogP, and hydrogen bonding.

Table 3.3. Summary of Surfactant Structures and Properties

Surfactant	Molecular Weight	Structure	HLB	LogP	H-Bond Donor, Acceptors
Span 85	957.5		1.8	21.5	1, 8
Span 80	428.6		4.3	6	3,6
PGPR	520.7		4.7	3.2	5,9
Span 40	402.6		6.7	5.8	3,6
Pluronic F108	~14,600		24	N/A *	1,4

### 3.3.2.2 *Emulsion Stability*

Surfactant chemistry effect on emulsion stability was determined by mixing blue-dyed water and chloroform with 30% w/w surfactant and 8% internal phase volume fraction. After emulsification, the samples were left undisturbed for 24 hours, with pictures taken at various time points throughout. The results are shown below (Figure 3.24).



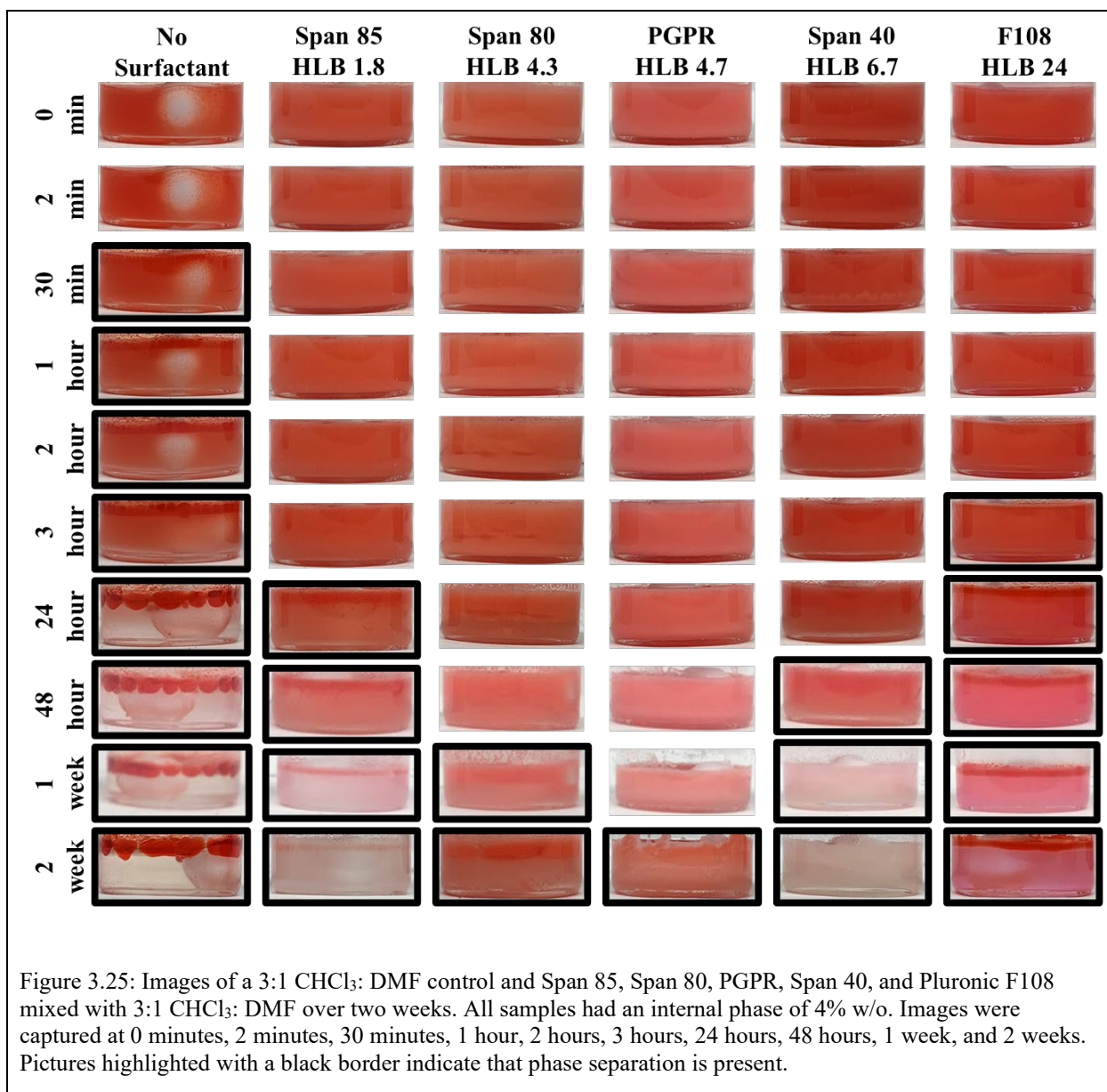
The control sample without any surfactant began showing clear signs of phase separation after 20 minutes. All samples with surfactant were able to remain completely emulsified for at least one hour. The surfactant with the lowest HLB value, Span 85, maintained emulsion stability for two hours, while the surfactant with the highest HLB value, Pluronic F108, only maintained the emulsion for one hour. Phase separation occurred in these samples first, likely because they fall outside of the optimal range of oil-in-water emulsions, which is approximately 3.5-6.<sup>40</sup>

For Span 85, the logP value is 21.5, indicating a strong preference for the organic phase. Furthermore, the favorable orientation of Span 85 has three long hydrocarbon chains surrounding the polar region that may reduce the effectiveness for the surfactant to remain at the interface and prevent coalescence of droplets due to steric hindrance. Pluronic F108 has an HLB value of approximately 24 and is classified as a good surfactant for oil-in-water emulsions. This is likely because it has a long hydrocarbon chain with only ether groups (which have comparatively weak intermolecular interactions) and one hydroxyl group to facilitate interaction with the aqueous phase. Although the logP value was not found for F108, it will likely prefer the organic phase based on its chemical structure. The groups capable of interacting with the aqueous phase are not strong enough to prevent the coalescence of the water droplets over time. This is because Pluronic F108 has fewer functional groups capable of hydrogen bonding, and the orientation of hydrocarbons in Span 85 creating steric hindrance.

Surfactants with more moderate HLB values, Span 80, PGPR, and Span 40, all maintained the emulsions for at least three hours. Span 80 and PGPR have HLB values in the range classified as water-in-oil emulsion stabilization, and Span 40 falls just outside of the upper 6 range with an HLB value of 6.7. PGPR performed by far the best with no visible phase separation after 48 hours. The PGPR used in this study was manufactured and donated by Palsgaard and advertised for use

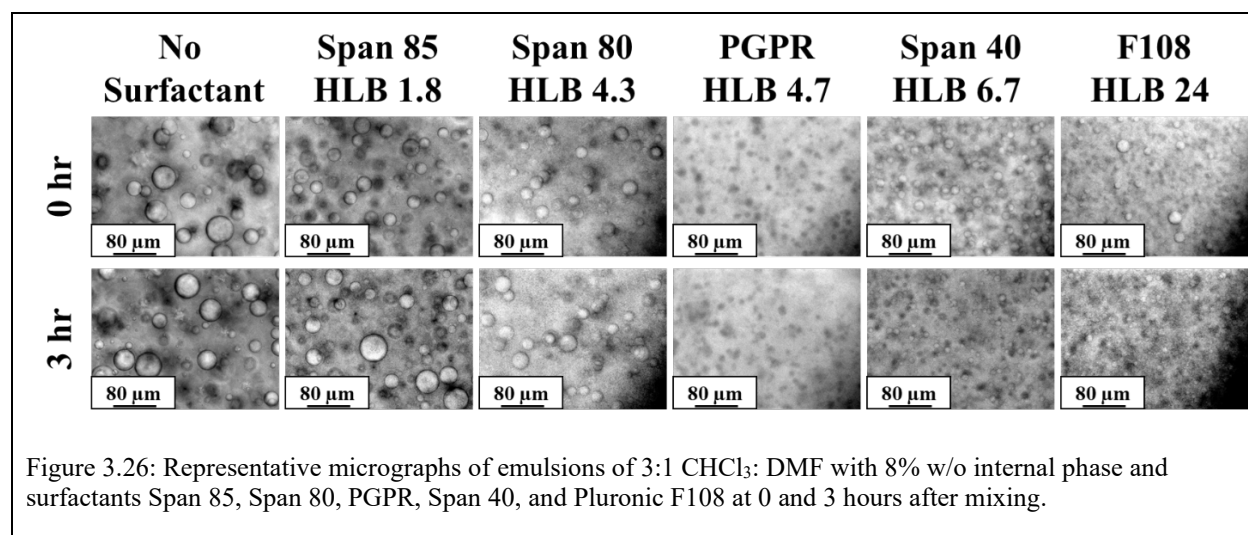
in chocolate and, according to a 2008 Food and Drug Administration report titled *GRAS Notification for Polyglycerol Polyricinoleate (PGPR) in Vegetable Fat Coatings* from Palsgaard, the PGPR manufactured is polydisperse. It has several isomers depending on the esterification. PGPR has an ideal structure to stabilize a water-in-oil emulsion with an HLB value of 4.7, which is right in the middle of the general HLB classifications, and the lowest partition coefficient ( $\log P = 3.2$ ) In addition to this, because PGPR is polydisperse and has several isomers, several different species could be present at the interface and competition could favor species that enhance the stability of the emulsion.

Emulsion stability was also studied using a 3:1  $\text{CHCl}_3$ : DMF emulsion with 4% w/o internal phase. The internal water phase was dyed red for phase separation visualization, mixed, and left undisturbed for two weeks. Similar trends as the  $\text{CHCl}_3$  only system were observed (Figure 3.25). The sample without any surfactant was the first to show signs of phase separation, occurring within the first 30 minutes. The surfactants with the highest and lowest HLBs, Pluronic F108 and Span 85, were the next to show phase separation at the 3-hour mark and 24-hour mark, respectively. The three surfactants with moderate HLBs lasted longer than one day, with PGPR maintaining a stable emulsion for up to two weeks. Comparing the stability of this study to the study with just  $\text{CHCl}_3$  solvent, emulsion stability lasted longer, potentially because a lower internal phase volume fraction of water was used and due to DMF being partially miscible in both  $\text{CHCl}_3$  and water, making it more challenging to see phase separation because the red dye was also in the DMF solvent. It appears that there is more phase separation in the no surfactant sample starting at 24 hour and beyond supporting the second hypothesis, but further tests would be needed to confirm.



Microscope images of the 3:1 CHCl<sub>3</sub>: DMF emulsions with 4% w/o internal phase were collected to analyze better the emulsification of the internal phase and coalescence of the internal phase over time (Figure 3.26). The largest internal phase droplets observed were in the no surfactant samples, and droplet size varied. In emulsions with Span 85, internal phase droplets appeared to increase in size, and droplet size distribution increased after three hours. In emulsions with Span 80, droplets were smaller than no surfactant and Span 85 and remained approximately

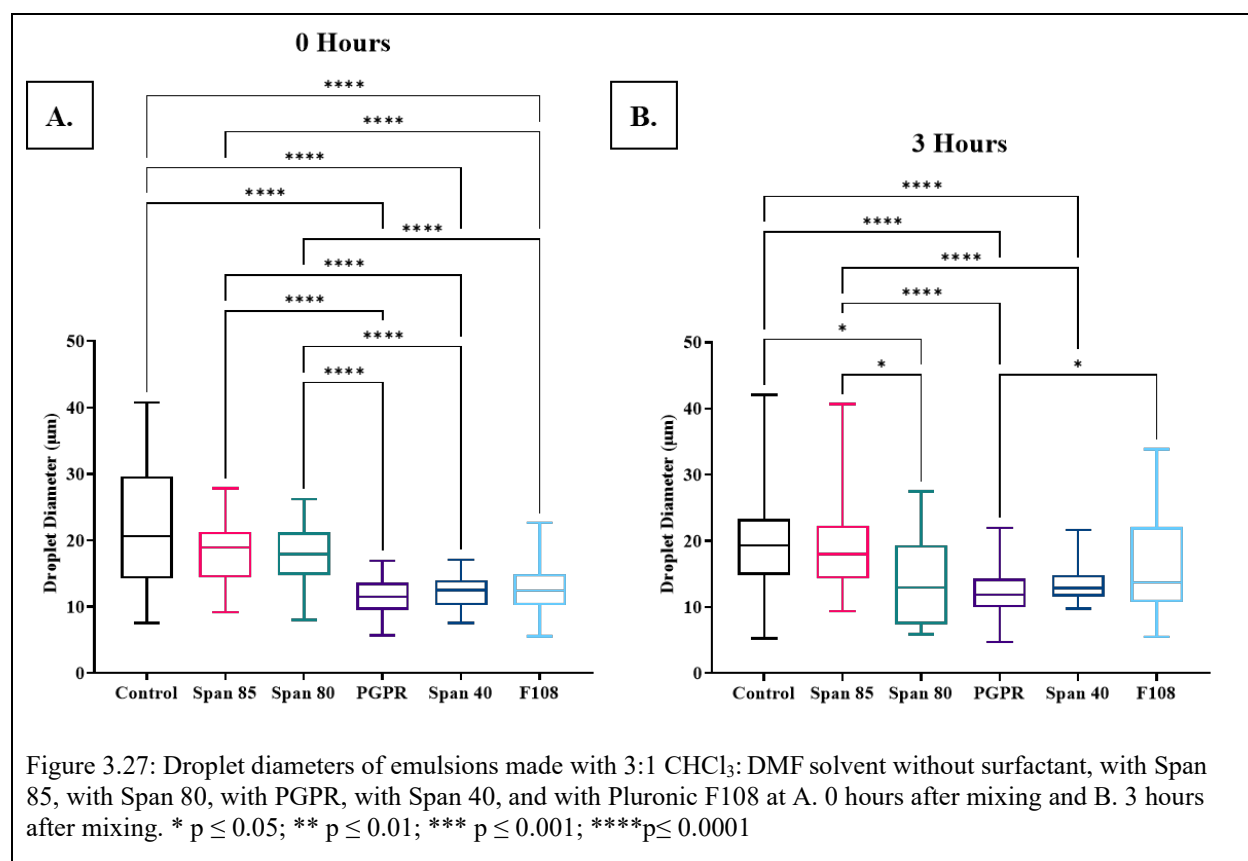
the same with a slight increase in droplet size over time. Emulsions with PGPR internal phase were difficult to image clearly and may have remained approximately the same within a 3-hour time frame. Span 40 and Pluronic F108 droplets appear to get slightly smaller after 3 hours, potentially because larger droplets have separated into another phase. The samples that had already begun to phase separate at the 3 hour mark have much larger and less dispersed suspended droplets (Figure 3.27). Larger droplets indicate phase separation and an unstable emulsion.



Microscope images were characterized by measuring droplet size at 0 hours and 3 hours for all surfactants and control. Overall, the droplet size at 0 hours decreased with increasing HLB number (Figure 3.27A). This indicates that surfactants with increasing HLB value may be better at emulsifying water in the 3:1 CHCl<sub>3</sub>: DMF initially. At 0 hours, average droplet sizes were  $22.34 \pm 9.24$ ,  $18.15 \pm 5.01$ ,  $18.03 \pm 4.23$ ,  $11.48 \pm 2.49$ ,  $12.35 \pm 2.42$ , and  $12.71 \pm 3.72$   $\mu\text{m}$  for the control sample, Span 85, Span 80, PGPR, Span 40, and Pluronic F108, respectively. At 3 hours, average droplet sizes were  $19.37 \pm 7.54$ ,  $19.14 \pm 6.86$ ,  $13.99 \pm 6.73$ ,  $12.20 \pm 3.35$ ,  $13.32 \pm 2.62$ , and  $16.03 \pm 7.19$   $\mu\text{m}$  for the control sample, Span 85, Span 80, PGPR, Span 40, and Pluronic F108, respectively.



After 3 hours, Span 85 droplets were not statistically different in size from the control droplet (Figure 3.27B). This indicates that Span 85 is likely ineffective at stabilizing the emulsion because of the steric hindrance discussed above. Pluronic F108 after 3 hours had a statistically smaller droplet size than the control, but the variability was a lot larger than at 0 hours. Further, in bulk emulsion studies, Pluronic F108 had visual evidence of phase separation, indicating that the image was taken from the organic bulk phase after some phase separation. The higher variability also supports this because droplets are coalescing. Span 85, PGPR, and Span 40 all maintained similar trends after 3 hours, indicating emulsion stability. This indicates that they all may be suitable candidates for emulsion stability.

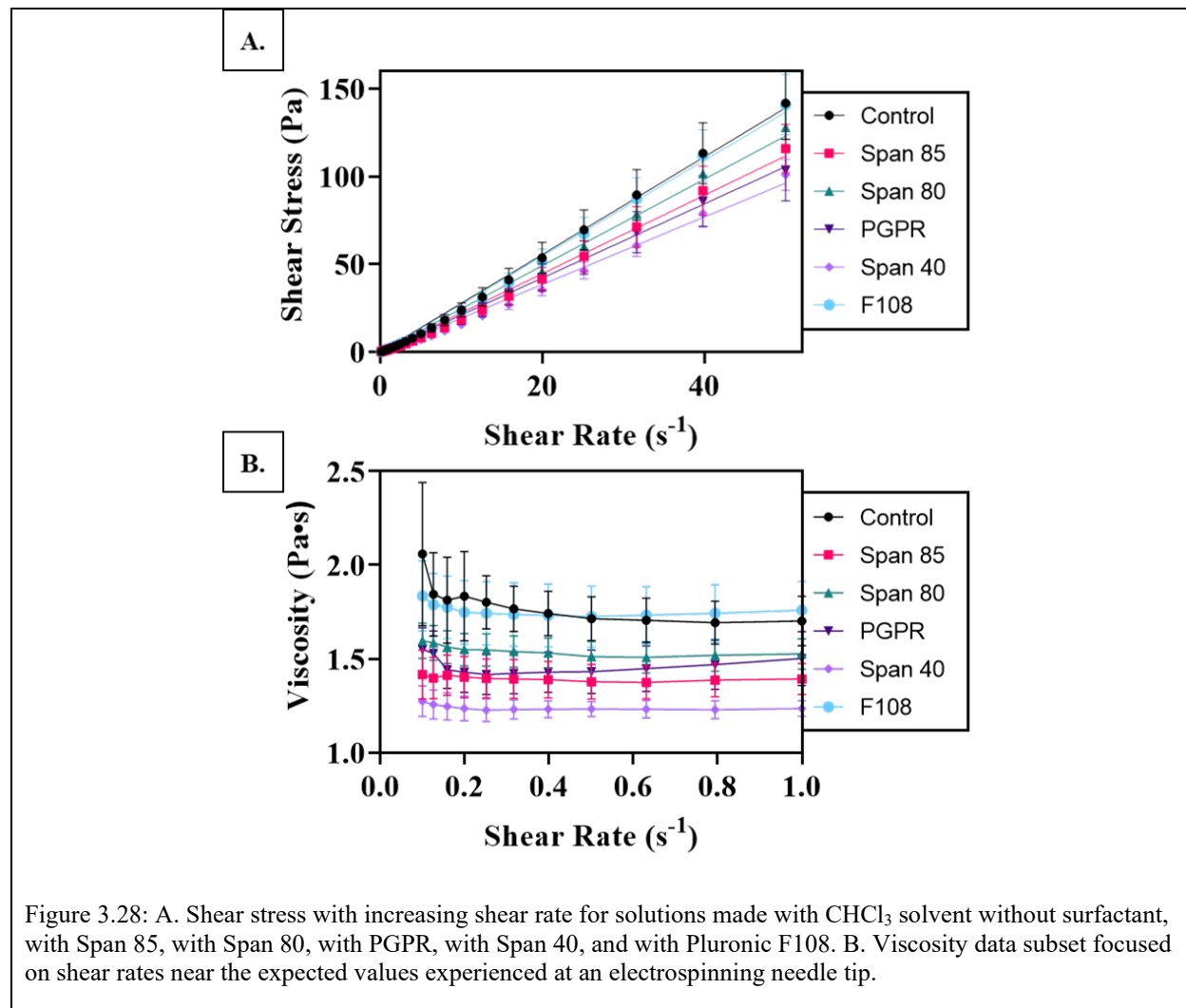


### 3.3.2.3 Solution Viscosity

Solution viscosity is an important parameter in determining the shape and behavior of the Taylor cone during electrospinning.<sup>14,41,42</sup> Low viscosity of the solution leads to bead on a string and electrospray collection because the polymer's insufficient chain entanglement is unable to resist surface tension. The shear stress versus shear rate and viscosity for all electrospinning solutions was measured to determine the effect of each surfactant (Figure 3.28A-B). Shear stress and viscosity data show that, in general, the addition of surfactant lowers the solution viscosity at most shear rates. At the low shear rates experienced at the needle tip during electrospinning, the solution without any surfactant and the solution with Pluronic F108 are the most viscous. This is because only Pluronic F108 end hydroxyl end groups form minimal and weak associations with PCL. The solutions with Span 80, PGPR, Span 85, and Span 40, listed in order of smallest change to greatest, all reduced viscosity. This behavior is likely due to the surfactant acting as a plasticizer for the PCL in the solution, allowing for greater mobility of the dissolved polymer chains. The shorter length of surfactants also may contribute to an overall lower molecular weight and therefore viscosity. Span 40 reduces viscosity the most because, in addition to having multiple hydroxyl groups to hydrogen bond with the ester group in PCL, it has a more linearly aligned structure that will have the least amount of friction due to steric hindrance of the hydrocarbon tails and also the lowest molecular weight.

At low viscosity ranges all solutions displayed some shear thinning behavior (Figure 3.28A-B). This is closest to the calculated value of shear rate going through the needle in the system used for electrospinning ( $0.06 \text{ s}^{-1}$ ). At low shear rates the shear thinning may be due to molecular alignment of the polymer.<sup>43</sup> This confirms that either through intermolecular interactions or

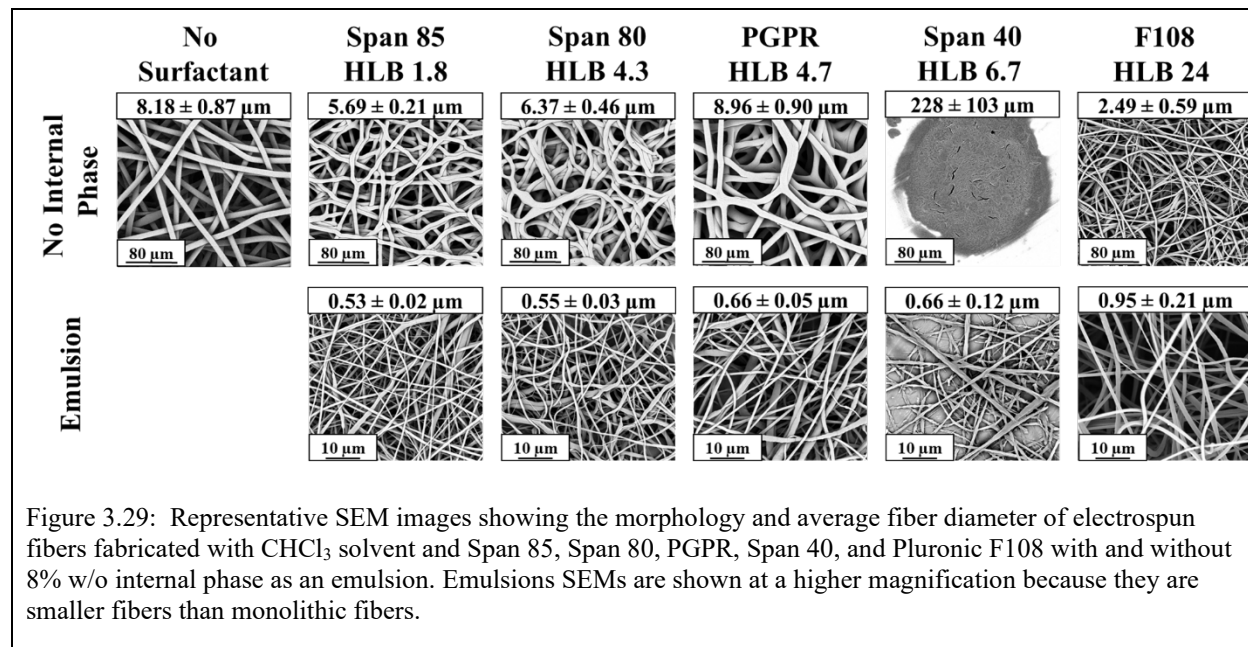
through a reduction in average molecular weight, viscosity is reduced when surfactants are added to the solution and this may be contributing to the collected mesh characteristics.



### 3.3.3 Effect on Fiber Diameter and Surface Topography

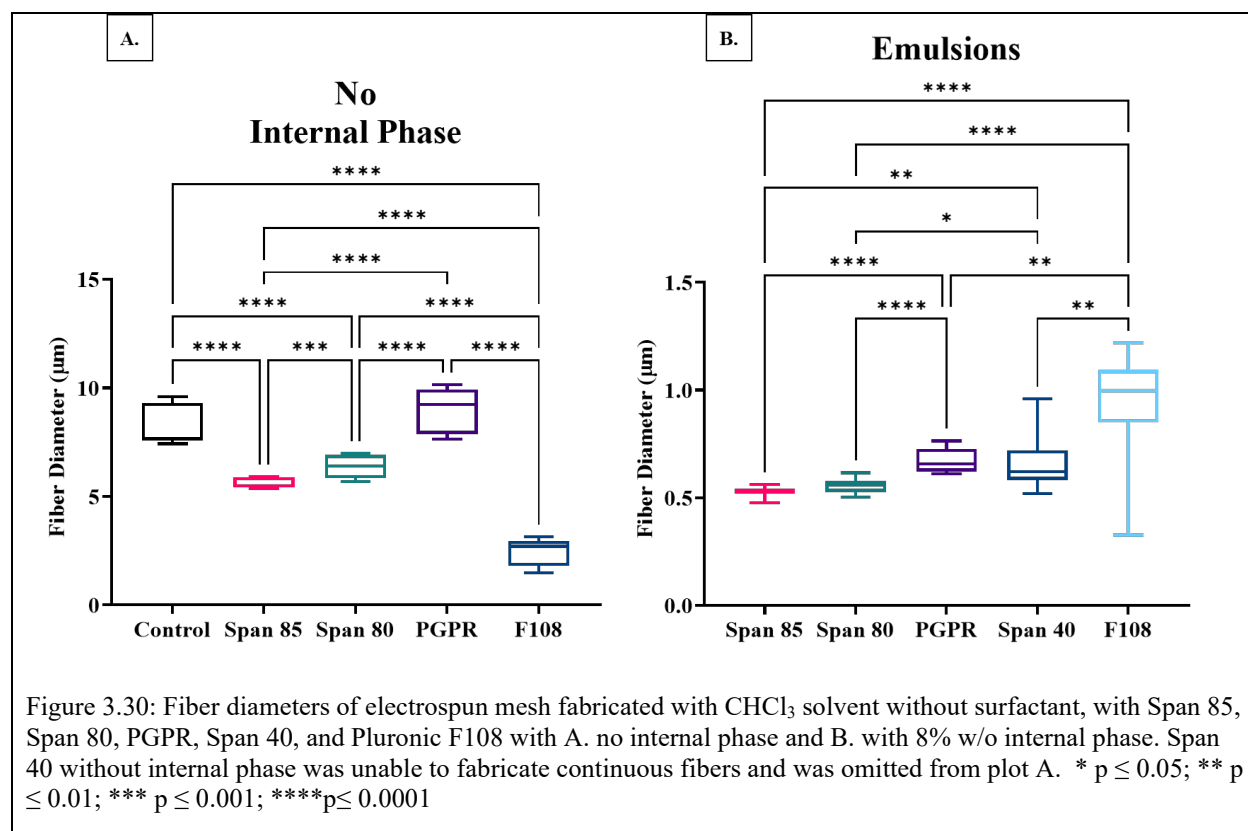
Single phase and emulsion electrospun fibers were fabricated with no surfactant control and 30 w/w% Span 85, Span 80, PGPR, Span 40, and Pluronic F108. All samples were electrospun with  $CHCl_3$  polymer solutions and as an emulsion with 8% w/o internal phase. After fabrication, the meshes were imaged using an SEM, and fiber diameters were analyzed with the ImageJ plugin

of Fiji. Representative images of each mesh and their average fiber dimeters are shown below (Figure 3.29).



Each mesh had significantly different fiber diameters for samples fabricated without internal phase, except between the CHCl<sub>3</sub> control and the mesh fabricated with PGPR (Figure 3.30A). Fiber diameter decreased or was about the same when comparing all groups with no internal phase compared to the control containing no surfactant except Span 40. This was likely due to surfactant lowering the surface tension and increasing acceleration of the jet and, therefore, reducing fiber diameter. The increased acceleration of the jet and surfactant at the surface of the jet also may have reduced the amount of evaporation of the solvent, causing samples with Span 85, Span 80, and PGPR to have a wet collection of fibers with adherence between overlapping fibers. When comparing samples with Span 85, Span 80, and PGPR, fiber diameter generally increased with increasing surfactant HLB value. This may be due to their ability to reduce surface tension at the surface of the fiber and the lower solution viscosity. Pluronic F108 had much smaller

fibers than all other samples and contained a second even smaller diameter which indicated that branching or multiple jets may have formed in this sample. Branching may have occurred because Pluronic F108 is classified as an oil-in-water surfactant and may have helped facilitate phase separation with smaller amounts of ambient water.



Span 40 with no internal phase collected as droplets instead of fibers. Generally, droplets occur when the conductivity of the solution is low, the surface tension is high, or the viscosity of the solution is low – a process known as electro spraying.<sup>41,44</sup> Span 40 is non-ionic and therefore unlikely to affect the conductivity, and surfactants reduce surface tension, so these are unlikely to be the cause of droplet formation. Span 40 is probably hydrogen bonding with the ester group in PCL, which may, in turn, change the viscosity of the solution. The chemical structure of Span 40 is the same as Span 80 except for an alkene group and, therefore, the lower viscosity between these

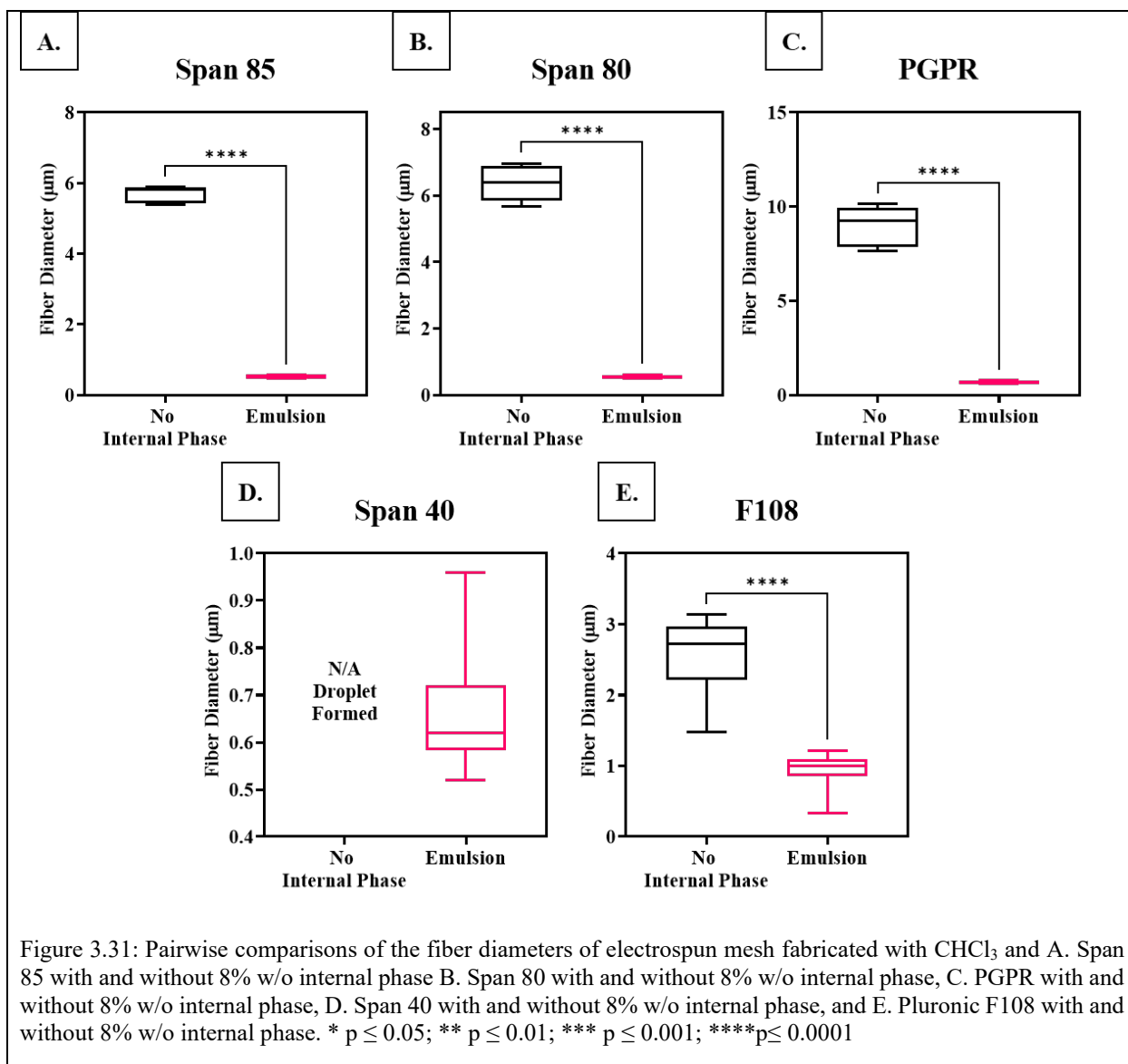
two groups may be attributed to steric hindrance of the Span 80 tail adding friction and limiting the ability for PCL polymer chains to slip past one another. Within the Taylor cone of an electrospun jet, electrostatic repulsive charge from the applied voltage builds in the jet and elongates the jet towards the collection plate. Surface tension acts in opposition to these charges to minimize surface area.<sup>45</sup> Viscoelastic interactions of the entangled polymer resists surface tension to keep the jet together. Therefore, when Span 40 was added to this system, it decreased the viscosity enough to allow surface tension to force polymer into droplets instead of fibers.

For samples fabricated with an emulsion, there was a significant difference in fiber diameter for all samples, except between Span 85 and Span 80 and between PGPR and Span 40 (Figure 3.30B). Overall, there was an increase in fiber diameter as the HLB value increased. Based on the emulsion stability studies, increasing surfactant HLB generally led to smaller internal phase droplet sizes. Decreased internal phase droplet size for the same amount of internal phase volume fraction can create relatively more surface area at the water-oil interface within the fiber. Increased water-oil interfacial area could mean that more surfactants are located at the water-oil interface than on the surface of the fibers. Less surfactant on the surface of the fibers results in more surface tension at the surface of the fibers. More surface tension and less surfactant at the surface of fibers leads to faster evaporation of solvent and less thinning of the Taylor Cone leading to larger fiber diameters. Therefore, using surfactants that produce smaller internal phase droplets such as seen through the HLB value may increase the fiber diameter.

For each surfactant system, the emulsion fabricated fibers were always significantly smaller in diameter than their no internal phase counterparts (Figure 3.31A-E). When internal phase water was added to the system, it increased overall conductivity, which increased the

whipping and stretching of the fibers. Emulsions also reduce surfactant at the surface of the jet that may otherwise slow down the rate of solvent evaporation.

This comparison was not done for samples fabricated with Span 40 because droplets were formed with no internal phase instead of fibers. However, Span 40 did form clumps of fibers when an emulsion was used, and this is significant for two reasons. First, the viscosity of emulsions is higher than that of monolithic polymer solutions.<sup>11</sup> As the internal phase was added to the system, this increased the viscosity to help transition the solution back to the electrospinning region. However, if viscosity were the *only* or dominating factor, then fibers with internal phase would all have *larger* fiber diameters than their monolithic counterparts. The emulsion electrospun fibers all had smaller fiber diameters, highlighting another and likely dominating factor in this mechanism on surfactant location. Second, emulsions may reduce surfactant concentration at the surface of the fibers because surfactants prefer the water-oil interface over the air-oil interface. This increase in surface tension at the Taylor cone may have also helped facilitate a transition back to the electrospinning region from the electrospraying region. The fibers collected in clumps which indicates that droplets may have been expelled during electrospinning and electrostatic forces cause them to expand into fibers during flight. The additional conductive force needed to achieve this expansion would have come from the internal phase adding conductivity to the system. This expansion of polymer droplets into electrospun mesh is described in greater detail by Ding et al..<sup>46</sup>



Along with fiber diameter, the surface topography of each mesh was analyzed with an SEM. For the samples fabricated without internal phase, no surface topography was completely smooth (Figure 3.32). The  $\text{CHCl}_3$  control had a wrinkled surface. The lower HLB surfactants Span 85, Span 80, and PGPR all had a rough surface topography, while the highest HLB surfactant, Pluronic F108, had a wrinkled surface. This surface topography was likely due to a small amount of ambient water droplets present at  $25\% \pm 5\%$  relative humidity causing some VIPS/TIPS phase



separation at the surface of the fibers. The rough surface structure of the low HLB samples may be due to surfactant facilitating small amounts of water to penetrate into the fiber, followed by solidification of a strong sheath at the surface and the subsequent pressure differences of water and  $\text{CHCl}_3$  causing solvent to explode out. This mechanism is based on the mechanism described by Zaarour et al., as detailed above in this chapter.<sup>34</sup>

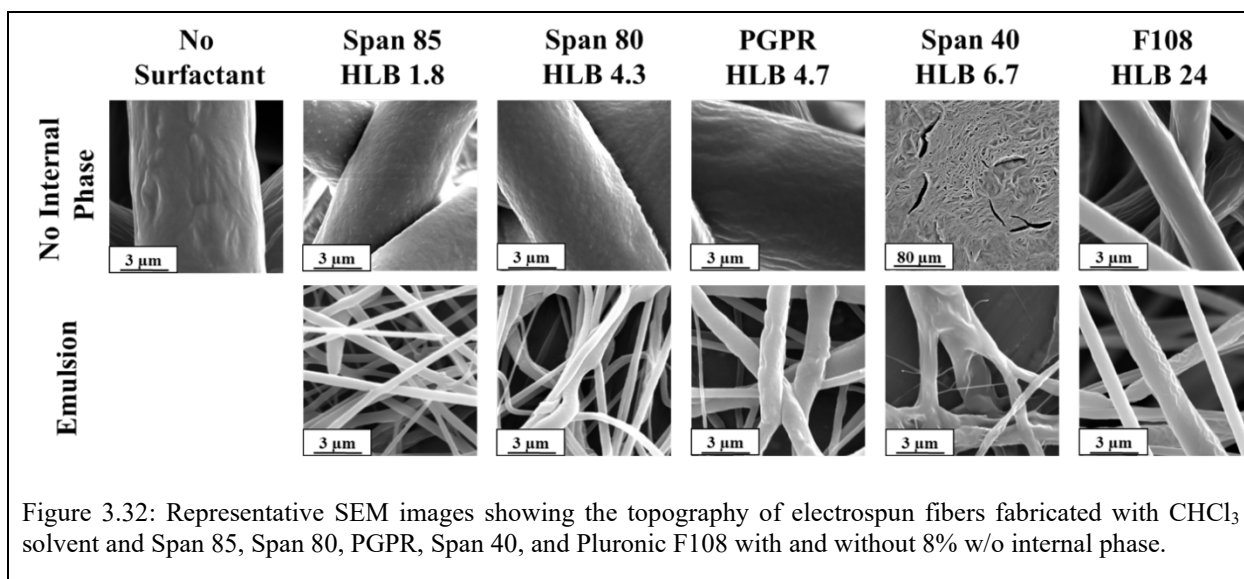


Figure 3.32: Representative SEM images showing the topography of electrospun fibers fabricated with  $\text{CHCl}_3$  solvent and Span 85, Span 80, PGPR, Span 40, and Pluronic F108 with and without 8% w/o internal phase.

The emulsion fabricated samples predominantly had smooth surface topography due to surfactant facilitating water penetration into the fiber (Figure 3.32). It is worth noting that a small amount of wrinkling in the F108 samples was observed, which resembled the control topography with no surfactant. This may indicate that F108 may not be facilitating water entering the fiber as other surfactants are, and, instead, droplets are condensing on the outside of the fiber. A summary of all the surfactant values is shown below (Table 3.4).

Table 3.4. Summary of Surface Topography, Fiber Diameter, and Emulsion Stability for Span 85, Span 80, PGPR, Span 40, and Pluronic F108

Solvent(s)	Surfactant, Internal Phase Volume Fraction	Surface Topography	Average Fiber Diameter ( $\mu\text{m}$ )	First Sign of Phase Separation, $\text{CHCl}_3$ , 3:1 $\text{CHCl}_3$ : DMF	Average Emulsion Droplet Diameter ( $\mu\text{m}$ ) t = 0 hours, t = 3 hours
	No Internal Phase 0% w/o				
$\text{CHCl}_3$	Internal Phase 0% w/o	Wrinkled	$8.18 \pm 0.87$	20 minutes, 30 minutes	$22.34 \pm 9.24$ , $19.37 \pm 7.54$
$\text{CHCl}_3$	Span 85 0% w/o	Rough	$5.69 \pm 0.21$	N/A	N/A
$\text{CHCl}_3$	Span 85 8% w/o	Smooth	$0.53 \pm 0.02$	3 hours, 24 hours	$18.15 \pm 5.01$ , $19.14 \pm 6.86$
$\text{CHCl}_3$	Span 80 0% w/o	Rough	$6.37 \pm 0.46$	N/A	N/A
$\text{CHCl}_3$	Span 80 8% w/o	Smooth	$0.55 \pm 0.03$	24 hours, One week	$18.03 \pm 4.23$ , $13.99 \pm 6.73$
$\text{CHCl}_3$	PGPR 0% w/o	Rough	$8.96 \pm 0.90$	N/A	N/A
$\text{CHCl}_3$	PGPR 8% w/o	Wrinkled	$0.66 \pm 0.05$	Stable, Two weeks	$11.48 \pm 2.49$ , $12.20 \pm 3.35$
$\text{CHCl}_3$	Span 40 0% w/o	Droplet	$288 \pm 103$	N/A	N/A
$\text{CHCl}_3$	Span 40 8% w/o	Wrinkled	$0.66 \pm 0.12$	24 hours, 48 hours	$12.35 \pm 2.42$ , $13.32 \pm 2.62$
$\text{CHCl}_3$	F108 0% w/o	Wrinkled	$2.49 \pm 0.59$	N/A	N/A
$\text{CHCl}_3$	F108 8% w/o	Wrinkled	$0.95 \pm 0.21$	2 hours, 3 hours	$12.71 \pm 3.72$ , $16.03 \pm 7.19$

Table 3.4: Summary of surface topography, fiber diameter, and emulsion stability for Span 85, Span 80, PGPR, Span 40, and Pluronic F108

### 3.4 CONCLUSION

In these studies, the relocation of Span 80 was assessed for electrospun fibers containing no surfactant, surfactant, and internal phase volume fractions of emulsions at 2, 4, and 8% w/o. These samples were repeated at a high and low relative humidity and with solvents  $\text{CHCl}_3$ , 3:1  $\text{CHCl}_3$ : DMF, and 3:1  $\text{CHCl}_3$ : MeOH. The relocation of surfactant to the surface of the fibers was determined by measuring contact angle over time and measuring for other factors over time such as fiber volume fraction and surface roughness. Overall, the contact angle remained relatively constant for control samples, and the droplets absorbed into the mesh for nearly all other samples containing internal phase. The absorption rate was slower for samples containing internal phase, potentially because of surfactant located at the water-oil interface instead of at the air-oil interface. The single solvent system  $\text{CHCl}_3$  demonstrated the fastest rate of absorption with surfactant because no interaction or phase separation with other solvents decreased surfactant at the surface of the fiber. Overall, controlling mesh contact with liquid can be used to tune drug release and cell response through the wettability of the scaffold.

Different surfactants with increasing HLB values were used to determine emulsion stability and used to electrospin single solvent and emulsion electrospun samples. In general, the longest bulk stability of an emulsion was seen with surfactants classified for water-in-oil emulsions, namely Span 80, PGPR, and Span 40. PGPR was able to stabilize surfactant for the longest time, creating a promising alternative surfactant for future studies. In general, surfactants with higher HLB values had smaller internal phase droplets. Interestingly, increasing HLB values generally created a trend of increasing fiber diameters both in single solvent and emulsion samples. This may indicate that increased HLB values are correlated with decreased surface tension in the Taylor cone of an electrospun jet. Fiber diameter of all samples decreased as the internal phase of the

emulsion was added to the system, due to increasing conductivity. Controlling electrospun fiber diameter and morphology through the use of non-ionic surfactant chemistry is promising and presents potential for new methods to tune electrospun fibers and control emulsion stability for drug release and biomedical applications.

### 3.5 BIBLIOGRAPHY

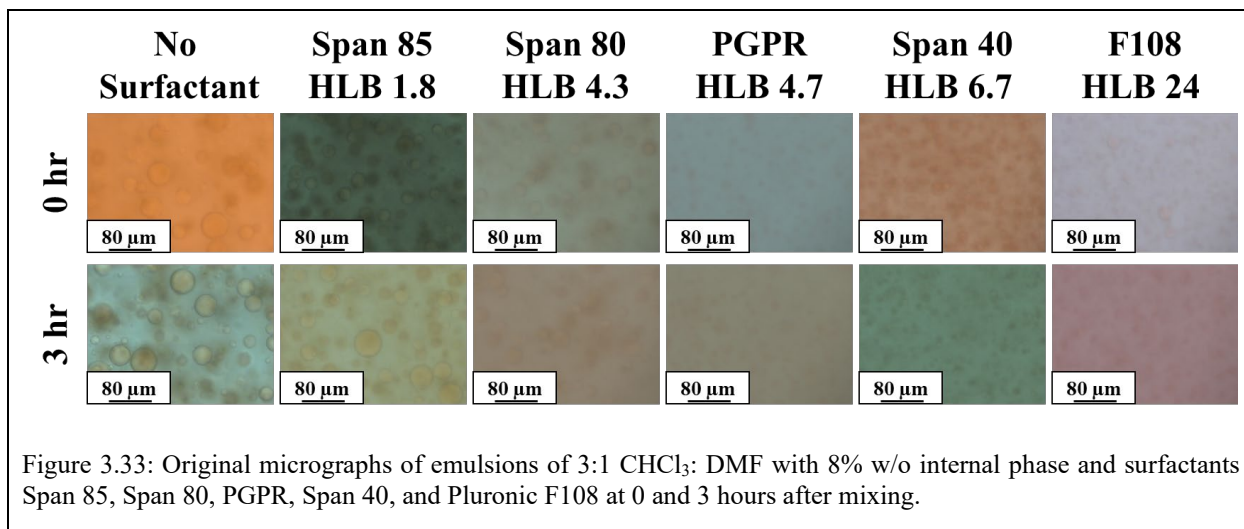
- 1 Abutaleb, A. *et al.* Effects of Surfactants on the Morphology and Properties of Electrospun Polyetherimide Fibers. *Fibers* **5**, 33, doi:10.3390/fib5030033 (2017).
- 2 Lin, T., Wang, H., Wang, H. & Wang, X. The charge effect of cationic surfactants on the elimination of fibre beads in the electrospinning of polystyrene. *Nanotechnology* **15**, 1375-1381, doi:10.1088/0957-4484/15/9/044 (2004).
- 3 Aykut, Y., Pourdeyhimi, B. & Khan, S. A. Effects of surfactants on the microstructures of electrospun polyacrylonitrile nanofibers and their carbonized analogs. *J Appl Polym Sci* **130**, 3726-3735, doi:10.1002/app.39637 (2013).
- 4 Johnson, P. M. *et al.* Surfactant location and internal phase volume fraction dictate emulsion electrospun fiber morphology and modulate drug release and cell response. *Biomater Sci-Uk*, doi:10.1039/D0BM01751E (2021).
- 5 Zhang, C., Feng, F. & Zhang, H. Emulsion electrospinning: Fundamentals, food applications and prospects. *Trends in Food Science & Technology* **80**, 175-186, doi:10.1016/j.tifs.2018.08.005 (2018).
- 6 Beigmoradi, R., Samimi, A. & Mohebbi-Kalhari, D. Fabrication of polymeric nanofibrous mats with controllable structure and enhanced wetting behavior using one-step electrospinning. *Polymer* **143**, 271-280, doi:<https://doi.org/10.1016/j.polymer.2018.04.025> (2018).
- 7 Li, X., Su, Y., Zhou, X. & Mo, X. Distribution of Sorbitan Monooleate in poly(L-lactide-co-epsilon-caprolactone) nanofibers from emulsion electrospinning. *Colloids Surf B Biointerfaces* **69**, 221-224, doi:10.1016/j.colsurfb.2008.11.031 (2009).
- 8 Vasita, R., Mani, G., Agrawal, C. M. & Katti, D. S. Surface hydrophilization of electrospun PLGA micro-/nano-fibers by blending with Pluronic® F-108. *Polymer* **51**, 3706-3714, doi:<https://doi.org/10.1016/j.polymer.2010.05.048> (2010).
- 9 Zheng, J.-Y. *et al.* The Effect of Surfactants on the Diameter and Morphology of Electrospun Ultrafine Nanofiber. *J Nanomater* **2014**, 1-9, doi:10.1155/2014/689298 (2014).
- 10 Hu, J., Prabhakaran, M. P., Ding, X. & Ramakrishna, S. Emulsion electrospinning of polycaprolactone: influence of surfactant type towards the scaffold properties. *Journal of Biomaterials Science, Polymer Edition* **26**, 57-75, doi:10.1080/09205063.2014.982241 (2015).
- 11 Yazgan, G. *et al.* Tunable release of hydrophilic compounds from hydrophobic nanostructured fibers prepared by emulsion electrospinning. *Polymer* **66**, 268-276, doi:10.1016/j.polymer.2015.04.045 (2015).
- 12 Wang, S.-Q., He, J.-H. & Xu, L. Non-ionic surfactants for enhancing electrospinnability and for the preparation of electrospun nanofibers. *Polym Int* **57**, 1079-1082, doi:10.1002/pi.2447 (2008).
- 13 Kriegel, C., Kit, K. M., McClements, D. J. & Weiss, J. Nanofibers as carrier systems for antimicrobial microemulsions. Part I: fabrication and characterization. *Langmuir* **25**, 1154-1161, doi:10.1021/la803058c (2009).

- 14 Xue, J., Wu, T., Dai, Y. & Xia, Y. Electrospinning and Electrospun Nanofibers: Methods, Materials, and Applications. *Chem Rev* **119**, 5298-5415, doi:10.1021/acs.chemrev.8b00593 (2019).
- 15 Jia, L. & Qin, X.-h. The effect of different surfactants on the electrospinning poly(vinyl alcohol) (PVA) nanofibers. *Journal of Thermal Analysis and Calorimetry* **112**, 595-605, doi:10.1007/s10973-012-2607-9 (2013).
- 16 Kriegel, C., Kit, K. M., McClements, D. J. & Weiss, J. Influence of Surfactant Type and Concentration on Electrospinning of Chitosan–Poly(Ethylene Oxide) Blend Nanofibers. *Food Biophysics* **4**, 213-228, doi:10.1007/s11483-009-9119-6 (2009).
- 17 Talwar, S., Krishnan, A. S., Hinestroza, J. P., Pourdeyhimi, B. & Khan, S. A. Electrospun Nanofibers with Associative Polymer–Surfactant Systems. *Macromolecules* **43**, 7650-7656, doi:10.1021/ma1013447 (2010).
- 18 Nilsson, S., Thuresson, K., Hansson, P. & Lindman, B. Mixed Solutions of Surfactant and Hydrophobically Modified Polymer. Controlling Viscosity with Micellar Size. *The Journal of Physical Chemistry B* **102**, 7099-7105, doi:10.1021/jp9812379 (1998).
- 19 Yu, D.-G., Chatterton, N. P., Yang, J.-H., Wang, X. & Liao, Y.-Z. Coaxial Electrospinning with Triton X-100 Solutions as Sheath Fluids for Preparing PAN Nanofibers. *Macromol Mater Eng* **297**, 395-401, doi:10.1002/mame.201100258 (2012).
- 20 Griffin, W. C. Calculation of HLB Values of Non-ionic surfactants. *Journal of The Society of Cosmetic Chemists*, 249-256 (1954).
- 21 Griffin, W. C. Classification of Surface-Active Agents by “HLB”. *Journal of the Society of Cosmetic Chemists* **1**, 311-326 (1949).
- 22 Davies, T. J. in *International Congress Surface Activity*. 426-438.
- 23 Nakama, Y. in *Cosmetic Science and Technology* (eds Kazutami Sakamoto, Robert Y. Lochhead, Howard I. Maibach, & Yuji Yamashita) 231-244 (Elsevier, 2017).
- 24 Kunieda, H. & Ishikawa, N. Evaluation of the hydrophile-lipophile balance (HLB) of non-ionic surfactants. II. Commercial-surfactant systems. *J Colloid Interf Sci* **107**, 122-128, doi:10.1016/0021-9797(85)90155-9 (1985).
- 25 Li, X. *et al.* Encapsulation of proteins in poly(L-lactide-co-caprolactone) fibers by emulsion electrospinning. *Colloids Surf B Biointerfaces* **75**, 418-424, doi:10.1016/j.colsurfb.2009.09.014 (2010).
- 26 Yazgan, G. *et al.* Steering surface topographies of electrospun fibers: understanding the mechanisms. *Sci Rep-Uk* **7**, doi:ARTN 158  
10.1038/s41598-017-00181-0 (2017).
- 27 Zaarour, B., Zhu, L., Huang, C. & Jin, X. Controlling the Secondary Surface Morphology of Electrospun PVDF Nanofibers by Regulating the Solvent and Relative Humidity. *Nanoscale Research Letters* **13**, 285, doi:10.1186/s11671-018-2705-0 (2018).
- 28 Nezarati, R. M., Eifert, M. B. & Cosgriff-Hernandez, E. Effects of humidity and solution viscosity on electrospun fiber morphology. *Tissue Eng Part C Methods* **19**, 810-819, doi:10.1089/ten.TEC.2012.0671 (2013).
- 29 Szewczyk, P. *et al.* Roughness and Fiber Fraction Dominated Wetting of Electrospun Fiber-Based Porous Meshes. *Polymers-Basel* **11**, 34, doi:10.3390/polym11010034 (2018).
- 30 Li, X., Su, Y., Zhou, X. & Mo, X. Distribution of Sorbitan Monooleate in poly(l-lactide-co-ε-caprolactone) nanofibers from emulsion electrospinning. *Colloids and Surfaces B: Biointerfaces* **69**, 221-224, doi:<https://doi.org/10.1016/j.colsurfb.2008.11.031> (2009).
- 31 Coimbra, P., Freitas, J. P., Goncalves, T., Gil, M. H. & Figueiredo, M. Preparation of gentamicin sulfate eluting fiber mats by emulsion and by suspension electrospinning. *Mater Sci Eng C Mater Biol Appl* **94**, 86-93, doi:10.1016/j.msec.2018.09.019 (2019).

- 32 Szewczyk, P. K. *et al.* Roughness and Fiber Fraction Dominated Wetting of Electrospun Fiber-Based Porous Meshes. *Polymers (Basel)* **11**, doi:10.3390/polym11010034 (2018).
- 33 Wang, L., Pai, C.-L., Boyce, M. C. & Rutledge, G. C. Wrinkled surface topographies of electrospun polymer fibers. *Appl Phys Lett* **94**, 151916, doi:10.1063/1.3118526 (2009).
- 34 Zaarour, B., Zhu, L., Huang, C. & Jin, X. Fabrication of a polyvinylidene fluoride cactus-like nanofiber through one-step electrospinning. *RSC Advances* **8**, 42353-42360, doi:10.1039/c8ra09257e (2018).
- 35 Naraghi, M., Chasiotis, I., Kahn, H., Wen, Y. & Dzenis, Y. Mechanical deformation and failure of electrospun polyacrylonitrile nanofibers as a function of strain rate. *Appl Phys Lett* **91**, 151901, doi:10.1063/1.2795799 (2007).
- 36 Zhang, X., Shi, X., Gautrot, J. E. & Peijs, T. Nanoengineered electrospun fibers and their biomedical applications: a review. *Nanocomposites* **7**, 1-34, doi:10.1080/20550324.2020.1857121 (2021).
- 37 Wang, C., Wang, L. & Wang, M. Evolution of core-shell structure: From emulsions to ultrafine emulsion electrospun fibers. *Mater Lett* **124**, 192-196, doi:<https://doi.org/10.1016/j.matlet.2014.03.086> (2014).
- 38 Sy, J. C., Klemm, A. S. & Shastri, V. P. Emulsion as a Means of Controlling Electrospinning of Polymers. *Advanced Materials* **21**, 1814-1819, doi:10.1002/adma.200701630 (2009).
- 39 Santhanalakshmi, J. & Maya, S. Solvent effects on reverse micellisation of Tween 80 and Span 80 in pure and mixed organic solvents. *Proc. Indian Acad. Sci.* **109**, 22=38 (1997).
- 40 Griffin, W. C. Classification of Surface-Active Agents By "HLB". *Journal of the Society of Cosmetic Chemists*, 311-326 (1949).
- 41 Fong, H., Chun, I. & Reneker, D. H. Beaded nanofibers formed during electrospinning. *Polymer* **40**, 4585-4592, doi:10.1016/s0032-3861(99)00068-3 (1999).
- 42 Rutledge, G. C. & Fridrikh, S. V. Formation of fibers by electrospinning. *Advanced drug delivery reviews* **59**, 1384-1391, doi:10.1016/j.addr.2007.04.020 (2007).
- 43 Zheng, J., He, A., Li, J., Xu, J. & Han, C. C. Studies on the controlled morphology and wettability of polystyrene surfaces by electrospinning or electrospraying. *Polymer* **47**, 7095-7102, doi:10.1016/j.polymer.2006.08.019 (2006).
- 44 Reneker, D. H. & Yarin, A. L. Electrospinning jets and polymer nanofibers. *Polymer* **49**, 2387-2425, doi:10.1016/j.polymer.2008.02.002 (2008).
- 45 Ding, B., Li, C. R., Miyauchi, Y., Kuwaki, O. & Shiratori, S. Formation of novel 2D polymer nanowebs via electrospinning. *Nanotechnology* **17**, 3685-3691, doi:10.1088/0957-4484/17/15/011 (2006).

### 3.6 APPENDIX

Uncorrected internal phase microscope droplet images.



## CHAPTER 4: DETERMINING THE EFFECTS OF INCREASING INTERNAL PHASE VOLUME FRACTION ON FIBER MORPHOLOGY, SURFACE TOPOGRAPHY, AND DIAMETER

### 4.1 INTRODUCTION

Emulsion electrospinning is a versatile technique used to fabricate fibers and is a particularly popular method in the food and pharmaceutical industries to encapsulate a wide range of bioactive compounds in food ingredients.<sup>1</sup> Focusing on the pharmaceutical industry, emulsion electrospinning is popular because it can encapsulate bioactive molecules and other small molecule drugs that otherwise would be incompatible with the solvent and polymer. Incorporating drugs within an internal phase of an emulsion can also alter the drug release kinetics to prevent burst release of drug, and further tuning the system affords control of drug release from electrospun fibers.<sup>1-3</sup>

An emulsion is composed of two immiscible liquids in which one liquid is suspended within the other liquid and is stabilized by a small amphiphilic molecule called the surfactant. As highlighted in previous chapters, incorporating an additional solvent within the electrospinning solution can have drastic effects on fiber morphology, topography, and diameter. The suspended internal phase in an emulsion is temporary; over time, internal droplets coalesce and the two immiscible phases will separate. Changing the chemistry of the emulsion, such as adding more of one of the phases, can affect electrospinning rate. These effects are particularly important in emulsion electrospinning because fluid flow, energy applied to the emulsion through the electric field, and solvent evaporation can affect emulsion stability and the resulting mesh characteristics.

In some emulsion electrospinning systems, the internal phase droplets will coalesce into the core of the fiber to create larger pores or a core shell structure (Figure 4.1A-B).<sup>4-6</sup> Coalescence



of emulsion droplets into the core of an emulsion electrospun fiber occurs when a viscosity gradient forms due to evaporation of solvent.<sup>4</sup> This may result in internal phase droplets moving towards the core of the fiber and coalescing.

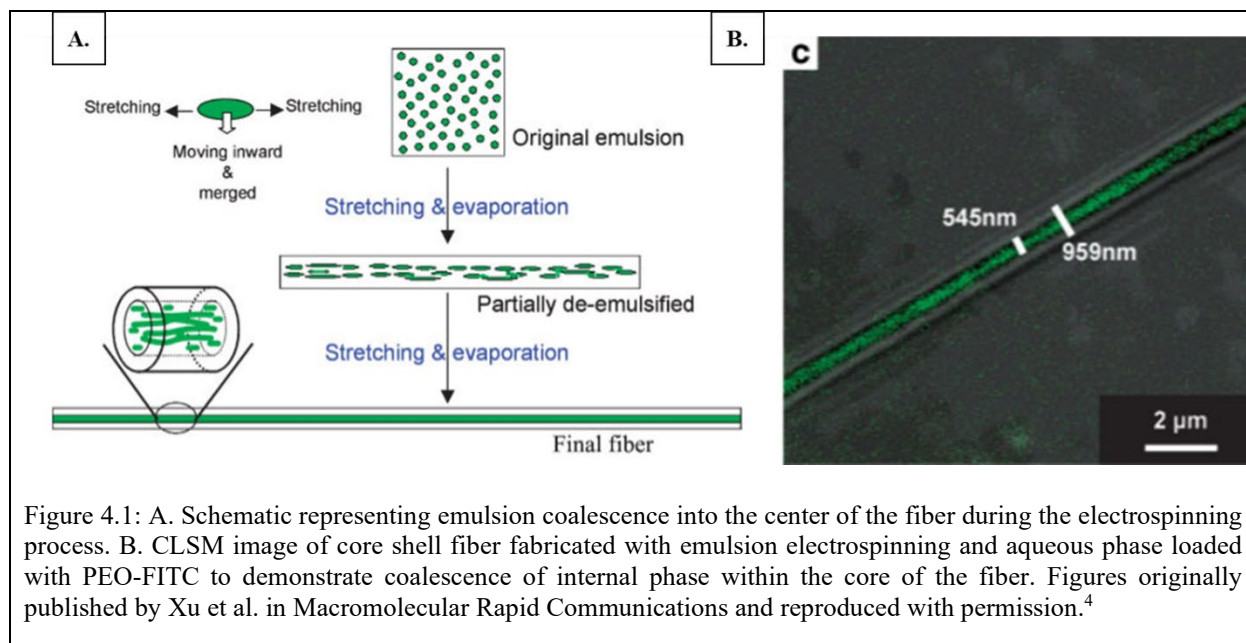
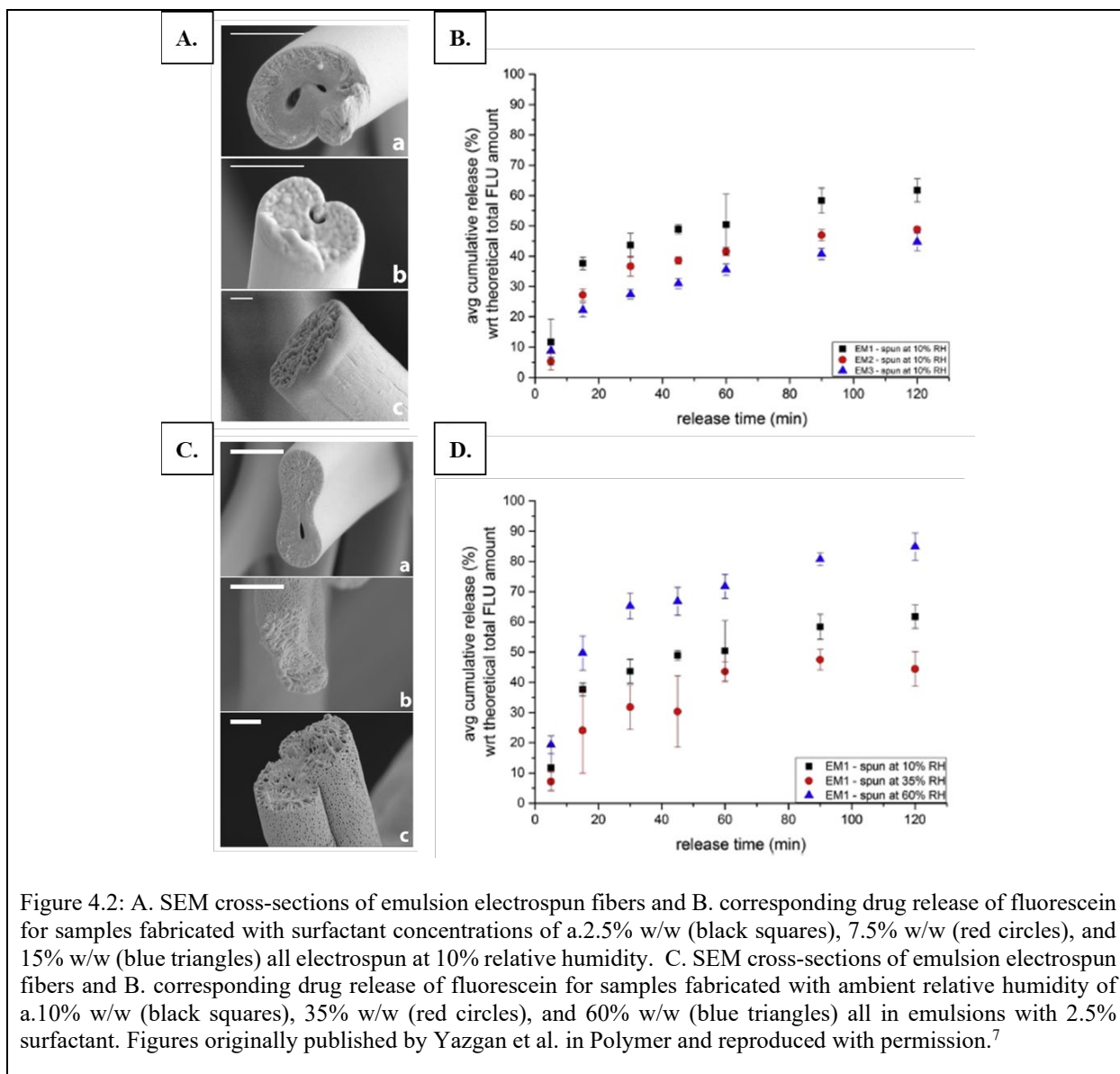


Figure 4.1: A. Schematic representing emulsion coalescence into the center of the fiber during the electrospinning process. B. CLSM image of core shell fiber fabricated with emulsion electrospinning and aqueous phase loaded with PEO-FITC to demonstrate coalescence of internal phase within the core of the fiber. Figures originally published by Xu et al. in *Macromolecular Rapid Communications* and reproduced with permission.<sup>4</sup>

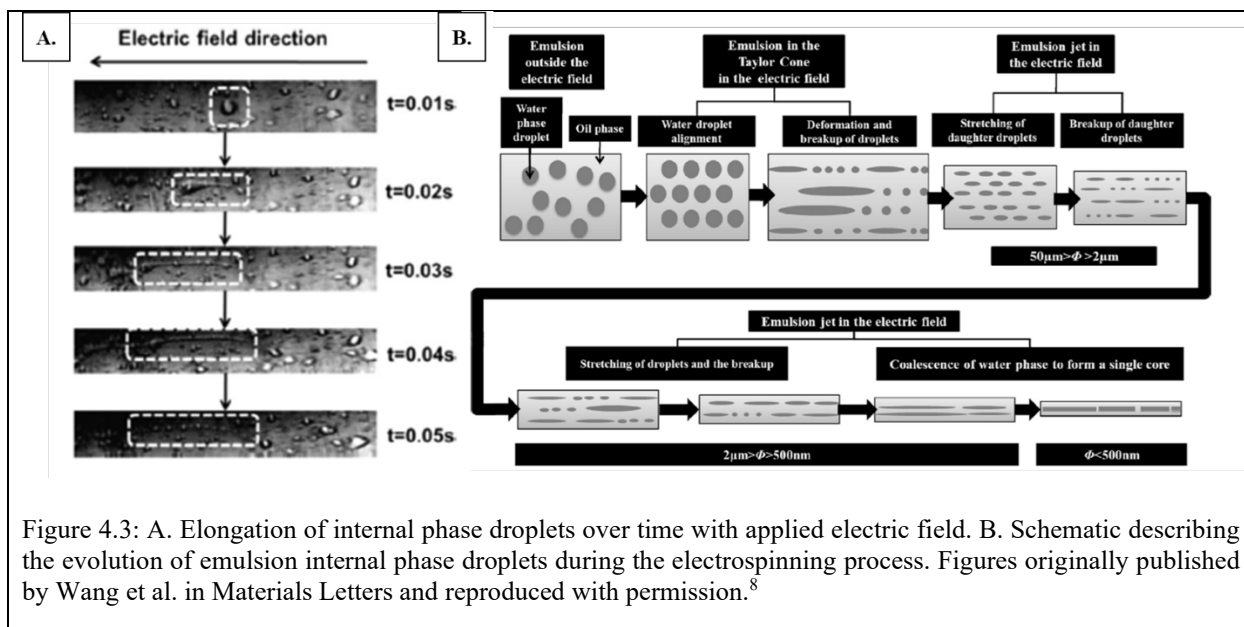
Coalescence of water droplets can be prevented by stabilizing droplets, such as by using increasing concentrations of surfactant. Yazgan et al. found that by increasing the concentration of Span 80 from 2.5% w/w to 15% w/w in a water-in-oil emulsion electrospun at 10% relative humidity, the PS in the internal phase of the electrospinning fibers transitioned from core shell to porous (Figure 4.2A).<sup>7</sup> Fibers with increasing concentration of surfactant corresponded with a slower rate of drug release (Figure 4.2B). Interestingly, using the same concentration of surfactants and electrospinning at high relative humidity, all fibers had internally porous architecture. This result indicated that the surfactant and ambient relative humidity are interrelated in the porosity of emulsion electrospun fibers and played a major role in the internal architecture of fibers. This study further showed that internal fiber porosity increased in emulsion electrospun fibers that were

electrospun at higher levels of ambient relative humidity (Figure 4.2C). Emulsion samples that were electrospun at ambient relative humidity levels of 10%, 35%, and 60% were then used to release a model drug fluorescein, and the results showed that fibers electrospun at higher ambient relative humidity with greater porosity released drug at a faster rate (Figure 4.2D).



Prior to the solidification of the fiber, the droplets within the fiber undergo stretching and can break up into smaller droplets with increased applied shear stress and electric field.<sup>1,5,8</sup> In a

study conducted by Wang et al., the longitudinal stretching of internal phase droplets was observed in emulsions under an electric field with increased stretching of the water droplets with time (Figure 4.3).<sup>8</sup> Droplets further broke up into smaller droplets upon elongation in the polymer jet due to capillary instability. As the polymer jet thinned and stretched during the electrospinning process and moved further away from the electric field, coalescence of water droplets increased and moved towards the core of the fiber. This highlights the importance of evaporation rate and degree of stretching for templating the shape and porosity of emulsion electrospun fibers.



It is essential to understand the role that internal phase plays in emulsion electrospinning to create reproducible fibers for tunable drug release systems for drug delivery and tissue engineering applications. This study aims to determine the effect that internal phase volume fraction has on emulsion electrospun fiber morphology, surface topography, fiber diameter, and distribution of fiber diameters.

## **4.2 MATERIALS AND METHODS**

### **4.2.1 Materials**

PCL (50,000  $M_w$ ) was purchased from CAPA lot # 120625. Sorbitan monooleate (Span 80) was purchased from Sigma Aldrich lot # MKCF4138. DMF solvent anhydrous with 99.8% purity was purchased from Sigma Aldrich lot # SHBJ7641.  $\text{CHCl}_3$  solvent with  $\geq 99.5\%$  purity was purchased from Sigma Aldrich lot # SHBL1580. MeOH solvent with 99.9% purity was purchased from Sigma Aldrich lot # 065112.

### **4.2.2 Polymer Solution Fabrication**

Polymer solutions were fabricated with PCL dispersed in single solvent systems of dichloromethane (DCM) and chloroform ( $\text{CHCl}_3$ ), and the dual solvent systems of 3:1  $\text{CHCl}_3$ : dimethylformamide (DMF) and 3:1  $\text{CHCl}_3$ : methanol (MeOH). Each solution was mixed for at least one hour on a stir plate with a stir bar spinning at a rate of 250 rpm, after which no solid polymer was visible in the solution. The molecular surfactant, Span 80, was added to the organic phase at 30 w/w%, mixing for at least one hour. Reverse osmosis (RO) water was added to the emulsion in 20  $\mu\text{L}$  increments, generating the internal, dispersed phase. After each incremental addition, the solution was mixed with a FlackTek Speed Mixer DAC 150.1FVZ-K for 30 seconds at a mixing speed of 2500 RPM.

### **4.2.3 Electrospun Scaffold Fabrication**

Electrospinning parameters were held constant with a Harvard Apparatus pump flow rate of 0.5 mL/h, a distance from needle tip to collection plate of 25 cm, an applied voltage of 15kV from a GAMMA high voltage research source, and a blunted 21-gauge needle. Samples were electrospun at high and low relative humidity of  $50\% \pm 10\%$  and  $10\% \pm 10\%$ , respectively, to evaluate the influence of ambient water moisture on fiber collection. At high relative humidity,

specimens were electrospun directly onto the copper collection plate, which was grounded both to the voltage source and to the fume hood. After each specimen was collected and removed from the collection plate, each was dried in the fume hood overnight. The collection plate was wiped down with chloroform followed by water before thoroughly drying between each specimen collection. Previous studies had demonstrated that delamination of the electrospun mesh and partial sticking to the collection plate could occur at low relative humidity. Therefore, the collection plate was covered in aluminum foil at low relative humidity with the grounding alligator clip wire attached to the collection plate over the foil. Specimens were further dried in a vacuum chamber prior to characterization. At least three specimens were fabricated per sample group.

#### **4.2.4 Fiber Characterization**

Electrospun mesh was analyzed using a Phenom Pro Desktop scanning electron microscope (SEM) to determine fiber morphology, surface topography, diameter, and fiber diameter distribution. All samples were coated with 8 nm of iridium prior to imaging. Fiber morphology was characterized by imaging each sample in at least five different locations to capture morphological effects using 10kV accelerating voltage, a backscatter detector, and a magnification appropriate to observe the fiber morphology. The overall morphology of the fibers was qualitatively analyzed for morphological evidence of round fibers, ribbon-like fibers, wet indistinct fibers, beading, fiber splitting, and garlands. Fiber topography was characterized by imaging with 10 kV accelerating voltage, a secondary electron detector, and a magnification of 25,000x.

Fiber diameter was determined by imaging each sample specimen in five different locations using 10kV of accelerating voltage and a backscatter detector. Mesh fabricated with the solvents  $\text{CHCl}_3$  and DCM had larger fibers, and therefore, to get a sufficient sampling of enough fibers for analysis, SEM images were captured at a magnification of 1000x. Mesh fabricated with

solvents 3:1 CHCl<sub>3</sub>: DMF and 3:1 CHCl<sub>3</sub>: MeOH had smaller fibers, and therefore, SEM images were captured at a magnification of 5000x. Each image was then analyzed with the software ImageJ using the plugin DiameterJ. From this initial segmentation, binary-colored segmented images produced with the algorithms M3, M5, M7, S2, S3, and S7 were used to determine fiber diameter and fiber diameter distribution. In a few rare cases, DiameterJ was unable to process a segmented image, in which case a segmented image produced with one of the additional algorithms that was judged to be most representative of the original image was substituted for further analysis.

The average fiber diameter for each algorithm was then used to determine the average fiber diameter per SEM image. These fiber diameters were then used for further statistical comparison between groups. For each set of sample parameters, fiber distribution histogram raw data, mean of fiber diameters, fiber diameters standard deviation, fibers skewness, and fiber kurtosis were also determined using DiameterJ. Raw fiber diameter histogram data were replotted using Graphpad Prism.

#### **4.2.5 Statistical Analysis**

The average fiber diameter for each set of sample parameters was determined from the average of each segmentation produced by ImageJ and plugin DiameterJ described above (n=15). First, a one-way ANOVA with Brown-Forsythe and Welch's tests was performed on each set of sample parameters to determine if the electrospun samples were statistically different. This was followed up with Dunnett's post hoc test. Within the same solvent systems, the effect of relative humidity on fiber diameter was determined using Welch's t-test and a 95% confidence level. The effect of solvent systems was determined using a one-way Brown-Forsythe and Welch's ANOVA with Dunnett's multiple comparison post hoc and a 95% confidence interval. This test was performed at both high and low relative humidity, respectively. All statistical tests and graphing

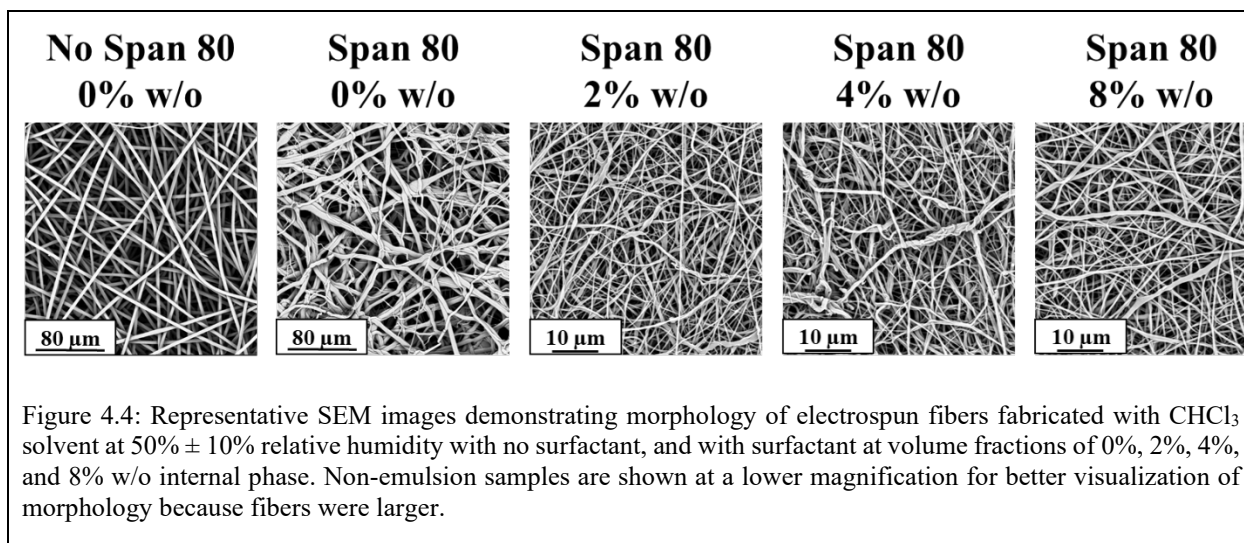
were performed using Prism Graphpad software. All statistical tests and graphing were performed using Prism Graphpad software.

## 4.3 RESULTS AND DISCUSSION

### 4.3.1 CHCl<sub>3</sub> System

#### 4.3.1.1 Fiber Morphology

Fiber morphology is a mesh characteristic influenced by surfactant, internal phase volume fraction, and solvent(s) used. Controlling fiber morphology is essential to create reproducible mesh with consistent drug release kinetics and cell response. At high relative humidity, samples electrospun with no surfactant and no internal phase had uniform morphology (Figure 4.4). No other morphological features were observed.



When surfactant was added to the system, morphologies including fused fibers, fiber branching, and fiber breaking were observed (Figure 4.5). Fused fiber morphology often occurs when fibers have had insufficient time to evaporate prior to collection on the collection plate.<sup>9,10</sup> The effect of non-ionic surfactant on electrospun fibers has been studied and there are proposed

mechanisms for their effect on fiber morphology. Fused fiber morphology was also observed in electrospun samples prepared with a surfactant, Span80, and PCL in a study by Hu et al., although the mechanism was not discussed in detail.<sup>11</sup> Non-ionic surfactants have been hypothesized to affect the surface tension in the system, the overall conductivity, and the rate of evaporation.<sup>3,12-16</sup> Wang et al. demonstrated that increasing the concentration of non-ionic surfactant Triton R X-100 decreased solution surface tension. Fiber diameter decreases with decreasing surface tension and increasing concentrations of non-ionic surfactant Triton R X-100.<sup>12</sup> In this study, the experimental data was compared to a theoretical model for a decrease in fiber radius and an increase in velocity due to force and conservation of mass. Lin et al. further showed that non-ionic surfactants with polar groups such as Triton X-405 may weakly contribute to increased conductivity in the system due to the polar groups ability to propagate charge.<sup>14</sup> Furthermore, studies by Li et al., Johnson et al., and Spano et al. have demonstrated that surfactants may move to the surface of the fiber due to charge repulsion and thermodynamic solvent preference.<sup>3,13,15</sup>



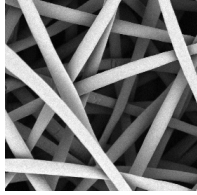
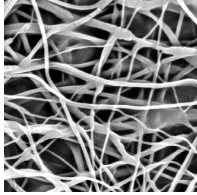
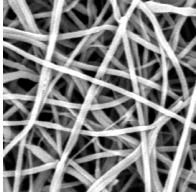
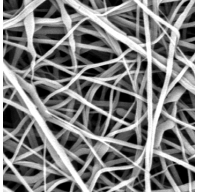

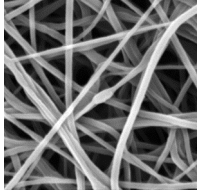
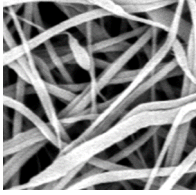
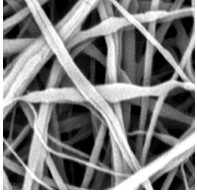
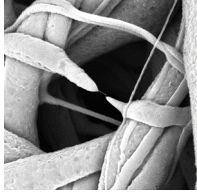
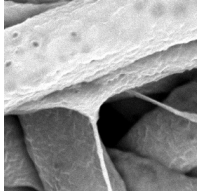
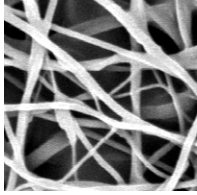
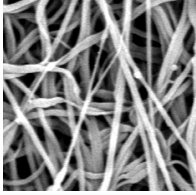
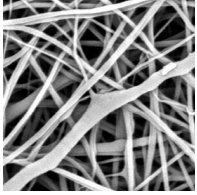
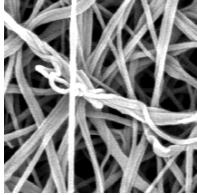
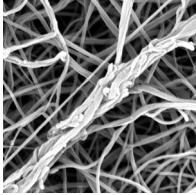
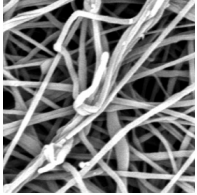
CHCL3 Selected Morphologies High RH					
	No Span 80 0% w/o	Span 80 0% w/o	Span 80 2% w/o	Span 80 4% w/o	Span 80 8% w/o
Uniform Cylinders		-			
Fused Fibers	-		-	-	-
Fiber Beading	-	-			
Fiber Breaking	-		-	-	-
Fiber Branching	-				
Garland Formation	-	-			

Figure 4.5: Representative SEM images of close-up selected fiber morphology in electrospun fibers fabricated with CHCL3 solvent at  $50\% \pm 10\%$  relative humidity with no surfactant and with surfactant at volume fractions of 0%, 2%, 4%, and 8% w/o internal phase. Setup was standardized for monolithic solution control.

These mechanisms can be applied to explain fused fiber morphology in this system because the addition of surfactant likely decreased surface tension, which would increase the acceleration of the jet from the needle tip and lead to less time for solvent evaporation. This could potentially lead to the collection of wet fibers. Span80 has hydroxyl groups that could be moderately polarized in the system to increase overall conductivity and lead to greater whipping during electrospinning, which is consistent with the smaller fiber diameter seen in this sample and the increase in the amplitude of collection. However, the presence of wet fibers indicates that any potential polarization of Span80 is moderate and changes to the system are more likely to be dominated by effects in surface tension. Furthermore, the morphology differences seen at high and low relative humidity indicate that surfactant relocation during the electrospinning process is likely slowing down the rate of evaporation, further encouraging fused fiber morphology.<sup>7,13</sup>

Branching morphology was also observed in samples electrospun with Span80 at high relative humidity (Figure 4.5). Yarin and Reneker have created comprehensive models and experimental data demonstrating that branching occurs in the electrospun jets in systems with high electrical potential differences, where a charged element of the polymer jet moves outwards from the jet in response to electrical Maxwell forces.<sup>17-19</sup> When this element moves outward from the fiber, the element will have uneven charge relative to the entire jet and will move outward from the primary jet, creating a branch as volume is conserved. In this system, at high relative humidity, water was able to enter and propagate charge differently from chloroform. This localized electrical charge difference may have contributed to small perturbations in the polymer jet, which subsequently formed branches. Furthermore, surfactant at the surface of these fibers would reduce

surface tension and, therefore, resistance to portions of the jet breaking away. Small and thin fibers were minimally observed with these sample parameters.

Broken fibers were also observed in samples electrospun with surfactant at high relative humidity (Figure 4.5). Fiber breaking morphology at high relative humidity has not been well documented or described in the field. One potential mechanism continues from the principle that surfactant lowering surface tension increases the acceleration of the jet and reduces the evaporation rate of the jet. This reduction in evaporation and increased acceleration led to the collection of wet fibers and the longitudinal orientation of polymer chains along the axis of the electrospun jet. Ero-Philips demonstrated that increasing the voltage of a jet beyond a threshold can decrease the crystallinity of PLLA electrospun fibers, and at high acceleration beyond this optimal threshold, crystallinity can be reduced due to reduced flight time.<sup>20</sup> In a study conducted by Kolbuk et al., the molecular orientation of PCL was weak within electrospun fibers and dependent on the applied voltage, concentration, and solvent type.<sup>21</sup>

Applying this to the breaking morphology in this system, due to decreased surface tension, acceleration is high, favoring orientation of the polymer along the longitudinal axis of the jet. When fibers collect on the electrospinning plate before completely drying, polymer chains in solvent can still reorient to a more thermodynamically favorable orientation: not elongated along the longitudinal axis of the fiber. Breaking morphology was seen in the fibers likely occurred due to viscoelastic contraction of the polymer chains. It is thermodynamically favorable for polymer chains to orient in the conformation that conserves entropy. Therefore, when the polymer chains are still in wet fibers, they would contract back from the elongated state formed during the electrospinning process, causing some sections of fibers to break. Breaking morphology is only observed only in sections of polymer where the broken section is over a void portion of the

scaffold. This is because when the top of fiber is laid down on previously collected fibers. The partially wet fiber will fuse at points of contact, fixing these areas, and therefore contraction of the polymer is towards these fixed points. As polymer contracts, the concentration of polymer decreases in the center of these fixed points (over unfixed voids), and this reduction in chain entanglement allows for fibers to thin until they break.

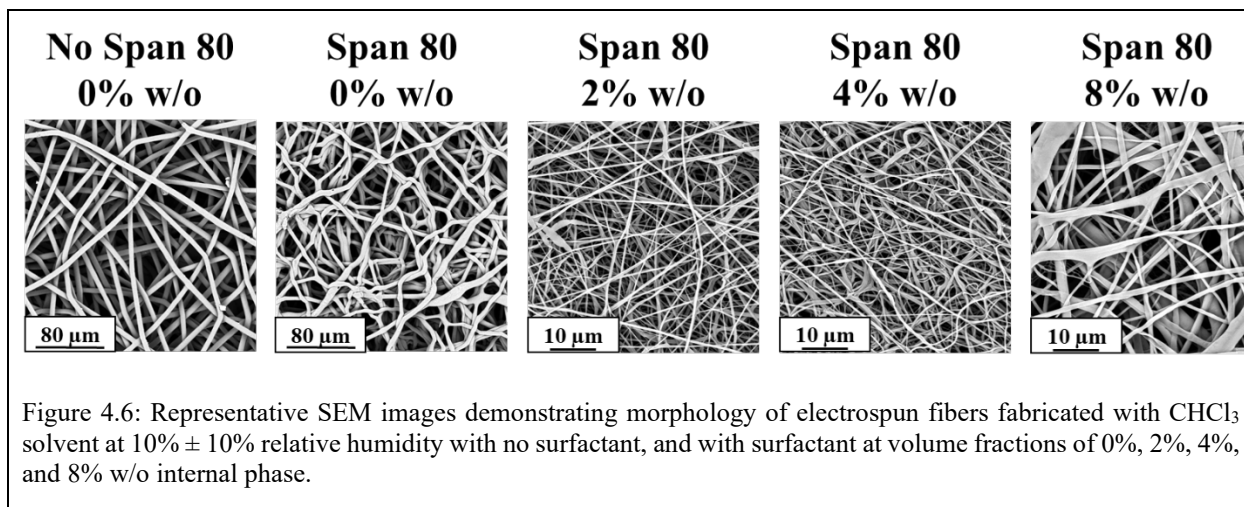
When internal phase volume fractions of 2% w/o, 4% w/o, and 8% w/o were added to the chloroform solvent system at high relative humidity, branching, beading, and garland morphologies were observed (Figure 4.5). Branching morphology in the system likely occurred due to the same mechanism described in the system with just surfactant; uneven distribution of water creating perturbations for potential branching. Reneker et al. and Yarin et al. also demonstrate that branching is more likely to occur in systems with increased whipping, especially at the bends in branches.<sup>17,18</sup> As internal phase volume fraction was added to the system, the overall conductivity of the system increased, likely leading to greater whipping.

Although most fibers were uniform and cylindrical, some evidence of beading in small fibers was observed. Beading morphology generally occurs due to the Raleigh instability where surface tension minimizes surface area in a spherical shape. Uniform fibers are achieved when polymer viscosity, molecular weight, or concentration, combined with applied voltage, are sufficient to overcome surface tension.<sup>18,22</sup> In emulsion electrospun systems, it is not uncommon for phase separation to occur when the polymer favors one solvent over another. In this case, PCL strongly prefers chloroform to water, and therefore phase separation can occur, creating polymer-rich and polymer-poor sections of electrospun fiber. If a branch occurs in an area of phase separation and one of the branches contains less polymer due to phase separation, viscosity may be insufficient to overcome surface tension and lead to beading morphology. Interestingly, as

internal phase volume fraction increases, beading morphology becomes more spindle-shaped and elongated. This change in bead shape is consistent with increasing applied voltage in the system.<sup>23</sup> Therefore, the change in bead shape may be due to increasing conductivity with increasing internal phase volume fraction.

Garlands in electrospun fibers are fibers that have been twisted together during flight to form a column of fibers on the collection plate. Garlands generally occur when multiple jets or branches from jets intersect during the electrospinning process while they are still wet.<sup>24,25</sup> In this system, surfactant at the surface of the jet may be slowing down evaporation, while increasing internal phase may be increasing the overall conductivity and encouraging branching. Further, at high relative humidity, water condensing on the surface of the jet decreases the surface charge density.<sup>26</sup> Theron et al. found that a reduction in surface charge density creates increased instability in the electrospinning jet and allows fibers to conglutinate and form garlands.<sup>25,27</sup> Therefore, in emulsion systems, when water condenses on the surface of the jet at high relative humidity, branching and instability can occur, allowing fibers to conglutinate and entangle to form garlands.

Fiber morphology of samples electrospun at low relative humidity with  $\text{CHCl}_3$  solvent, no surfactant, and no internal phase were uniform and cylindrical in morphology (Figure 4.6). This indicates that relative humidity alone does not play a major role in fiber morphology changes for fibers without surfactant or relative humidity and with uniform processing parameters.



Samples electrospun in  $\text{CHCl}_3$  solvent at low relative humidity with surfactant and 0% w/o internal phase demonstrated fused fiber and broken fiber morphology (Figure 4.7). The mechanism for fused fibers and broken fibers is similar to the mechanism at high relative humidity; increased surfactant increasing acceleration and decreasing evaporation and viscoelastic contraction, respectively.

		CHCL3 Selected Morphologies Low RH				
		No Span 80	Span 80	Span 80	Span 80	Span 80
		0% w/o	0% w/o	2% w/o	4% w/o	8% w/o
Uniform Cylinders	Uniform Cylinders		-			
	Fused Fibers	-		-	-	-
	Fiber Beading	-	-			
	Fiber Breaking	-		-		
	Film Filled Voids	-	-			
	Ribbon Morphology	-	-			
	Nano Webbing	-	-	-	-	

Figure 4.7: Representative SEM images of close-up selected fiber morphology in electrospun mesh fabricated with CHCl<sub>3</sub> solvent at 10% ± 10% relative humidity with no surfactant, and with surfactant at volume fractions of 0%, 2%, 4%, and 8% w/o internal phase.

In systems electrospun at low relative humidity with  $\text{CHCl}_3$  solvent, surfactant, and internal phase volume fractions of 2%, 4%, and 8% w/o, most of the fibers were uniform in a cylindrical morphology (Figure 4.6). However, morphologies of fiber beading, film filled voids, and ribbon morphology were also observed (Figure 4.7). The mechanism proposed for beading morphology at low relative humidity is the same as described for beading occurring at high relative humidity.

Samples electrospun at low relative humidity with  $\text{CHCl}_3$  solvent and with internal phase volume fractions of 2% w/o and 4% w/o fiber breaking morphology was also observed (Figure 4.7). The mechanism for breaking morphology is the same as described for samples with surfactant and no internal phase.

An interesting morphology was observed in some of the samples electrospun with 8% w/o internal phase volume fraction. This morphology included the presence of nano netting or nano webbing usually adjacent to flat ribbon-shaped fibers. Zaarour and Li et al. hypothesized that large differences in vapor pressure of solvent trapped within the skin of an electrospun fiber can cause solvent to “explode” from the fibers to escape.<sup>15,28</sup>

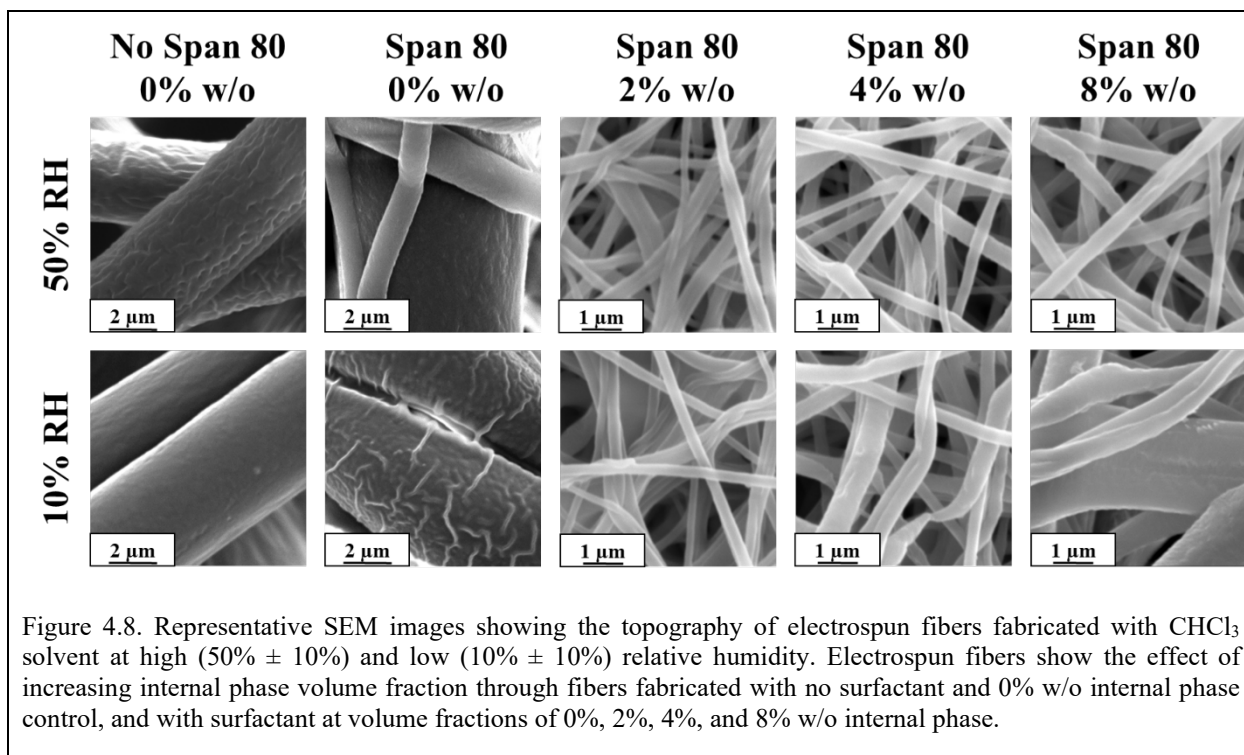
Based on all of the described mechanisms, it is possible that the ribbon fiber morphology was caused by coalescence of internal phase within the fiber during electrospinning. At low relative humidity, solvent evaporation from the surface of the jet, especially with a highly volatile solvent like chloroform, would occur rapidly, creating a skin shell structure. After the fibers collected on the collection plate, larger fibers with the higher internal phase core collapsed into ribbon morphology as they started to dry. As ribbons began to collapse, liquid polymer solution still trapped within the fibers may have exploded through weaknesses in the shell into the surrounding mesh. In some cases, when the polymer solution exploded from the jet, sufficient charge was on neighboring fibers to create a localized electric field, which caused the formation



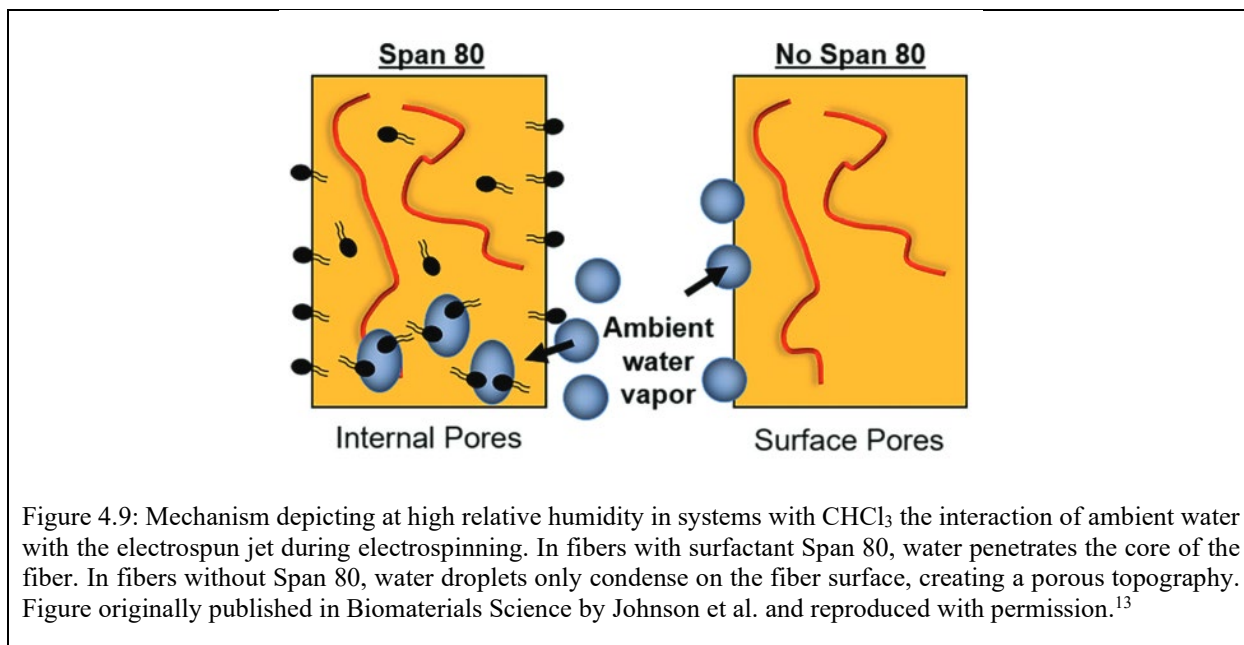
of nanonets. That may have occurred in samples with high internal phase volume fraction because increased water in the system allowed for increased charge and, therefore, potentially more charge on the overall fiber to create the localized electric field. Another possible mechanism described by Barakat and Massaglia is attraction to near neighbor jets during electrospinning, encouraging nano webbing morphology, but these studies were done with solutions containing electrically conductive elements such as salts.<sup>29,30</sup> This is because salts are ionized molecules with polarized charge are capable of attracting charge with conservation of volume from neighboring fibers during electrospinning and from interconnected webs. The morphology of these nets appeared to cover multiple pore areas, unlike the ones observed in this system, and are further described in Chapter 1.

#### *4.3.1.2 Fiber Surface Topography*

Fiber surface topography is a mesh characteristic influenced by surfactant, internal phase volume fraction, and solvent(s) used. Surface topography is important to control because it can influence the interaction with the surrounding fluid, drug release, and cell response. Electrospun fibers were characterized for surface topography through qualitative analysis of SEM images. Fibers electrospun at high relative humidity ( $50\% \pm 10\%$ ) demonstrated a porous surface topography when no surfactant was present in the system and a smooth topography with surfactant and internal phase in the system (Figure 4.8). Smooth fiber topography may be due to surfactant relocating to the surface of the fiber, lowering the vapor induced phase separation occurring between the chloroform solvent and immiscible water condensing on the surface of the jet from ambient relative humidity. This mechanism is described by and is consistent with studies conducted by Yazgan et al.<sup>7</sup>



Although most fibers were smooth at high relative humidity when electrospun with surfactant Span80, a range of topographies were observed, as discussed in Chapter 3. The porous topography in the control sample with no surfactant and no internal phase was likely due to ambient water vapor condensing on the surface of the fiber, causing precipitation of polymer upon contact and templating the porous architecture. As discussed in Chapter 2, chloroform is a hydrophobic solvent and therefore would create a barrier preventing ambient hydrophilic water vapor from penetrating into the fiber due to solvent miscibility. The smooth surface topography observed in samples with surfactant and emulsion samples was likely due to ambient water vapor both encouraging surfactant to relocate at the oil-air interface at the surface of the fibers and surfactant, promoting water vapor penetration into the fiber during the electrospinning process (Figure 4.9).<sup>13</sup>



The surface topography of fibers electrospun at high relative humidity with increasing internal phase volume fractions was smooth (Figure 4.8) due to sufficient surfactant remaining at the surface of the fibers to disrupt the vapor induced phase separation observed by water condensing on the surface of the jet.

Fibers from all groups except the surfactant control that were electrospun at low relative humidity had smooth surface topography (Figure 4.8). Samples that were electrospun at low relative humidity with surfactant and no internal phase had wrinkles or neck sections perpendicular to the longitudinal axis of the fiber. To the best of my knowledge, no other group has published similar surface topography for PCL electrospun fibers. Therefore, the following mechanism is proposed. At low relative humidity, solvent evaporates quickly from the fibers creating a solid outer shell. Surfactant in the system lowers surface tension which increases the jet's acceleration rate towards the plate. During this flight to the collection plate, a high strain rate is applied to the fiber with the solid shell resulting in some stretching and necking on the surface of the fiber

creating the lateral wrinkle morphology. A similar lateral wrinkled morphology has been observed in electrospun fibers after undergoing mechanical strain rates.<sup>31,32</sup>

All other fibers electrospun at low relative humidity with internal phase volume fractions of 2% w/o, 4% w/o, and 8% w/o had smooth surface topography because there was no ambient water vapor to template surface pores or induce VIPs.

#### *4.3.1.3 Fiber Diameter and Distribution*

Fiber diameter and distribution of fibers are mesh characteristics influenced by surfactant, internal phase volume fraction, and solvent(s) used. Fiber diameter and distribution are important parameters in controlling drug release and cell response. Fiber diameters and distribution are shown in Figure 4.10. At high relative humidity, the average fiber diameter for control samples with no surfactant and no internal phase was  $4.16 \pm 1.07 \mu\text{m}$  (Figure 4.10). In samples containing surfactant with internal phase volume fractions of 0%, 2%, 4%, and 8% w/o the average fiber diameter was  $3.65 \pm 1.97 \mu\text{m}$ ,  $0.42 \pm 0.16 \mu\text{m}$ ,  $0.42 \pm 0.16 \mu\text{m}$ , and  $0.45 \pm 0.17 \mu\text{m}$ , respectively. The diameter of distributions consisted of a single evenly distributed peak with no surfactant and no internal phase, two peaks and a slight positive distribution with surfactant and no internal phase, and a positive single peak skewed for samples containing 2%, 4%, 8% w/o internal phase. The overall skew and kurtosis for each set of sample parameters also confirm this distribution, and histogram representation of fiber diameter distribution, shown in Table 4.1 below.

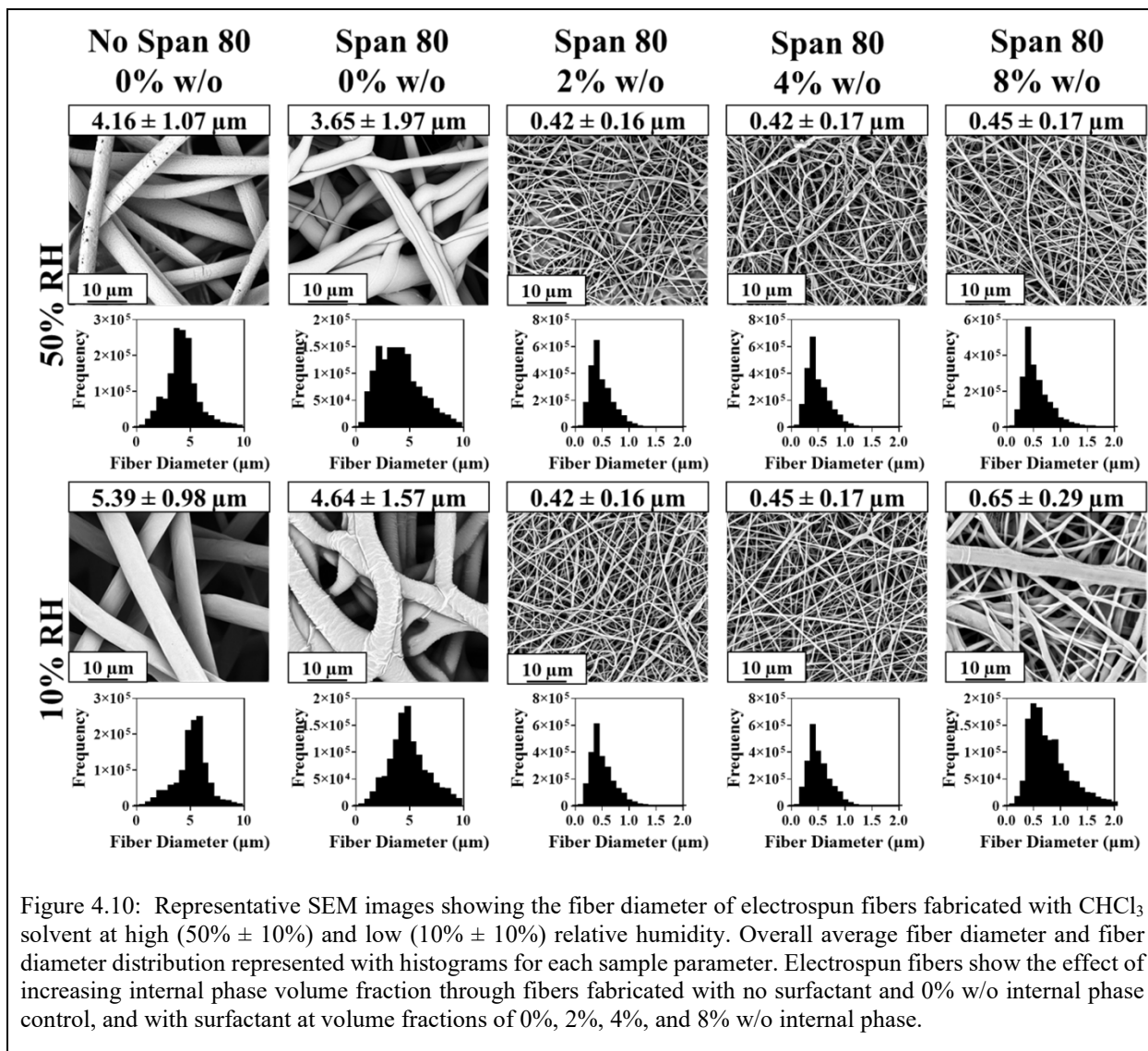
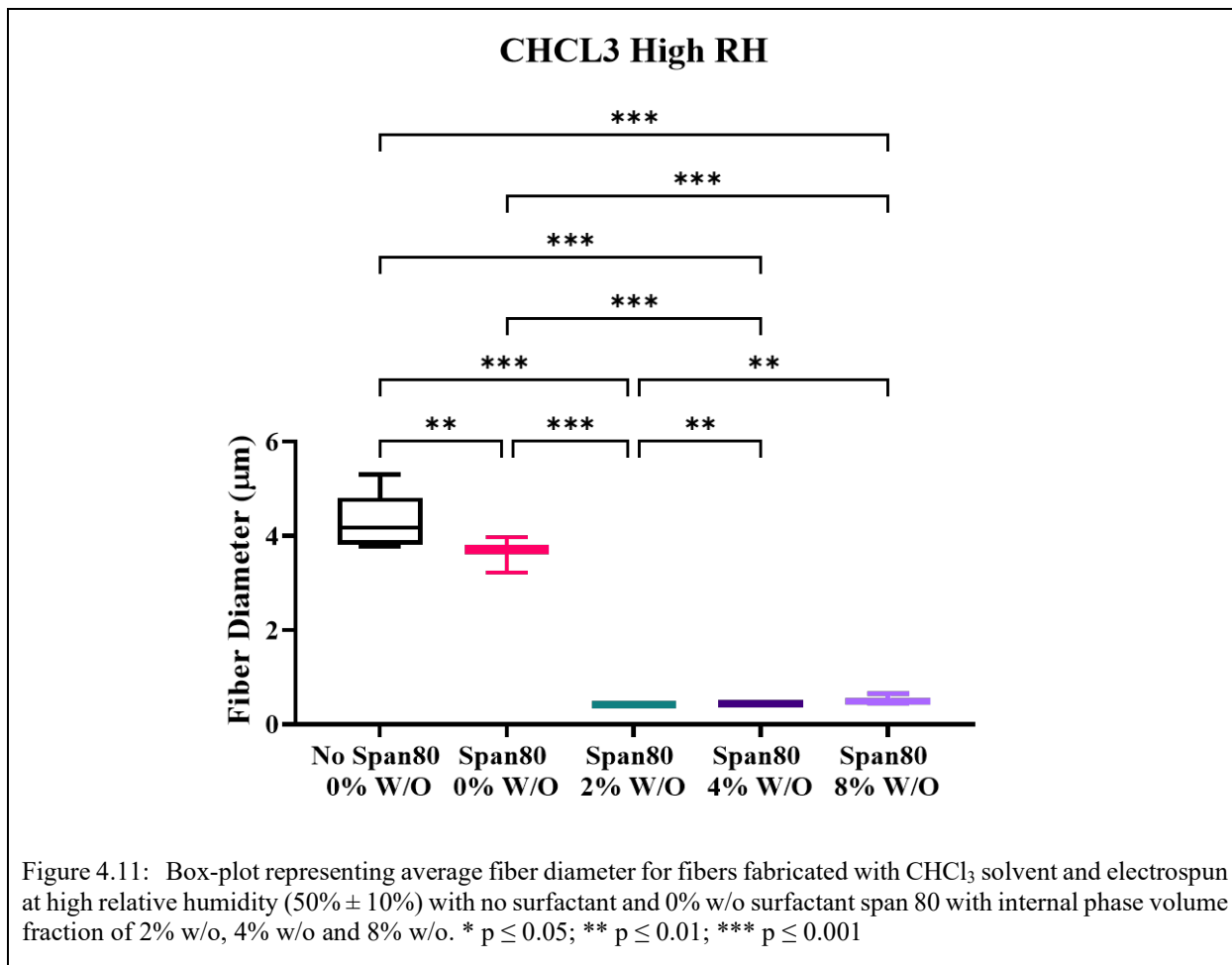


Figure 4.10: Representative SEM images showing the fiber diameter of electrospun fibers fabricated with  $\text{CHCl}_3$  solvent at high ( $50\% \pm 10\%$ ) and low ( $10\% \pm 10\%$ ) relative humidity. Overall average fiber diameter and fiber diameter distribution represented with histograms for each sample parameter. Electrospun fibers show the effect of increasing internal phase volume fraction through fibers fabricated with no surfactant and 0% w/o internal phase control, and with surfactant at volume fractions of 0%, 2%, 4%, and 8% w/o internal phase.

Fiber diameter at high relative humidity significantly decreased when surfactant was added to the system (Figure 4.11). This decrease in fiber diameter was likely due to surfactant slowing down the evaporation rate from the fiber and thus allowing for greater stretching of the fiber during the whipping process prior to solidification.<sup>7</sup> Surfactant also allowed water to penetrate the fiber, increasing the overall conductivity of the system and allowing for a greater amplitude of whipping and, therefore, more stretching of the fiber. Another factor that likely played a role is the reduction in surface tension, which likely reduced the width of the Taylor cone, allowing for thinning to occur in the stable region of the jet.<sup>12</sup> The splitting of some fibers at high relative humidity may

also have contributed to the overall lower fiber diameter and the two-peak distribution of fibers. This two peak distribution further confirms the morphology of fiber branching in this sample.

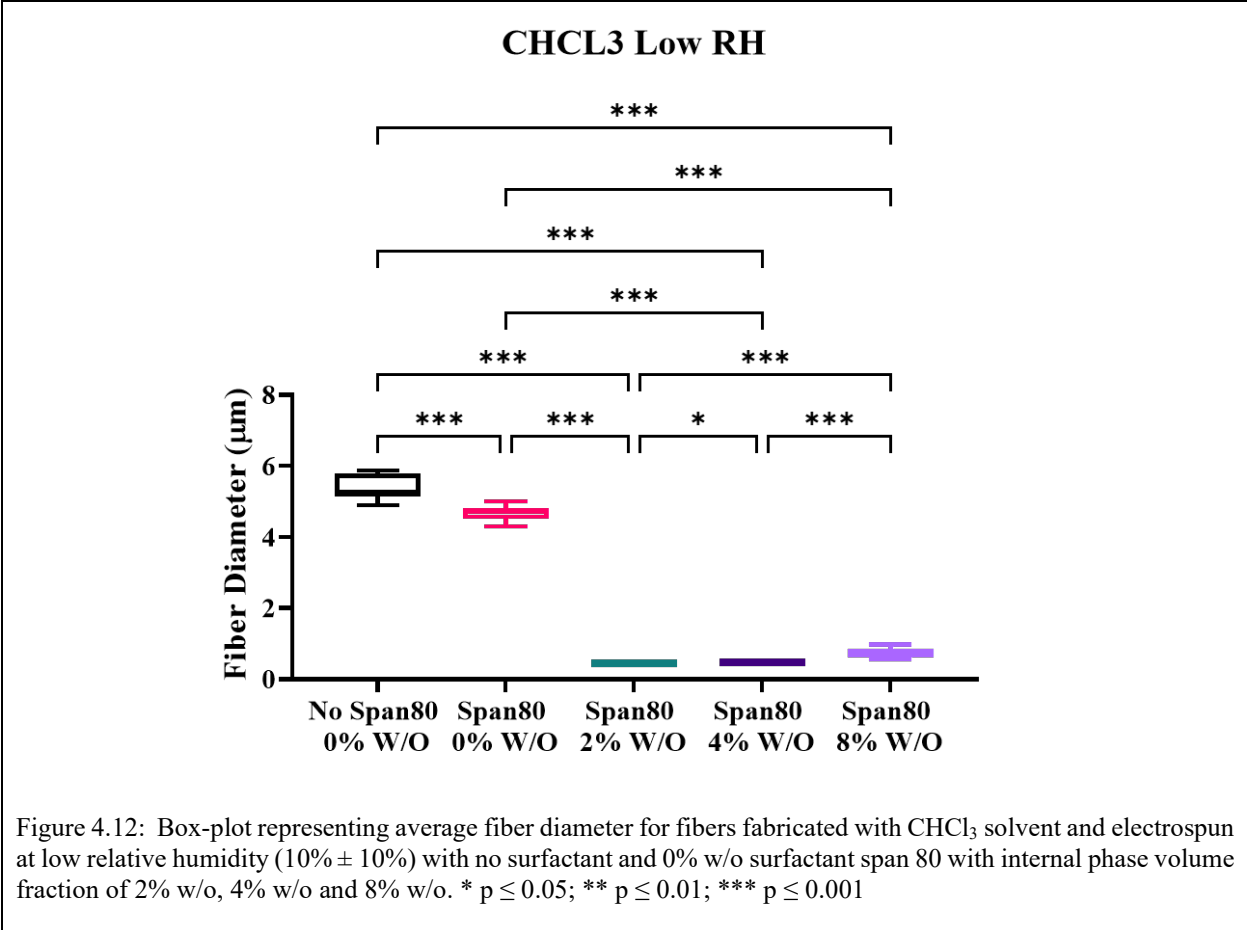


When internal phase was added to the system, fiber diameter statistically decreased compared to controls containing no internal phase (Figure 4.11). This reduction in fiber diameter was likely due to the presence of highly conductive water within the fiber, increasing the overall conductivity and thus increasing whipping and stretching of the electrospinning jet. Fiber diameter increased minimally and was statistically different in samples with increasing internal phase volume fractions of 2% w/o to 4% w/o and 2% to 8% w/o (Figure 4.11). This increase in fiber diameter was likely due to increased jet stabilization with more water evenly dispersed within the

fiber to prevent fiber branching.<sup>33</sup> Furthermore, studies show that below a threshold, increasing internal phase volume fraction generally increases viscosity which also is generally correlated to increasing fiber diameter.<sup>34</sup> Although the overall change in fiber diameter with increasing internal phase volume fraction was minimal, the statistical increase in fiber diameter highlights how even small changes in the amount of internal phase volume can affect the collected fiber.

At low relative humidity, the fibers for control samples with no surfactant and no internal phase had an average fiber diameter of  $5.39 \pm 0.98 \mu\text{m}$  (Figure 4.10). In samples containing surfactant with internal phase volume fractions of 0%, 2%, 4%, and 8% w/o the average fiber diameter was  $4.64 \pm 1.57 \mu\text{m}$ ,  $0.43 \pm 0.17 \mu\text{m}$ ,  $0.45 \pm 0.17 \mu\text{m}$ , and  $0.65 \pm 0.29 \mu\text{m}$ , respectively. The distribution of diameters consisted of a single evenly distributed peak in samples with no internal phase both with and without surfactant and a positive skew single peak for samples containing surfactant and 2%, 4%, 8% w/o internal phase. The fiber diameter skew and kurtosis can be found in Table 4.1 below.

Fiber diameter statistically decreased when surfactant was added to the system at low relative humidity (Figure 4.12). This decrease in fiber diameter was likely due to a reduction in surface tension as described above. Unlike the samples electrospun at high relative humidity, fiber diameter was relatively homogeneous across samples, and therefore the distribution of fibers was approximately normally distributed. This consistency in fiber distribution was due to the absence of small branches caused by water condensing on the surface of the jet and reducing the surface charge density.<sup>26,27</sup>



In systems with low relative humidity, when internal phase was added to the system, fiber diameter statistically decreased compared to controls containing no internal phase and no surfactant (Figure 4.12). This reduction in fiber diameter was likely due to the presence of highly conductive water within the fiber, increasing the overall conductivity and thus increasing whipping and stretching of the electrospinning jet. Fiber diameter increased and was statistically different for each sample with increasing internal phase volume fractions of 2% w/o, 4% w/o, and 8% w/o. This increase in fiber diameter was likely due to stabilization of the jet with a more evenly dispersed conductive water phase as internal phase volume fraction increased as described in the high relative humidity system. Although the overall change in fiber diameter with increasing internal phase volume fraction was minimal, the statistical increase in fiber diameter highlights

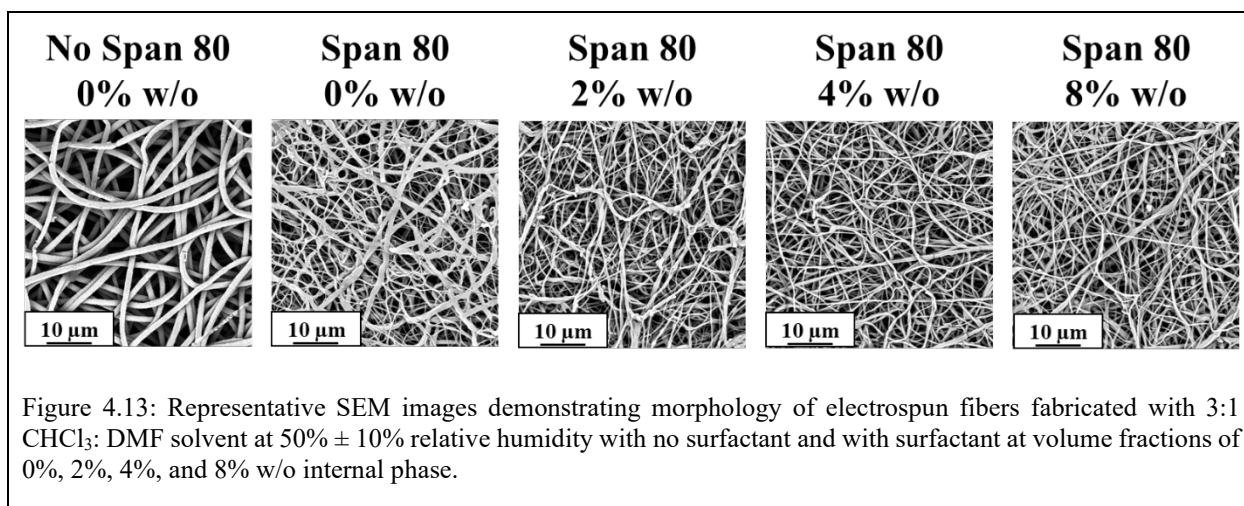


how even small changes in the amount of internal phase volume and added conductivity can affect the collected fiber. Compared to samples collected at high relative humidity, all these samples were statistically different, indicating that water vapor penetrating the fiber at high relative humidity may also be playing a role in the fiber diameter.

### 4.3.2 3:1 CHCl<sub>3</sub>: DMF Solvent System

#### 4.3.2.1 Fiber Morphology

The morphology of fibers electrospun at high relative humidity with no surfactant and no internal phase was uniform cylindrical fibers (Figure 4.13). This demonstrates that at high relative humidity, 3:1 CHCl<sub>3</sub>: DMF is a good solvent, and the processing parameters used to produce these control samples were within acceptable ranges. The addition of DMF in this system increased the overall conductivity of the system compared to CHCl<sub>3</sub> and therefore encouraged increased whipping and stretching of the fiber during electrospinning.



Fibers fabricated with surfactant and no internal phase had fiber morphologies of fused fibers, film filled voids, and ribbon-shaped fibers (Figure 4.14). The fused fiber morphology was likely due to the same mechanism described in fibers electrospun at high relative humidity with CHCl<sub>3</sub>: surfactant added to the system decreased surface tension and increased jet acceleration and

while relocating to the surface of the fiber to further decrease the rate of solvent evaporation. The ribbon morphology likely formed because the volatile  $\text{CHCl}_3$  solvent probably evaporated first, encouraging the formation of a polymer skin around the outside of the fiber. Once the fiber landed on the collection plate. The skin collapsed as the remaining solvent evaporated, and the Coulomb force was sufficient to laterally elongate the polymer shell to form a ribbon-like fiber morphology. This wet collection and presence of ribbon fibers may have contributed to the formation of film filled voids in these fibers. Polymer film filled voids are macroscopic pores within the mesh that had been filled with a polymer membrane. In some cases, as wet fibers dried on the collection plate, internal polymer solution leaked out of the fibers to near neighbor pores, creating a polymer filled void.

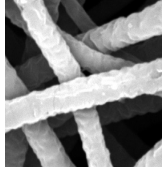
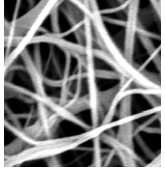
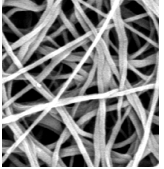
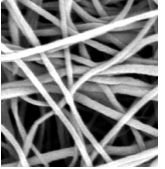
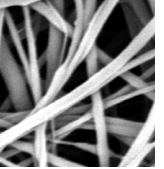
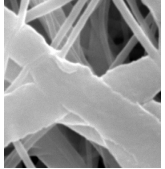
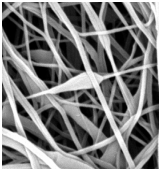
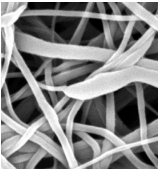
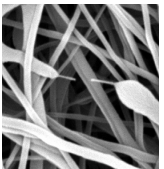
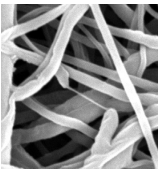
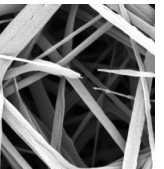
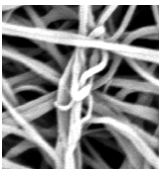
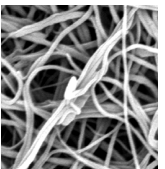
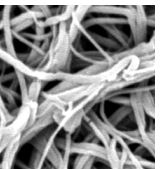
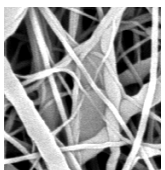
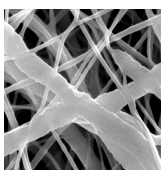
		3:1 CHCL <sub>3</sub> :DMF Selected Morphologies High RH					
		No Span 80	Span 80	Span 80	Span 80	Span 80	
		0% w/o	0% w/o	2% w/o	4% w/o	8% w/o	
<b>Uniform Cylinders</b>  <b>Fused Fibers</b>  <b>Fiber Beading</b>  <b>Fiber Breaking</b>  <b>Garland Formation</b>  <b>Film Filled Void</b>  <b>Ribbon Morphology</b>							
		<p style="text-align: center;">-</p>		<p style="text-align: center;">-</p>	<p style="text-align: center;">-</p>	<p style="text-align: center;">-</p>	
		<p style="text-align: center;">-</p>	<p style="text-align: center;">-</p>			<p style="text-align: center;">-</p>	
		<p style="text-align: center;">-</p>	<p style="text-align: center;">-</p>				
		<p style="text-align: center;">-</p>	<p style="text-align: center;">-</p>				
		<p style="text-align: center;">-</p>		<p style="text-align: center;">-</p>	<p style="text-align: center;">-</p>	<p style="text-align: center;">-</p>	
		<p style="text-align: center;">-</p>		<p style="text-align: center;">-</p>	<p style="text-align: center;">-</p>	<p style="text-align: center;">-</p>	

Figure 4.14: Representative SEM images of close-up selected fiber morphology in electrospun fibers fabricated with 3:1 CHCl<sub>3</sub>:DMF solvent at 50% ± 10% relative humidity with no surfactant, and with surfactant at volume fractions of 0%, 2%, 4%, and 8% w/o internal phase.

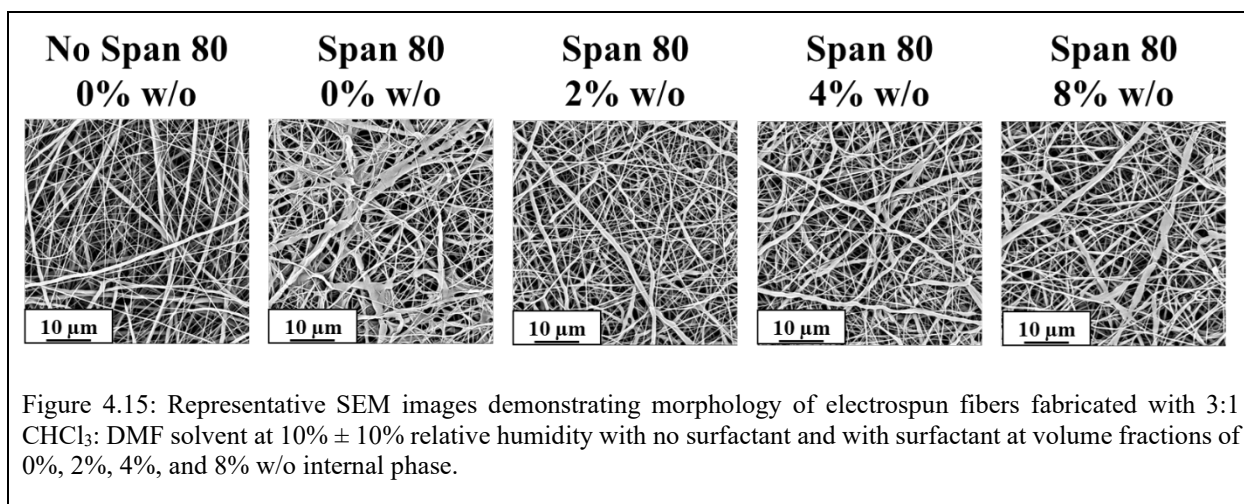
When internal phase was added to the system, the fiber morphology was predominantly uniform cylinders (Figure 4.13). However, morphologies of fiber beading, fiber breaking, garland formation, and ribbon morphology were also observed in the samples (Figure 4.14). Beading morphology was observed in samples with 2% w/o and 4% w/o internal phase volume fraction. The formation of beading may have been due to phase separation within the emulsion, creating polymer-rich and polymer-poor sections. Beading morphology is not observed in samples electrospinning with 8% w/o, which could indicate that sufficient internal phase was added to the system to create an even core within the center of the fiber.

Fiber breaking morphology was observed in samples electrospun with internal phase volume fractions of 2% w/o, 4% w/o, and 8% w/o (Figure 4.14). As described in detail in the CHCl<sub>3</sub> morphology section, fiber breaking can occur under high acceleration where polymer chains elongate along the longitudinal axis of the jet during electrospinning. When collecting wet on the electrospinning plate, the viscoelastic contraction of the polymer can cause fibers to break. Breaking morphology was observed in samples electrospun at high relative humidity with internal phase with 3:1 CHCl<sub>3</sub>: DMF solvent and not samples with the same conditions and CHCl<sub>3</sub> solvent. This may have been due to the higher conductivity of the DMF solvent increasing whipping, and therefore increased shear stress would be applied to the polymer jet, the lower viscosity of 3:1 CHCl<sub>3</sub>: DMF solvent may also have been insufficient to overcome surface tension.

Garland morphology was observed in samples electrospun with internal phase volume fractions of 2% w/o, 4% w/o, and 8% w/o (Figure 4.14). The mechanism for garland formation is similar to the mechanism described at high relative humidity and internal phase in the CHCl<sub>3</sub> solvent. At high relative humidity, the rate of solvent evaporation is decreased, and therefore wet

fibers that intersect during electrospinning can conglutinate and entangle to form garlands. Fiber branching may have also occurred in the system due to unequal charge attributed to emulsion droplets within the polymer jet. Fiber branching was not observed in the SEM images collected, but it is possible that this formation was simply missed. Another possible explanation for the presence of garlands and the entanglement of polymer jets during electrospinning is the increased conductivity from the DMF solvent and internal phase. Internal water phase may have created multiple jets at the needle tip or branching in the bending region. Multiple jets are often observed in systems with high voltage or with solutions with higher dielectric constants.<sup>35,36</sup>

At low relative humidity, electrospun fibers fabricated with 3:1  $\text{CHCl}_3$ : DMF solvent, no surfactant, and no internal phase had uniform cylindrical morphology (Figure 4.15). This uniform cylindrical morphology was also the predominant fiber morphology for samples electrospun with internal phase.



Within samples electrospun at low relative humidity with no surfactant and no internal phase, morphologies of fiber, beading, fiber breaking, and fiber branching were also observed (Figure 4.16). Increased branching morphology may be attributed to increased conductivity charge

from DMF solvent. While at high relative humidity, water condensing on the surface of the charge helped evenly distribute surface charge and reduced net charge density. The lack of ambient water condensation on the outside of the fiber could lead to unequal distribution of and excess charge. The solvents in this system, DMF and  $\text{CHCl}_3$ , propagate charge at different rates as evident by their dielectric constant, and this could create perturbations in the polymer jet during electrospinning causing branching morphology. PCL is more soluble in  $\text{CHCl}_3$  than in DMF, and therefore it is also possible that some phase separation occurred in which polymer-rich and polymer-poor regions occurred in the polymer jet. These regions with higher concentrations of a specific solvent could create an unequal charge to facilitating branching. Furthermore, if a branch from the fiber contained sufficient polymer concentration to overcome surface tension through the viscoelasticity, then beading morphology will occur. Beading morphology in the main jet may also be due to NIPS.

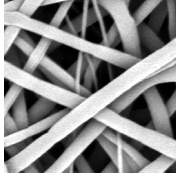
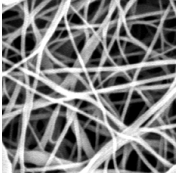
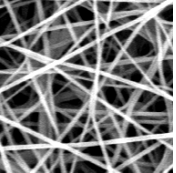
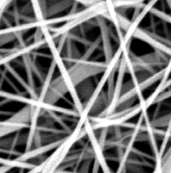
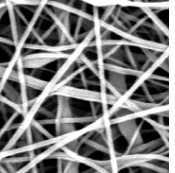
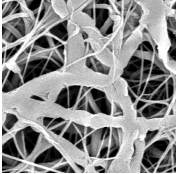
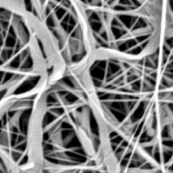
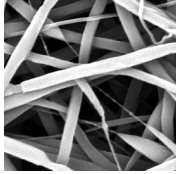
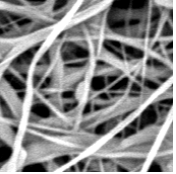
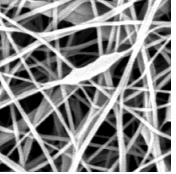
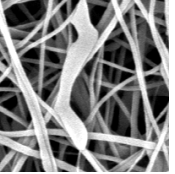
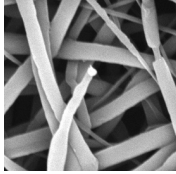
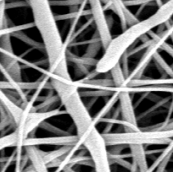
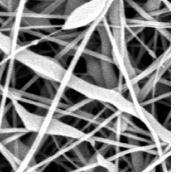
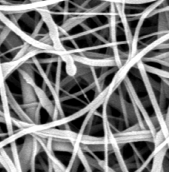
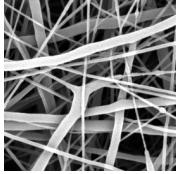
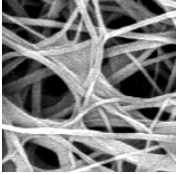
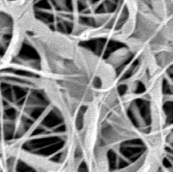
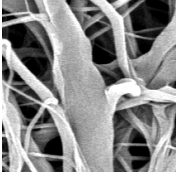
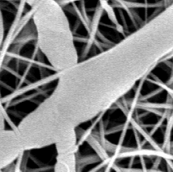
		3:1 CHCL <sub>3</sub> :DMF Selected Morphologies Low RH				
		No Span 80	Span 80	Span 80	Span 80	Span 80
		0% w/o	0% w/o	2% w/o	4% w/o	8% w/o
<b>Uniform Cylinders</b>  <b>Fused Fibers</b>  <b>Fiber Beading</b>  <b>Fiber Breaking</b>  <b>Fiber Branching</b>  <b>Film Filled Voids</b>  <b>Ribbon Morphology</b>						
	-			-	-	
		-				
		-				
		-	-	-	-	
	-			-	-	
	-			-	-	

Figure 4.16: Representative SEM images of close-up selected fiber morphology in electrospun fibers fabricated with 3:1 CHCl<sub>3</sub>: DMF solvent at 10% ± 10% relative humidity with no surfactant, and with surfactant at volume fractions of 0%, 2%, 4%, and 8% w/o internal phase.

Fiber breaking at low relative humidity in samples with no surfactant and no relative humidity may have been due to the rapid evaporation of DMF solvent from the fiber creating a polymer skin on the outside of the electrospinning jet. As the electrospinning jet is whipped back and forth, the shear rate on this thin film may cause necking in specific areas, and upon drying, viscoelastic contraction can cause the neck area to break. Within this set of sample parameters, necking-like morphology, which may be attributed to shear stress on the fiber, was observed. This necking stretch fiber can also be seen on the right-hand side of the close-up morphology fiber breaking SEM image in Figure 4.16. Another possible explanation for many of these fiber morphologies is that at low relative humidity, polymer solutions containing two solvents in which one solvent is more volatile than the other can sometimes result in the more volatile solvent creating a film that can intermittently clog the polymer jet.<sup>37,38</sup> Clogging in the jet can create branching morphology, multiple jets, beading, and may cause branches to break. However, if clogging were occurring in the sample, more morphology defects would have been anticipated, and complete clogging would have been more likely to have occurred during the one-hour electrospinning process. In these samples, complete clogging of the polymer jet was not observed.

Samples electrospun at low relative humidity with 3:1 CHCl<sub>3</sub>: DMF solvent with surfactant and no internal phase demonstrated morphologies of fused fiber, film filled voids, and ribbon morphology (Figure 4.16). Fused fiber morphology may have been due to the same mechanism described at high relative humidity. Surfactant lowers the surface tension and reduces the rate of evaporation of the polymer jet, allowing for fibers to collect wet on the collection plate and fused together. Ribbon morphology is likely due to rapid solvent evaporation of DMF forming a polymer skin on the outside of the polymer jet during electrospinning. When fibers dry on the electrospinning collection plate, this polymer skin that was formed on the outside of the polymer



jet flattens as solvent evaporates, creating a ribbon-like morphology. As solvent evaporates from the ribbon morphologies and other wet fibers, sometimes polymer solution can spill out of the jet and into neighboring scaffold pores, creating a film filled void.

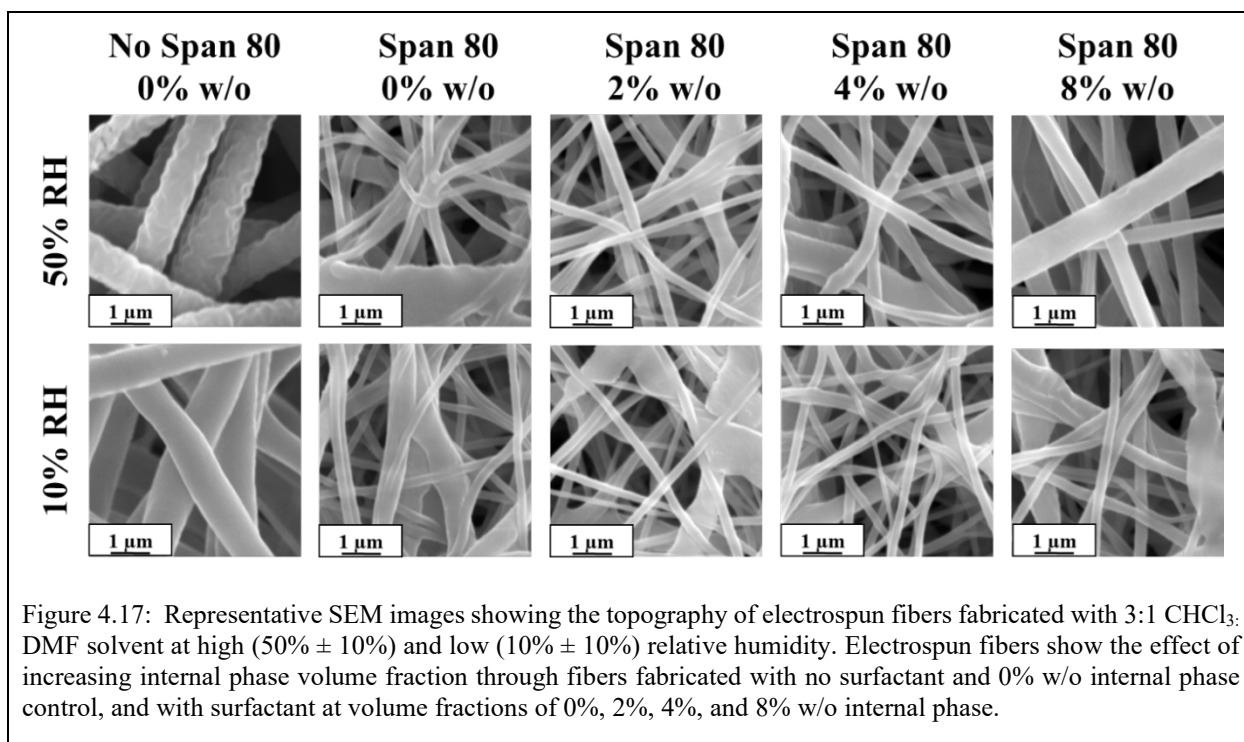
Fibers electrospun at low relative humidity with solvent 3:1 CHCl<sub>3</sub>: DMF containing surfactant and internal phase volume fractions of 2% w/o, 4% w/o, and 8% w/o demonstrated fiber morphologies including, fused fibers, fiber, beading, fiber breaking, film filled voids, and ribbon morphology (Figure 4.16). All internal phase volume fractions exhibited fiber, beading, and fiber breaking. Fiber beading and fiber breaking morphology may have been due to the same mechanism as in high relative humidity. Briefly, fiber breaking is likely due to the rapid acceleration of the jet along with a wet fiber collection and viscoelastic contraction of polymer within fibers. Beading is likely due to NIPS creating polymer-rich and polymer-poor regions and the polymer-poor regions having insufficient polymer viscoelastic force to overcome surface tension.

Only the fibers electrospun internal phase volume fractions of 2% w/o exhibited morphologies of fused fibers, film filled voids, and ribbon morphology (Figure 4.16). These morphologies are likely attributed to surfactant lowering surface tension, causing increased acceleration in the jet, and reduced the rate of solvent evaporation, causing polymer fibers to collect wet on the electrospinning plate. Interestingly, the fiber morphology seen in internal phase volume fractions of 2% w/o is similar to that seen in 0% w/o, indicating that 2% w/o may not be playing a dominant role with these parameters.

#### *4.3.2.2 Fiber Surface Topography*

The surface topography of electrospun fibers fabricated with 3:1 CHCl<sub>3</sub>: DMF at high relative humidity with no surfactant and no internal phase was wrinkled (Figure 4.17). At high relative humidity, this wrinkled or grooved surface topography was formed due to competitive

penetration and diffusion of ambient water vapor into the fibers, evaporation of  $\text{CHCl}_3$  solvent, and formation of an outer sheath layer. Ambient water vapor was able to enter the system because it is miscible with DMF. This competitive absorption of water and evaporation of solvent slowed down the formation of polymer sheath, allowing for greater stretching of the fiber during whipping, the additional water in the system further contributed to this increased whipping due to increased conductivity from the water, and VIPS did not cause templating of the condensing water only at the surface of the polymer jet. Buckling may have also occurred upon further evaporation of the solvent from the core of the fiber.<sup>39</sup> This mechanism is consistent with studies in the field that observe similar surface topography of fibers.<sup>40,41</sup> The surface topography of electrospun fibers with surfactant Span80 and with internal phase was smooth for all internal phase volume fractions. Fiber topography was smooth because surfactant at the surface of the polymer jet reduced phase separation caused by ambient water vapor condensing on the surface of the jet.



At low relative humidity, the surface topography of fibers was smooth for samples fabricated without surfactant, with surfactant, and at internal phase volume fractions of 0% w/o, 2% w/o, 4% w/o, 8% w/o (Figure 4.17). This smooth surface topography was due to low ambient relative humidity having fewer water droplets in the air to template surface topography through the VIPS mechanism.

#### 4.3.2.3 Fiber Diameter and Distribution

At high relative humidity, the fiber diameter for control samples with no surfactant and no internal phase the average fiber diameter of  $1.28 \pm 0.25 \mu\text{m}$  (Figure 4.18). In samples containing surfactant with internal phase volume fractions of 0%, 2%, 4%, and 8% w/o the average fiber diameter was  $0.37 \pm 0.16 \mu\text{m}$ ,  $0.40 \pm 0.17 \mu\text{m}$ ,  $0.45 \pm 0.18 \mu\text{m}$ , and  $0.50 \pm 0.25 \mu\text{m}$ , respectively. The diameter of distributions consisted of a single evenly distributed peak with no surfactant and no internal phase, two peaks and a slight positive distribution with surfactant and no internal phase, and a positive single peaked skew for samples containing 2%, 4%, 8% w/o internal phase. The

overall skew and kurtosis for each set of sample parameters also confirm this distribution, and histogram representation of fiber diameter distribution, shown in Table 4.1 below.

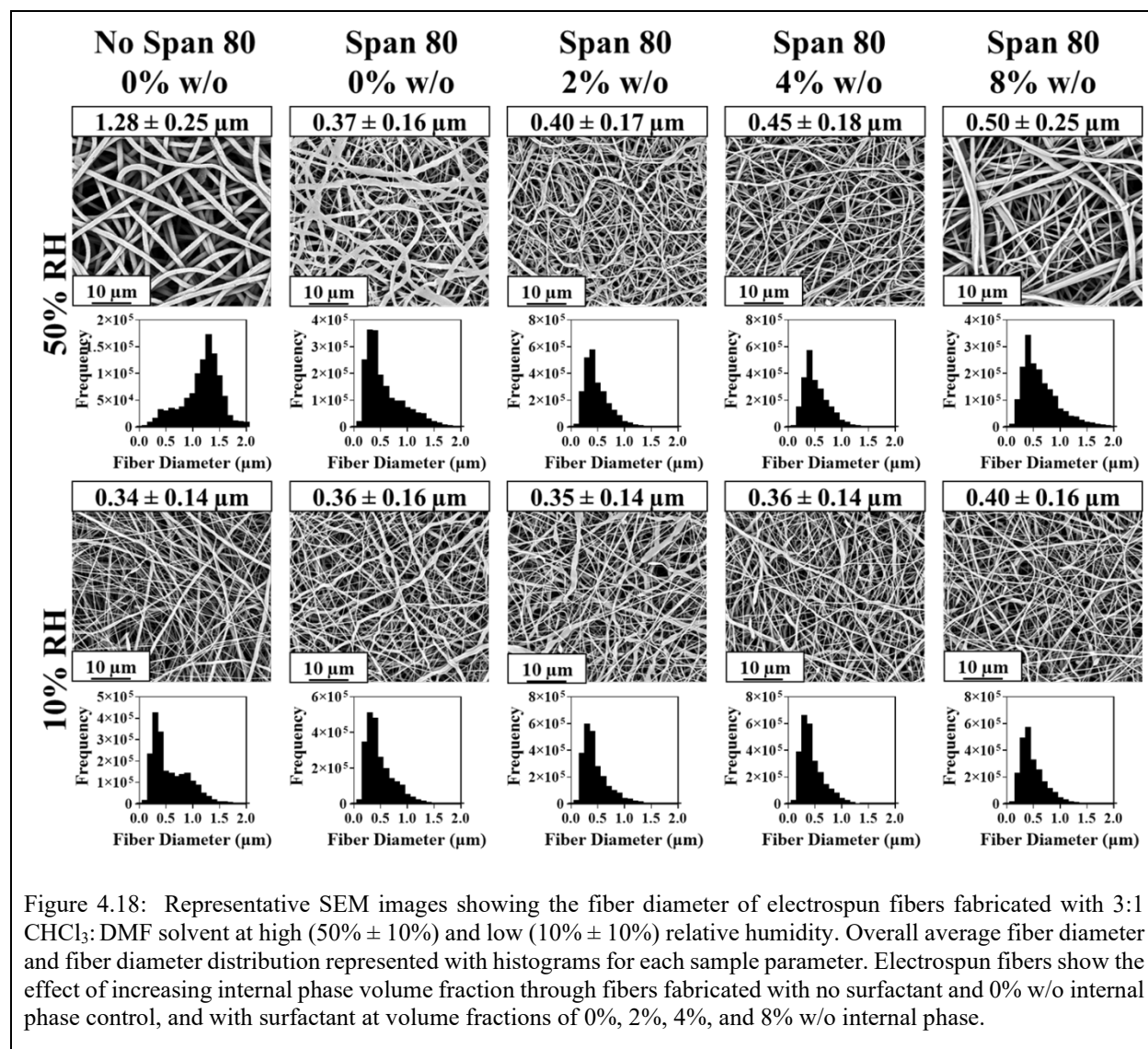
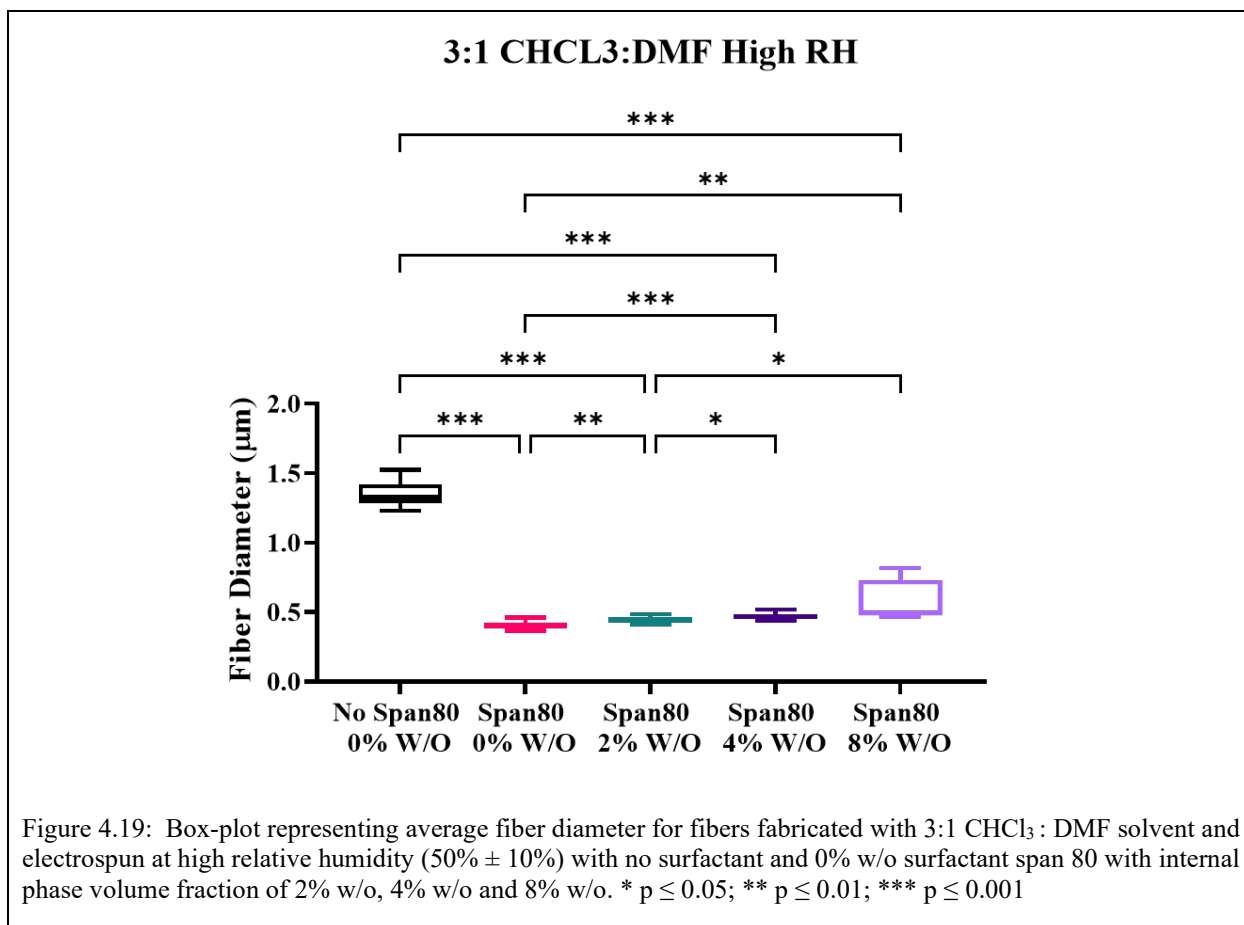


Figure 4.18: Representative SEM images showing the fiber diameter of electrospun fibers fabricated with 3:1 CHCl<sub>3</sub>:DMF solvent at high (50% ± 10%) and low (10% ± 10%) relative humidity. Overall average fiber diameter and fiber diameter distribution represented with histograms for each sample parameter. Electrospun fibers show the effect of increasing internal phase volume fraction through fibers fabricated with no surfactant and 0% w/o internal phase control, and with surfactant at volume fractions of 0%, 2%, 4%, and 8% w/o internal phase.

At high relative humidity, when surfactant was added to the system, fiber diameter statistically decreased (Figure 4.19). This decrease in fiber diameter was likely due to surfactant slowing down the evaporation rate from the polymer jet during electrospinning, thus allowing for greater stretching before hitting the collection plate.<sup>7</sup> Furthermore, adding surfactant to the system reduces the surface tension and allows thinning of the jet in the stable Taylor cone region as described in the CHCl<sub>3</sub> solvent system. Additionally, surfactant allowed for water to penetrate the

fiber and increase the overall conductivity of the solution. Increasing the conductivity of the system allows for an increased amount of whipping and stretching to occur during the electrospinning process. Compared to the solvent system fabricated with  $\text{CHCl}_3$  solvent, the samples with surfactant and no internal phase had fiber diameters closer to the fiber diameters of samples with internal phase. This change in diameter is likely because DMF is miscible with water, facilitating penetration into the fiber through VIPS and increasing conductivity and whipping. Decreased surface tension from the surfactant may also be playing a role.



Fiber diameter significantly increased with increasing internal phase when comparing all internal phase volume fractions except 4% w/o and 8% w/o (Figure 4.19). Fiber diameter increased

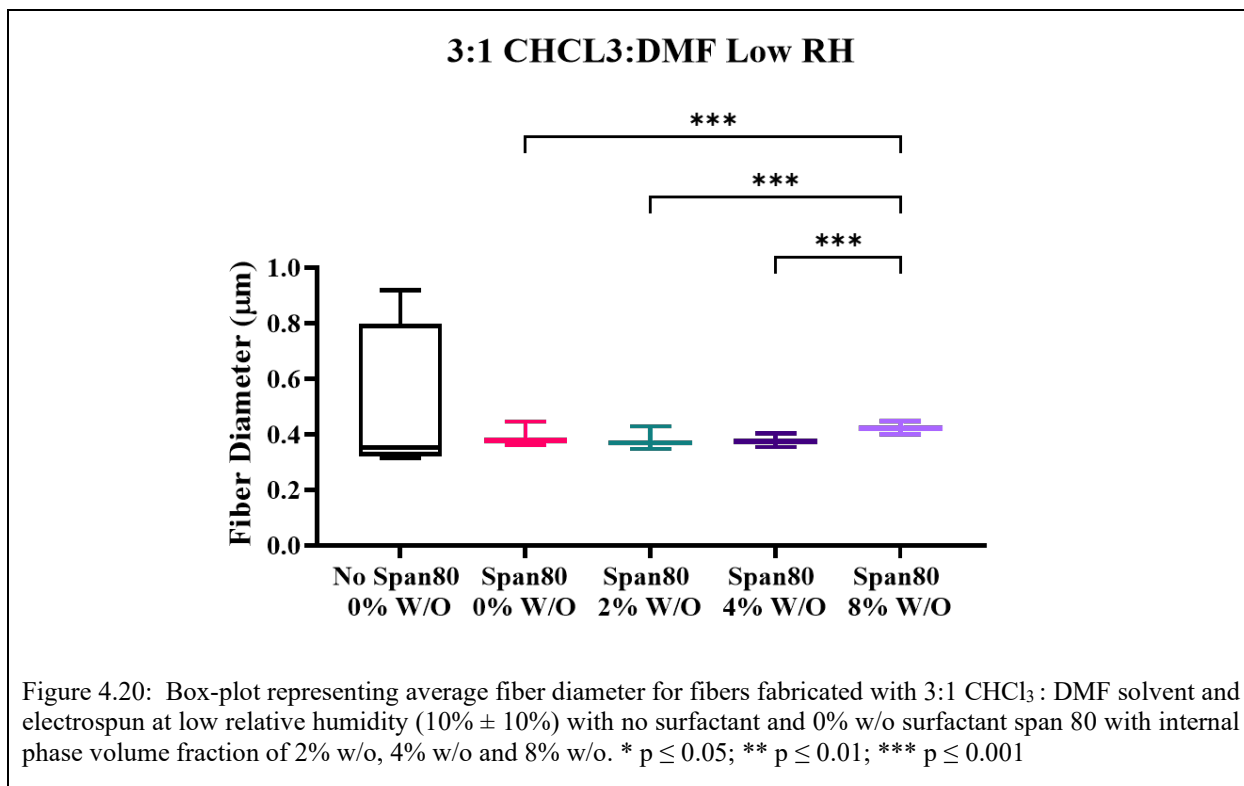
minimally with increasing internal phase volume fraction. The mechanism for increasing fiber diameter is the same as described in the  $\text{CHCl}_3$  solvent system. As internal phase volume fraction increases in the fiber, the jet becomes more stable due to phase separation, creating a core of internal phase within the center of the fiber, thus stabilizing charge distribution throughout the fiber.<sup>34</sup> The relatively larger fiber diameters in the samples with 8% w/o internal phase volume fraction also may indicate that multiple jets or branching were forming and are stabilizing back into a single jet. This stabilization may be due to the distribution of internal phase droplets, surfactant relocating from the surface of the fiber to the internal water-oil interface as surface area increases, or increased viscosity of the polymer solution as internal phase volume fraction increased.

At low relative humidity, the average fiber diameter for control samples with no surfactant and no internal phase was  $0.34 \pm 0.14 \mu\text{m}$  (Figure 4.18). In samples containing surfactant with internal phase volume fractions of 0%, 2%, 4%, and 8% w/o, the average fiber diameter was  $0.36 \pm 0.16 \mu\text{m}$ ,  $0.35 \pm 0.14 \mu\text{m}$ ,  $0.36 \pm 0.14 \mu\text{m}$ , and  $0.40 \pm 0.16 \mu\text{m}$ , respectively. The fiber distribution for samples fabricated with no internal phase and no surfactant had two peaks with the dominant peak in the smaller fiber diameter range. This distribution was due to thin, smaller fibers that resulted from the lack of ambient water droplets condensing on the surface of the fiber, reducing surface charge density, and stabilizing the jet.

The distribution of fiber diameters for samples fabricated with surfactant and 0%, 2%, 4%, 8% w/o internal phase consisted of a single peak with an overall positive skew (Figure 4.18). This positive skew was likely due to multiple jet formation and uneven distribution of the Taylor 1 cone favoring smaller fibers. The overall skew and kurtosis for each set of sample parameters also

confirm this distribution, and histogram representation of fiber diameter distribution, shown in Table 4.1 below.

Change in fiber diameter was not statistically significant with the addition of surfactant (Figure 4.20). This indicates that surfactant was not playing a major role in fiber diameter in this system and further supports the multiple jets hypothesis. The change in fiber diameter was only statistically significant in internal phase volume fraction of 8% w/o internal phase, which was statistically different from all other internal phase volume fractions. This indicates that internal phase volume fraction may not play a major role in the fiber diameter in this system until a threshold (8% w/o) has been reached. Internal phase volume fraction is not playing a major role in this system because of the multiple jet formation until the internal phase volume fraction is high enough to stabilize the charge, increase surface tension on the outside of the fiber due to surfactant at the water-oil interface, and an increase in solution viscosity.

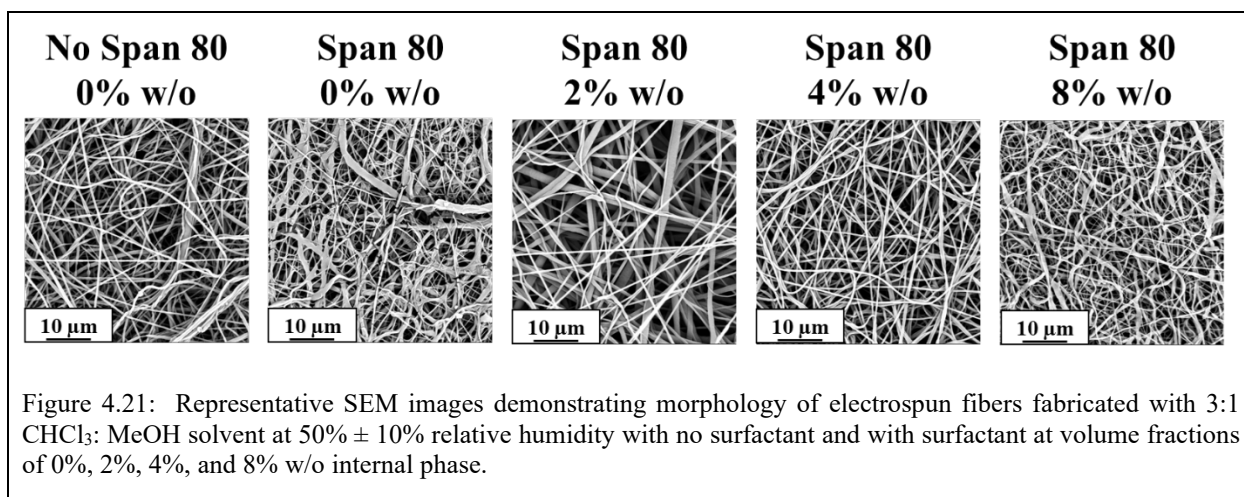


### 4.3.3 3:1 CHCl<sub>3</sub>: MeOH Solvent System

#### 4.3.3.1 Fiber Morphology

At high relative humidity, when samples were electrospun with 3:1 CHCl<sub>3</sub>: MeOH samples were predominantly uniform and cylindrical in morphology (Figure 4.21). However, some morphologies were seen in each of the emulsion and control samples.





Control samples with no surfactant and no internal phase were also observed to have beading and garland formation (Figure 4.22). The presence of garland formation. At high relative humidity, the absence of evidence of fiber branching indicates that multiple jets may have been present at the needle tip during electrospinning. Multiple jets may have formed in this solvent system because MeOH and CHCl<sub>3</sub> are immiscible solvents, encouraging phase separation. Moreover, MeOH is a highly conductive solvent, and this further would have encouraged multiple jet formation.<sup>36,38</sup> Multiple jet formation would provide an opportunity for jets to intersect during electrospinning, conglutinate, and entangle to form garlands. Moreover, if multiple jets were formed and the MeOH solvent facilitated phase separation, then the distribution of polymer between the multiple jets may not be even and resulted in jets with insufficient polymer concentration to overcome surface tension and therefore present beading morphology.

		3:1 CHCL <sub>3</sub> :MeOH Selected Morphologies High RH				
		No Span 80 0% w/o	Span 80 0% w/o	Span 80 2% w/o	Span 80 4% w/o	Span 80 8% w/o
<b>Uniform Cylinders</b>  <b>Fused Fibers</b>  <b>Fiber Beading</b>  <b>Fiber Breaking</b>  <b>Garland Formation</b>  <b>Film Filled Voids</b>  <b>Ribbon Morphology</b>	Uniform Cylinders		-			
	Fused Fibers	-		-	-	-
	Fiber Beading		-	-	-	-
	Fiber Breaking	-			-	-
	Garland Formation					
	Film Filled Voids	-		-	-	-
	Ribbon Morphology	-		-	-	-

Figure 4.22: Representative SEM images of close-up selected fiber morphology in electrospun fibers fabricated with 3:1 CHCl<sub>3</sub>: MeOH solvent at 50% ± 10% relative humidity with no surfactant, and with surfactant at volume fractions of 0%, 2%, 4%, and 8% w/o internal phase.

In samples electrospun at high relative humidity with surfactant and no internal phase, fiber morphologies of fused fibers, fiber breaking, garland formation, film filled voids, and ribbon morphology were observed (Figure 4.22). When surfactant is added to the system, surface tension is decreased, causing an increase in jet acceleration, thinning of the Taylor cone, and surfactant relocation at the surface of the fiber, which decreases the rate of solvent evaporation. This can cause fibers to collect on the collection plate while still wet, causing fused fibers and ribbon morphology. As wet fibers evaporate, polymer solution can leak out of their core to fill near neighbor mesh pores with polymer solution, creating film filled voids. Fiber breaking may be due to the increased acceleration of the polymer jet due to decreased surface tension, causing elongation of polymer chains that, when drawing on the collection plate, contract causing fibers to break. Garland formation is likely due to multiple jets present at the needle tip for electrospinning.

Samples electrospun at high relative humidity with 2% w/o internal phase volume fraction also demonstrated fiber breaking morphology (Figure 4.22). This indicates that surfactant is still playing a major role in reducing surface tension and slowing down the evaporation rate at this amount of internal phase volume fraction. Broken fiber morphology was not observed in samples with 4% w/o and 8% w/o, indicating that internal phase volume fraction may have reached a threshold to prevent fiber breaking.

Samples electrospun at high relative humidity with internal phase volume fractions of 2% w/o, 4% w/o, and 8% w/o all were observed to have garland formation morphology. Garland formation is likely due to multiple jets conglutinating and entangling during the electrospinning process. The presence of garlands at all internal phase volume fractions indicates that internal phase volume fraction may not be stabilizing the jet as seen in the 3:1 CHCl<sub>3</sub>: DMF solvent system.

This may be due to MeOH encouraging immediate phase separation because it is not miscible with  $\text{CHCl}_3$ .

At high relative humidity, the formation of nanowebs was observed in at least one sample containing 8% w/o internal phase (Figure 4.23). The formation of nanowebs in this system is likely due to branching between fibers as they were drying due to localized charge on the fibers. To the best of my knowledge, the formation of nano webs with emulsion electrospun fibers has not been published. The beginning of nano webbing was also observed in samples with lower internal phase volume fractions. Small fiber-like protrusions were observed on the surface of fibers with 2% w/o internal phase. At 4% w/o internal phase, small nanofibers were observed connecting fibers near junctions. These connections near fiber junctions may be due to smaller localized electric fields that are only strong enough to encourage nanofiber formation when fibers are close together, such as where they intersect when collecting on a mesh while still partially wet. As internal phase volume fraction increases in these samples, this localized charge increases, allowing for more nano webbing to form between fibers and localized to specific pores. This may be due to increasing conductivity with increasing internal phase volume fraction leading to a stronger surface charge density, and therefore stronger localized charge to encourage nanowebbing morphology.

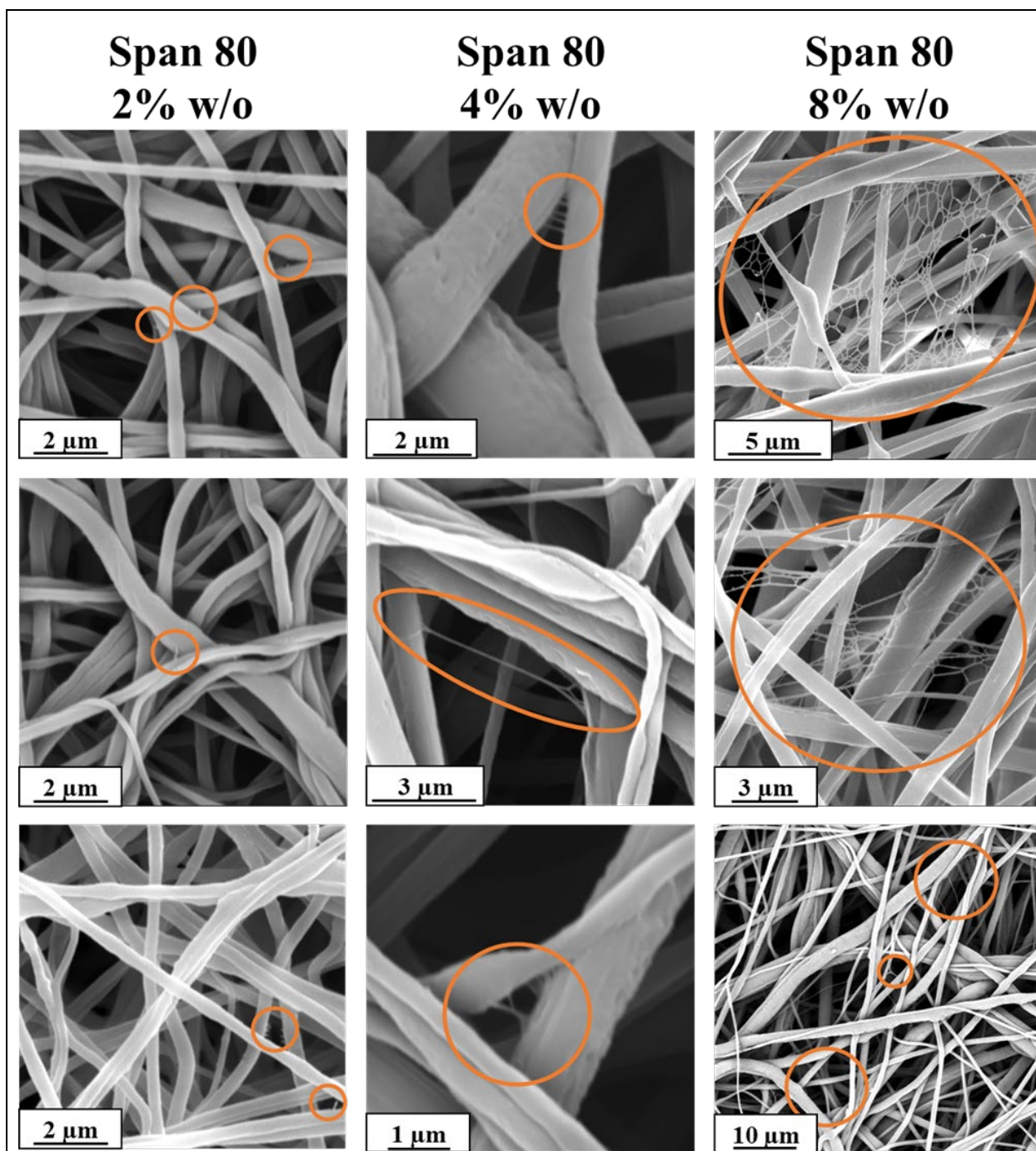
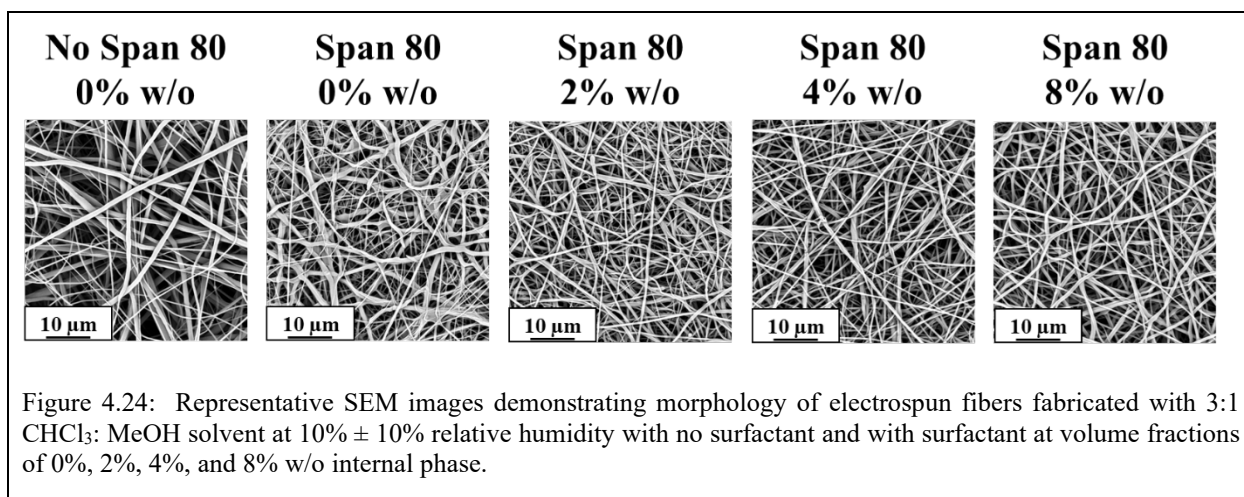


Figure 4.23: Formation of nanowebbing with increasing internal phase volume fractions of 2%, 4%, and 8% w/o in samples electrospun at high relative humidity ( $50\% \pm 10\%$ ) and solvent 3:1  $\text{CHCl}_3$ :MeOH.

Samples electrospun at low relative humidity with 3:1  $\text{CHCl}_3$ : MeOH solvent were predominately uniform and cylindrical in fiber morphology (Figure 4.24).



Control samples with no surfactant and no internal phase also were observed to have morphologies of fused fibers, fiber, beading, fiber breaking, and fiber branching (Figure 4.25). Fused fiber morphology may be due to multiple jets forming in this electrospinning system and intersecting early in flight prior to total solvent evaporation allowing for conglutination to occur. Fused fiber morphology was rarely seen, however, in samples with these parameters. Fiber beading morphology was observed in samples with these parameters and may be due to solvents CHCl<sub>3</sub> and MeOH immiscibility causing immediate phase separation at the needle tip if some of the jets contained more of the MeOH solvent. It would also likely have far less polymer because PCL has low solubility in MeOH. A decrease in the concentration of polymer could cause insufficient viscoelastic forces to overcome surface tension and therefore result in beading morphology. Fiber breaking morphology was also observed. Fiber breaking may have been due to phase separation within the fiber and regions of the polymer jet containing MeOH upon drying on the collection plate having very little polymer dissolved. Finally, fiber branching was also observed in samples with these parameters. Fiber branching may be due to instability of the jet caused by unequal

distribution of charge from the two immiscible solvents resulting in perturbations during electrospinning that cause branching.

		3:1 CHCL <sub>3</sub> :MeOH Selected Morphologies Low RH				
		No Span 80	Span 80	Span 80	Span 80	Span 80
		0% w/o	0% w/o	2% w/o	4% w/o	8% w/o
	Uniform Cylinders					
	Fused Fibers			-	-	-
	Fiber Beading				-	-
	Fiber Breaking			-	-	-
	Fiber Branching		-			
	Ribbon Morphology	-				
	Garland Formation	-				
	Nano Webbing	-	-	-		

Figure 4.25: Representative SEM images of close-up selected fiber morphology in electrospun fibers fabricated with 3:1 CHCl<sub>3</sub>: MeOH solvent at 10% ± 10% relative humidity with no surfactant, and with surfactant at volume fractions of 0%, 2%, 4%, and 8% w/o internal phase.



Samples electrospun with surfactant and 0% w/o internal phase had fiber morphologies, including fused fibers, fiber, beading, fiber breaking, ribbon morphology, and garland formation (Figure 4.25). Fiber breaking in these samples may be due to phase separation of MeOH and CHCl<sub>3</sub> creating regions of predominately methanol which is a poor solvent for PCL. Upon drying, areas with high concentrations of MeOH would result in fiber breaking when the MeOH solvent evaporated. Fiber beading morphology in samples containing surfactant may be due to multiple jets forming in the system and creating either jets with higher concentrations of polymer, due to phase separation of MeOH and CHCl<sub>3</sub>, or regions within individual jets of phase separation. When phase separation occurs and polymer prefers one solvent over the other, solvent areas with less polymer can have insufficient polymer to overcome surface tension, thus resulting in beading morphology. When surfactant is added to the system, it reduces the surface tension, increasing the acceleration and thinning the Taylor cone. In addition to slowing down the rate of solvent evaporation at the surface of the fiber. This may lead to fused fiber morphology when fibers collect wet on the collection plate. Garland formation was also observed in samples containing surfactant and no internal phase. Garland formation indicates that during the electrospinning process. Fibers were either branching or had multiple jets and resulted in conglutination of wet fibers and entanglement during the electrospinning process.

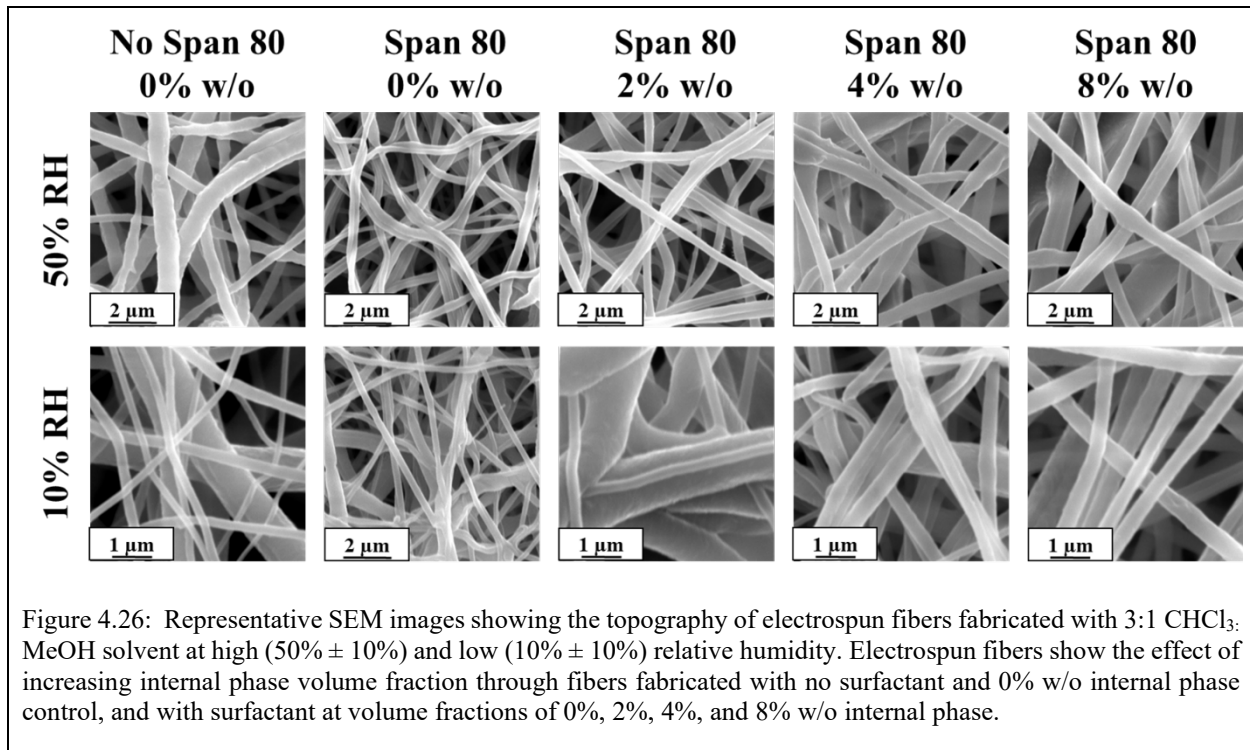
When internal phase was added to the system at a volume fraction of 2% w/o at low relative humidity, beading morphology was observed (Figure 4.25). Beading morphology may have been due to phase separation occurring between the MeOH and CHCl<sub>3</sub> solvent, resulting in areas of higher concentration of polymer due to higher solubility of PCL in CHCl<sub>3</sub> compared to MeOH solvent. The regions with lower concentrations of polymer may have had insufficient polymer viscoelastic forces to overcome surface tension resulting in beading morphology.

When internal phase volume fractions of 2% w/o, 4% w/o, and 8% w/o were added to the system, fiber morphologies of fiber branching, ribbon morphology, garland morphology, and nano web in were observed (Figure 4.25). Fiber branching may have occurred due to instability in the jet caused by unequal distribution of internal phase droplets causing differences in charge propagation through the jet. On the surface of the jet and due to conservation of volume would result in branching. The presence of branching and likely multiple jets in the system also resulted in garland formation due to branches entangling during electrospinning. Ribbon morphology was also observed at all internal phase volume fractions. The presence of ribbon morphology may be due to rapid evaporation of MeOH solvent in this system forming a skin around the outside of the fiber. This skin collapsed as the fibers dried and the remaining solvent evaporated out of the jet. This ribbon morphology may have been seen in samples with internal phase because the internal phase would coalesce during electrospinning into the center of the jet and create a wet core of predominantly water that has slower evaporation than the other solvent systems also contributing to some of these fibers collapsing into ribbon morphology.

The presence of nanowebbing was observed in at least one of the samples electrospun with 4% w/o and 8% w/o internal phase volume fraction at low relative humidity (Figure 4.25). Initiation of webbing and small fibers near the junctions of fibers was also observed in at least one of the samples with internal phase volume fractions of 0% w/o and 2% w/o. The mechanism of this nanowebbing morphology may be due to the same mechanism described at high relative humidity. The presence of a continuation of nanowebbing and only full webbing at higher internal phase volume fraction further supports the hypothesis that localized charge during the drying process may be contributing to the formation of these nanowebs.

#### 4.3.3.2 Fiber Surface Topography

The surface topography of fibers electrospun at both high and low relative humidity had smooth surface topography for samples electrospun with no surfactant and samples with surfactant at internal phase volume fractions of 0% w/o, 2% w/o, 4% w/o, and 8% w/o (Figure 4.26).



The samples electrospun with 3:1 CHCl<sub>3</sub>: MeOH solvent had smooth topography where samples fabricated with CHCl<sub>3</sub> and DMF had porous surface topography in the absence of surfactant when electrospun at high relative humidity. These control fibers may have had smooth fibers rather than porous topography because the presence of MeOH solvent allowed water to penetrate into the fiber rather than condensing on the surface of the fiber facilitation VIPS.

#### 4.3.3.3 Fiber Diameter and Distribution

At high relative humidity, the fiber diameter for control samples with no surfactant and no internal phase the average fiber diameter of  $0.52 \pm 0.20 \mu\text{m}$  (Figure 4.27). In samples containing surfactant with internal phase volume fractions of 0%, 2%, 4%, and 8% w/o the average fiber

diameter was  $0.39 \pm 0.18 \mu\text{m}$ ,  $0.50 \pm 0.20 \mu\text{m}$ ,  $0.50 \pm 0.18 \mu\text{m}$ , and  $0.53 \pm 0.26 \mu\text{m}$ , respectively. The diameter of distributions consisted of a single positive skewed peak phase for all samples. This positive skew is likely due to the presence of small, branched fibers skewing the overall population towards smaller fiber diameters of multiple jets at the needle tip with an unequal volume of jet splitting. This distribution of fibers is consistent with a study by Liu et al. in which increasing applied voltage increased the number of polymer jets and distribution of fiber diameter.<sup>42</sup> The overall skew and kurtosis for each set of sample parameters also confirm this distribution, and histogram representation of fiber diameter distribution, shown in Table 4.1.

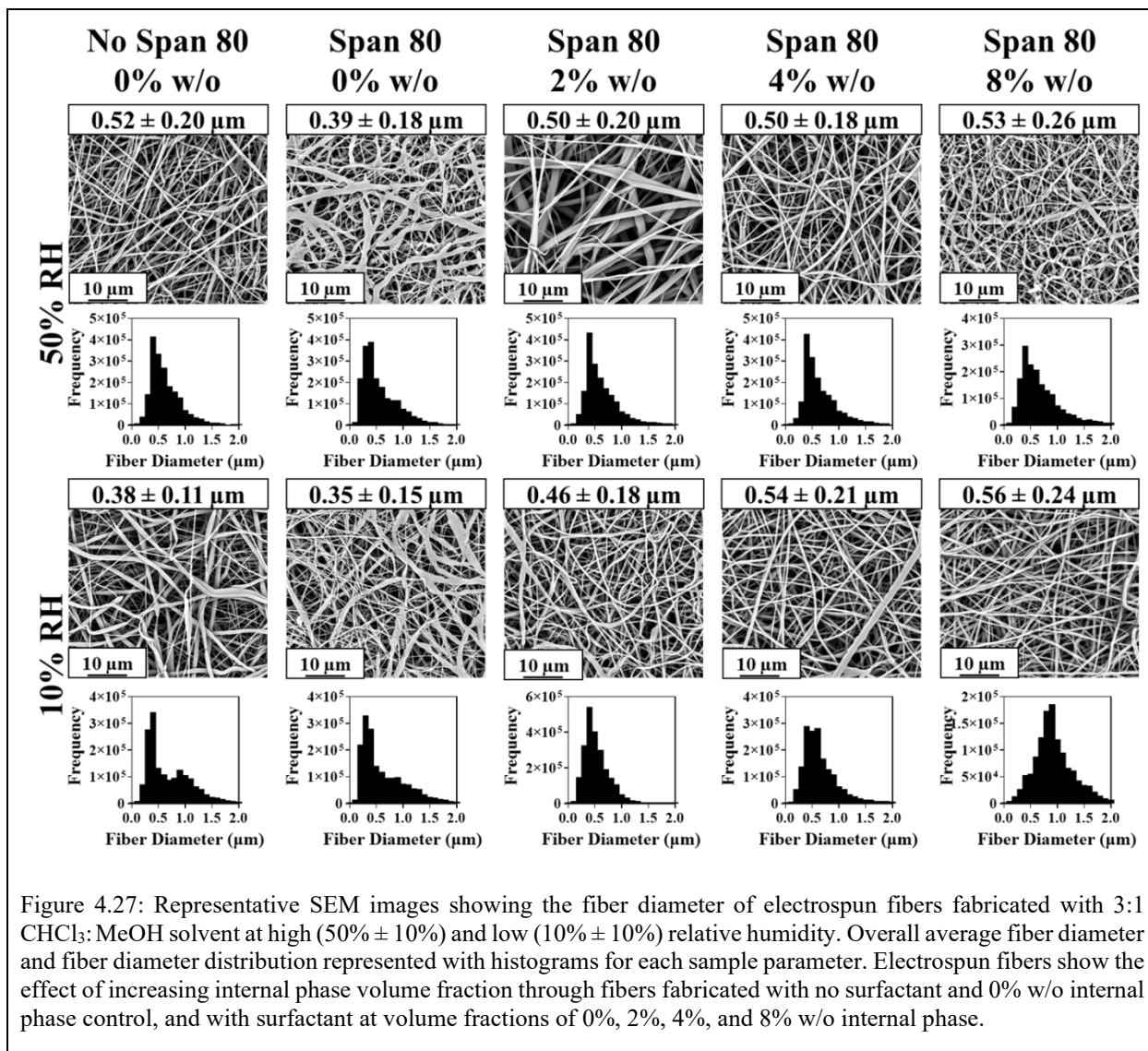
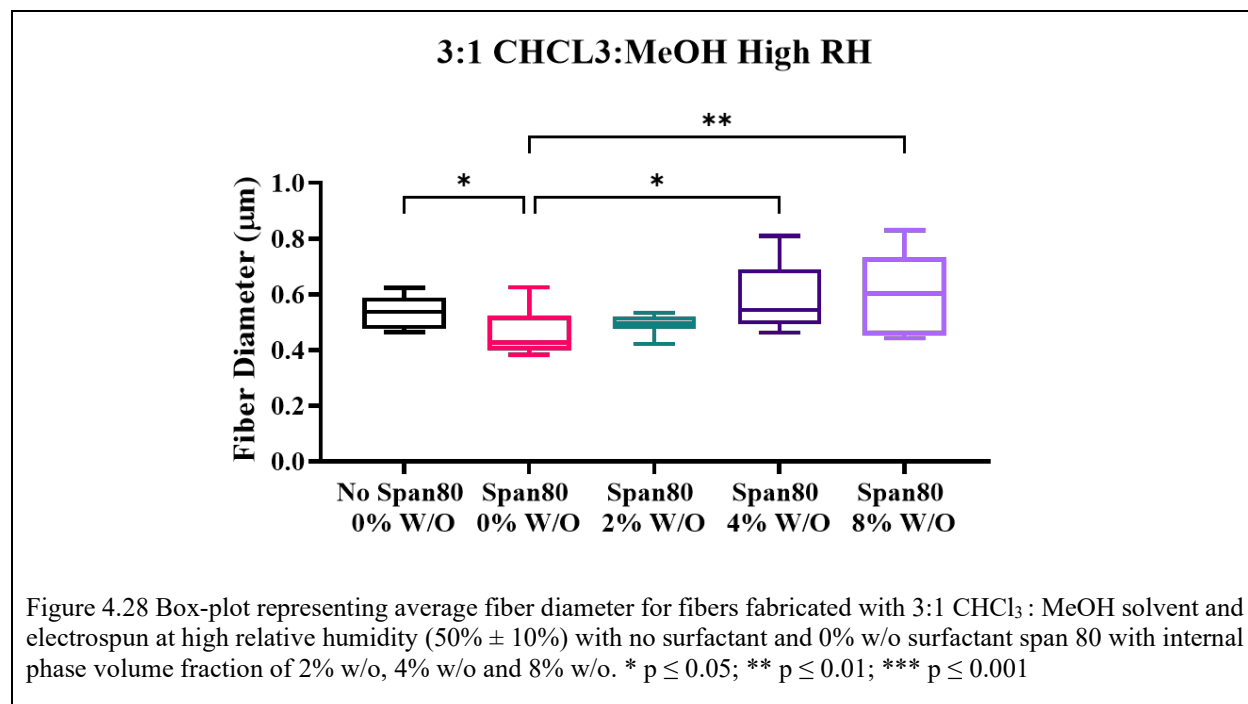


Figure 4.27: Representative SEM images showing the fiber diameter of electrospun fibers fabricated with 3:1  $\text{CHCl}_3$ : $\text{MeOH}$  solvent at high (50%  $\pm$  10%) and low (10%  $\pm$  10%) relative humidity. Overall average fiber diameter and fiber diameter distribution represented with histograms for each sample parameter. Electrospun fibers show the effect of increasing internal phase volume fraction through fibers fabricated with no surfactant and 0% w/o internal phase control, and with surfactant at volume fractions of 0%, 2%, 4%, and 8% w/o internal phase.

When surfactant was added to the system at high relative humidity, the fiber diameter significantly decreased (Figure 4.28). This decrease in fiber diameter is likely due to decreased surface tension, causing thinning of the polymer jet. Fiber diameter significantly increased when comparing samples with 0% w/o internal phase to samples with 4% w/o internal phase and 8% w/o internal phase. This increase in fiber diameter may have been due to stabilizing the polymer jet as sufficient internal phase volume fraction was added to the system to allow for more even charge distribution. It is also possible that increasing the internal phase volume fraction moderately increased overall solution viscosity creating increased resistance to stretching and, therefore, larger

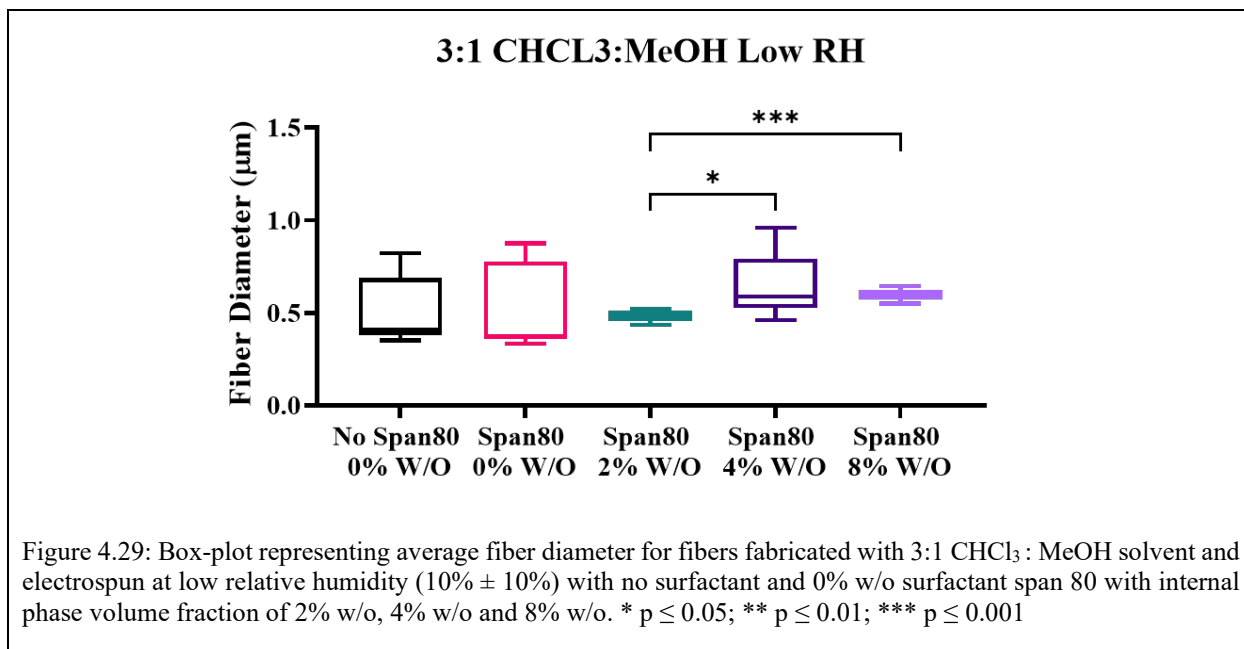
overall fiber diameters. The control fiber diameters were similar to the fibers with internal phase because the conductivity of the MeOH is high, facilitating more stretching in the bending instability region.



At low relative humidity, the fiber diameter for control samples with no surfactant and no internal phase the average fiber diameter of  $0.38 \pm 0.11 \mu\text{m}$  (Figure 4.27). In samples containing surfactant with internal phase volume fractions of 0%, 2%, 4%, and 8% w/o the average fiber diameter was  $0.35 \pm 0.15 \mu\text{m}$ ,  $0.46 \pm 0.18 \mu\text{m}$ ,  $0.54 \pm 0.21 \mu\text{m}$ , and  $0.56 \pm 0.24 \mu\text{m}$ , respectively. The diameter distribution for fibers with no surfactant and no internal phase had a positive skew and a two peak distribution. These two peaks were likely due to increased breaking and beading resulting from excess charge at the surface of the jet that was not stabilized and reduced by ambient water vapor as seen at high relative humidity. The distribution of fibers with 0% w/o, 2% w/o, and 4% w/o all have single peaks and are positively skewed in terms of distribution. As internal

phase increases, the degree to which the peak is positively skewed becomes less extreme, and in samples fabricated with 8% w/o, the distribution of fibers has a single peak and is approximately normally distributed. This indicates that as internal phase volume fraction is added to the fibers, the internal phase has a stabilizing effect and leads to more consistent fiber collection. The overall skew and kurtosis for each set of sample parameters also confirm this distribution, and histogram representation of fiber diameter distribution, shown in Table 4.1.

At low relative humidity, when surfactant was added to the system, fiber diameter did not significantly change with the addition of surfactant (Figure 4.29). This may have been due to multiple jet formation causing a decrease in surface tension to play a minor role during electrospinning. The fibers electrospun with internal phase volume fractions of 2% w/o, 4% w/o, and 8% w/o also were not significantly different from the controls with no internal phase both with and without surfactant. This may indicate that internal phase volume fraction was not playing a major role in fiber diameter in this system. The less significant role of internal phase in this system compared to fibers electrospun with  $\text{CHCl}_3$  solvent and 3:1  $\text{CHCl}_3$ :DMF may be due to differences in miscibility of  $\text{CHCl}_3$  and MeOH in addition to polymer solubility in each of the solvents. The solvents electrospun with surfactant and 2% w/o internal phase were significantly smaller than fibers electrospun with surfactant and 4% w/o and 8% w/o internal phase potentially because the jet was stabilized with increasing internal phase volume fraction. This system illustrates the potential to encapsulate drug within fibers with increasing internal phase volume fractions while having minimal effect on fiber diameter.



#### 4.4 CONCLUSION

Understanding the effect that internal phase volume fraction play on emulsion electrospun fibers is essential to create tunable and reproducible fibers for drug delivery and tissue engineering applications. The effect of the solvents used to emulsion electrospin fibers plays a major role in the evaporation rate, miscibility, polymer solubility, and conductivity of the solution. Understanding all of these parameters in high and low relative humidity environments further allows the development of fibers with morphology, surface topography, and fiber diameter desirable to match the needs of a particular system. Table 4.1 summarizes the major findings in this chapter. Overall, increasing internal phase volume fraction, even in small amounts, played a major role in electrospinning fiber collection. Controlling mesh characteristics is important because they can affect drug release and cell response.



Table 4.1: Summary table of fiber morphology, topography, diameter, and distribution electrospun at high ( $50\% \pm 10\%$ ) and low ( $10\% \pm 10\%$ ) relative humidity with control containing no surfactant and increasing internal phase volume fractions of 0% w/o, 2% w/o, 4% w/o, and 8% w/o internal phase volume fraction.

Table 4.1. Summary of Fiber Morphology, Topography, Diameter, and Distribution for Varying Emulsions					
Solvent(s)	Surfactant, Internal Phase Volume Fraction	Relative Humidity	Fiber Morphology	Fiber Topography	Average Fiber Diameter ( $\mu\text{m}$ ), Skewness, Kurtosis
$\text{CHCl}_3$	No Surfactant, 0%	50%	Uniform Cylinders	Porous	$4.16 \pm 1.07$ , 1.84, 9.59
$\text{CHCl}_3$	No Surfactant, 0%	10%	Uniform Cylinders	Smooth	$5.39 \pm 0.98$ , 0.76, 5.14
$\text{CHCl}_3$	Span 80, 0%	50%	Fused Fibers, Fiber Breaking, Fiber Branching	Smooth, Cactus	$3.65 \pm 1.97$ , 1.08, 2.04
$\text{CHCl}_3$	Span 80, 0%	10%	Fused Fibers, Fiber Breaking	Lateral Wrinkles	$4.64 \pm 1.57$ , 0.94, 1.78
$\text{CHCl}_3$	Span 80, 2%	50%	Uniform Cylinders, Fiber Beading, Fiber Branching, Garland Formation	Smooth	$0.42 \pm 0.16$ , 1.32, 3.08
$\text{CHCl}_3$	Span 80, 2%	10%	Uniform Cylinders, Fiber Beading, Film Filled Voids, Ribbon Morphology	Smooth	$0.43 \pm 0.17$ , 1.42, 3.54
$\text{CHCl}_3$	Span 80, 4%	50%	Uniform Cylinders, Fiber Beading, Fiber Branching, Garland Formation	Smooth	$0.42 \pm 0.16$ , 1.25, 2.49
$\text{CHCl}_3$	Span 80, 4%	10%	Uniform Cylinders, Fiber Beading, Fiber Breaking, Film Filled Voids, Ribbon Morphology	Smooth	$0.45 \pm 0.17$ , 1.10, 1.71
$\text{CHCl}_3$	Span 80, 8%	50%	Uniform Cylinders, Fiber Beading, Fiber Branching, Garland Formation	Smooth	$0.45 \pm 0.17$ , 2.43, 13.42

Table 4.1. Summary of Fiber Morphology, Topography, Diameter, and Distribution for Varying Emulsions

Solvent(s)	Surfactant, Internal Phase Volume Fraction	Relative Humidity	Fiber Morphology	Fiber Topography	Average Fiber Diameter ( $\mu\text{m}$ ), Skewness, Kurtosis
$\text{CHCl}_3$	Span 80, 8%	10%	Uniform Cylinders, Fiber Beading, Fiber Breaking, Film Filled Voids, Ribbon Morphology, Nano Webbing	Smooth	$0.65 \pm 0.29$ , 2.71, 12.18
3:1 $\text{CHCl}_3$ : DMF	No Surfactant, 0%	50%	Uniform Cylinders	Wrinkled	$1.28 \pm 0.25$ , 0.31 1.87
3:1 $\text{CHCl}_3$ : DMF	No Surfactant, 0%	10%	Uniform Cylinders, Fiber Beading, Fiber Breaking, Fiber Branching	Smooth	$0.34 \pm 0.14$ , 1.18, 1.58
3:1 $\text{CHCl}_3$ : DMF	Span 80, 0%	50%	Uniform Cylinders, Fused Fibers, Film Filled Voids, Ribbon Morphology	Smooth	$0.37 \pm 0.16$ , 1.37, 1.99
3:1 $\text{CHCl}_3$ : DMF	Span 80, 0%	10%	Uniform Cylinders, Fused Fibers, Film Filled Voids, Ribbon Morphology	Smooth	$0.36 \pm 0.16$ , 1.65, 5.36
3:1 $\text{CHCl}_3$ : DMF	Span 80, 2%	50%	Uniform Cylinders, Fiber Beading, Fiber Breaking, Garland Formation	Smooth	$0.40 \pm 0.17$ , 1.44 3.35
3:1 $\text{CHCl}_3$ : DMF	Span 80, 2%	10%	Uniform Cylinders, Fused Fibers, Fiber Beading, Fiber Breaking, Film Filled Voids, Ribbon Morphology	Smooth	$0.35 \pm 0.14$ , 1.90, 5.49
3:1 $\text{CHCl}_3$ : DMF	Span 80, 4%	50%	Uniform Cylinders, Fiber Beading, Fiber Breaking, Garland Formation	Smooth	$0.45 \pm 0.18$ , 1.21, 2.17

Table 4.1. Summary of Fiber Morphology, Topography, Diameter, and Distribution for Varying Emulsions

Solvent(s)	Surfactant, Internal Phase Volume Fraction	Relative Humidity	Fiber Morphology	Fiber Topography	Average Fiber Diameter ( $\mu\text{m}$ ), Skewness, Kurtosis
3:1 $\text{CHCl}_3$ : DMF	Span 80, 4%	10%	Uniform Cylinders, Fiber Beading, Fiber Breaking	Smooth	$0.36 \pm 0.14$ , 1.38, 2.46
3:1 $\text{CHCl}_3$ : DMF	Span 80, 8%	50%	Uniform Cylinders, Fiber Breaking, Garland Formation	Smooth	$0.50 \pm 0.25$ , 1.74, 4.52
3:1 $\text{CHCl}_3$ : DMF	Span 80, 8%	10%	Uniform Cylinders, Fiber Beading, Fiber Breaking	Smooth	$0.40 \pm 0.16$ , 1.62, 3.96
3:1 $\text{CHCl}_3$ : MeOH	No Surfactant, 0%	50%	Uniform Cylinders, Fiber Beading, Garland Formation	Smooth	$0.52 \pm 0.20$ , 1.77, 5.39
3:1 $\text{CHCl}_3$ : MeOH	No Surfactant, 0%	10%	Uniform Cylinders, Fused Fibers, Fiber Beading, Fiber Breaking, Fiber Branching	Smooth	$0.38 \pm 0.11$ , 1.57, 4.28
3:1 $\text{CHCl}_3$ : MeOH	Span 80, 0%	50%	Fused Fibers, Fiber Breaking, Garland Formation, Film Filled Voids, Ribbon Morphology	Smooth	$0.39 \pm 0.18$ , 1.39 2.33
3:1 $\text{CHCl}_3$ : MeOH	Span 80, 0%	10%	Uniform Cylinders, Fused Fibers, Fiber Beading, Fiber Breaking, Ribbon Morphology, Garland Formation	Smooth	$0.35 \pm 0.15$ , 1.30, 1.67
3:1 $\text{CHCl}_3$ : MeOH	Span 80, 2%	50%	Uniform Cylinders, Fiber Breaking, Garland Formation	Smooth	$0.50 \pm 0.20$ , 2.54, 11.74
3:1 $\text{CHCl}_3$ : MeOH	Span 80, 2%	10%	Uniform Cylinders, Fiber Beading, Fiber Branching, Ribbon Morphology, Garland Formation	Smooth	$0.46 \pm 0.18$ , 1.68, 6.99

Table 4.1. Summary of Fiber Morphology, Topography, Diameter, and Distribution for Varying Emulsions

Solvent(s)	Surfactant, Internal Phase Volume Fraction	Relative Humidity	Fiber Morphology	Fiber Topography	Average Fiber Diameter ( $\mu\text{m}$ ), Skewness, Kurtosis
3:1 CHCl <sub>3</sub> : MeOH	Span 80, 4%	50%	Uniform Cylinders, Garland Formation	Smooth	0.50 $\pm$ 0.18, 1.92, 5.37
3:1 CHCl <sub>3</sub> : MeOH	Span 80, 4%	10%	Uniform Cylinders, Fiber Branching, Ribbon Morphology, Garland Formation, Nano Webbing	Smooth	0.54 $\pm$ 0.21, 2.79, 11.72
3:1 CHCl <sub>3</sub> : MeOH	Span 80, 8%	50%	Uniform Cylinders, Garland Formation, Nano Webbing	Smooth	0.53 $\pm$ 0.26, 2.06, 6.06
3:1 CHCl <sub>3</sub> : MeOH	Span 80, 8%	10%	Uniform Cylinders, Fiber Branching, Ribbon Morphology, Garland Formation, Nano Webbing	Smooth	0.56 $\pm$ 0.24, 1.23, 2.84

#### 4.5 BIBLIOGRAPHY

- Zhang, C., Feng, F. & Zhang, H. Emulsion electrospinning: Fundamentals, food applications and prospects. *Trends in Food Science & Technology* **80**, 175-186, doi:10.1016/j.tifs.2018.08.005 (2018).
- Tian, L., Prabhakaran, M. P., Ding, X. & Ramakrishna, S. Biocompatibility evaluation of emulsion electrospun nanofibers using osteoblasts for bone tissue engineering. *J Biomater Sci Polym Ed* **24**, 1952-1968, doi:10.1080/09205063.2013.814096 (2013).
- Spano, F. *et al.* Fibrous scaffolds fabricated by emulsion electrospinning: from hosting capacity to in vivo biocompatibility. *Nanoscale* **8**, 9293-9303, doi:10.1039/c6nr00782a (2016).
- Xu, X. *et al.* Preparation of Core-Sheath Composite Nanofibers by Emulsion Electrospinning. *Macromol Rapid Comm* **27**, 1637-1642, doi:10.1002/marc.200600384 (2006).
- Yarin, A. L. Coaxial electrospinning and emulsion electrospinning of core-shell fibers. *Polym Advan Technol* **22**, 310-317, doi:10.1002/pat.1781 (2011).
- Cai, N. *et al.* Fabrication of Core/Shell Nanofibers with Desirable Mechanical and Antibacterial Properties by Pickering Emulsion Electrospinning. *Macromol Mater Eng* **302**, 1600364, doi:10.1002/mame.201600364 (2017).
- Yazgan, G. *et al.* Tunable release of hydrophilic compounds from hydrophobic nanostructured fibers prepared by emulsion electrospinning. *Polymer* **66**, 268-276, doi:10.1016/j.polymer.2015.04.045 (2015).

- 8 Wang, C., Wang, L. & Wang, M. Evolution of core-shell structure: From emulsions to ultrafine emulsion electrospun fibers. *Mater Lett* **124**, 192-196, doi:<https://doi.org/10.1016/j.matlet.2014.03.086> (2014).
- 9 Kim, I. *et al.* Cross-Linked Poly(vinylidene fluoride-co-hexafluoropropene) (PVDF-co-HFP) Gel Polymer Electrolyte for Flexible Li-Ion Battery Integrated with Organic Light Emitting Diode (OLED). *Materials (Basel)* **11**, doi:10.3390/ma11040543 (2018).
- 10 Ghelich, R., Rad, M. K. & Youzbashi, A. A. Study on Morphology and Size Distribution of Electrospun NiO-GDC Composite Nanofibers. *J Eng Fiber Fabr* **10**, 155892501501000, doi:10.1177/155892501501000102 (2015).
- 11 Hu, J., Prabhakaran, M. P., Ding, X. & Ramakrishna, S. Emulsion electrospinning of polycaprolactone: influence of surfactant type towards the scaffold properties. *Journal of Biomaterials Science, Polymer Edition* **26**, 57-75, doi:10.1080/09205063.2014.982241 (2015).
- 12 Wang, S.-Q., He, J.-H. & Xu, L. Non-ionic surfactants for enhancing electrospinnability and for the preparation of electrospun nanofibers. *Polym Int* **57**, 1079-1082, doi:10.1002/pi.2447 (2008).
- 13 Johnson, P. M. *et al.* Surfactant location and internal phase volume fraction dictate emulsion electrospun fiber morphology and modulate drug release and cell response. *Biomater Sci-Uk*, doi:10.1039/D0BM01751E (2021).
- 14 Lin, T., Wang, H., Wang, H. & Wang, X. The charge effect of cationic surfactants on the elimination of fibre beads in the electrospinning of polystyrene. *Nanotechnology* **15**, 1375-1381, doi:10.1088/0957-4484/15/9/044 (2004).
- 15 Li, X. *et al.* Encapsulation of proteins in poly(L-lactide-co-caprolactone) fibers by emulsion electrospinning. *Colloids Surf B Biointerfaces* **75**, 418-424, doi:10.1016/j.colsurfb.2009.09.014 (2010).
- 16 Beigmoradi, R., Samimi, A. & Mohebbi-Kalhari, D. Fabrication of polymeric nanofibrous mats with controllable structure and enhanced wetting behavior using one-step electrospinning. *Polymer* **143**, 271-280, doi:<https://doi.org/10.1016/j.polymer.2018.04.025> (2018).
- 17 Yarin, A. L., Kataphinan, W. & Reneker, D. H. Branching in electrospinning of nanofibers. *J Appl Phys* **98**, 064501, doi:10.1063/1.2060928 (2005).
- 18 Reneker, D. H. & Yarin, A. L. Electrospinning jets and polymer nanofibers. *Polymer* **49**, 2387-2425, doi:10.1016/j.polymer.2008.02.002 (2008).
- 19 Reneker, D. H., Yarin, A. L., Fong, H. & Koombhongse, S. Bending instability of electrically charged liquid jets of polymer solutions in electrospinning. *J Appl Phys* **87**, 4531-4547, doi:10.1063/1.373532 (2000).
- 20 Ero-Phillips, O., Jenkins, M. & Stamboulis, A. Tailoring Crystallinity of Electrospun PLLa Fibres by Control of Electrospinning Parameters. *Polymers-Basel* **4**, 1331-1348, doi:10.3390/polym4031331 (2012).
- 21 Kolbuk, D., Urbanek, O., Denis, P. & Choinska, E. Sonochemical coating as an effective method of polymeric nonwovens functionalization. *Journal of biomedical materials research. Part A*, doi:10.1002/jbm.a.36751 (2019).
- 22 Fong, H., Chun, I. & Reneker, D. H. Beaded nanofibers formed during electrospinning. *Polymer* **40**, 4585-4592, doi:10.1016/s0032-3861(99)00068-3 (1999).
- 23 Chen, S.-H., Chang, Y., Lee, K.-R. & Lai, J.-Y. A three-dimensional dual-layer nano/microfibrous structure of electrospun chitosan/poly(d,l-lactide) membrane for the improvement of cytocompatibility. *J Membrane Sci* **450**, 224-234, doi:10.1016/j.memsci.2013.08.007 (2014).
- 24 Xin, Y. & Reneker, D. H. Garland formation process in electrospinning. *Polymer* **53**, 3629-3635, doi:10.1016/j.polymer.2012.05.060 (2012).

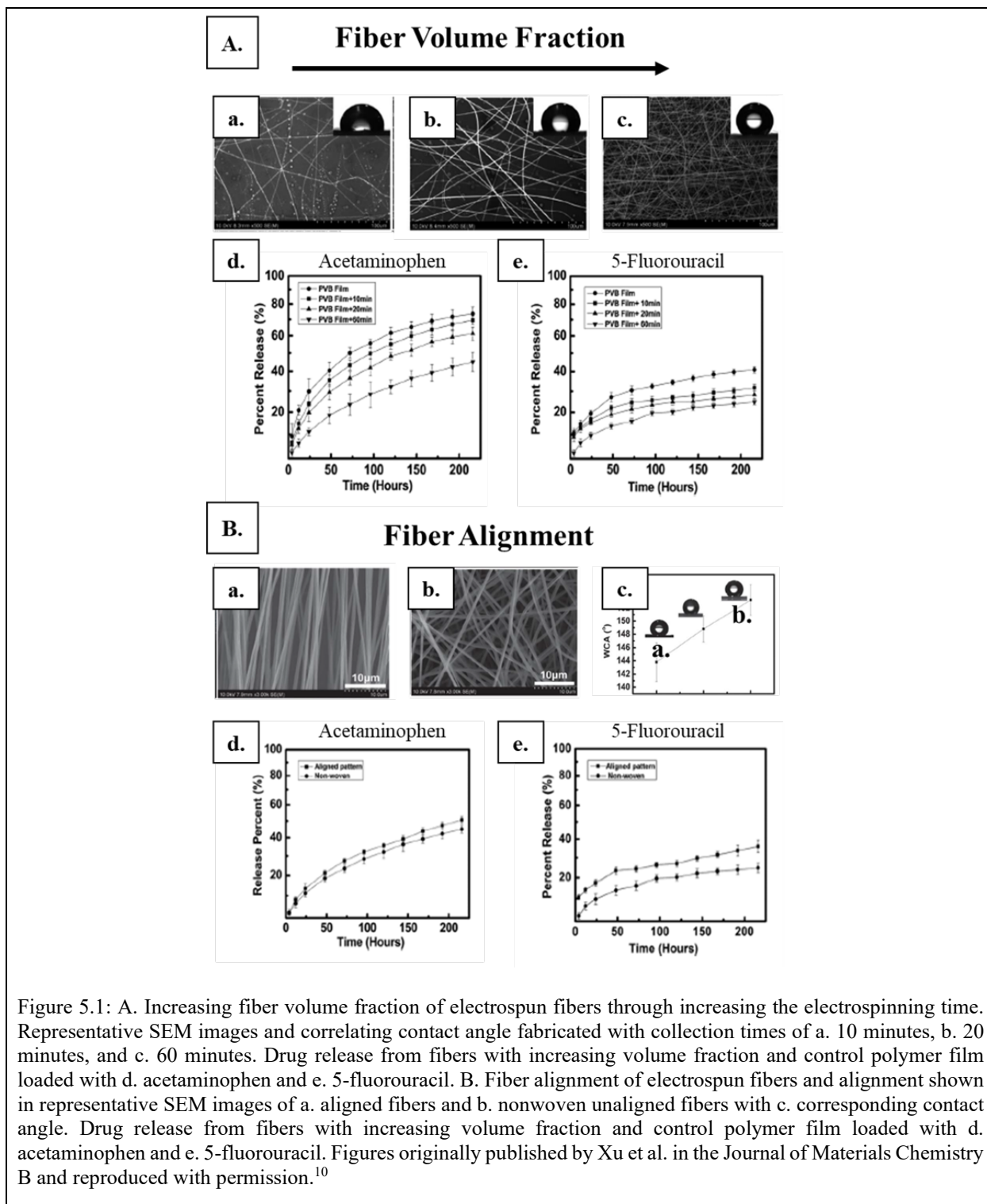
- 25 Reneker, D. H., Kataphinan, W., Theron, A., Zussman, E. & Yarin, A. L. Nanofiber garlands of polycaprolactone by electrospinning. *Polymer* **43**, 6785-6794, doi:10.1016/s0032-3861(02)00595-5 (2002).
- 26 Moutsatsou, P., Coopman, K., Smith, M. B. & Georgiadou, S. Conductive PANI fibers and determining factors for the electrospinning window. *Polymer* **77**, 143-151, doi:10.1016/j.polymer.2015.08.039 (2015).
- 27 Theron, S. A., Zussman, E. & Yarin, A. L. Experimental investigation of the governing parameters in the electrospinning of polymer solutions. *Polymer* **45**, 2017-2030, doi:10.1016/j.polymer.2004.01.024 (2004).
- 28 Zaarour, B., Zhu, L., Huang, C. & Jin, X. Fabrication of a polyvinylidene fluoride cactus-like nanofiber through one-step electrospinning. *RSC Advances* **8**, 42353-42360, doi:10.1039/c8ra09257e (2018).
- 29 Barakat, N. A. M., Kanjwal, M. A., Sheikh, F. A. & Kim, H. Y. Spider-net within the N6, PVA and PU electrospun nanofiber mats using salt addition: Novel strategy in the electrospinning process. *Polymer* **50**, 4389-4396, doi:10.1016/j.polymer.2009.07.005 (2009).
- 30 Massaglia, G. *et al.* Defining the role of nanonetting in the electrical behaviour of composite nanofiber/nets. *RSC Advances* **7**, 38812-38818, doi:10.1039/c7ra05573k (2017).
- 31 Naraghi, M., Chasiotis, I., Kahn, H., Wen, Y. & Dzenis, Y. Mechanical deformation and failure of electrospun polyacrylonitrile nanofibers as a function of strain rate. *Appl Phys Lett* **91**, 151901, doi:10.1063/1.2795799 (2007).
- 32 Zhang, X., Shi, X., Gautrot, J. E. & Peijs, T. Nanoengineered electrospun fibers and their biomedical applications: a review. *Nanocomposites* **7**, 1-34, doi:10.1080/20550324.2020.1857121 (2021).
- 33 Ahn, S. K. *et al.* Development of dye-sensitized solar cells composed of liquid crystal embedded, electrospun poly(vinylidene fluoride-co-hexafluoropropylene) nanofibers as polymer gel electrolytes. *ACS Appl Mater Interfaces* **4**, 2096-2100, doi:10.1021/am3000598 (2012).
- 34 Sy, J. C., Klemm, A. S. & Shastri, V. P. Emulsion as a Means of Controlling Electrospinning of Polymers. *Advanced Materials* **21**, 1814-1819, doi:10.1002/adma.200701630 (2009).
- 35 Wu, Y. K. *et al.* Multi-Jet Electrospinning with Auxiliary Electrode: The Influence of Solution Properties. *Polymers (Basel)* **10**, doi:10.3390/polym10060572 (2018).
- 36 Kong, C. S. *et al.* Multi-jet ejection and fluctuation in electrospinning of polyvinyl alcohol with various nozzle diameters. *Polymer Engineering & Science* **49**, 2286-2292, doi:10.1002/pen.21528 (2009).
- 37 Knopf, J. A. *Investigation of Linear Electrospinning Jets* Bachelor of Science thesis, University of Delaware, (2009).
- 38 Abdel-Hady, F., Alzahrany, A. & Hamed, M. Experimental Validation of Upward Electrospinning Process. *ISRN Nanotechnology* **2011**, 851317, doi:10.5402/2011/851317 (2011).
- 39 Wang, L., Pai, C.-L., Boyce, M. C. & Rutledge, G. C. Wrinkled surface topographies of electrospun polymer fibers. *Appl Phys Lett* **94**, 151916, doi:10.1063/1.3118526 (2009).
- 40 Lu, P. & Xia, Y. N. Maneuvering the Internal Porosity and Surface Morphology of Electrospun Polystyrene Yarns by Controlling the Solvent and Relative Humidity. *Langmuir* **29**, 7070-7078, doi:10.1021/la400747y (2013).
- 41 Zaarour, B., Zhu, L., Huang, C. & Jin, X. Controlling the Secondary Surface Morphology of Electrospun PVDF Nanofibers by Regulating the Solvent and Relative Humidity. *Nanoscale Research Letters* **13**, 285, doi:10.1186/s11671-018-2705-0 (2018).
- 42 Liu, Z. *et al.* Electrospun Jets Number and Nanofiber Morphology Effected by Voltage Value: Numerical Simulation and Experimental Verification. *Nanoscale Research Letters* **14**, doi:10.1186/s11671-019-3148-y (2019).

## CHAPTER 5: DETERMINING THE EFFECTS OF DRUG RELEASE FROM POROUS ELECTROSPUN FIBERS AND COMPARING RELEASE OF HYDROPHILIC AND HYDROPHOBIC MODEL DRUGS

### 5.1 INTRODUCTION

Controlling drug release from fibers is important to ensure that the drug is released at therapeutically effective concentrations while minimizing toxicity and adverse side effects to the patient. Numerous studies have been conducted to demonstrate that electrospun fibers are capable of encapsulating a wide variety of drugs, bioactive molecules, and proteins.<sup>1-9</sup> Factors that can affect the rate of drug release include polymer degradation rate, polymer-solvent drug compatibility, fiber volume fraction and alignment, and fiber diameter.

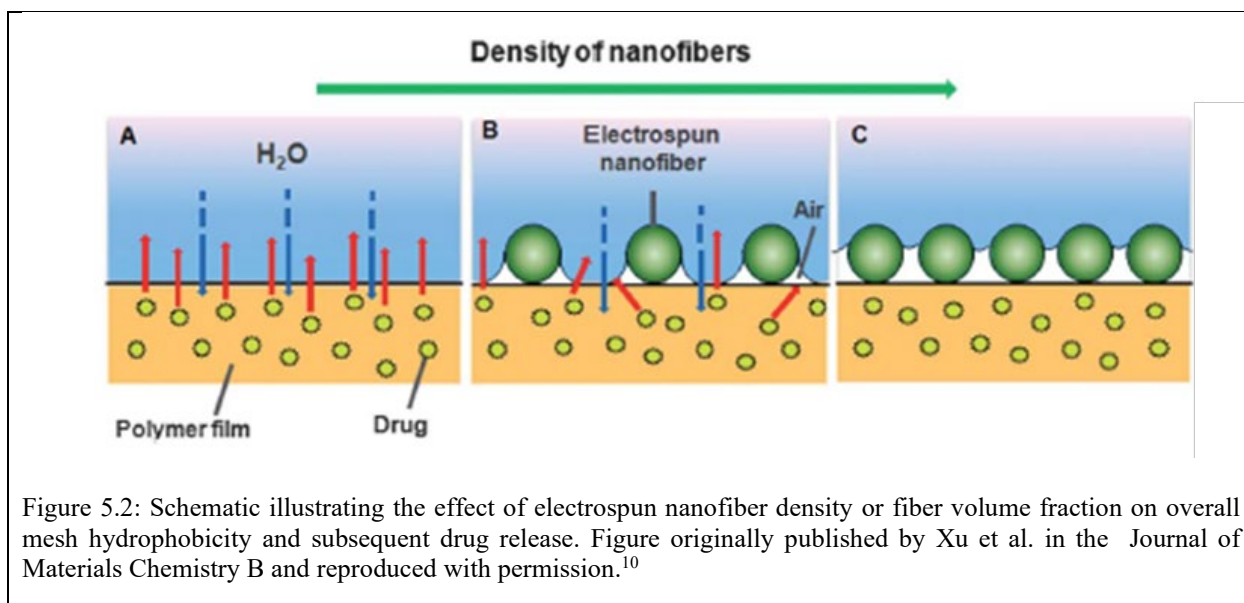
The fiber volume fraction and alignment of electrospun fibers play a critical role in drug release. In a study by Xu et al., the fiber alignment and fiber volume fraction were shown to affect overall fiber hydrophobicity and subsequent drug release.<sup>10</sup> Electrospun fiber volume fraction was increased through electrospinning fibers on a polymer film for increasing electrospinning times. Despite no changes in solution chemistry, as the time of electrospinning increased, the fiber volume fraction and corresponding contact angle also increased (Figure 5.1A a-c). Fiber volume fraction was only assessed qualitatively through the SEM images. Data results indicate that at a higher fiber volume fraction, the overall mesh is more hydrophobic and contact with an aqueous liquid is less likely due to the trapping of air. Model drugs acetaminophen and 5-fluorouracil were released from a control polyvinyl butyral (PVB) film and from PVB electrospun fibers that were electrospun for time periods of 10, 20, and 60 minutes, respectively (Figure 5.1A d-e). Overall, the rate of drug release for both acetaminophen and 5-fluorouracil decreased with increasing fiber volume fraction. This indicates that fiber volume fraction may be playing a role in drug release rate, potentially due to solvent contact with fibers.



Xu et al. also looked at the effect of fiber alignment on overall mesh hydrophobicity and the subsequent release of drugs from PVB electrospun fibers. Aligned electrospun fibers were

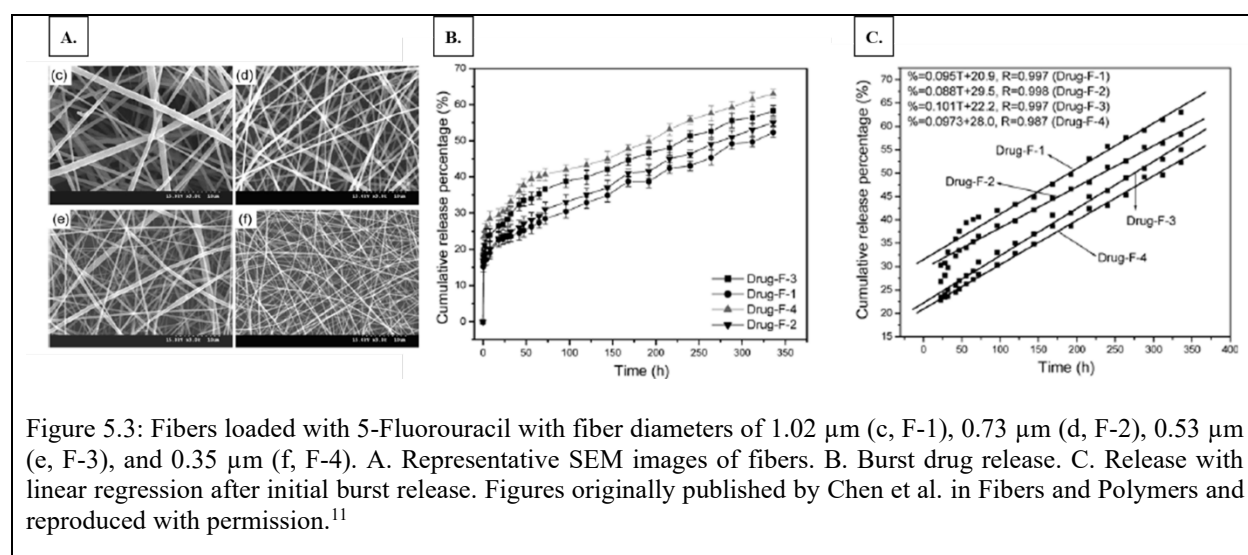


compared to nonwoven, unaligned electrospun fibers (Figure 5.1B a-b). Aligned fibers had a lower contact angle compared to nonwoven, unaligned electrospun fibers (Figure 5.1B-c). The higher contact angle observed in unaligned, nonwoven fibers may be due to pores creating more void space for air trapping. The subsequent release of model drugs acetaminophen and 5-fluorouracil both demonstrated a faster release rate from aligned fibers compared to nonwoven fibers (Figure 5.1B d-e). This further supports the hypothesis that as fiber volume fraction increases, mesh hydrophobicity also increases, creating less contact of the solvent with overall mesh and therefore reducing the rate of drug release (Figure 5.2).



The spacing and volume fraction of electrospun fibers, the diameter of the fibers, and the compatibility of the drug with the polymer-solvent system are all important in the rate of drug release. In a study by Chen et al., the role of fiber diameter in drug release rate was shown.<sup>11</sup> In this study, poly(lactic acid) fibers were loaded with 5-Fluorouracil as a model drug and electrospun with either a  $\text{CHCl}_3$  and DMF solvent system or a 1,1,1,3,3,3-Hexafluoro-2-isopropanol (HFIP) and  $\text{CHCl}_3$  solvent system. Processing parameters of flow rate and applied voltage were altered in

order to achieve fibers with 1.02  $\mu\text{m}$  ( $\text{CHCl}_3$  and DMF), 0.73  $\mu\text{m}$  ( $\text{CHCl}_3$  and DMF), 0.53  $\mu\text{m}$  (DMF and HFIP), and 0.35  $\mu\text{m}$  ( $\text{CHCl}_3$  and HFIP) diameters (Figure 5.3A). Overall, fibers fabricated with both solvent systems demonstrated a larger burst release with larger fiber diameters (Figure 5.3B). This was due to an increase in surface area of larger fibers allowing for more drugs to separate onto the surface of the fiber than in smaller fibers. Drug release after the initial burst demonstrated that the release rate from fibers with smaller fiber diameters was faster than in fibers with larger fiber diameters (Figure 5.3C). This is because the diffusional path for a drug to diffuse from larger fiber diameters is longer than the diffusional path in smaller fiber diameters. Chen et al. also proposes that higher burst release may be due to drug solubility in the polymer-drug system but does not expand on this concept with regard to their experimental results and chemistry of their solvents and drug.



When analyzing the results of Chen et al.'s study, the model drug, 5-Fluorouracil, is a highly hydrophilic drug with a calculated partition coefficient of -0.9, according to PubChem. The dielectric constants, which are correlated to solvent polarity, of DMF, HFIP, and  $\text{CHCl}_3$  are 36.7, 16.7, and 4.9, respectively.<sup>12,13</sup> Therefore, it would be expected that systems with less polar solvents are more likely to be incompatible with the highly hydrophilic model drug. In the study

conducted by Chen et al., 5-Fluorouracil would be expected to have less compatibility in the systems fabricated with  $\text{CHCl}_3$  and DMF solvents (F-3 and F-4) than in the systems fabricated with HFIP and DMF solvents (F-1 and F-2). This is indeed supported by the higher burst release of F-3 and F-4 compared to F-1 and F-2 fibers seen in Figure 5.3B.

The importance of matching drug compatibility and polarity with the solvent and polymers used in electrospinning has been well documented.<sup>4,14</sup> Further, tuning of electrospun fibers can be achieved by using an emulsion. Emulsion electrospun fibers can have the advantage of improved stability, bioavailability, encapsulation efficiency, and controlled release.<sup>14</sup> Increasing the concentration of surfactant in electrospun fibers can increase pores distributed throughout the fiber instead of coalesced within the core.<sup>15</sup> Samples with this distributed porous internal architecture are also known to have decreased burst and overall release rates.<sup>15,16</sup> Using an emulsion to fabricate fibers has also been shown to decrease drug release rate in systems with hydrophobic polymers.<sup>15,17,18</sup>

Emulsion electrospinning is an attractive fabrication method to control drug release, improve encapsulation efficiency, and maintain bioavailability. Focusing on controlled release, it is important to understand the effects that surfactant, internal phase, and drug-polymer-solvent compatibility have on drug release from electrospun fibers. This study is designed to determine the effect of surfactant and internal porosity on drug release from emulsion electrospun fibers. The study further investigates the role that drug hydrophobicity plays in fibers electrospun with no surfactant (control), surfactant, and internal phase in drug release.

## 5.2 MATERIALS & METHODS

### 5.2.1 Materials

Poly( $\epsilon$ -caprolactone) (PCL) (50,000  $M_w$ ) was purchased from CAPA lot # 120625. Span80 was purchased from Sigma Aldrich lot # MKCF4138. Solvent N, N-Dimethylformamide (DMF) anhydrous with 99.8% purity was purchased from Sigma Aldrich lot # SHBJ7641. Chloroform solvent ( $CHCl_3$ ) with  $\geq 99.5\%$  purity was purchased from lot # SHBL1580. Anhydrous ethanol was purchased from Thermo Fisher Scientific lot # 201284. Nile Red with 99% purity was purchased from ACROS Organics lot # A0395995 and lot# 0082001. Rhodamine B with 99% purity was purchased from ACOS Organics lot # A0406070.

### 5.2.2 Polymer Solution Fabrication

#### 5.2.2.1 Drug Release from Solid and Porous Fibers of Increasing Fiber Diameter

Polymer solutions were fabricated with PCL dissolved in  $CHCl_3$  at a concentration of 20% w/v. Span80 was added to half of the samples at a concentration of 30% w/v relative to polymer to facilitate internal porosity in downstream electrospun fibers. Each solution was mixed for at least one hour on a stir plate with a stir bar spinning at a rate of 250 rpm, after which no solid polymer was visible in the solution. The model drug, Nile Red, was then added to the solution at a concentration of 1 mg/mL, and the solution was mixed using a FlackTek Speed Mixer DAC 150.1FVZ-K for 30 seconds at a mixing speed of 2500 RPM.

#### 5.2.2.2 Surfactant Vs. Emulsion Release of Hydrophilic and Lipophilic Drugs

Polymer solutions were fabricated with PCL dissolved in 3:1  $CHCl_3$ :DMF at a concentration of 20% w/v. Span80 was added to surfactant control with no internal phase and emulsion samples at a concentration of 30% w/v. Each solution was mixed for at least one hour on a stir plate with a stir bar spinning at a rate of 250 rpm, after which no solid polymer was visible

in the solution. Model drugs, Nile Red or Rhodamine B, were then added to the solution at a concentration of 1 mg/mL, and the solution was mixed using a FlackTek Speed Mixer DAC 150.1FVZ-K for 30 seconds at a mixing speed of 2500 rpm. In samples containing the internal phase, water was added in 20  $\mu$ m increments until a total of 8% w/o internal phase volume fraction was achieved. After each internal phase increment was added, the solution was mixed for 30 seconds at a mixing speed of 2500 rpm to ensure that internal phase droplets were adequately suspended within the continuous phase.

### **5.2.3 Electrospun Scaffold Fabrication**

#### *5.2.3.1 Drug Release from Solid and Porous Fibers of Increasing Fiber Diameter*

Polymer solutions were electrospun using two different sets of processing parameters to achieve release from two different sized diameter fibers. The fibers were solid or had internal porosity created with vapor induced phase separation from ambient water droplets penetrating fibers at high relative humidity. In the first method to achieve smaller fiber diameters, electrospinning parameters were held constant with a Harvard Apparatus pump flow rate of 0.5 mL/h, a collection plate distance needle tip to collection plate of 25 cm, an applied voltage of 15 kV from a GAMMA high voltage research source, and a blunted 21-gauge needle. Samples using these processing parameters were electrospun for one hour in a relative humidity environment of  $43\% \pm 3\%$  and a temperature of  $24 \pm 1$  °C. Samples that have been fabricated with these parameters with chloroform have smaller fiber diameters and have no surfactant and will be referred to hereafter as CSN. Samples that have been fabricated with this set of parameters with chloroform have smaller fiber diameters and have surfactant and will be referred to hereafter as CSS.

In the second method used to achieve larger fiber diameters, electrospinning parameters were held constant with a pump flow rate of 1.8 mL per hour, a collection plate distance needle tip

to collection plate of 33 cm, an applied voltage of 18 kV, and a blunted 21gauge needle. Samples using these parameters were electrospun for 15 minutes at a high relative humidity environment of  $58\% \pm 1\%$  and  $17 \pm 1$  °C. Samples that have been fabricated with these parameters and no with chloroform, have larger fiber diameters, and have no surfactant will be referred to as CLN. Samples that have been fabricated with these parameters with chloroform have larger fiber diameters and have surfactant and, therefore, will be referred to as CLS. All sample parameters are summarized in Table 5.1 below.

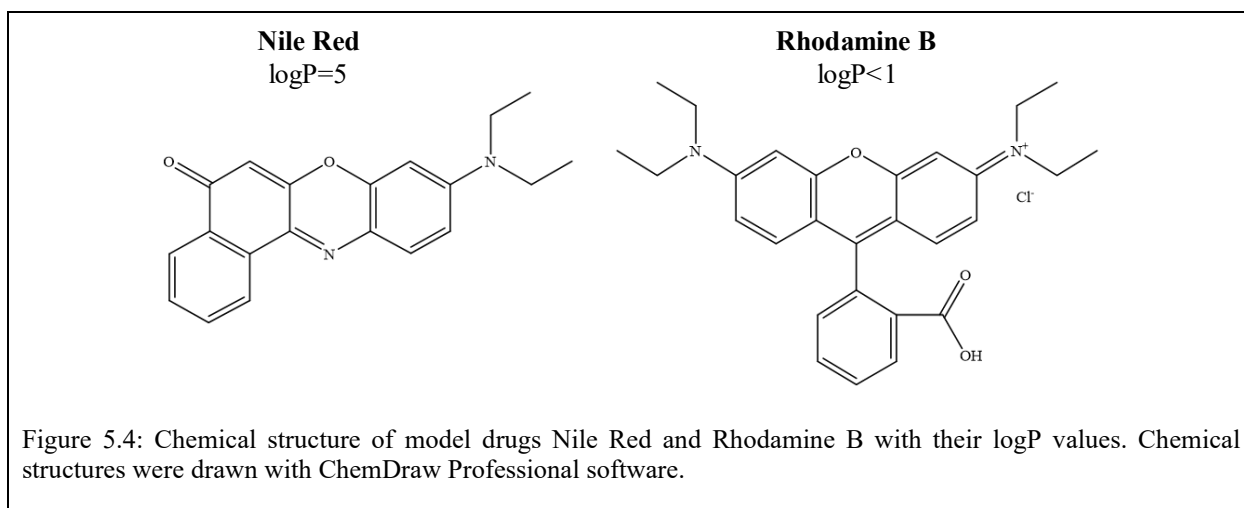
All samples were electrospun onto aluminum foil to avoid potential contamination of the collection plate with the model drug Nile Red. All samples were loaded into a 5 mL glass syringe for electrospinning. After each specimen was collected, it was carefully peeled off the collection plate and left to dry thoroughly in the fume hood overnight. Specimens were further dried in a vacuum chamber before characterization. All samples were electrospun for at least one hour. At least three specimens were fabricated per set of sample parameters.

#### *5.2.3.2 Emulsions with Hydrophobic and Hydrophilic Drug*

To compare the release of both a model hydrophilic and model hydrophobic small molecules from samples containing no surfactant, surfactant, and emulsion internal phase, the following samples were electrospun. Electrospinning parameters were held constant with a Harvard Apparatus pump flow rate of 1.5 mL/h, distance from needle tip to collection plate of 20 cm, an applied voltage of 18 kV from a GAMMA high voltage research source, and a blunted 21-gauge needle. All samples were loaded into a plastic 10 mL syringe for electrospinning. Samples using these processing parameters were electrospun for 20 minutes in a low relative humidity environment of  $18\% \pm 3\%$  and a temperature of  $23 \pm 2$  °C. All samples were electrospun onto aluminum foil to avoid potential contamination of the collection plate with the model drugs Nile

Red or Rhodamine B. After each sample was collected, it was carefully peeled off the collection plate and left to dry thoroughly in the fume hood overnight. Samples were further dried in a vacuum chamber before characterization. At least three samples were fabricated per set of sample parameters.

To compare the effects of polymer-solvent compatibility with the hydrophobicity of a model drug, fluorescent molecules Nile Red and Rhodamine B were encapsulated within fibers as models for drug release. They will be referred to as model drugs throughout this section. Nile Red ( $\log P = 5$ ) is soluble in  $\text{CHCl}_3$  and Rhodamine B ( $\log P < 1$ ) is soluble in water (Figure 5.4).<sup>19,20</sup>



Samples electrospun with these parameters all were fabricated using a solvent blend of 3:1  $\text{CHCl}_3$ : DMF (D), have a model drug Nile Red (N) or Rhodamine B (R), have either no surfactant and no internal phase (N), surfactant and no internal phase (S), or surfactant and internal phase to make an emulsion (E). Therefore, samples with each of the following fabrication parameters will be known as DNN, DNS, DNE, DRN, DRS, and DRE, respectively, for brevity (Table 5.1).

Table 5.1: Sample Parameters for all electrospun mesh fabricated.

<b><u>Acronyms</u></b>							
<b><u>First Position</u></b> C= CHCl <sub>3</sub> D= 3:1 CHCl <sub>3</sub> : DMF			<b><u>Second Position</u></b> S= Small fiber diameter L= Large fiber diameter N= Nile Red R= Rhodamine B			<b><u>Third Position</u></b> N= No surfactant S= Surfactant E= Emulsion	
<b>Sample Name</b>	<b>Solvent</b>	<b>Surfactant Conc. (w/w %)</b>	<b>Internal Phase Volume Fraction (%)</b>	<b>Loaded Drug, Conc. (mg/mL)</b>	<b>Applied Voltage (kV), Pump Flow Rate (mL/h), Distance from Needle Tip to Collection Plate (cm)</b>	<b>Spinning Time (mins)</b>	<b>Range of Ambient Relative Humidity (%), Temperature (°C)</b>
CSN (n=3)	CHCl <sub>3</sub>	0	0	Nile Red, 0.1	15, 0.5, 25	60	40-43, 23.6-24
CSS (n=3)	CHCl <sub>3</sub>	30	0	Nile Red, 0.1	15, 0.5, 25	60	40-45, 23.6-24
CLN (n=3)	CHCl <sub>3</sub>	0	0	Nile Red, 0.1	18, 1.8, 33	30	58-59, 17.2-17.7
CLS (n=3)	CHCl <sub>3</sub>	30	0	Nile Red, 0.1	18, 1.8, 33	30	58-59, 17.0-17.1
DNN (n=3)	3:1 CHCl <sub>3</sub> : DMF	0	0	Nile Red, 1	1.5, 18, 20	20	16-17, 24.6-24.7
DNS (n=3)	3:1 CHCl <sub>3</sub> : DMF	30	0	Nile Red, 1	1.5, 18, 20	20	15-16, 24.5-24.6
DNE (n=3)	3:1 CHCl <sub>3</sub> : DMF	30	8	Nile Red, 1	1.5, 18, 20	20	15, 24.5-24.6
DRN (n=3)	3:1 CHCl <sub>3</sub> : DMF	0	0	Rhodamine B, 1	1.5, 18, 20	20	18, 24.3-24.5
DRS (n=3)	3:1 CHCl <sub>3</sub> : DMF	30	0	Rhodamine B, 1	1.5, 18, 20	20	21, 24.4-24.6
DRE (n=3)	3:1 CHCl <sub>3</sub> : DMF	30	8	Rhodamine B, 1	1.5, 18, 20	20	17-18, 24.4-22.5



#### 5.2.4 Fiber Characterization

Mesh was analyzed using a Phenom Pro Desktop scanning electron microscope (SEM) to capture fiber morphology, surface topography, and diameter. Specimens were cut from the electrospun samples in an approximately 1 cm x 1 cm square from the center of the collection to avoid potential edge effects. All samples were coated with 8 nm of iridium before imaging. Fiber morphology was characterized by imaging each sample in at least five different locations to capture morphological effects using 10 kV accelerating voltage, a backscatter detector, and a magnification appropriate to observe the fiber morphology. Fiber morphology was assessed for overall homogeneity and appearance of wet fibers. Fiber topography was determined through visual assessment and captured for samples electrospun at high relative humidity by imaging with 10 kV accelerating voltage, a backscatter detector, and at a magnification of 25,000x.

Fiber diameter was determined by imaging each sample specimen in five different locations using 10 kV of accelerating voltage and a backscatter detector. Locations were selected for each of the four corners of the square specimen and the central location. Mesh fabricated with  $\text{CHCl}_3$  had larger fiber diameters and therefore was captured at a magnification of 1,000x. Mesh fabricated with 3:1  $\text{CHCl}_3$ : DMF solvent had smaller fiber diameters and therefore was captured at a magnification of 5,000x. Each image was then analyzed with the software ImageJ using the plugin DiameterJ. From this initial segmentation, binary-colored segmented images produced with the algorithms M3, M5, M7, S2, S3, and S7 were used to determine fiber diameter and fiber diameter distribution using DiameterJ. In a few rare cases, DiameterJ was unable to process a segmented image, in which case a segmented image produced with an un-used algorithm that was judged as the most representative of the original image was substituted for further analysis. The average fiber diameter for each algorithm was then averaged to determine the average fiber per

SEM image. These fiber diameters were then used for further statistical comparison between groups and plotted in GraphPad Prism.

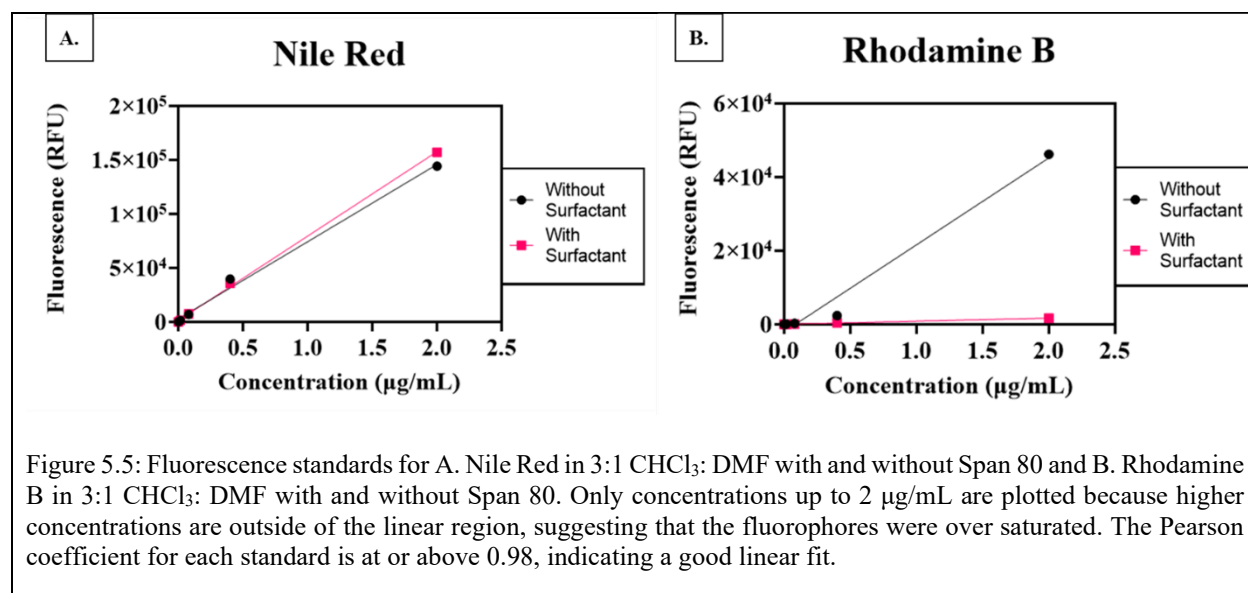
The same binary-colored, segmented images from ImageJ used to determine fiber diameter were used to calculate the fiber fraction, which is described in Equation 5.1. Each image had all of its white pixels, which represent the fiber area, and all of the black pixels, which represent the void area, counted. The number of pixels representing fibers was divided by the total number of pixels and multiplied by 100 to calculate the percent fiber fraction.

$$Fiber\ Fraction = \frac{Fiber\ Area}{(Fiber\ Area + Void\ Area)} * 100 \quad (Eq. 5.1)$$

### 5.2.5 Drug Loading

Specimens were cut from each electrospun mesh in triplicate using an 8 mm diameter histology punch. Each specimen was weighed in order to normalize for localized differences in mesh thickness. Each mesh was then dissolved in 2 mL of CHCl<sub>3</sub> and manually mixed by shaking until the mesh visually appeared to be entirely dissolved in the solvent. Each solution was mixed using a vortex, and 200 μL of the solution was pipetted in triplicate into a black 96 well plate. Within the same well plate, standards of the drug in known concentrations were prepared with a serial dilution in CHCl<sub>3</sub>. The serial dilution of standards was prepared at concentrations of 10, 2, 0.4, 0.08, and 0.016 μg/mL for CSN, CSS, CLN, and CLS samples. For DRN, DRS, DRE, DNN, DNS, and DNE samples, concentrations of standards were 50, 10, 2, 0.4, 0.08, and 0.016 μg/mL. To compensate for any potential interactions between the fluorescent drugs and the surfactants, additional standards that included surfactants were made at the same concentrations (Figure 5.1). In the case of Rhodamine B, the effect of surfactant on the fluorescence was dramatic, significantly lowering the fluorescence at all concentrations. Meshes that included surfactant were analyzed

against standards that included surfactant, and meshes without surfactant were analyzed against standards without surfactant. All samples were measured for fluorescence using a Biotek Cytation 5 microplate reader. Samples loaded with Nile Red were measured using an excitation of  $552 \pm 20$  nm and emission at  $636 \pm 20$  nm, and samples loaded with Rhodamine B were measured using an excitation of  $553 \pm 20$  nm and emission at  $627 \pm 20$  nm. Concentration was calculated for each mesh using the standard curve and normalized per weight of each individual mesh.



### 5.2.6 Drug Release

Specimens were cut from each electrospun mesh in triplicate using an 8 mm diameter histology punch. Each specimen was weighed to normalize for localized differences in mesh thickness. Each specimen loaded with Nile Red was placed in 1 mL of ethanol. Each specimen loaded with Rhodamine B was placed in 1 mL of water. Water and ethanol were used based on solubility of Rhodamine B and Nile Red in these solvents. At time points of 0.5, 1, 1.5, 2, 2.5, 3, 4, 5, 10, 15, 30, 45, and 60 minutes, all of the solvent (either water or ethanol) was removed and stored temporarily in an Eppendorf tube for future analysis of concentration and the solvent in the

specimen tube was replenished. Stored samples were covered in aluminum foil to minimize the effects of photobleaching. Upon completion of the collection of each sample, aliquots were mixed before 200  $\mu\text{L}$  aliquots were removed from the sample and pipetted into 96 well plates in triplicate. All samples loaded with Nile Red were measured for fluorescence using a Biotek Cytation 5 microplate reader with an excitation of  $554 \pm 20$  nm and emission at  $638 \pm 20$  nm. All samples loaded with Rhodamine B were measured for fluorescence using a Biotek Cytation 5 microplate reader with an excitation of  $553 \pm 20$  nm and emission at  $627 \pm 20$  nm.

Concentration was determined with a standard curve of the drug in release media. Standard curves of Nile Red in ethanol were prepared using a serial dilution to create concentrations of 0.01,  $2 \times 10^{-3}$ ,  $4 \times 10^{-4}$ ,  $8 \times 10^{-5}$ , and  $1.6 \times 10^{-5}$  mg/mL. Rhodamine B's standard curves in water were prepared with a serial dilution to create concentrations of 0.01,  $2 \times 10^{-3}$ ,  $4 \times 10^{-4}$ ,  $8 \times 10^{-5}$ , and  $1.6 \times 10^{-5}$  mg/mL.

### **5.2.7 Statistical Analysis**

Fiber diameter per SEM image was determined with ImageJ and the plugin DiameterJ as described above. The average fiber diameter of each SEM image was used to compare fiber diameter and fiber fraction between groups. First, a one-way ANOVA with Brown-Forsythe and Welch's tests was performed on each set of sample parameters, respectively, to determine that the electrospun samples were statistically different. This was followed up with Dunnett posthoc test. Groups were compared using a one-way Brown-Forsythe and Welch's ANOVA with Dunnett's multiple comparisons posthoc and 95%, 99%, 99.9%, and 99.999% confidence intervals.

The drug loading was compared using the average amount encapsulated in a specimen calculated using the average per well on the well plate's theoretical concentration based on the standard curve. The average concentration in each specimen was used to compare the set of sample

parameters for respective groupings. The comparison was performed using Welch's test for pairwise comparisons and one-way ANOVA for Brown-Forsythe and Welch's tests and 95%, 99%, 99.9%, and 99.999% confidence intervals. Data with confidence intervals were plotted between respective groups on boxplots to show variance in the data. The amount of cumulative drug release was normalized by the individual samples' weight and plotted relative to the theoretical amount of drug encapsulated w/w%. All statistical tests and graphing were performed using Prism Graphpad software.

## **5.3 RESULTS AND DISCUSSION**

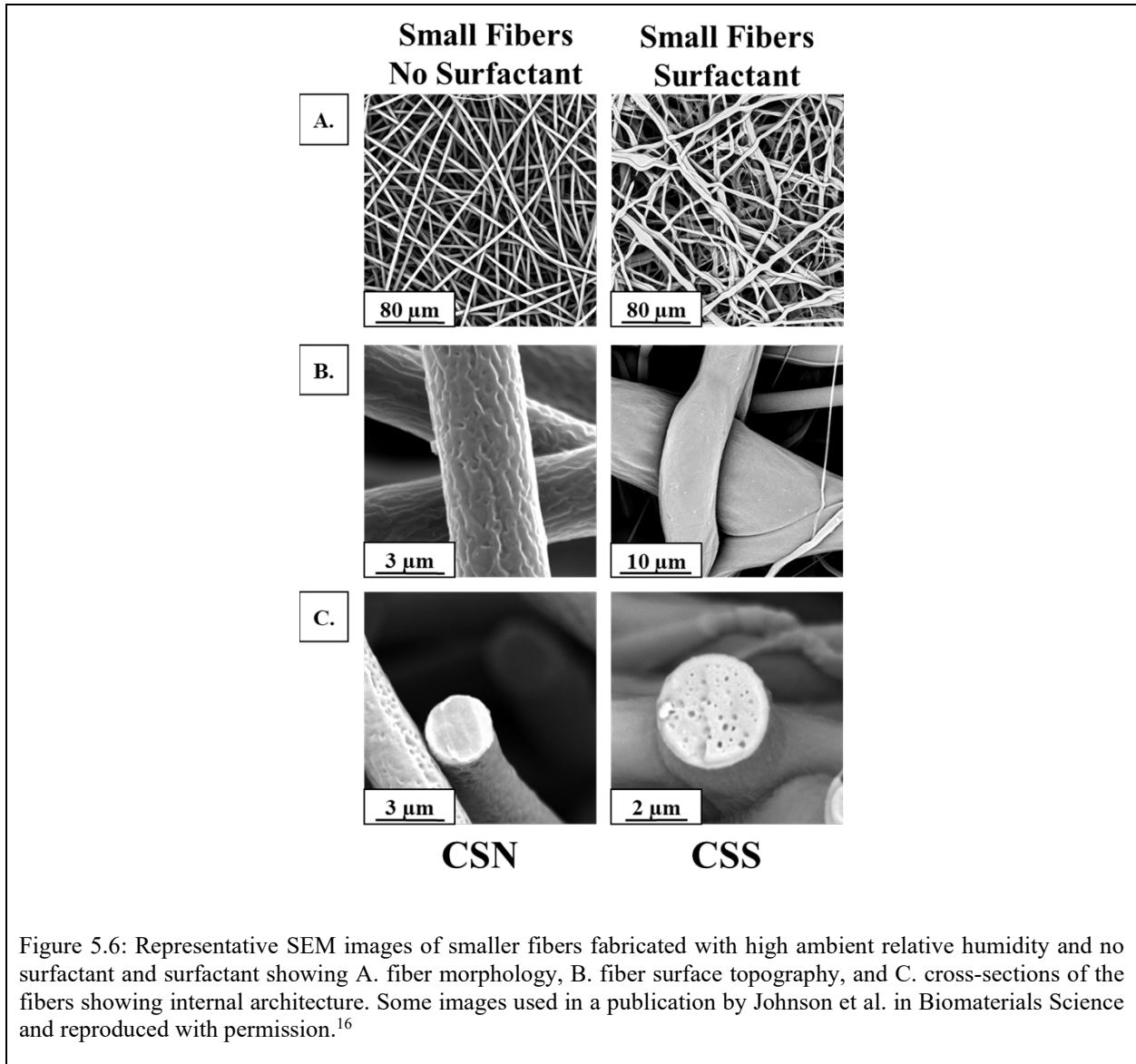
### **5.3.1 Drug Release from Solid and Porous Fibers of Increasing Fiber Diameter**

#### *5.3.1.1 Smaller Fiber Diameters*

##### 5.3.1.1.1 Fiber Characteristics

Samples electrospun with  $\text{CHCl}_3$  solvent at high relative humidity and processing parameters to make smaller fiber diameters (CSN and CSS) had fibers with predominantly uniform cylindrical fiber morphology (Figure 5.6). CSS samples had some samples with broken fibers and smaller fibers, but overall the predominant morphology was cylindrical. This indicates that solution chemistry, processing parameters, and ambient conditions were appropriately balanced to create uniform fibers. The surface topography of CSN fibers was porous, and the surface topography of CSS fibers was smooth. This was likely due to the surfactant relocating to the fibers' surface in CSS fibers and allowing water to penetrate into the fibers' depth. CSN fibers were porous because ambient water droplets condensed on the fibers' surface to create vapor-induced phase separation and templated surface pores. The cross-sections of CSN fibers were solid, indicating that ambient water vapor was only able to penetrate the fibers' surface. The cross-section

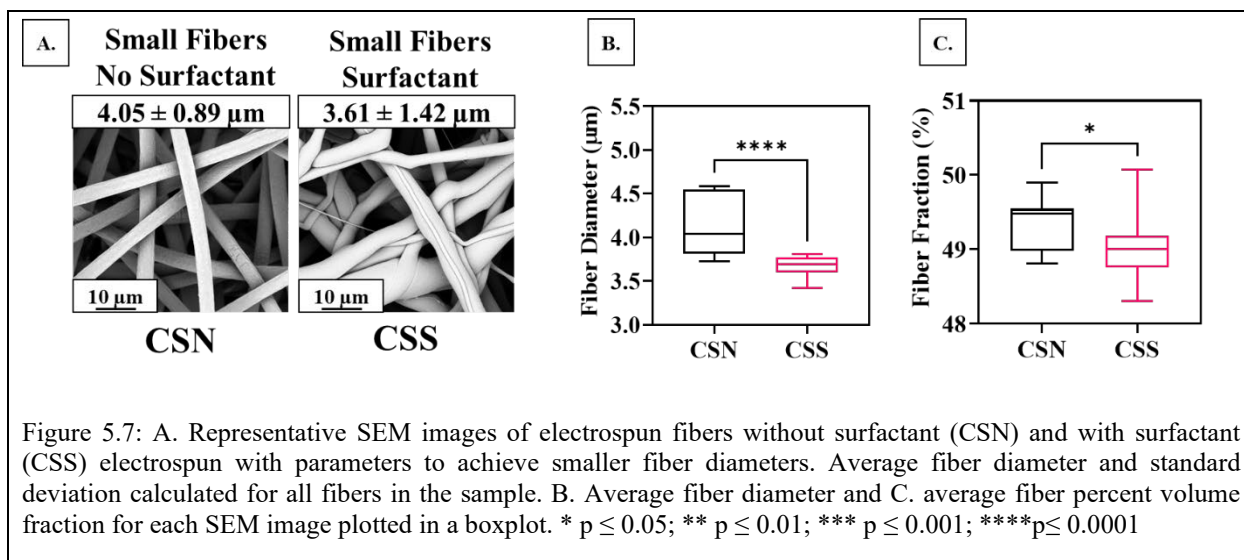
of CSS fibers was porous, indicating that water vapor could penetrate into and throughout the fiber during the electrospinning process.



#### 5.3.1.1.2 Fiber Diameter and Fiber Fraction

The average fiber diameter for CSN and CSS fibers was  $4.05 \pm 0.89 \mu\text{m}$  and  $3.61 \pm 1.42 \mu\text{m}$ , respectively (Figure 5.7A). CSS fibers' average fiber diameter was significantly smaller than the average fiber diameter for CSN fibers (Figure 5.7B). This fiber diameter reduction may have

been due to surfactant reducing surface tension and causing an increased jet acceleration and Taylor cone thinning. It is crucial to control fiber diameter because fiber diameter can affect the rate of drug release. Studies by Chen et al. have shown that electrospun fibers with larger fiber diameters generally release drugs at a slower rate and have a reduced burst release of drugs than smaller fibers.<sup>11</sup> Although the fiber diameters were statistically different in this case; the overall fiber diameters are within the error range and, therefore, may be compared to show general trends in drug release from fibers with and without surfactant.



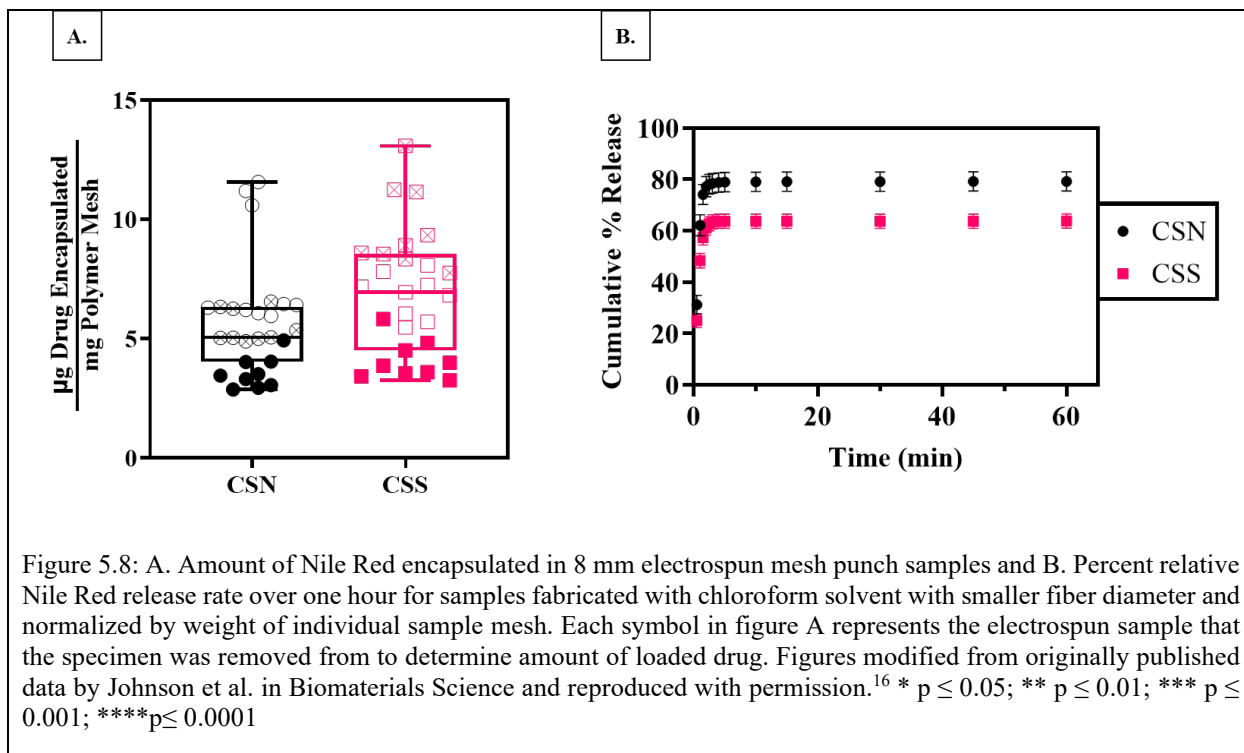
Fiber fraction was also statistically different for CSS and CSN samples (Figure 5.7C). Fiber fraction is the fraction of the mesh taken up by fibers vs. the mesh amount taken up by air. According to Szewczyk et al., fiber fraction and surface topography play a dominant role in electrospun mesh's overall hydrophobicity.<sup>21</sup> In a study by Xu et al., the effect of mesh orientation on overall mesh hydrophobicity also played a role in drug release rate based on liquid contact with fibers.<sup>10</sup> Although the fiber fraction was statistically different in this case; the average fiber fractions were close in values indicating that fiber fraction may be a less dominant effect when

comparing these samples. Based on studies conducted in Chapter 2, it should also be recognized that surfactant relocating to the surface of the fibers in samples with a surfactant are likely to have overall higher hydrophilicity and, therefore, greater contact with release media. This higher hydrophilicity is due to surfactant relocating at the fiber's surface and, therefore, reducing surface tension in contact with a hydrophilic release media.

#### 5.3.1.1.3 Drug Loading and Release

The amount of drug encapsulated in each sample was determined by dissolving samples in chloroform and measuring the amount of Nile Red (Figure 5.8A). The amount of Nile Red loaded in samples with the surfactant and no surfactant was not statistically different. This indicates that any difference in release rates from a given mesh is likely not due to differences in concentration of loading. The release of CSN fibers had a greater burst release than the CSS fibers (Figure 5.8B). Burst release of drug from electrospun fibers can occur at high loading concentrations and when the drug is incompatible with the polymer-solvent system.<sup>4</sup>





The smaller burst release of Nile Red from fibers with surfactant is likely due to two factors. First, Nile Red and Span80 interact at the fiber's oil-water interface, minimizing the amount of initial Nile Red at the oil-air interface in the mesh fabricated with no surfactant. Interactions may be due to hydrogen bonding between the hydroxyl groups on Span 80 with the ketone, ether, or amide group in Nile Red. Second, the PCL control fibers have increased surface area due to the surface roughness, which may increase the release compared to the smooth Span80 fibers, which have a relatively lower surface area. The reduction in burst release of the drug and subsequent similar release rates indicate that although the fiber diameter and fiber volume fraction were statistically different, they likely did not play a major role. If fiber diameter played a major role, CSN with higher fiber diameters and fiber volume fraction would be expected to release the drug at a slower rate due to increased diffusional path for the drug and decreased contact with release media.

### *5.3.1.2 Larger Fiber Diameters*

#### 5.3.1.2.1 Fiber Characteristics

This trend was similar for samples electrospun with no surfactant (CLN) and surfactant (CLS) with processing parameters designed to fabricate larger fiber diameters. The fiber morphology was uniform and cylindrical and the samples fabricated with surfactant had fewer defects than the ones optimized to fabricate smaller fiber diameters (Figure 5.9A). The lower defect morphology in CLS fibers compared to CSS fibers may have been due to a larger area created by an increased flow rate for the surfactant to distribute within the fiber and at the fiber's surface, decreasing the effect of surface tension. The surface topography of CLN fibers was porous with distinct pore morphology, while the surface topography of CLS fibers was smooth with slight longitudinal wrinkles potentially caused by buckling (Figure 5.9B). Surface pores in CLN fibers are caused by ambient relative humidity condensing on the polymer's surface and templating the porous architecture. CLS fibers had smooth surface topography because surfactant at the oil-air interface disrupted phase separation caused by condensation on the jet's surface.

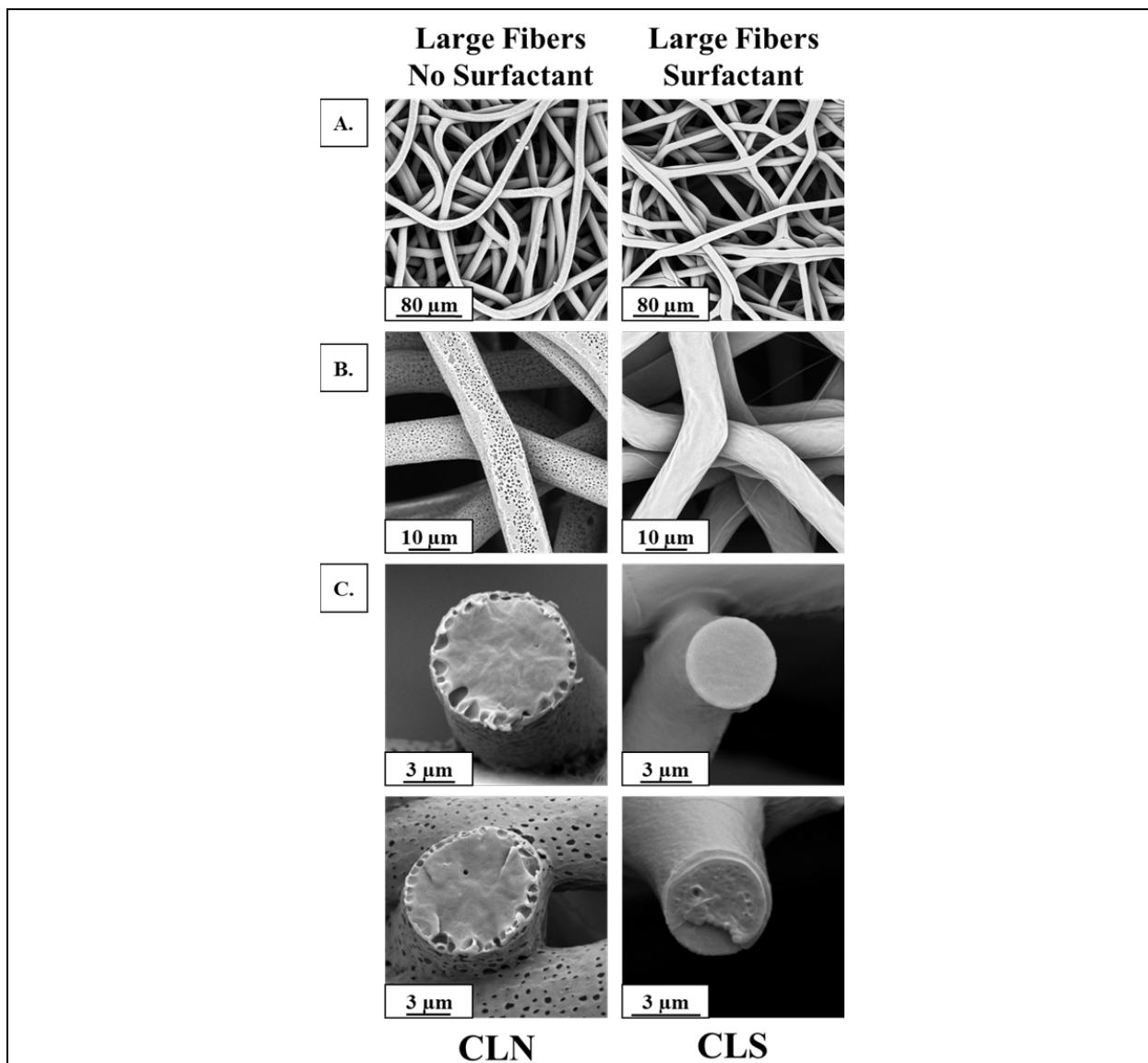


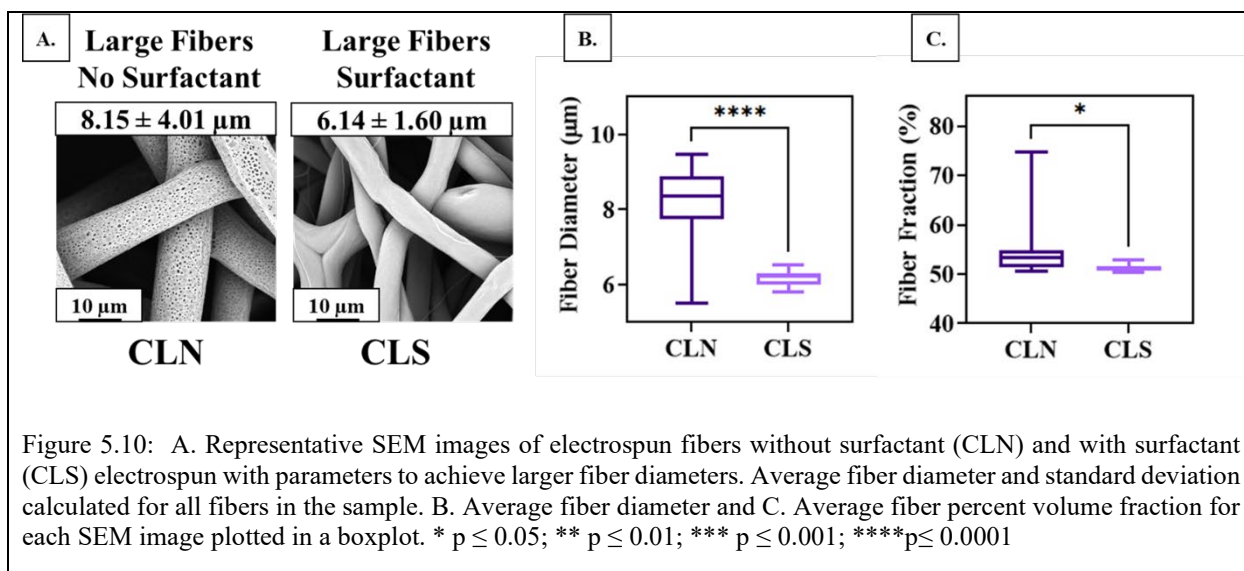
Figure 5.9: Representative SEM images of larger fibers fabricated with high ambient relative humidity and no surfactant and surfactant showing the A. fiber morphology, B. fiber surface topography, and C. cross-sections of the fibers showing solid and small pore internal architecture.

The cross-sectional internal architecture of CLN fibers was predominantly solid with a halo of pores around the fiber's shell (Figure 5.9C). In rare fibers, a small pore was observed in the cross-section of the CLN fibers. This internal architecture indicates that water predominantly stayed at the surface of the fibers and shell and only occasionally penetrated the fibers. The cross-sectional internal architecture of CLS fibers was predominantly solid with no porous halo. A

minority of the CLS fibers also had a few pores indicating that ambient water vapor may have been able to penetrate into the fiber and, in this case, coalesced into larger pores.

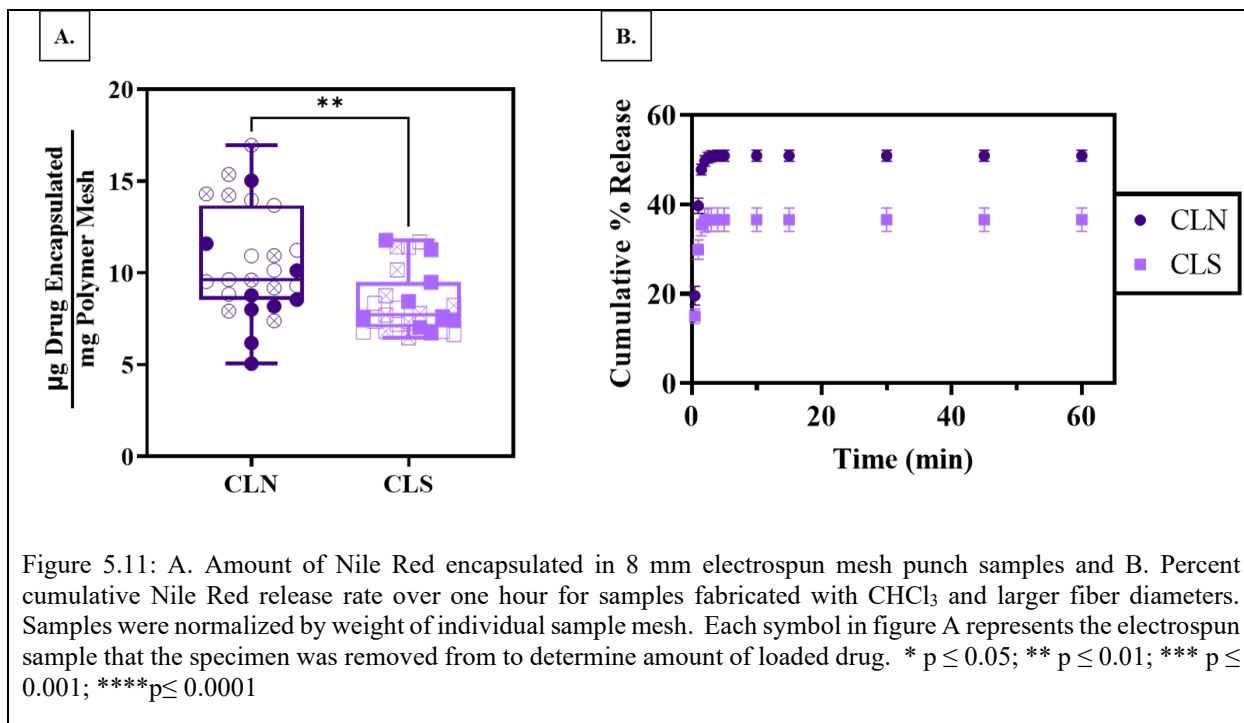
#### 5.3.1.2.2 Fiber Diameter and Fiber Fraction

The average fiber diameter for CLN and CLS fibers was  $8.15 \pm 4.01 \mu\text{m}$  and  $6.14 \pm 1.60 \mu\text{m}$ , respectively (Figure 5.10A). CLS fibers' average fiber diameter was smaller and statistically different from the average fiber diameter for CLN fibers (Figure 5.10B). This fiber diameter reduction may have been due to surfactant reducing surface tension and causing an increased jet acceleration and Taylor Cone thinning. Furthermore, surfactant located at the oil-air interface likely facilitated water entering the electrospun fiber and increasing the overall conductivity causing increasing whipping and, therefore, stretching of the fiber, decreasing the overall fiber diameter. The difference in fiber diameter, in this case, may result in differences in drug release and loading in the mesh. The fiber volume fraction was also statistically different, with CLN fibers having a higher fiber fraction (Figure 5.10C). Although the fiber volume fractions were statistically different, the average volume fraction was comparable between the two samples, indicating that this is not a dominant factor in overall mesh hydrophobicity and subsequent drug release.



#### 5.3.1.2.3 Drug Loading and Release

The amount of Nile Red encapsulated in CLN fibers was similar and slightly higher than the amount encapsulated in CLS fibers (Figure 5.11A). This increase in loading of Nile Red in CLN fibers compared to CLS fibers may be due to surfactant interacting with Nile Red and causing some sedimentation during electrospinning or may be due to experimental error. The burst release of drug for CLN fiber was higher than in CLS fibers (Figure 5.11B). This indicates that the surfactant may be interacting with the drug and helping solubilize the drug so that it is not pushed to the surface of the fiber during electrospinning. This finding is consistent with Li et al., who used cationic and anionic surfactant mixtures, and in Radisavjevic et al. with Span 80.<sup>22</sup>



### 5.3.1.3 Large and Small Fiber Comparison

Comparing the mesh characteristics, drug loading, and drug release from fibers fabricated with processing parameters (CSN and CSS) to fibers fabricated with processing parameters to produce smaller fiber diameters (CLN and CLS), both differences and similarities can be seen. One of the more unexpected differences was that the internal architectures of CSS fibers were porous, while the internal architecture of CLS was predominantly solid with occasional pores (Figure 5.12A). This may indicate those processing parameters combined with solution chemistry play a role in dictating the internal architecture of fibers. The internal architecture of CLS could be due to the water entering the system due to VIPS having time to coalesce within the droplet because it would take longer for the core to solidify in larger fibers. It is also possible that the packing of surfactants at the oil-air interface and phase separation could be influencing water entering the fiber and the rate of solvent evaporation.

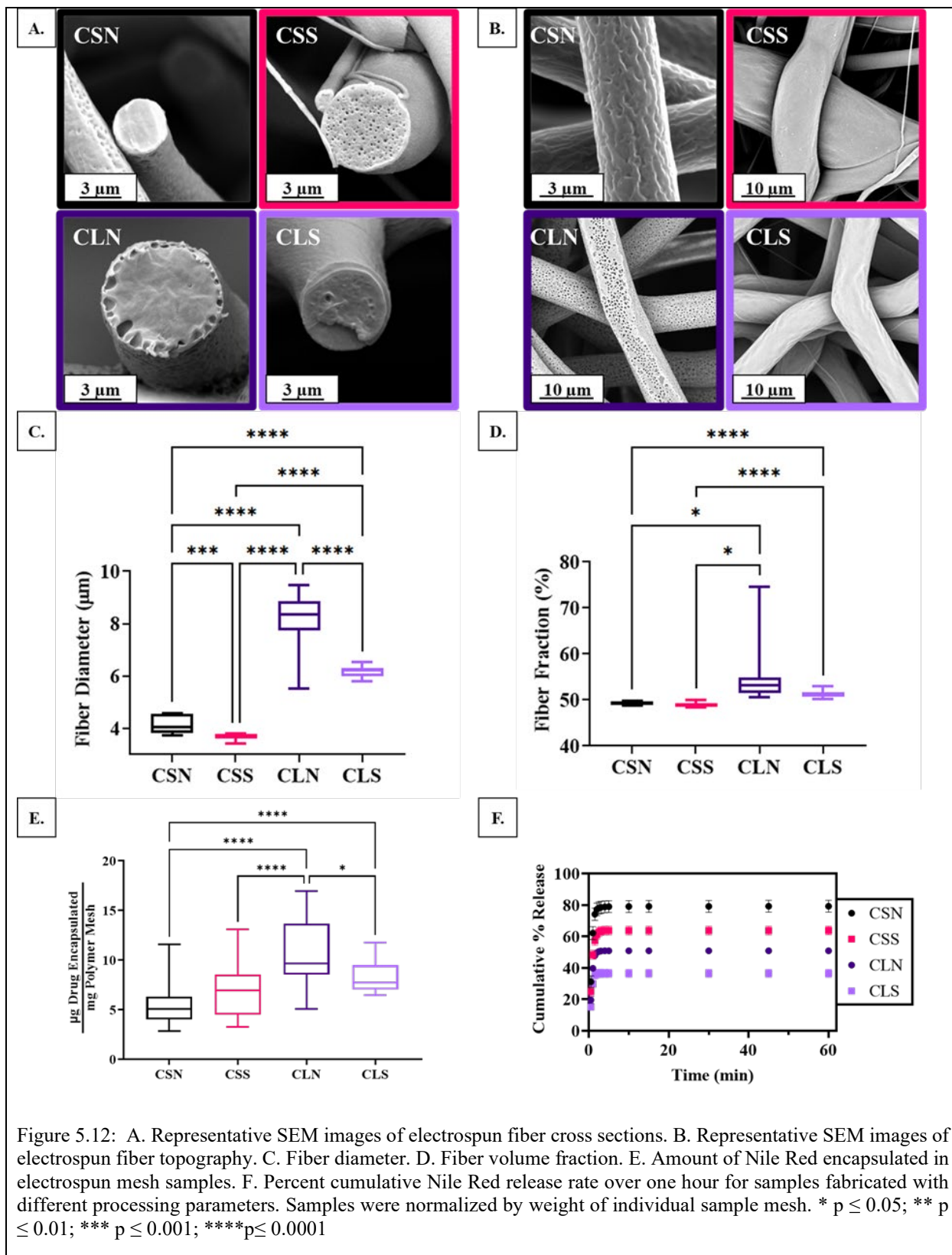


Figure 5.12: A. Representative SEM images of electrospun fiber cross sections. B. Representative SEM images of electrospun fiber topography. C. Fiber diameter. D. Fiber volume fraction. E. Amount of Nile Red encapsulated in electrospun mesh samples. F. Percent cumulative Nile Red release rate over one hour for samples fabricated with different processing parameters. Samples were normalized by weight of individual sample mesh. \*  $p \leq 0.05$ ; \*\*  $p \leq 0.01$ ; \*\*\*  $p \leq 0.001$ ; \*\*\*\*  $p \leq 0.0001$

The surface topography of these fibers also differed, with CLN having a higher porosity than CSN and both CSS and CLS having smooth surface topography (Figure 5.12B). The higher porosity of CLN may be attributed to less stretching of the jet before collection, but it was also electrospun at a relative humidity range approximately 10% higher than CSN, so further studies would need to be run to confirm this trend. The consistently smooth topography of fibers with surfactant CSS and CLS further supports that surfactant is at the oil-air interface and influencing phase separation.

Fiber diameter for CSN and CSS were smaller than CLN and CLS (Figure 5.12C). This difference is likely primarily due to the flow rate affecting the shape of the Taylor cone and the initial thinning of the jet. At higher flow rates, the Taylor cone has more volume and, therefore, more surface area for electrostatic repulsion to spread out before it overcomes surface tension.<sup>23</sup> This leads to less thinning of the initial jet and larger fiber diameters. Fiber diameters in both samples were also smaller for CSS and CLS fibers containing surfactant compared to their no surfactant counterparts. This is probably due to decreased surface tension in the Taylor cone by the surfactant, allowing for thinning of the cone and increased acceleration of the jet.<sup>9</sup>

Fiber volume fraction was similar for all samples with slightly higher fiber volume fractions for CLN and CLS compared to CSN and CSS (Figure 5.12D). Qin et al. found that this fiber volume fraction is influenced by the collection distance and applied voltage.<sup>24</sup> Differences used in processing parameters, therefore, may explain these differences.

Drug loading in all samples was similar, with slightly more loaded into CLN and CLS fibers than in CSN and CSS fibers (Figure 5.12E). This result was unexpected and may be due to CSN and CSS mesh electrospun for 30 minutes and CLN and CLS fibers electrospun for 60



minutes. The mesh electrospun for a longer period of time would be susceptible to more sedimentation of the drug and photobleaching.

The burst release of drug from fibers with smaller diameters was higher than the burst release from fibers with larger fiber diameters (Figure 5.12F). This may be due to the larger fibers having a larger surface area to volume ratio, and therefore more of the drug would remain in the bulk than in smaller fibers.

Overall, these results show that processing parameters in addition to solution chemistry can impact the internal architecture, fiber diameter, fiber fraction, and drug release. Processing parameters may also alter the location of surfactant within a fiber due to the evaporation and charge of the surfactant. Therefore, controlling fibers with solution chemistry can create additional methods to control drug release. Moreover, controlling for fiber volume fraction, fiber diameter, surface topography in addition to processing parameters is critical to understand the effects that solution chemistry has on drug release.

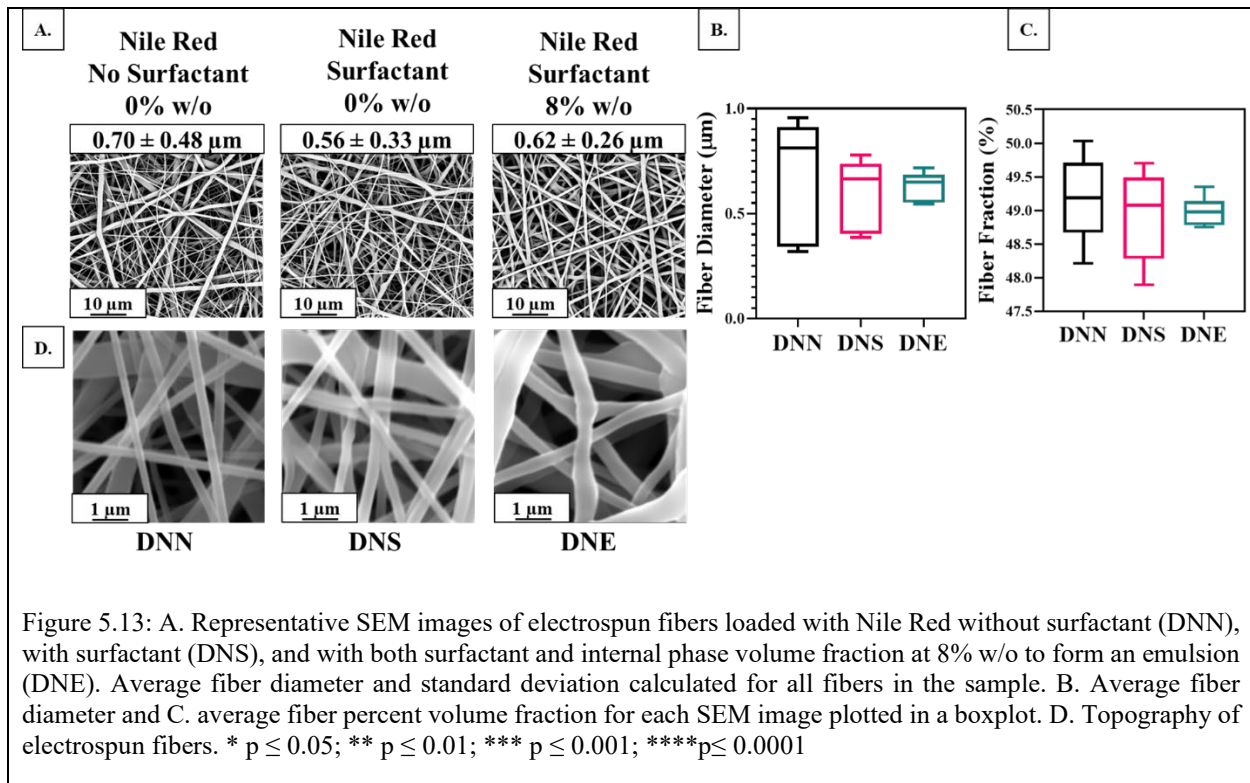
### **5.3.2 Surfactant and Emulsion Release of Hydrophilic and Lipophilic Drugs**

To determine the effects of surfactant and internal phase on the drug release of both a model hydrophilic and hydrophobic drug, Nile Red ( $\log P=5$ )<sup>20</sup> and Rhodamine B ( $\log P<1$ )<sup>20</sup> were loaded into electrospun fibers. A solvent system of 3:1 CHCl<sub>3</sub>: DMF at low relative humidity was used to ensure that the fibers had comparable fiber diameters and fiber fractions between the surfactant and no surfactant emulsion groups. This was important to ensure that differences seen were not due to the effect of fiber diameter, surface topography, or mesh volume fraction, all of which are known to affect drug release from electrospun fibers. Further, all fibers were electrospun at low relative humidity in order to minimize the effects of ambient water vapor.

### 5.3.2.1 Fibers Loaded with Nile Red

#### 5.3.2.1.1 Fiber Morphology, Diameter, and Fiber Fraction

Fibers encapsulated with Nile Red containing no surfactant (DNN), surfactant (DNS), and internal phase of 8% w/o to create an emulsion (DNE) had average fiber diameters of  $0.70 \pm 0.48$ ,  $0.56 \pm 0.33$ ,  $0.62 \pm 0.26$   $\mu\text{m}$ , respectively (Figure 5.13A). The fiber morphology for these samples was predominantly uniform and cylindrical, with some smaller fibers. The distribution of fiber diameter decreased with the addition of the internal phase, and the surface topography of all of these fibers was smooth (Figure 5.13D). Uniform fiber topography is important because it influences air trapping and resulting media contact with the mesh and, therefore, drug release. Fiber topography was smooth because all fibers were electrospun at low relative humidity, so insufficient ambient water vapor was present to template porosity.



Fiber diameters (Figure 5.13B) and fiber volume fraction (Figure 5.13C) were not statistically different for DNN, DNS, and DNE samples, indicating that fiber diameter and fiber volume are relatively equivalent and fraction likely would not play a major role in drug release data from these samples.

#### 5.3.2.1.2 Drug Loading and Release

The amount of drug loaded in DNN, DNS, and DNE was statistically different for each group (Figure 5.14A). The highest levels of loading were in DNN samples, followed by DNS samples and finally DNE samples. Santhanalakshmi et al. found that due to intermolecular interactions between  $\text{CHCl}_3$  and DMF, the aggregation of Tween 80 was higher in this blend of solvents than the pure solvents individually.<sup>25</sup> This could also be true for Span 80 and Nile Red in a blend of these solvents, and hydrogen bonding would also cause associations of Span 80 and Nile Red. This could cause some of the larger aggregated Span 80- Nile Red complexes to flocculate and a small degree of sedimentation during electrospinning. Small amounts of sedimentation would account for lower encapsulation of Nile Red in DNS samples compared to DNN samples, but overall differences in encapsulation are marginal. DNE samples had a moderately even lower amount of encapsulated than the DNN samples. This result was not expected and may have been due to experimental error or a degree of phase separation when water was added to the system.

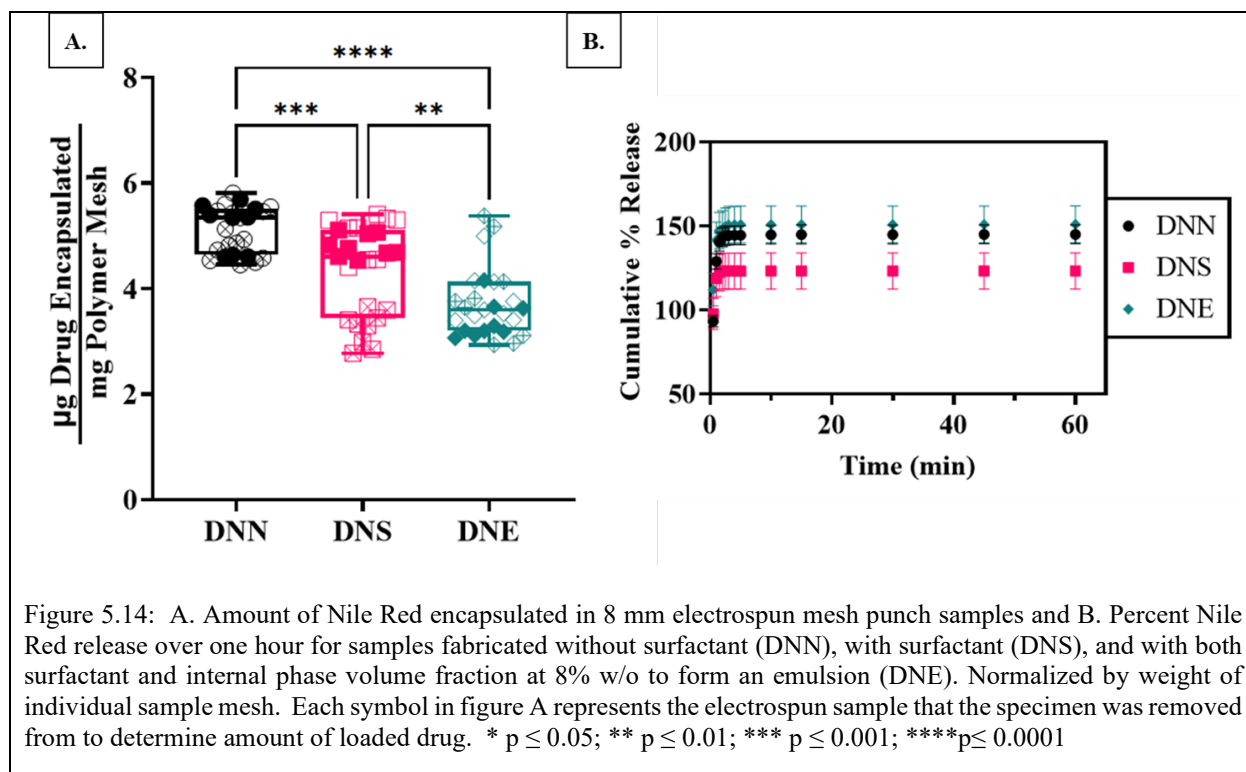


Figure 5.14: A. Amount of Nile Red encapsulated in 8 mm electrospun mesh punch samples and B. Percent Nile Red release over one hour for samples fabricated without surfactant (DNN), with surfactant (DNS), and with both surfactant and internal phase volume fraction at 8% w/o to form an emulsion (DNE). Normalized by weight of individual sample mesh. Each symbol in figure A represents the electrospun sample that the specimen was removed from to determine amount of loaded drug. \*  $p \leq 0.05$ ; \*\*  $p \leq 0.01$ ; \*\*\*  $p \leq 0.001$ ; \*\*\*\*  $p \leq 0.0001$

Burst release was highest for DNE, followed by DNS, and lowest in DNN (Figure 5.14B). The burst release rates of DNN and DNE were quite similar and indicated that Nile Red may not be completely compatible with this polymer solvent system. Nile Red in these systems is likely forced to the surface through a combination of electrostatic repulsion and phase separation. DNS had a smaller burst release compared to both DNE and DNN. This is consistent with the trends seen in the  $\text{CHCl}_3$  systems and indicates that the Span 80 may be helping solubilize Nile Red.

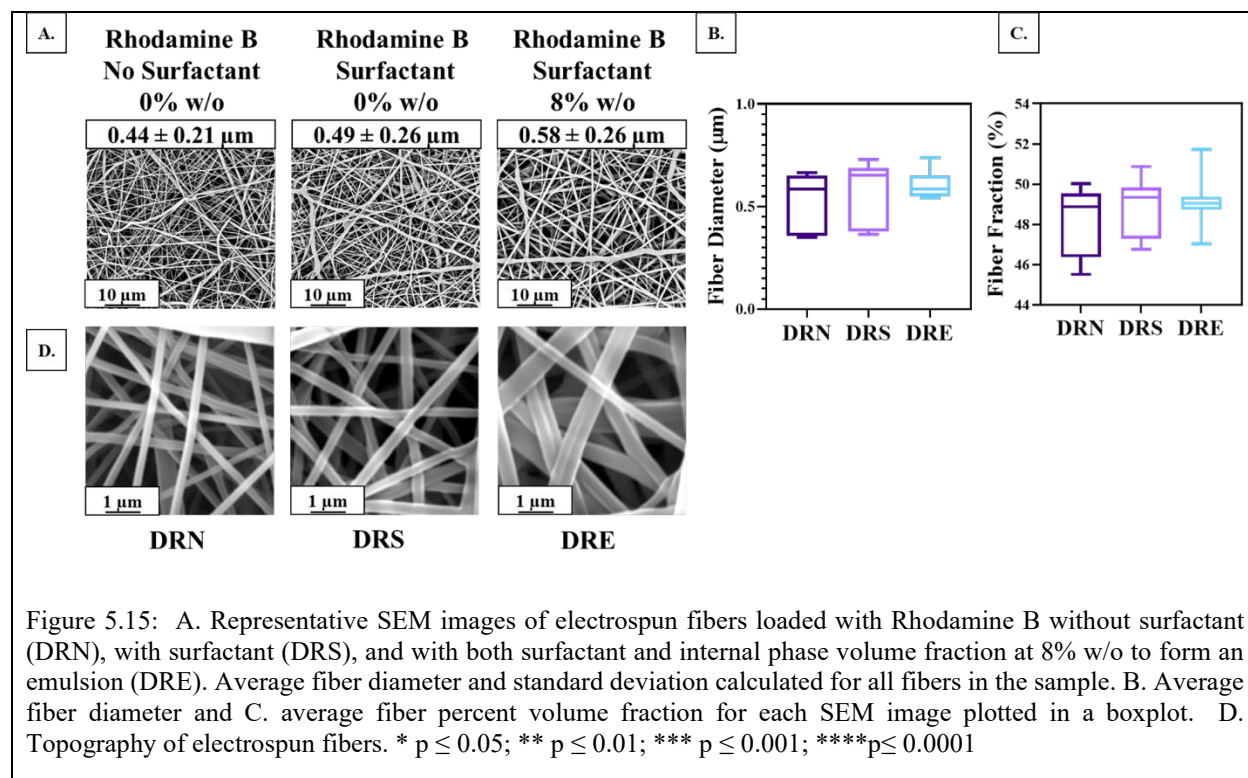
Nile Red is a small molecule with a preference for organic solvent. Therefore, in systems with a mixture of 3:1  $\text{CHCl}_3$ : DMF, Nile Red will probably prefer the  $\text{CHCl}_3$  to DMF. In an emulsion system, DMF is miscible with both  $\text{CHCl}_3$  and water but has a stronger preference for water. Due to vapor pressure,  $\text{CHCl}_3$  will evaporate from the fiber first.<sup>26</sup> Phase separation will force  $\text{CHCl}_3$  to the surface of the fiber, and most Nile Red will move with it to the surface of the

fiber, and therefore the largest burst releases were seen in the DNE samples. DNS samples experienced the second highest burst release of drug. This was because interactions between Nile Red and the surfactant forced some of the drugs to the surface of the fiber due to the preference of the surfactant for the air-oil interface and charge repulsion. DNN had the smallest burst release because only some were forced to the surface of the fiber due to charge repulsion.

### *5.3.2.2 Fibers Loaded with Rhodamine B*

#### 5.3.2.2.1 Fiber Morphology, Diameter, and Fiber Fraction

Fibers encapsulated with Rhodamine B containing no surfactant (DRN), surfactant (DRS), and emulsion with internal phase of 8% (DRE) had average fiber diameters of  $0.44 \pm 0.21$ ,  $0.49 \pm 0.26$ , and  $0.58 \pm 0.26$   $\mu\text{m}$ , respectively (Figure 5.15A). The fiber morphology for these samples was predominantly uniform and cylindrical, with some smaller fibers. The distribution of fiber diameter decreased with the addition of the internal phase. The surface topography of all of these fibers was smooth (Figure 5.15D). Fiber topography was smooth because all fibers were electrospun at low relative humidity, so insufficient ambient water vapor was present to template porosity.



Differences in fiber diameter between DRN, DRS, and DRE were not statistically different (Figure 5.15B). When fiber diameter is not statistically different, it is unlikely to play a major role in drug release. Fiber volume fraction was not statistically different between DRM, DRS, and DRE samples, indicating that it also is unlikely to play a major role in drug release (Figure 5.15C). Standardizing fiber diameter and fiber volume fractions across samples is essential to thoroughly compare solution and drug solubility parameters.

#### 5.3.2.2.2 Drug Loading and Release

The amount of drug loaded in DRN, DRS, and DRE were statistically different for each group, with DRE containing the highest loading followed by DRS and DRN (Figure 5.16A). In DRN, the loading of Rhodamine B was lowest because Rhodamine B has low solubility in  $\text{CHCl}_3$ , and therefore some phase separation would cause lower amounts of the drug to be encapsulated in the fibers. DRS had the second lowest encapsulation because Rhodamine B interacts with the

amphiphilic surfactant, and that could help solubilize the complex and allow more to be loaded in the fiber. Finally, DRE had the highest loading because Rhodamine B would primarily be in the water internal phase of the fibers because it prefers the polar water phase. This result is significant because it proves that using an internal phase and a surfactant can improve the loading of hydrophilic molecules in hydrophobic solvent- polymer systems. This is consistent with other studies loading hydrophilic drugs within emulsions in the field.<sup>14,27-29</sup>

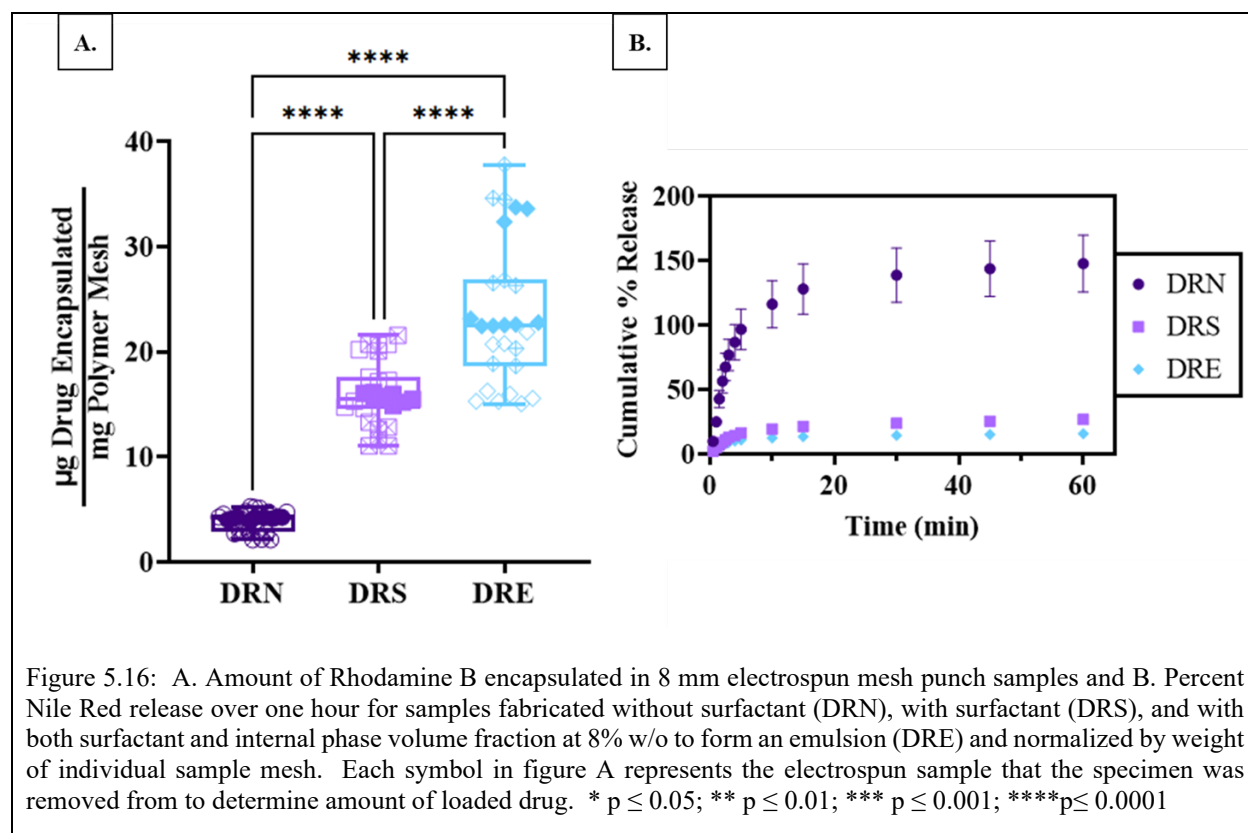


Figure 5.16: A. Amount of Rhodamine B encapsulated in 8 mm electrospun mesh punch samples and B. Percent Nile Red release over one hour for samples fabricated without surfactant (DRN), with surfactant (DRS), and with both surfactant and internal phase volume fraction at 8% w/o to form an emulsion (DRE) and normalized by weight of individual sample mesh. Each symbol in figure A represents the electrospun sample that the specimen was removed from to determine amount of loaded drug. \*  $p \leq 0.05$ ; \*\*  $p \leq 0.01$ ; \*\*\*  $p \leq 0.001$ ; \*\*\*\*  $p \leq 0.0001$

The release of Rhodamine B from DRN had the biggest burst release because Rhodamine B has poor solubility in  $\text{CHCl}_3$ , and charge repulsion forced it to the surface of the fiber (Figure 5.16B). The burst release for DRS and DRE were remarkably lower than DRN. This is because, in DRE, Rhodamine B preferred the internal phase, and therefore most was protected from burst release. All fibers were electrospun at approximately 20% RH, which is sufficient to create some

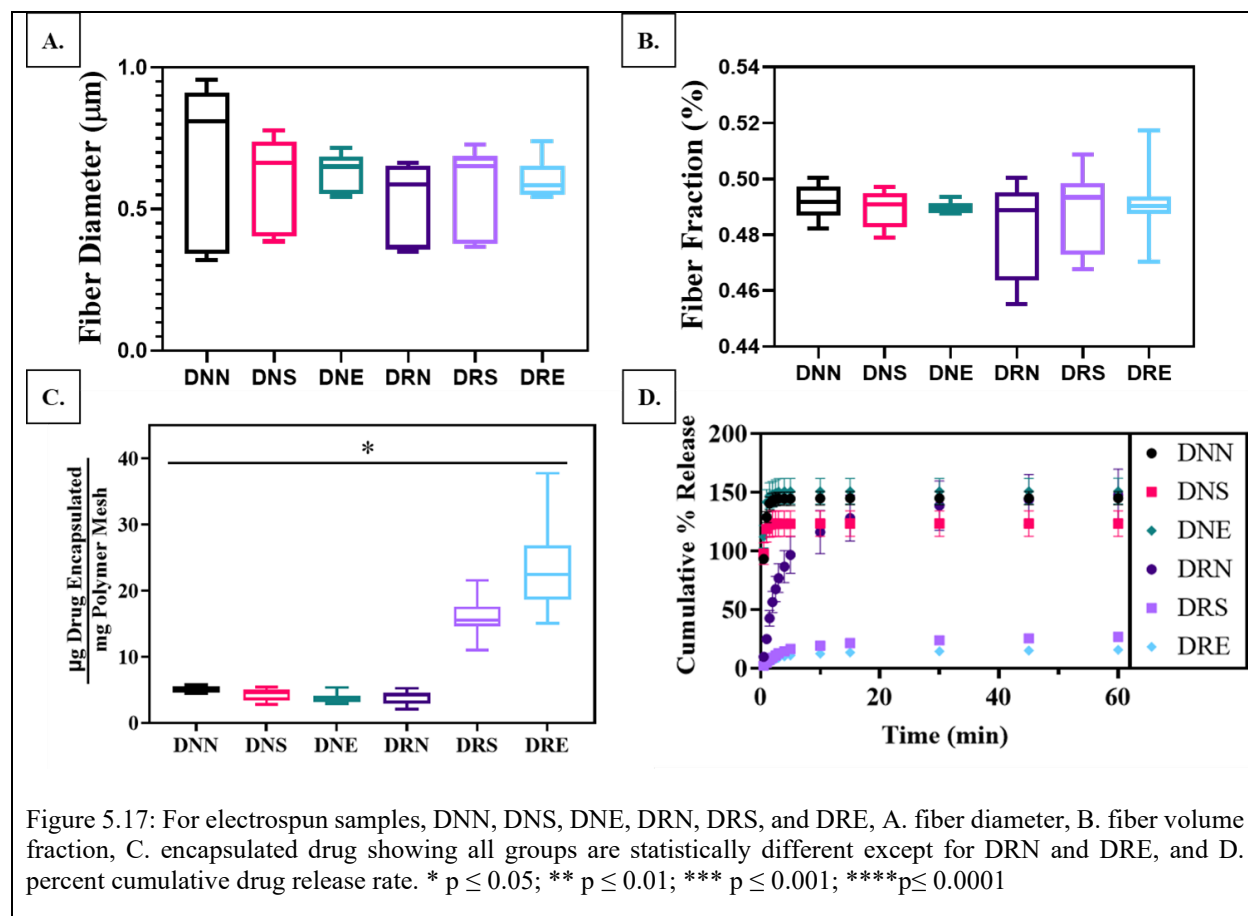
VIPS (see Chapter 3), and together with NIPS from the DMF preferring the water phase, Rhodamine B would prefer the internal aqueous phase and be protected from burst release. DRS is slightly higher than DRE in drug release rate after the burst, possibly because there is less internal phase or the internal phase did not have as much time to coalesce one inside the fiber. This same reduction in burst release and reduction in overall release rate has been observed in several other electrospinning studies.<sup>15,17,30,31</sup> However, in all of these studies, the comparison of no surfactant, surfactant, and emulsion has not been made between fibers with insignificant differences in fiber diameter and fiber volume fraction, potentially leading to other confounding variables in release profiles. Interestingly, the burst release of Rhodamine B from fibers containing surfactant and emulsion fibers was quite similar. This indicates that surfactant alone may reduce the burst effect of drugs that prefer the continuous organic phase from hydrophobic polymer. The release rate from fibers containing surfactant after the drug's burst release was faster than the emulsion electrospun fibers. This may indicate that when initial water is added to the system in an emulsion, Rhodamine B prefers this water phase, and, therefore, more is encapsulated within the water phase leading to a slower diffusional drug release rate. It is also possible that the internal phase coalesced within these fibers to form a core or aqueous phase and drug, which would have a longer diffusional path than fibers with evenly distributed porosity. This is consistent with the hypothesis and studies conducted by Radisavljevic et al.<sup>18</sup>

### *5.3.2.3 Nile Red and Rhodamine B Release Comparison*

Comparing groups loaded with Nile Red to groups loaded with Rhodamine B, fiber diameter and fiber fraction was not statistically different (Figure 5.17A-B). Controlling fiber diameter and fiber fraction while altering solution chemistry can be difficult because each component can change the behavior of the electrospinning jet during the electrospinning process.



Controlling fiber diameter and fiber fraction also removes potentially confounding variables that can alter the interpretation of drug hydrophobicity and release rates due to the effects of the solvent.



The amount of drug loaded into the scaffolds normalized for the weight of the sample was similar for DNN, DNS, DNE, and DRN (Figure 5.17C). Adding a surfactant to DRS remarkably improved encapsulation of Rhodamine B, possibly because it was able to improve solubility. DRE had the highest encapsulation of drug for all samples, probably because Rhodamine B was concentrated in the aqueous internal phase because it is a hydrophilic drug. DNN, DNS, DNE, and DRN samples all experienced a high initial burst release of drug. The primary reason for this is phase separation and charge repulsion, forcing the drug to the outside of the fibers. DRS and DRE had remarkably smaller burst drug release because Rhodamine B was encapsulated within the internal phase. Several burst release profiles were above 100%, which may

be due to the encapsulation data studies run on a later date and potentially photobleaching of the fluorescent molecules. These results indicate that hydrophilic drugs may be incorporated within hydrophobic fibers with minimal burst drug release through including a non-ionic surfactant. The burst release of Nile Red was unexpected and indicated that Nile Red may not be compatible with this polymer-solvent system. Future studies should consider using an even more hydrophobic drug to see if better incorporation can be achieved with this solvent system.

#### **5.4 CONCLUSION**

Overall, these studies demonstrated that increasing fiber diameter through modulating processing parameters and keeping the solution chemistry constant may result in changes to internal porosity and resulting drug release. At high and low relative humidity, samples with surfactant demonstrated a reduced burst drug release compared to samples electrospun without surfactant. When comparing systems encapsulating a more hydrophobic model drug, Nile Red, to a more hydrophilic drug, Rhodamine B, the drug release of Nile Red had a larger burst release. The rate of drug release in Rhodamine B encapsulated fibers was slightly slower for samples containing an emulsion compared to surfactant. Overall, all of these trends demonstrate the capabilities of controlling drug loading and tuning drug release from electrospun scaffolds, specifically with surfactant and emulsions. Adding non-ionic surfactant reduced burst release of drug in all cases compared to the control without surfactant, potentially making it a promising candidate for reducing burst release from electrospun fibers with all drug chemistry. Tuning the drug release rate from electrospun scaffolds is essential to ensure that the drug is at therapeutically effective levels and. Another advantage of this system is that by increasing stability during loading, the released time can be tuned based on drug preference and structure.

## 5.5 BIBLIOGRAPHY

- 1 Cheng, H., Yang, X., Che, X., Yang, M. & Zhai, G. Biomedical application and controlled drug release of electrospun fibrous materials. *Mater Sci Eng C Mater Biol Appl* **90**, 750-763, doi:10.1016/j.msec.2018.05.007 (2018).
- 2 Weng, L. & Xie, J. Smart electrospun nanofibers for controlled drug release: recent advances and new perspectives. *Current pharmaceutical design* **21**, 1944-1959, doi:10.2174/1381612821666150302151959 (2015).
- 3 Zeng, J. *et al.* Biodegradable electrospun fibers for drug delivery. *Journal of Controlled Release* **92**, 227-231, doi:[https://doi.org/10.1016/S0168-3659\(03\)00372-9](https://doi.org/10.1016/S0168-3659(03)00372-9) (2003).
- 4 Chou, S. F., Carson, D. & Woodrow, K. A. Current strategies for sustaining drug release from electrospun nanofibers. *Journal of controlled release : official journal of the Controlled Release Society* **220**, 584-591, doi:10.1016/j.jconrel.2015.09.008 (2015).
- 5 Hu, X. *et al.* Electrospinning of polymeric nanofibers for drug delivery applications. *Journal of controlled release : official journal of the Controlled Release Society* **185**, 12-21, doi:10.1016/j.jconrel.2014.04.018 (2014).
- 6 Lu, Y. *et al.* Coaxial electrospun fibers: applications in drug delivery and tissue engineering. *Wiley Interdiscip Rev Nanomed Nanobiotechnol* **8**, 654-677, doi:10.1002/wnan.1391 (2016).
- 7 Ball, C., Chou, S. F., Jiang, Y. & Woodrow, K. A. Coaxially electrospun fiber-based microbicides facilitate broadly tunable release of maraviroc. *Mater Sci Eng C Mater Biol Appl* **63**, 117-124, doi:10.1016/j.msec.2016.02.018 (2016).
- 8 Sill, T. J. & von Recum, H. A. Electrospinning: applications in drug delivery and tissue engineering. *Biomaterials* **29**, 1989-2006, doi:10.1016/j.biomaterials.2008.01.011 (2008).
- 9 Wang, S.-Q., He, J.-H. & Xu, L. Non-ionic surfactants for enhancing electrospinnability and for the preparation of electrospun nanofibers. *Polym Int* **57**, 1079-1082, doi:10.1002/pi.2447 (2008).
- 10 Xu, H., Li, H. & Chang, J. Controlled drug release from a polymer matrix by patterned electrospun nanofibers with controllable hydrophobicity. *J Mater Chem B* **1**, 4182, doi:10.1039/c3tb20404a (2013).
- 11 Chen, S. C. *et al.* The influence of fiber diameter of electrospun poly(lactic acid) on drug delivery. *Fiber Polym* **13**, 1120-1125, doi:10.1007/s12221-012-1120-x (2012).
- 12 Gu, X. *et al.* Electrospinning of poly(butylene-carbonate): Effect of Solvents on the Properties of the Nanofibers Film. *Int J Electrochem Sc* **9**, 8045-8056 (2014).
- 13 Zhang, X., Yin, Q., Cui, P., Liu, Z. & Gong, J. Correlation of Solubilities of Hydrophilic Pharmaceuticals versus Dielectric Constants of Binary Solvents. *Ind Eng Chem Res* **51**, 6933-6938, doi:10.1021/ie202624d (2012).
- 14 Zhang, C., Feng, F. & Zhang, H. Emulsion electrospinning: Fundamentals, food applications and prospects. *Trends in Food Science & Technology* **80**, 175-186, doi:10.1016/j.tifs.2018.08.005 (2018).
- 15 Yazgan, G. *et al.* Tunable release of hydrophilic compounds from hydrophobic nanostructured fibers prepared by emulsion electrospinning. *Polymer* **66**, 268-276, doi:10.1016/j.polymer.2015.04.045 (2015).
- 16 Johnson, P. M. *et al.* Surfactant location and internal phase volume fraction dictate emulsion electrospun fiber morphology and modulate drug release and cell response. *Biomater Sci-Uk*, doi:10.1039/D0BM01751E (2021).

- 17 Tipduangta, P. *et al.* Electrospun Polymer Blend Nanofibers for Tunable Drug Delivery: The Role of Transformative Phase Separation on Controlling the Release Rate. *Mol Pharm* **13**, 25-39, doi:10.1021/acs.molpharmaceut.5b00359 (2016).
- 18 Radisavljevic, A. *et al.* Cefazolin-loaded polycaprolactone fibers produced via different electrospinning methods: Characterization, drug release and antibacterial effect. *Eur J Pharm Sci* **124**, 26-36, doi:10.1016/j.ejps.2018.08.023 (2018).
- 19 Greenspan, P. & Fowler, S. D. Spectrofluorometric studies of the lipid probe, Nile red. *J Lipid Res* **26**, 781-789 (1985).
- 20 K uchler, S. *et al.* Influence of nanocarrier type and size on skin delivery of hydrophilic agents. *Int J Pharmaceut* **377**, 169-172, doi:10.1016/j.ijpharm.2009.04.046 (2009).
- 21 Szewczyk, P. K. *et al.* Roughness and Fiber Fraction Dominated Wetting of Electrospun Fiber-Based Porous Meshes. *Polymers (Basel)* **11**, doi:10.3390/polym11010034 (2018).
- 22 Li, W., Luo, T., Yang, Y., Tan, X. & Liu, L. Formation of controllable hydrophilic/hydrophobic drug delivery systems by electrospinning of vesicles. *Langmuir* **31**, 5141-5146, doi:10.1021/la504796v (2015).
- 23 Rutledge, G. C. & Fridrikh, S. V. Formation of fibers by electrospinning. *Advanced drug delivery reviews* **59**, 1384-1391, doi:10.1016/j.addr.2007.04.020 (2007).
- 24 Qin, X.-H. & Xin, D.-P. The study on the air volume fraction of electrospun nanofiber nonwoven mats. *Fiber Polym* **11**, 632-637, doi:10.1007/s12221-010-0632-7 (2010).
- 25 Santhanalakshmi, J. & Maya, S. Solvent effects on reverse micellisation of Tween 80 and Span 80 in pure and mixed organic solvents. *Proc. Indian Acad. Sci.* **109**, 22-38 (1997).
- 26 Yazgan, G. *et al.* Steering surface topographies of electrospun fibers: understanding the mechanisms. *Sci Rep-Uk* **7**, doi:ARTN 158  
10.1038/s41598-017-00181-0 (2017).
- 27 Liao, Y., Zhang, L., Gao, Y., Zhu, Z.-T. & Fong, H. Preparation, characterization, and encapsulation/release studies of a composite nanofiber mat electrospun from an emulsion containing poly(lactic-co-glycolic acid). *Polymer* **49**, 5294-5299, doi:10.1016/j.polymer.2008.09.045 (2008).
- 28 Hu, J., Wei, J., Liu, W. & Chen, Y. Preparation and characterization of electrospun PLGA/gelatin nanofibers as a drug delivery system by emulsion electrospinning. *J Biomater Sci Polym Ed* **24**, 972-985, doi:10.1080/09205063.2012.728193 (2013).
- 29 Yan, S., Xiaoqiang, L., Shuiping, L., Xiumei, M. & Ramakrishna, S. Controlled release of dual drugs from emulsion electrospun nanofibrous mats. *Colloids Surf B Biointerfaces* **73**, 376-381, doi:10.1016/j.colsurfb.2009.06.009 (2009).
- 30 Qi, H., Hu, P., Xu, J. & Wang, A. Encapsulation of drug reservoirs in fibers by emulsion electrospinning: morphology characterization and preliminary release assessment. *Biomacromolecules* **7**, 2327-2330, doi:10.1021/bm060264z (2006).
- 31 Burgess, K., Li, H., Abo-Zeid, Y., Fatimah & Williams, G. R. The Effect of Molecular Properties on Active Ingredient Release from Electrospun Eudragit Fibers. *Pharmaceutics* **10**, doi:10.3390/pharmaceutics10030103 (2018).

## CHAPTER 6: CONCLUSIONS

### 6.1 SUMMARY

The studies described in this body of work detail the fabrication of emulsion electrospun mesh and a mechanistic understanding of how each component of the emulsion solution chemistry plays a role in resulting mesh characteristics. These meshes were specifically developed to understand how emulsion electrospinning chemistry can affect incorporating bioactive molecules and hydrophilic drugs in tunable fibers for controlled drug release and tissue engineering applications.

Electrospinning is a technique in which non-woven mesh with fiber diameters in the nano- to micrometer range are generated. Electrospun fibers are generated by extruding a polymer solution out of the tip of a syringe needle and stretching in an electric field to collect dry mesh. This mesh is particularly useful in tissue engineering and drug delivery applications. Understanding fundamental parameters are essential in the electrospinning process to modulate mesh characteristics such as fiber diameter, surface topography, hydrophobicity, fiber volume fraction, and morphology because they can alter downstream applications controlling cell response to fibers and drug release rates. In particular, cell responses such as adherence, viability, proliferation, and differentiation can be dictated by mesh porosity, surface topography, morphology, and fiber diameter. Emulsion electrospinning is a specific technique commonly used to incorporate drugs within electrospun fibers. However, a fundamental understanding of how compositional parameters play a role, independently, in the resulting mesh characteristics has not previously been fully explored.

Overall, this body of work focuses on how components of an emulsion, including solvent, surfactant, and internal phase volume fraction, play a role in the resulting mesh characteristics of

emulsion electrospun fibers. All the studies are conducted through a lens of relative humidity to understand how to further phase separation may be impacted at different levels of relative humidity and used to control fiber properties. Finally, this work has created a library and understanding of solvent properties to further develop tunable scaffolds for many applications, including encapsulating and controlling the release of both hydrophilic and hydrophobic drugs.

## 6.2 SIGNIFICANCE OF WORK

Emulsion electrospinning is a useful method to incorporate bioactive molecules, hydrophilic drugs, and template porosity for further tunability of drug release from electrospun fibers. Bioactive molecules and hydrophilic drugs can be forced to the surface of hydrophobic polymer fibers during the electrospinning process, which results in a burst release and often the loss of bioactivity. Therefore, emulsion electrospinning is an effective method to retain bioactivity, incorporate hydrophilic drugs with reduced or eliminated burst release effects, and create further tunability of scaffolds by creating internal porosity for media contact with the core of the fibers.

Emulsion electrospun fibers are fabricated using one or more continuous phase solvents, a polymer that is soluble in at least one of the solvents, an internal phase, and a surfactant located at the interface of the continuous phase and the internal phase stabilizing droplets by reducing interfacial tension. This work focuses on how each component of emulsion chemistry plays a role in the resulting electrospun mesh characteristics.

In Chapter 2, PCL was dissolved in solvents later used as the continuous phase of the emulsion. These solvents consisted of DCM,  $\text{CHCl}_3$ , 3:1  $\text{CHCl}_3$ : DMF, and 3:1  $\text{CHCl}_3$ : MeOH. Solvents were selected because they provide insight into a range of different solution parameters affecting the electrospinning process, including solvent evaporation, solvent conductivity, polymer solubility in respective solvents, and miscibility of solvents. Each solution was electrospun both

at high relative humidity and low relative humidity. Determining the role that relative humidity plays with each of the solution parameters further provides insight into the mechanism of solution phase separation within electrospun fibers and the resulting effects on mesh characteristics. The fiber morphology, surface topography, and fiber diameter were evaluated for each of these electrospun fibers to compare to each other. It is essential to understand the building blocks and phase separation mechanisms within an electrospinning system in order to create an emulsion from the continuous phase. Overall, using solvents with increasing conductivity resulted in decreased fiber diameter at both high and low relative humidity due to increased stretching of the fibers within the whipping phase of electrospinning. In single solvent systems, increasing the relative humidity led to a decrease in fiber diameter and created templating of pores on the surface of fibers. In the dual solvent system, fiber diameter either increased with increasing relative humidity or did not statistically change. Increased solvent conductivity coupled with phase separation also led to the formation of multiple jet fibers or branches within fibers, further decreasing the average fiber diameter.

In Chapter 2, the effects of surfactant both in emulsions and in solutions with and without surfactant were compared. First, the effect of surfactant relocation during the electrospinning process was evaluated by comparing a control sample containing no surfactant and no internal phase, a solution containing surfactant with no internal phase, and emulsions with increasing internal phase volume fractions. In order to evaluate the role of solvents on polymer solubility and phase separation and resulting effects on fiber morphology and properties,  $\text{CHCl}_3$ , 3:1  $\text{CHCl}_3$ :DMF, and 3:1  $\text{CHCl}_3$ :MeOH were used. Each of these scaffolds was additionally fabricated at high and low relative humidity. This is important because relative humidity may play a role in encouraging surfactant to relocate to the surface of the electrospun fiber due to a higher saturation

of water in the ambient air. The fiber volume fraction, surface topography, and contact angle over time on dry fabricated mesh were compared.

Overall, water droplets remained constant on the surface of fibers without surfactant or internal phase for all solvent systems because PCL is a hydrophobic polymer. The contact angle for nearly all groups with surfactant and internal phase absorbed into the mesh within 2 minutes. For samples electrospun with  $\text{CHCl}_3$  or 3:1  $\text{CHCl}_3$ : MeOH, the trend of the relative rate of absorbance of water droplet into the mesh was fastest for samples containing surfactant and no internal phase and gradually decreased as internal phase volume fraction increased. This is probably due to less surfactant located at the surface of fibers in emulsion systems because more are located at the water-oil interface within the fiber. The results of these studies indicate that the hydrophilicity or hydrophobicity of the electrospun mesh may be tuned with non-ionic surfactants. Furthermore, compositional parameters of internal phase volume fraction play a role in surfactant relocation to the surface of the fibers, which is important when designing an emulsion electrospinning system and may be a strategy to alter cell response to scaffolds and drug release rate.

Previous literature has primarily focused on the effects of cationic and anionic surfactants within emulsion and solutions containing surfactants for electrospinning. Chapter 3 further evaluates the chemistry of non-ionic surfactants by comparing Span 85, Span 80, PGPR, Span 40, Pluronic F108, and control containing no surfactant. Surfactants were selected with increasing HLB values. Emulsion bulk stability was determined by measuring the internal phase droplet size from microscope images. Finally, these solutions were electrospun with and without an emulsified internal phase to understand the role that surfactant plays in emulsion and without internal phase emulsion electrospun fibers. Internal phase droplet size decreased with increasing HLB value, and



bulk emulsions maintained stability for the longest period of time for surfactants with HLB values ranging from 4.3-6.7.

Fiber diameter decreased or remained relatively the same for all surfactant groups compared to the control with no surfactant. This was because surfactant was located at the surface of the electrospinning jet and reduce the surface tension at the Taylor cone, resulting in a thinning of the Taylor cone and increased acceleration of the jet. The fiber diameter of surfactants with HLB values of 1.8 through 4.7 demonstrated an increasing fiber diameter with increasing HLB value. This may be due to the increasing ability to reduce surface tension within the Taylor cone and, therefore, further elongation of the Taylor cone. Span 40 within HLB of 6.7 exhibited droplets with no internal phase, which may indicate that at this level of HLB, the surface tension was so low that continuous fibers were unable to form. Emulsion electrospun fibers increased in fiber diameter with increasing HLB value. This increasing HLB value may be related to the internal phase droplet size, where smaller droplet sizes have more interfacial area for surfactants to relocate and therefore less surfactant at the oil-air interface on the surface at the surface of the fiber.

In Chapter 4, the effect of increasing internal phase volume fractions of 0%, 2%, 4%, and 8% in solvents consisting of  $\text{CHCl}_3$ , 3:1  $\text{CHCl}_3$ : DMF, or 3:1  $\text{CHCl}_3$ : MeOH was evaluated at both high and low relative humidity. Continuous phase solvents were selected to evaluate the roles of phase separation with solvent miscibility and polymer solubility. Internal phase volume fraction increased the overall conductivity of the solvent and had significant effects on fiber morphology. The surfactant in these systems prevented the formation of surface porosity for all internal phase volume fractions. The understanding of small defects in mesh morphology enlightened potential mechanisms and areas of instability during the electrospinning process. This understanding is critical to create uniform and reproducible meshes that are capable of controlled release of drugs

or bioactive molecules and in tailoring individual fibers for tunable release profiles of the drug. Additionally, controlling the fiber surface topography and morphology can create opportunities to use emulsion electrospun meshes to elicit specific and targeted cell responses in tissue engineering.

Finally, in Chapter 5, drug releases from emulsion electrospun fibers were compared for fibers with a solid-core and porous surface topography with mesh containing surfactant and porous core and smooth surface topography. In a larger diameter system, fibers with a solid-core and porous surface topography were also compared to mech fabricated with surfactant and containing smooth surface topography and predominantly solid internal architecture. In both cases, encapsulating the model drug, Nile Red, within fibers containing surfactant resulted in a decreased burst release of the drug regardless of surface or internal architecture. This indicates that adding a surfactant to a system reduces burst effects even without the internal phase of an emulsion.

Understanding of the emulsion electrospinning systems from previous chapters then allowed a further study to compare the effects of drug release of a hydrophilic and hydrophobic model drug from fibers containing no surfactant and no internal phase, surfactant, and no internal phase, and form an emulsion. These drugs were prepared in electrospun systems containing insignificant differences in fiber diameter and fiber volume fraction, parameters that can both alter drug release effects. This is difficult to control because surfactant and internal phase result in significant effects on fiber diameter and fiber volume fraction. Overall, the results demonstrated that encapsulation of model hydrophilic drug was higher in emulsion electrospun samples, and a burst relative drug release was observed. Electrospun fibers containing no surfactant and no internal phase with the hydrophilic drug exhibited a much higher burst release and lower encapsulation, likely due to the hydrophilic drug being forced to the surface of the fibers due to incompatibility with polymer and organic solvent. Conversely, loading of hydrophobic drug in

electrospun fibers was highest in samples with no surfactant and no internal phase, indicating that adding internal phase of an emulsion with a hydrophobic drug likely is causing phase separation and more hydrophobic drug to relocate at the surface of the fibers. Hydrophobic drug burst release was highest in samples with internal phase because of forced phase separation. This study proves that drug and solvent-polymer compatibility is important in designing drug release from electrospun fibers and that emulsions may be used to increase encapsulation efficiency and reduce burst drug release effects.

### **6.3 FUTURE DIRECTIONS AND CHALLENGES**

Based on studies from Chapter 2, relative humidity plays a major role in interacting with different solvent systems used for electrospinning. In some cases where an aqueously miscible solvent was used, this facilitated vapor-induced phase separation. Understanding phase separation and the relative evaporation rates paired with the conductivity of the solution can be utilized to tune fiber characteristics. In particular, the surface topography of fibers has shown promise for dictating cell response. Understanding the relationship between relative humidity and solvents can further be explored to create tunable porosity that elicits the desired cell response in a given system. One potential area for further exploration is the use of electrospun fibers in the regeneration of fibrocartilage. Surface topography has shown promise in differentiating osteoblasts progenitor cells and, therefore, may be used to elicit a response from progenitor cells to differentiate into fibrochondrocytes. Furthermore, research has shown that a gradient electrospun fiber diameter and alignment have been used to create a gradient of responses. Therefore, through altering solution chemistry, a gradient of electrospun fibers could be fabricated with different surface topographies, fiber diameters, and encapsulated growth factors to create a gradient of different differentiated

cells mimicking the natural gradient found in fibrocartilage structures such as the knee meniscus, temporomandibular joint meniscus, and the intervertebral disc.

In Chapter 3, the relocation of surfactant on the surface of fibers was confirmed with contact angle. One of the challenges in this study included a high variability between samples. This may have been due to small defects in morphology, creating differences in the contact between the electrospun fibers and water droplets used to measure contact angle. A larger sample size of trials on the mesh may help further clarify trends in the data. Furthermore, it is possible that this data had variability due to user error. Emerging methods of measuring contact angle have helped eliminate the potential for error by having a robotic component place the water droplet on the specimen surface and eliminating the need to normalize for the time of contact of the water droplet with the surface of the fibers. These new methods also include a tilt feature to test contact angles at different levels of tilt which may reduce variability caused by surface imperfections.

Interestingly, initial studies indicate that both internal phase volume fraction and the solvent system used both influences the amount of surfactant located at the surface of the fibers. Further studies can further explore modeling of internal phase volume fraction interfacial area over the lifetime of the electrospun jet to understand saturation at the oil-water interface. These studies would be helpful in addition to measuring the saturation of surfactant at the oil-water interface and at the oil-air interface to understand concentration effects on fibers. Additionally, the effect of multiple solvents used in the continuous phase could further be explored by measuring surfactant at these interfaces to determine if it is facilitating phase separation. Understanding the location of surfactant within the electrospun fiber dovetails with studies investigating surfactant chemistry as a means for controlling emulsification and for internal phase droplet size. Decreasing the internal phase droplet size created more surface area within the fiber for surfactants to locate at the

interface. Further studies could evaluate how different surfactant chemistries behave under shear stress and electric field in order to understand how the droplets are breaking up within the fiber and changing surface area over time.

Chapter 3 also evaluated the effect of non-ionic surfactants characterized by HLB value and their effect on electrospun and emulsion electrospun mesh characteristics and emulsion stability. Interestingly, increasing HLB value was correlated with increasing fiber diameter in full samples with no internal phase and internal phase. In samples with internal phase, it is likely correlated to internal phase droplet size and remaining surfactant at the surface of the fibers. In samples with no internal phase, this increase in fiber diameter may indicate that surfactants with a higher affinity for the oil-air interface may be more effective at lowering surface tension in the electrospinning Taylor cone. Further studies should measure this surface tension for samples with non-ionic surfactants in oil at increasing concentrations. Studies could also evaluate how surface tension is affecting the Taylor cone in electrospinning by using a high-speed camera to capture the Taylor cone at increasing concentrations of different non-ionic surfactants used in electrospinning.

Span 40 with an HLB value of 6.7 exhibited droplet formation when no internal phase was present in the solution. This may have been due to the highest amount of surface tension reduction at the Taylor cone, allowing the fiber to collect as droplets instead of fibers, or because of surfactant lowering the viscosity. This is promising because other methods to transition from electrospun fibers to electrospray particles involve reducing the viscosity of the polymer solution, decreasing conductivity, or increasing surface tension. Decreasing conductivity to transition to the electrospray region is difficult to control because insufficient conductivity also means low electrostatic repulsion to project the droplets towards the collection plate and can result in a wider distribution of particle sizes. An increase in surface tension is also difficult to modify in the

electrospinning system, and the most common way to produce electrospay particles is through lowering the solution viscosity. If the mechanism described for Span 40 can be controlled, this would create opportunities to fabricate particles with a higher viscosity solution. This would be valuable because it could lead to further control of encapsulated drugs within electrospun particles with the ability to further tune through surfactant chemistry and the internal phase of an emulsion. Future studies would need to reproducibly determine when this transition from fibers to particles occurs at surfactant concentrations, flow rates for sufficient volume in the Taylor cone, and other processing parameters. Visualization of this process through imaging the Taylor cone with a high-speed camera could also confirm this effect and better understand the mechanism for this transition.

Chapter 4 focused on the effect of internal phase volume fraction on the resulting electrospun mesh characteristics. Adding internal phase significantly decreased the fiber diameter in solvent systems containing  $\text{CHCl}_3$  and 3:1  $\text{CHCl}_3$ : DMF at both high and low relative humidity. Further understanding of phase separation at the needle tip could confirm if multiple fibers are occurring in some solvent systems through visualization of the Taylor cone with a high-speed camera. Additionally, imaging the internal architecture of these electrospun fibers could help understand how the internal phase is coalescing at different internal phase volume fractions. Initial work was conducted to cross-section fibers through cryofracturing in liquid nitrogen below the glass transition temperature ( $T_g = -60\text{C}$ ) of PCL, but the challenge is that with fibers below  $1\ \mu\text{m}$  in diameter, clear cross-sections are difficult to achieve as the ends undergo necking when tensile force is applied even in liquid nitrogen. Initial studies have been started to account for this by developing an apparatus that holds consistent tension across the mesh for cutting within liquid nitrogen. Another issue with cross-sectional imaging of fibers below  $1\ \mu\text{m}$  is despite sputter

coating the fibers, fibers will move when electrons from the SEM hit the fiber, making it difficult to image and reducing the voltage in the SEM makes the resolution of cross-sections difficult. Further understanding of the effective internal phase volume fraction through cross-sectional imaging may be possible by altering processing parameters or solution chemistry in order to achieve larger fiber diameters of emulsion electrospun fibers.

Chapter 5 focused on drug release from samples containing no surfactant and surfactant with different properties of the surface and internal architecture. Incorporating a model drug within samples containing surfactant reduced the burst effects of drug release for samples containing porous internal architecture and predominantly solid internal architecture. Longer-term studies evaluating subsequent release could determine how internal porosity may affect drug release rates. Controls for the studies should also be created to normalize the effect of surfactant, fiber diameter, fiber fraction, and media contact with the mesh.

Chapter 5 also focused on loading and drug release of a model hydrophilic and hydrophobic drug from monolithic, surfactant, and emulsion electrospun fibers with controlled fiber fraction and fiber diameter. Loading of hydrophobic drugs was higher in samples with samples containing no internal phase, while loading of hydrophilic drugs was higher in emulsion samples. Information on the relative loading of the drug was important because this technique is difficult to do with other traditional methods of drug release. Since only the loaded drug will fluoresce using this technique, the polymer and surfactant does not alter the amount of drug loading measured. Measuring drug concentration is difficult to do in drug release techniques that use UV-Vis because polymer and surfactant will affect the amount of light passing through a sample and, therefore, the concentration measurement. However, measuring drug release with fluorescent molecules is challenging because photobleaching can occur over time, and the surfactant fluorescence is

dampened by interactions with polymer and surfactant. Standard curves of drug with known amounts of surfactant and polymer can account for interactions and dampening of fluorescence. However, drug release was above 100% for many samples because the drug release data was gathered before the loading data. Therefore, the samples used to determine the amount of drug loaded likely underwent a degree of photobleaching which does not change the trend in the data but would reduce the amount of loaded drug measured and contribute to the release amounts above 100%. Further studies could account for this by running all studies in an environment with no light that will cause photobleaching.

Furthermore, the hydrophilic model drug used, rhodamine B, was partially soluble in chloroform, indicating that some of the drug may have been in the continuous phase. Further studies could include a third model drug that is only soluble in the aqueous phase to understand encapsulation based on polymer-solvent drug compatibility fully. Also, all studies could be run at high relative humidity to understand the effects that vapor-induced phase separation may play in drug release and phase separation. Finally, rhodamine B release after one hour was marginal. To fully understand the rate of release beyond the burst and initial release effects would help in understanding the bulk diffusion and degradation differences of release from different types of mesh by measuring release rates over a longer period of time, such as several weeks.

Including a non-ionic surfactant improved burst release effect in all cases. This indicates that including surfactants in electrospun fibers with tailored chemistry to match the drug and solution chemistry could improve control of release. Furthermore, initial studies indicate that surfactant may help solubilize hydrophilic drugs within hydrophobic polymer-solvent complexes, which is promising for improving encapsulation of drugs in fibers.



While additional studies and challenges exist before emulsion electrospun fibers may be implanted in the body for tissue regeneration and fully control for drug release applications, a mechanistic understanding of the compositional components in emulsion electrospun fibers and their effect on electrospinning has been developed to control emulsion electrospun fibers. Altering the continuous phase solvent chemistry, surfactant chemistry, and location within the fiber, internal phase volume fraction, and drug release study design has created a platform for further studies and understanding of the effects on resulting mesh characteristics. Overall, emulsion electrospun fibers have the potential to be used in tissue engineering applications to control cell response and encapsulate drugs and bioactive molecules for tunable and controlled drug release.